VOLUME 78 JANUARY 3, 1974 NUMBER 1

JPCHAx

THE JOURNAL OF PHYSICAL CHEMISTRY

PUBLISHED BIWEEKLY BY THE AMERICAN CHEMICAL SOCIETY

THE JOURNAL OF

PHYSICAL CHEMISTRY

AMERICAN CHEMICAL SOCIETY, *1155 Sixteenth St., N.W., Washington, D.C. 20036*

Books and Journals Division

JOHN K CRUM *Director*
RUTH REYNARD *Assistant to the Director*

CHARLES R. BERTSCH *Head, Editorial Processing Department*
D. H. MICHAEL BOWEN *Head, Journals Department*
BACIL GUILEY *Head, Graphics and Production Department*
SELDON W. TERRANT *Head, Research and Development Department.*

All manuscripts should be sent to *The Journal of Physical Chemistry*, Department of Chemistry, University of Minnesota, Minneapolis, Minn. 55455.

Additions and Corrections are published once yearly in the final issue. See Volume 77, Number 26 for the proper form.

Extensive or unusual alterations in an article after it has been set in type are made at the author's expense, and it is understood that by requesting such alterations the author agrees to defray the cost thereof.

The American Chemical Society and the Editor of *The Journal of Physical Chemistry* assume no responsibility for the statements and opinions advanced by contributors.

Correspondence regarding accepted copy, proofs, and reprints should be directed to Editorial Processing Department, American Chemical Society, 20th and Northampton Sts., Easton, Pa. 18042. Head: CHARLES R. BERTSCH. Assistant Editor: EDWARD A. BORGER. Editorial Assistant: JOSEPH E. YURVATI.

Advertising Office: Centcom, Ltd., 142 East Avenue, Norwalk, Conn. 06851.

Business and Subscription Information

Send all new and renewal subscriptions *with payment* to: Office of the Controller, 1155 16th Street, N.W., Washington, D.C. 20036. Subscriptions should be renewed promptly to avoid a break in your series. All correspondence and telephone calls regarding changes of address, claims for missing issues, subscription service, the status of records, and accounts should be directed to Manager, Membership and Subscription Services, American Chemical Society, P.O. Box 3337, Columbus, Ohio 43210. Telephone (614) 421-7230.

On changes of address, include both old and new addresses with ZIP code numbers, accompanied by mailing label from a recent issue. Allow four weeks for change to become effective.

Claims for missing numbers will not be allowed (1) if loss was due to failure of notice of change in address to be received before the date specified, (2) if received more than sixty days from date of issue plus time normally required for postal delivery of journal and claim, or (3) if the reason for the claim is "issue missing from files."

Subscription rates (1974): members of the American Chemical Society, $20.00 for 1 year; to nonmembers, $60.00 for 1 year. Those interested in becoming members should write to the Admissions Department, American Chemical Society, 1155 Sixteenth St., N.W., Washington, D.C. 20036. Postage to Canada and countries in the Pan-American Union, $5.00; all other countries, $6.00. Single copies for current year: $3.00. Rates for back issues from Volume 56 to date are available from the Special Issues Sales Department, 1155 Sixteenth St., N.W., Washington, D.C. 20036.

Subscriptions to this and the other ACS periodical publications are available on microfilm. Supplementary material not printed in this journal is now available in microfiche form on a current subscription basis. For information on microfilm or microfiche subscriptions, write Special Issues Sales Department at the address above.

Notice to Authors last printed in the issue of December 6, 1973

From the borders of organic chemistry . . . To the borders of theoretical physics:

Inorganic Chemistry brings you a broad range of authoritative information presenting both experimental and theoretical studies in all phases of inorganic chemistry.

Each month, this rapidly growing journal brings you the data you need on synthesis and properties of new compounds, quantitative studies regarding structure, and thermodynamics of inorganic reactions.

When you've seen the 50 or more papers offered in each issue, you'll also want to look through the Notes and Correspondence sections for their concise exchange of scientific views and ideas.

To order INORGANIC CHEMISTRY today, just complete and return the form below.

. . *another ACS service*

Inorganic Chemistry

Inorganic Chemistry
American Chemical Society
1155 Sixteenth Street, N.W.
Washington, D.C. 20036

Yes, I would like to receive INORGANIC CHEMISTRY at the one-year rate checked below:

	U.S.	*Canada*	*Latin America*	*Other Nations*
ACS Member Personal-Use One-Year Rate	☐ $18.00	☐ $22.00	☐ $22.00	☐ $23.00
Nonmember	☐ $54.00	☐ $58.00	☐ $58.00	☐ $59.00

Bill me ☐ Bill company ☐ Payment enclosed ☐

Name

Street Home ☐ Business ☐

City State Zip

P-73

THE JOURNAL OF

PHYSICAL CHEMISTRY

Volume 78, Number 1 January 3, 1974

JPCHAx 78(1) 1-92 (1974)
ISSN 0022-3654

COMMUNICATIONS TO THE EDITOR

■ Supplementary material for this paper is available separately, in photocopy of microfiche form. Ordering information is given in the paper.

* In papers with more than one author, the asterisk indicates the name of the author to whom inquiries about the paper should be addressed.

AUTHOR INDEX

THE JOURNAL OF
PHYSICAL CHEMISTRY

VOLUME 78, NUMBER 1 JANUARY 3, 1974

Photolysis of Nitric Acid Vapor

Harold S. Johnston,* Shih-Ger Chang, and Gary Whitten

Department of Chemistry, University of California, Berkeley, and Inorganic Materials Research Division, Lawrence Berkeley Laboratory, Berkeley, California 94720 *(Received July 16, 1973)*

The primary reaction in the photolysis of nitric acid vapor by ultraviolet radiation is $HNO_3 + h\nu \rightarrow HO + NO_2$ and the primary quantum yield is 1. This article gives experimental evidence in favor of these two conclusions for the wavelengths 200, 255, 290, and 300 nm. The photolysis of nitric acid vapor in laboratory apparatus is subject to several unwanted side reactions, and conditions must be carefully selected to eliminate the effect of such reactions.

Introduction

Nitric acid has been observed in the stratosphere by Murcray, *et al.*[1] It is presumably formed from hydroxyl radicals and nitrogen dioxide

$$HO + NO_2 \xrightarrow{M} HNO_3$$

and it may also be formed by gaseous dinitrogen pentoxide abstracting water from aqueous sulfuric acid droplets

$$N_2O_5 + H_2O \xrightarrow[\text{particles}]{\text{on}} 2HNO_3$$

The maximum mole fraction of nitric acid vapor is found between 20 and 24 km. The decreasing mole fraction above the maximum is probably caused by the photolysis of nitric acid vapor. Recently the absorption spectrum of nitric acid vapor has been obtained.[2] However, quantitative modeling calculations of the photolysis of nitric acid in the stratosphere require knowledge of the products of the primary photochemical reaction and the quantum yield as a function of wavelength. The primary products could be

$$HNO_3 + h\nu \longrightarrow HO + NO_2$$
$$\longrightarrow H + NO_3$$
$$\longrightarrow O + HNO_2$$

Berces and Forgeteg[3] reported a quantum yield of about 0.1 at 265 nm, but their conclusions involved assumed values of other rate constants that have since been shown by Morris and Niki[4] to be in error by several orders of magnitude. The purpose of this study was to identify the primary products and obtain the primary quantum yield for the photolysis of nitric acid vapor by ultraviolet radiation.

Experimental Section

Materials. Anhydrous nitric acid was prepared by vacuum distillation from a 50–50 slurry of concentrated sulfuric acid and sodium nitrate. The high temperature should not exceed 30° in order to avoid the thermal decomposition of liquid nitric acid to form nitrogen dioxide, and the low temperature should not be below −40° to avoid distillation of water from the concentrated sulfuric acid. The pure nitric acid was completely colorless, and it remained pure indefinitely when stored at Dry Ice temperature and in the dark. The oxygen (Matheson, research grade) was passed through traps at Dry Ice temperature. Carbon monoxide (Matheson UHP grade) was passed through a 5-ft long column of activated charcoal on glass wool in order to remove iron carbonyl.

Apparatus. The glass vacuum apparatus was of conventional design. Stopcocks were lubricated with Kel-F stopcock grease, which is inert to nitric acid, or were of the nonlubricated variety with a Teflon plug and Viton O rings. Pressures were measured by a Pace transducer, which we calibrated against an oil manometer. The reaction cells were cylindrical, 100 mm in length, and 35 mm in diameter. Two grease-free stopcocks with Viton O rings were sealed to the cell with quartz-to-glass graded seals. The silica windows were fused to the cell.

Several different light sources were used: a 50-W deuterium arc at 200 and 215 nm with a Bausch and Lomb high-intensity grating monochromator; a 200-W high-pressure mercury arc with the same monochromator; a 1600-W xenon arc with a 500-mm Bausch and Lomb monochromator. Light intensities were measured by two methods: (1) potassium ferrioxalate actinometry[5] above 255 nm and HBr photolysis actinometry[6] at 200 and 215 nm and (2) a Hewlett-Packard 8330-A radiant fluxmeter. The intensi-

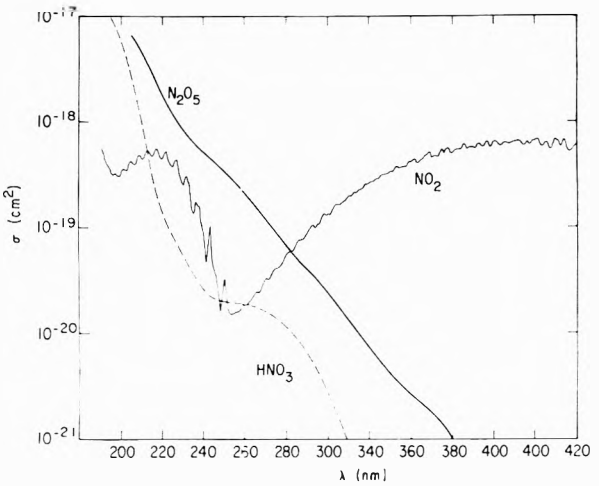

Figure 1. Ultraviolet absorption spectra of HNO_3, NO_2, and N_2O_5: $\ln I_0/I = \sigma NL$, where σ has units cm^2, L cm, and N molecules cm^{-3}.

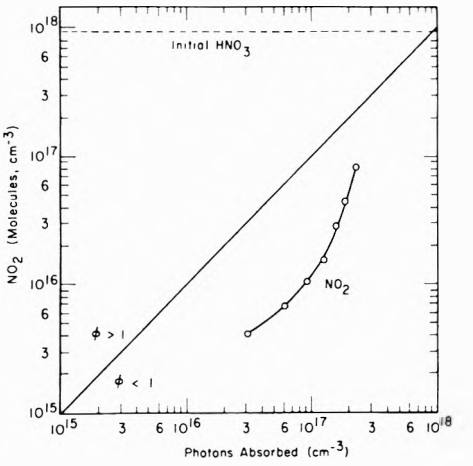

Figure 2. Photolysis of pure nitric acid vapor with 290-nm ultraviolet radiation. The straight line corresponds to unit quantum yield. The formation of NO_2 from pure HNO_3 occurs with a quantum yield much less than 1.

ties obtained by these methods were in good agreement, but all quantitative data are based on the chemical actinometry. The optical band width (full width at half-maximum) was 2.2 nm at 300 nm, 6.5 nm at 290 nm, 2.5 nm at 255 nm, and 6.5 nm below 225 nm.

Procedure. Three types of runs were carried out: (1) with pure nitric acid alone, (2) with nitric acid plus carbon monoxide, and (3) with nitric acid plus carbon monoxide and oxygen. Nitrogen dioxide in the cell was measured by stopping the photolysis, by transferring the reaction cell to a Beckman DU or a Cary 14 spectrophotometer, and by measuring optical density at 405 nm ($\sigma = 6.24 \times 10^{-19}$ cm^2 $molecule^{-1}$, compare Figure 1). The carbon dioxide produced was measured in a Consolidated Electronics Corporation 21-110 high-resolution mass spectrometer. Appropriate blanks were measured with no photolysis. Most runs were carried to only very small degrees of conversion (1 or 2%), and thus it was not practicable to follow the course of the reaction in terms of disappearance of HNO_3 or of CO. The course of the reaction was followed from time to time by optical analysis of NO_2 formed; or it was followed by ending the run, freezing out the nitric acid, and analyzing the CO and CO_2 with the mass spectrometer. All runs were made at 25°.

Results and Discussion

The photolysis of nitric acid vapor was studied at 25° with initial nitric acid pressures between 5 and 40 Torr. During the course of the photolysis at 40 Torr of HNO_3, it was noticed that liquid droplets (presumably aqueous nitric acid) condensed out on the walls of the reaction cell, and all runs at 40 Torr have been rejected. At 5 Torr of HNO_3 the rate of formation of products was exceedingly slow. Most runs were made at 15 or 30 Torr.

Photolyses were carried out at wavelengths between 200 and 315 nm. The absorption spectrum of NO_2, HNO_3, and N_2O_5 is given as Figure 1. At all wavelengths the absorption cross section of N_2O_5 is substantially greater than that of HNO_3, and thus secondary photolysis of N_2O_5 is a complicating feature of certain experiments. The absorption spectrum of NO_2 occurs in two bands, above and below 250 nm. Between about 250 and 400 nm the product of the photolysis of NO_2 is NO and ground-state oxygen atoms, $O(^3P)$. Below 250 nm the product of the photolysis of NO_2 is NO and an excited singlet oxygen atom, $O(^1D)$.[7] The excited singlet oxygen atom reacts very rapidly with H_2O, H_2, CH_4, etc.[8] and presumably it would react very rapidly with HNO_3. On the other hand, the ground-state oxygen atom, $O(^3P)$, reacts very slowly (if at all) with nitric acid vapor.[4] Thus the reactions following the secondary photolysis of the product NO_2 are quite different above and below 250 nm. Most runs were made at 255 nm (where the cross section for light absorption by HNO_3 is greater than that for NO_2) or at 290 or 300 nm (where the cross section of NO_2 greatly exceeds that of HNO_3). At 200 nm the cross section of HNO_3 greatly exceeds that of NO_2, and successful runs were made at this wavelength.

A series of photolyses was carried out at 290-nm radiation, 30 Torr of pure HNO_3, and the progress of the reaction was followed by light absorption by NO_2. The results are given in Figure 2 where the logarithm of concentration of NO_2 is plotted against the logarithm of photons absorbed per cm^3. The initial nitric acid concentration is indicated at the top of the figure. The primary quantum yield Φ is defined as

$$\Phi = \frac{\text{number of molecules of } HNO_3 \text{ destroyed}}{\text{number of photons absorbed by } HNO_3} \quad (1)$$

The quantum $\Phi(x)$ with respect to some product x is defined as

$$\Phi(x) = \frac{\text{number of molecules of x formed}}{\text{number of photons absorbed by } HNO_3} \quad (2)$$

If NO_2 were produced with a quantum yield of 1, the experimental points would lie on the 45° line given on the figure; points above the line would correspond to a quantum yield greater than 1; and points below the line correspond to quantum yields less than 1. The first four experimental points represent quantities of NO_2 which are less than 1% of the initial HNO_3 and the quantum yield for formation of NO_2 is about 0.1, in rather close agreement with the results of Berces and Forgeteg.[3] Our interpretation of the results, however, is quite different from that of Berces and Forgeteg.

These experimental results were interpreted by a model of 42 reactions (Table I) carried out by the complete Gear routine,[9] modified for this photochemical study. This discussion focuses on the dominant reactions to give the reader a qualitative understanding of what is involved; quantitative conclusions are based on the integration of

TABLE I: Reactions Considered

Reaction[a]	k (298°K)[b]
1. $HNO_3 \xrightarrow{h\nu} NO + NO_2$	
2. $HO + NO_2 + M \rightarrow HNO_3 + M$	4.0×10^{-12}[c]
3. $HO + HNO_3 \rightarrow H_2O + NO_3$	1.5×10^{-13}
4. $NO_2 + NO_3 + M \rightarrow N_2O_5 + M$	3.0×10^{-12}[c]
5. $N_2O_5 + M \rightarrow NO_2 + NO_3 + M$	0.10[c]
6. $NO_2 + NO_3 \rightarrow NO + O_2 + NO_2$	2.4×10^{-16}
7. $NO_3 + NO \rightarrow 2NO_2$	0.87×10^{-11}
8. $NO_2 \xrightarrow{h\nu} NO + O$	
9. $O + NO_2 \rightarrow NO + O_2$	9.1×10^{-12}
10. $O + NO + M \rightarrow NO_2 + M$	6.8×10^{-32}
11. $O + O_2 + M \rightarrow O_3 + M$	3.6×10^{-34}
12. $NO + O_3 \rightarrow NO_2 + O_2$	1.73×10^{-14}
13. $HO + CO \rightarrow H + CO_2$	1.88×10^{-13}
14. $H + NO_2 \rightarrow HO + NO$	4.8×10^{-11}
15. $H + O_2 + M \rightarrow HOO + M$	5.6×10^{-32}
16. $H + HNO_3 \rightarrow H_2 + NO_3$	$<10^{-15}$
$\rightarrow HO + HNO_2$	$<10^{-13}$
17. $HOO + NO \rightarrow NO_2 + HO$	2×10^{-13}
18. $HO + HO \rightarrow H_2O + O$	1.6×10^{-12}
19. $HO + HOO \rightarrow H_2O + O_2$	2×10^{-10}
20. $HOO + HOO \rightarrow H_2O_2 + O_2$	3.3×10^{-12}
21. $NO + NO + O_2 \rightarrow NO_2 + NO_2$	3.9×10^{-38}
22. $HO + NO + M \rightarrow HNO_2 + M$[c]	4.1×10^{-31}
23. $HNO_2 + HNO_2 \rightarrow H_2O + NO + NO_2$	1.24×10^{-17}
24. $H_2O_2 + HO \rightarrow H_2O + HOO$	7.9×10^{-13}
25. $H_2O_2 \xrightarrow{h\nu} HO + HO$	
26. $H_2O_2 + O \rightarrow HOO + HO$	9.0×10^{-16}
27. $H_2O_2 + O \rightarrow H_2O + O_2$	9.0×10^{-16}
28. $H_2O_2 + H \rightarrow H_2 + HOO$	4.8×10^{-15}
29. $H_2O_2 + H \rightarrow H_2O + HO$	4.8×10^{-15}
30. $O_3 + NO_2 \rightarrow NO_3 + O_2$	6.1×10^{-17}
31. $N_2O_5 \xrightarrow{h\nu} O + 2NO_2$	
32. $O + HNO_3 \rightarrow HO + NO_3$	$<2 \times 10^{-14}$
33. $HO + HNO_2 \rightarrow H_2O + NO_2$	6.8×10^{-12}
34. $O + N_2O_5 \rightarrow O_2 + 2NO_2$	2×10^{-13}
35. $HO + O \rightarrow H + O_2$	4.2×10^{-11}
36. $HOO + H \rightarrow H_2 + O_2$	1.3×10^{-11}
37. $HOO + H \rightarrow HO + HO$	1.7×10^{-11}
38. $NO + 2HNO_3 \rightarrow H_2O + 3NO_2$	Surface reaction
39. $N_2O_5 + H_2O \rightarrow 2HNO_3$	Surface reaction
40. $H_2O_2 + 2NO_2 \rightarrow 2HNO_3$	Surface reaction
41. $H_2O_2 + NO \rightarrow H_2O + NO_2$	Surface reaction
42. $HOO + NO_2 \rightarrow HNO_2 + O_2$[d]	2×10^{-13}

[a] References: reaction 23, S.-K. Neoh, unpublished results, this laboratory; reaction 42, ref 13; other cases, D. Garvin, Ed., National Bureau of Standards Report No. NBS-IR-203, May 1973. [b] Units are cm^3 molecule^{-1} sec^{-1} for second-order reactions and cm^6 molecule^{-2} sec^{-1} for third-order reactions. [c] A function of total gas concentration; this value refers to 1 atm total pressure of CO + O_2.

the full set of reactions. From the Gear integration of the 38 homogeneous reactions under the conditions of Figure 2, it was seen that for the first few experimental points, the predominant product is not NO_2, but N_2O_5.

$$HNO_3 + h\nu \longrightarrow HO + NO_2 \quad (3a)$$

$$HO + HNO_3 \longrightarrow H_2O + NO_3 \quad (3b)$$

$$NO_2 + NO_3 \xrightarrow{M} N_2O_5 \quad (3c)$$

Berces and Forgeteg[3] looked for N_2O_5 in their reaction cells but found none. We have observed repeatedly that N_2O_5 reacts fairly rapidly with water on the walls of reaction cells to produce nitric acid

$$N_2O_5 + H_2O \xrightarrow{W} 2HNO_3 \quad (3d)$$

where W signifies a reaction on the walls of the cell. The net result of these four reactions is to return all photolysis products back to the starting material; all quantum yields are zero by this four-step mechanism.

The observed quantum yield of NO_2 is about 0.1, however. This formation of products occurs by way of (a) the photolysis of N_2O_5

$$N_2O_5 + h\nu \longrightarrow 2NO_2 + O \text{ (assumed products)} \quad (4a)$$

(b) the photolysis of NO_2 and by its reaction with oxygen atoms

$$NO_2 + h\nu \longrightarrow NO + O \quad (4b)$$

$$NO_2 + O \longrightarrow NO + O_2 \quad (4c)$$

(c) the fast reaction of NO with N_2O_5 which occurs *via* the mechanism

$$N_2O_5 \xrightarrow{M} NO_2 + NO_3 \quad (4d)$$

$$NO + NO_3 \longrightarrow 2NO_2 \quad (4e)$$

$$\text{net } NO + N_2O_5 \longrightarrow 3NO_2$$

(d) the thermal decomposition of N_2O_5

$$N_2O_5 \overset{M}{\rightleftharpoons} NO_2 + NO_3 \quad (4f)$$

$$NO_2 + NO_3 \longrightarrow NO + O_2 + NO_2$$

$$NO + NO_3 \longrightarrow 2NO_2$$

$$\text{net } 2N_2O_5 \longrightarrow 4NO_2 + O_2$$

These numerous, relatively slow, secondary reactions 4 compete with the reconversion of N_2O_5 to HNO_3 by reaction 3d, giving the small observed quantum yield of about 0.1.

The detailed calculations of the homogeneous reactions show that N_2O_5 decreases precipitously during the course of the photolysis in Figure 2. Because of the great speed of the reaction of NO with N_2O_5, these two species are incompatible with each other. The photolysis of NO_2 (compare Figure 1) forms NO which destroys N_2O_5. At the midpoint of the observed points in Figure 2, N_2O_5 has been reduced to a very low level, the back reaction (3d) no longer occurs, and the slope of the line curves upward. Late in the reaction NO_2 is being produced much faster than nitric acid is being photolyzed. According to the detailed mechanism and in terms of homogeneous reactions, nitric oxide exceeds NO_2 after 10^{17} photons have been absorbed per cm^3. As noted by Smith,[10] NO reacts at a moderate rate with nitric acid as a heterogeneous reaction on the walls of the reaction cell

$$NO + 2HNO_3 \xrightarrow{W} H_2O + 3NO_2 \quad (5)$$

The rapid increase in NO_2 during the last half of the observed points in Figure 2 results from the photolysis of NO_2 (reactions 4b,c) to form NO and the reaction of this NO with nitric acid.

These considerations show that the direct photolysis of pure nitric acid vapor is an unsuitable method for obtaining the primary quantum yield. During the early stages of the reaction the results are dominated by a heterogeneous reaction (3d) that gives a quantum yield of NO_2 much less than the primary quantum yield, and during late stages of the reaction the results are dominated by another heterogeneous reaction (5), which in conjunction with reaction 4 gives a chain reaction for destroying HNO_3.

It is well known that carbon monoxide reacts rapidly with hydroxyl radicals to produce carbon dioxide.[11] Thus

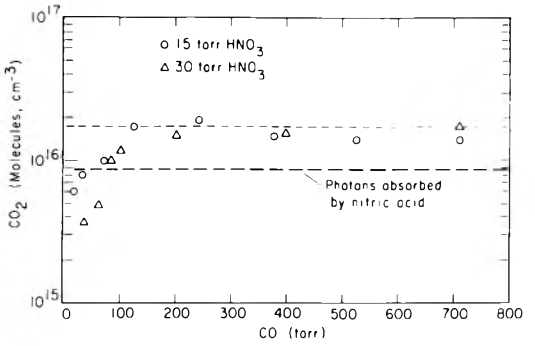

Figure 3. Photolysis of nitric acid vapor in the presence of carbon monoxide with 8.7 × 10^{15} photons cm^{-3} absorbed by HNO_3, 290-nm wavelength. The lower dashed line corresponds to a quantum yield for CO_2 of 1; the upper dashed line corresponds to a quantum yield of 2.

the formation of carbon dioxide gives a sensitive method to detect the rate of production of HO, presumably the rate of the primary photochemical process

$$HNO_3 + h\nu \longrightarrow HO + NO_2 \qquad (3a)$$

For this discussion we assume this primary quantum yield to be 1. To the extent that the hydroxyl radical reacts with nitric acid

$$\text{(a)}\quad HO + HNO_3 \longrightarrow H_2O + NO_3 \qquad (3b)$$

the quantum yield for formation of carbon dioxide is 0

$$\Phi_a(CO_2) = 0$$

The reaction of the hydroxyl radical with carbon monoxide

$$\text{(b)}\quad HO + CO \longrightarrow CO_2 + H$$

contributes unit quantum yield to carbon dioxide formation

$$\Phi_b(CO_2) = 1$$

What happens to the hydrogen atom determines the total quantum yield of CO_2. If the hydrogen atom reacts with nitrogen dioxide

$$\text{(c)}\quad H - NO_2 \longrightarrow HO + NO$$

the quantum yield is

$$\Phi_{bcb}(CO_2) = 2$$

If the hydrogen atom reacts with nitric acid to form H_2

$$\text{(d)}\quad H + HNO_3 \longrightarrow H_2 + NO_3$$

the total quantum yield of CO_2 is 1

$$\Phi_{bd}(CO_2) = 1$$

If the hydrogen atom reacts with nitric acid to form HO, there is a chain reaction that produces carbon dioxide

$$\begin{array}{ll} \text{(b)} & HO + CO \longrightarrow CO_2 + H \\ \text{(e)} & H + HNO_3 \longrightarrow HO + HNO_3 \\ \hline \text{net} & HNO_3 + CO \longrightarrow CO_2 + HNO_3 \end{array} \qquad (6)$$

In this case the quantum yield could be indefinitely large

$$\Phi_{be}(CO_2) \gg 1$$

Berces, Forgeteg, and Marta[12] interpreted their data on added CO in terms of a primary quantum yield of 0.1 and a chain length of reactions b, e up to 17. The rate constant that they required for reaction e was 10^{-12} cm^3 $molecule^{-1}$ sec^{-1}. Morris and Niki[4] attempted to measure this rate constant, but they were unable to detect it. From the sensitivity of their experiment, they found that reactions e plus d must be at least 10 times and probably 100 times slower than the value used by Berces, Forgeteg, and Marta.[12] Thus, the predominant mechanism is bcb, and the quantum yield for formation of CO_2 at small degrees of conversion of HNO_3 is expected to approach 2 for a great excess of carbon monoxide over nitric acid.

TABLE II: Effect of Wavelength on the Quantum Yield of Formation of Carbon Dioxide with Approximately Equal Nitric Acid and Carbon Monoxide

λ, nm	Photons absorbed, 10^{16} cm^{-1}	HNO_3, Torr	CO, Torr	$\Phi(CO_2)$	NO_2 Product
315	1.75	29	33	0.39	$O(^3P)$
300	0.55	26	26	0.43	
290	0.92	30	40	0.43	
290	2.33	30	28	0.25	
290	3.08	30	29	0.30	
280	0.83	27	24	0.26	
225	1.16	29	30	1.31	$O(^1D)$
215	2.25	30	18	2.2	
215	0.08	16	29	1.8	
215	0.72	15	28	1.0	
200	0.54	9	11	0.98	

A series of experiments was carried out with either 15 or 30 Torr of HNO_3 and with various amounts of CO from 30 to 700 Torr. The wavelength was 290 nm, and (8.8 ± 0.2) × 10^{15} photons cm^{-3} were absorbed in each case. From Figure 2 this can be seen to be about 1% of the nitric acid present at 30 Torr and about 2% at 15 Torr. Thus these experiments represent initial conditions, and the effect of nitric oxide reacting with nitric acid was minimized. The ratio of CO_2/CO was measured on a mass spectrometer. The concentration of CO_2 produced as a function of initial carbon monoxide is given as Figure 3. At large excess CO, the quantum yield approaches 2, as expected from mechanism bcb. The quantum yield is less than 2 for small amount of CO, as expected from the competition of HNO_3 and CO for the available HO radical. These results strongly indicate that the primary quantum yield for the photolysis of nitric acid is 1 at 290 nm, since the quantum yield for formation of CO_2 becomes 2 with excess CO over HNO_3.

The most complicated condition is that of about equal HNO_3 and CO. In this case some N_2O_5 is formed, some NO_2 is formed, and the quantum yield for forming CO_2 is 0.4 ± 0.1. This complicated condition was chosen for a study of the effect of wavelength, Table II. In the wavelength region where the photolysis of NO_2 leads to $O(^3P)$, the quantum yield of formation of CO_2 is around 0.3 to 0.4. At short wavelengths where photolysis of NO_2 leads to $O(^1D)$, the quantum yield for formation of CO_2 is between 0.98 and 2.2. This increase in quantum yield appears to arise from

$$\begin{gathered} HNO_3 + h\nu \longrightarrow HO + NO_2 \\ NO_2 + h\nu \longrightarrow NO + O(^1D) \\ O(^1D) + HNO_3 \longrightarrow HO + NO_3, \text{ etc.} \end{gathered} \qquad (7)$$

In view of the lack of rate constant for the $O(^1D)$ reactions with HNO_3, it is not possible to do complete model calculations on this system. It was decided to work primarily on the relatively simple system where photolysis of NO_2 produces $O(^3P)$.

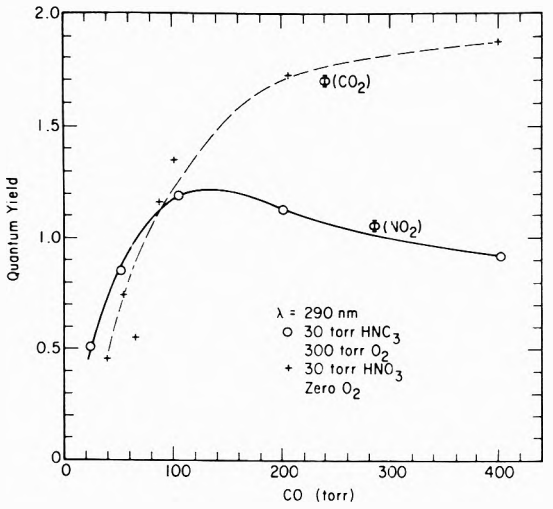

Figure 4. Photolysis of nitric acid vapor with added CO and with added CO and O_2, 290-nm radiation. The quantum yield of CO_2 is in a system with added CO but no added O_2. The quantum yield of NO_2 is in a system with added CO and with 300 Torr of O_2. Note the parallelism between $\Phi(CO_2)$ and $\Phi(NO_2)$ below 100 Torr of CO. With excess CO, the quantum yield of CO_2 approaches 2 and the quantum yield of NO_2 approaches 1.

In the system with added CO, there is some ambiguity about the fate of the hydrogen atom, NO_2 is stripped down to NO, and the role of the heterogeneous reaction between NO and HNO_3 is uncertain. If excess oxygen is added to the system, the hydrogen atom will be trapped to form HOO, the oxygen atom from the photolysis of NO_2 will add to molecular oxygen to form ozone, and both HOO and O_3 rapidly convert NO to NO_2, reducing the impact of the NO-HNO_3 reaction. From the values of the rate constants for H + NO_2 and H + O_2 + M, it can be seen that several hundred Torr of oxygen are needed to suppress the reaction of H with NO_2. The optimum amount of carbon monoxide was found by varying CO from 23 to 400 Torr at a constant 300 Torr of O_2. The quantum yield for the formation of nitrogen dioxide is given by Figure 4, where the degree of dissociation of HNO_3 is 1%. On this figure the quantum yield for formation of CO_2 from the situation with no added oxygen (Figure 3) is plotted against CO, and the quantum yield for forming NO_2 with 300 Torr of oxygen is plotted on the same scale.

At small concentrations of CO there is a striking parallel between quantum yield to produce CO_2 and to produce NO_2. The reason for this parallelism is given in terms of the competition between HNO_3 and CO for the hydroxyl radical. The fraction of reaction of HO with HNO_3 is given as α

$$(\alpha)\ HO + HNO_3 \longrightarrow H_2O + NO_3 \xrightarrow{NO_2} N_2O_5 \xrightarrow{H_2O} 2HNO_3 \quad (8)$$

and the fractional reaction of HO with CO is

$$(1-\alpha)\ HO + CO \longrightarrow CO_2 + H \xrightarrow{O_2} \tfrac{1}{2}H_2O_2 + \tfrac{1}{2}O_2 \quad (9)$$

The quantum yield to form carbon dioxide is

$$\phi(CO_2) = (1-\alpha) \quad (10)$$

The quantum yield to form nitrogen dioxide is

$$\Phi(NO_2) = 1-(\alpha) = (1-\alpha) = \Phi(CO_2) \quad (11)$$

Thus to the first approximation, the quantum yields to form CO_2 and NO_2 are equal and in the limit of excess

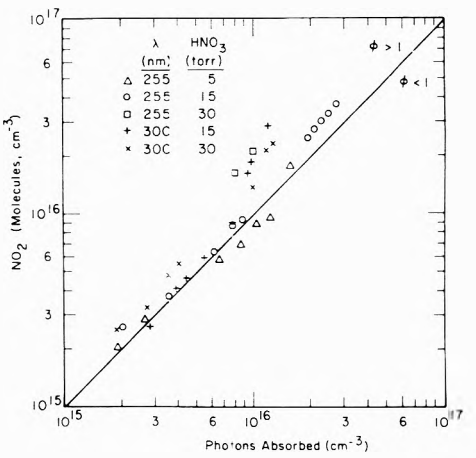

Figure 5. Photolysis (255 and 300 nm) of nitric acid vapor in the presence of excess CO and excess O_2, at different wavelengths, and at different initial pressures of HNO_3. The straight line corresponds to unit quantum yield.

CO the quantum yield of NO_2 approaches the primary Φ of HNO_3. However, when HO reacts with HNO_3, N_2O_5 is formed, and its reactions with NO, O, H, and $h\nu$ produce some additional NO_2. These secondary reactions of N_2O_5 cause the initial yield of NO_2 to exceed that of CO_2 (Figure 4), and they lead to a quantum yield of NO_2 somewhat greater than 1 when CO is about 100 Torr. However, when both CO and O_2 are about 300-400 Torr, this exceedingly complicated system becomes surprisingly simple.

If the primary photolysis of nitric acid yielded a hydrogen atom

$$HNO_3 + h\nu \longrightarrow H + NO_3$$

the added oxygen would remove the hydrogen atom and any NO_2 present would be converted to N_2O_5 and then to nitric acid.

$$H + O_2 \xrightarrow{M} HOO \longrightarrow \tfrac{1}{2}H_2O_2 + \tfrac{1}{2}O_2$$

$$NO_3 + NO_2 \xrightarrow{M} N_2O_5 \xrightarrow{H_2O} 2HNO_3$$

Even with added CO, the quantum yield both to produce NO_2 and to produce CO_2 would approach zero with excess oxygen. Thus the primary photochemical reaction is not to produce H and NO_3.

If the primary photolysis of nitric acid yielded an oxygen atom and nitrous acid

$$HNO_3 + h\nu \longrightarrow O + HNO_2$$

there would not be a large production of CO_2. The primary photochemical reaction thus appears to be

$$HNO_3 + h\nu \longrightarrow HO + NO_2$$

Detailed calculations with a model of 38 homogeneous reactions showed that with 400 Torr of O_2 and 300 Torr of CO, there was only a very small contribution from N_2O_5, NO, or HNO_2 both to the composition of the products and to the reaction rates. The quantum yield of NO_2 should be very close to the primary quantum yield of HNO_3. The experimental data for various pressures of nitric acid (5, 15, and 30 Torr) at 255-nm wavelength and with 400 Torr of O_2 and 300 Torr of CO are plotted on Figure 5. Also included is a comparison between 255- and 300-nm radiation for 15 and 30 Torr of HNO_3. A similar plot for 200-nm radiation is presented as Figure 6, where both CO_2

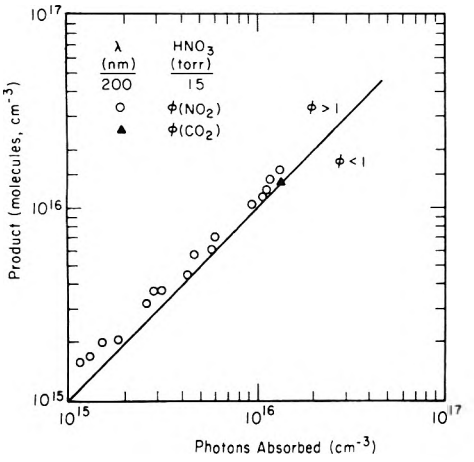

Figure 6. Photolysis (200 nm) of nitric acid vapor in the presence of excess CO and excess O_2, at different wavelengths, and at different initial pressures of HNO_3. The straight line corresponds to unit quantum yield.

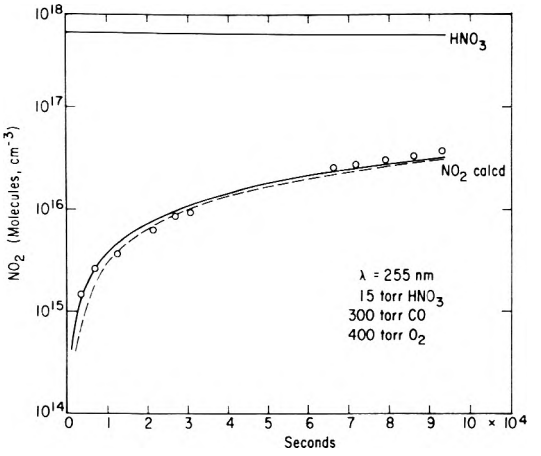

Figure 7. The buildup of NO_2 during one photolysis with excess CO and excess O_2. The calculated curve is based on a mechanism of 37 homogeneous reactions as solved by the Gear program and on the assumption that $\Phi(-HNO_3)$ is 1. The smooth line omits reaction 42; the dashed line includes reaction 42.

and NO_2 yields are shown. Results are plotted as photons absorbed by nitric acid *vs.* molecules of NO_2 formed. The line corresponds to unit quantum yield. The region above the line corresponds to quantum yield greater than 1, and the region below the line corresponds to quantum yield less than 1. Regardless of wavelength (200, 255, or 300 nm) and regardless of initial pressure of nitric acid (5, 15, or 30 Torr), the experimental results gave a quantum yield of 1 for nitric acid conversions of less than 1%. For the cases with 15 Torr of HNO_3, the quantum yield of NO_2 at 255 nm was 1 up to 2% conversion of HNO_3, and it became slightly higher than 1 (about 1.2) for 4–6% conversion of HNO_3; but the quantum yield of NO_2 at 300 nm was 1 up to about 1.5% conversion of HNO_3 and rapidly rose to 2 as the conversion of HNO_3 exceeded 2%. From Figure 1 it can be seen that at 255 nm HNO_3 absorbs radiation about 1.5 times faster than NO_2; at 300 nm, NO_2 absorbs radiation 40 times faster than HNO_3; and at 200 nm HNO_3 absorbs radiation 20 times faster than NO_2. The rapid rise of NO_2 quantum yield above 2% HNO_3 conversion at 300 nm comes from the photolysis of NO_2 and the subsequent reaction of nitric oxide with nitric acid

$$NO_2 + h\nu \longrightarrow NO + O \qquad (12)$$

$$NO + 2HNO_3 \xrightarrow{W} H_2O + 3NO_2$$

Since results at all wavelengths agree very well below 1% conversion of HNO_3, it is reasonable to assume that this surface reaction is negligible under these conditions. Thus with added CO (which suppresses N_2O_5), added O_2 (which removes hydrogen atoms), and at low conversions, it appears that the quantum yield for formation of NO_2 is 1.0 between 200 and 300 nm.

In the discussion of mechanism above, we have looked at the computer print-out for the complete 38-reaction model and have discussed only the major factors involved in each case. In addition to the major reactions discussed there are numerous other reactions giving an effect of a few per cent in one sense or another. In Figure 7 we plot an extensive run with 15 Torr of HNO_3, 300 Torr of CO, 400 Torr of O_2, and at 255-nm radiation. The solid curve is based on the complete model of 37 homogeneous reactions and on the assumption that the primary quantum yield for the photolysis of nitric acid is 1; the dashed curve includes a reaction recently discovered by Simonaitis and Heicklen[13]

$$HOO + NO_2 \longrightarrow HNO_2 + O_2 \qquad (13)$$

The points are observations at various stages of the reaction up to 7% conversion of the original nitric acid. There is excellent agreement between calculated and observed results at the initial stage of conversion, at intermediate stages of conversion the observed points are somewhat below the calculated curve, and at high degrees of conversion the observed points are somewhat above the calculated curve.

The buildup of nitrogen dioxide in Figure 7 is very nearly the same with or without the reaction represented by eq 13. The nitrous acid formed by reaction 13 decomposes to give NO, NO_2, and H_2O, but there is enough HOO and O_3 in the system to convert the NO to NO_2. Reaction 13, however, has a very strong effect on the formation of hydrogen peroxide. Without reaction 13, hydrogen peroxide is calculated to be one of the major products. With the rate constant for reaction 13 assigned to be 2×10^{-13} cm^3 molecule^{-1} sec^{-1} (Simonaitis and Heicklen's[13] lower limit), H_2O_2 is reduced to a value less than 1% of the water formed. With these small amounts of hydrogen peroxide, the surface reactions[14]

$$NO + H_2O_2 \xrightarrow{W} H_2O + NO_2 \qquad (14)$$

$$2NO_2 + H_2O_2 \xrightarrow{W} 2HNO_3 \qquad (15)$$

are unimportant in this system.

Conclusions

The primary reaction in the photolysis of nitric acid vapor is

$$HNO_3 + h\nu \longrightarrow HO + NO_2$$

and the primary quantum yield is 1 at all wavelengths between 200 and 315 nm. These conclusions are based on studies with added excess carbon monoxide and oxygen, which suppress unwanted secondary reactions. These secondary reactions are the reaction of hydroxyl radicals with nitric acid and the photolysis of nitrogen dioxide. The reaction of HO with HNO_3 leads to water and N_2O_5, which react on the surface to re-form HNO_3. The photoly-

sis of NO_2 below 250 nm yields $O(^1D)$, which reacts with HNO_3 at an unknown rate. The photolysis of NO_2 at all wavelengths produces nitric oxide which reacts heterogeneously with nitric acid. Quantitative results are obtained only under conditions where this secondary reaction is effectively eliminated. The experimental conditions with most nearly negligible side reactions were the following: 255 nm, the wavelength of minimum NO_2 absorption; degree of reaction less than 1%; and added excess CO and O_2 to quench undesirable secondary reactions. A firm base line was established under these most favorable conditions, and it was then possible to extend the conclusions to other wavelengths and to other conditions.

Acknowledgment. This work was supported by the Climatic Impact Assessment Program by means of an interagency agreement between the Department of Transportation and the Atomic Energy Commission through the Inorganic Materials Research Division, Lawrence Berkeley Laboratory. We are grateful to Lawrence Livermore Laboratory for providing us with their Gear-B computer program, to Mr. R. Graham for the NO_2 and N_2O_5 spectra, and to Dr. Charles Koch for the mass spectra.

References and Notes

(1) D. G. Murcray, A. Goldman, F. G. Murcray, W. J. Williams, J. N. Brooks, and D. B. Barker, AIAA 11th Aerospace Science Meeting, Washington, D. C. Jan 10–12, 1973.
(2) H. S. Johnston and R. Graham, *J. Phys. Chem.*, **77** 62 (1973).
(3) T. Berces and S. Forgeteg, *Trans. Faraday Soc.*, **66**, 633 (1970).
(4) E. D. Morris, Jr., and H. Niki, *J. Phys. Chem.*, **75**, 3193 (1971).
(5) (a) G. G. Hatchard and C. A. Parker, *Proc. Roy. Soc., Ser. A*, **235**, 518 (1956); (b) J. H. Baxendale and N. K. Bridge, *J. Phys. Chem.*, **59**, 787 (1955).
(6) Von E. Warburg, *Sitzungsber. Preuss. Akad. Wiss.*, **314** (1916).
(7) R. Simonaitis and J. Heicklen, *Int. J. Chem. Kinet.*, **4**, 529 (1972).
(8) G. Paraskevopoulos, V. B. Symonds, and R. J. Cvetanovic, *Can. J. Chem.*, **50**, 1838 (1972), and references cited therein.
(9) C. W. Gear, *Proc. Int. Fed. Inform. Proc. Congr.*, A-81 (1968).
(10) J. H. Smith, *J. Amer. Chem. Soc.*, **69**, 1741 (1947).
(11) W. E. Wilson, Jr., *J. Phys. Chem. Ref. Data*, **1**, 535 (1972).
(12) T. Berces, S. Forgeteg, and F. Marta, *Trans. Faraday Soc.*, **66**, 648 (1970).
(13) R. Simonaitis and J. Heicklen, private communication.
(14) D. Gray, E. Lissi, and J. Heicklen, *J. Phys. Chem.*, **76**, 1919 (1972).

Photophysics of Isolated Molecules. Disubstituted Benzenes

Mark G. Rockley and David Phillips*

Department of Chemistry, The University, Southampton SO9 5NH, England *(Received June 14, 1973)*

Fluorescence quantum yields and decay times of o-, *m*-, *p*-fluorotoluene, o-, *m*-, *p*-fluorobenzotrifluoride and *m*- and *p*-hexafluoroxylene in the gas phase at low pressures are reported. The variation in rate constant for radiative and nonradiative decay with increasing vibrational energy in the singlet manifold is discussed in relation to results for benzene and to current theories of nonradiative decay of aromatic molecules. In all cases k_R was found to decrease almost linearly with excess energy as would be expected either for excitation in successive members of a vibrational sequence, or if fast vibrational redistribution occurred, in which case the microcanonical average rate constant is observed. The variation in k_{NR} with excess energy can in all cases be explained on the basis of recent theory, from which it is concluded that frequency changes for the ν_1 vibration between the singlet and triplet manifolds are small, and comparable to benzene ($\sim$25 cm^{-1}), for all molecules studied except *m*- and *p*-fluorotoluene in which the changes are apparently much greater ($\sim$80 cm^{-1}).

Introduction

Recent detailed studies on the fluorescence of benzene,[1] perdeuteriobenzene,[2] and fluorobenzene[2] using narrow bandpass radiation for excitation and low pressures such that during its fluorescence lifetime the molecule suffers no collisions with the environment have provided a foundation for understanding the variations in nonradiative decay of these molecules upon excitation to single vibronic levels of the excited singlet state.[3] Similar studies on the simply substituted benzene have some experimental advantages in that the oscillator strength for the ground state to first excited singlet state is generally greater than that for benzene, leading to a shorter radiative decay time. Therefore, higher pressures can be used while still maintaining the "isolated molecule" conditions, with the added advantage of increased absorptivity. However, with the increase in complexity of the molecule there is a corresponding increase in complexity of the absorption spectrum. Thus, truly single vibronic level selection experiments can no longer be performed. Nevertheless, excitation of the more prominent features in the absorption spectra of these molecules, with overlapping bands, may still yield information of interest concerning the energy dependence of radiative and nonradiative decay rates, although obviously less well defined than that obtained in single vibronic level studies. We report here some results on several disubstituted benzenes.

Experimental Section

Fluorescence decay times were measured using the system described in an earlier report.[4] It need to be men-

TABLE I: Rate Constant Data for Isolated *o*-Fluorotoluene

E, cm^{-1}	Assignments	τ_F, nsec	Φ_F	k_R, 10^7 sec^{-1}	k_{NR}, 10^7 sec^{-1}
37,520	e	10.5	0.28	2.7 ± 0.3	6.9 ± 0.5
38,228	e + 707	9.2	0.21	2.2 ± 0.2	8.6 ± 0.6
38,447	e + 924	8.9	0.186	2.1 ± 0.2	9.2 ± 0.7
38,740	e + 1230	8.3	0.165	2.0 ± 0.2	10.1 ± 0.7
38,911	e + 2 × 707	7.8	0.160	2.1 ± 0.2	10.8 ± 0.8
39,155		7.8	0.155	2.0 ± 0.2	10.8 ± 0.9
39,398	e + 2 × 924	7.2	0.142	2.0 ± 0.2	11.9 ± 1.0
40,000	e + 2 × 1230	6.6	0.100	1.5 ± 0.2	13.6 ± 1.2
40,500		5.3	0.069	1.3 ± 0.2	17.6 ± 1.9
41,000		4.0	0.039	1.0 ± 0.2	24.0 ± 3.5

TABLE II: Rate Constant Data for Isolated *m*-Fluorotoluene

E, cm^{-1}	Assignments	τ_F, nsec	Φ_F	k_R, 10^7 sec^{-1}	k_{NR}, 10^7 sec^{-1}
37,430	e	12.5	0.33	2.6 ± 0.2	5.4 ± 0.4
38,105	e + 684 e + 965 − 253	9.5	0.21	2.2 ± 0.2	8.3 ± 0.6
38,398	e + 965 e + 684 + 282	9.5	0.172	1.8 ± 0.2	8.7 ± 0.6
38,691	e + 1261	8.6	0.171	2.0 ± 0.2	9.6 ± 0.7
39,069	e + 965 + 684	8.3	0.152	1.8 ± 0.2	10.2 ± 0.8
39,350	e + 2 × 965	8.0	0.135	1.7 ± 0.2	10.8 ± 0.8
39,630	e + 965 + 1261	7.0	0.109	1.6 ± 0.2	12.7 ± 1.1
40,033	e + 2 × 965 + 684	6.6	0.088	1.3 ± 0.2	13.8 ± 1.2
40,313	e + 3 × 965	5.4	0.064	1.2 ± 0.2	17.3 ± 1.9
40,581	e + 2 × 965 + 1261	4.3	0.040	0.9 ± 0.2	22.3 ± 3.0
40,935	e + 3 × 965 + 684	1.8	0.023	1.3 ± 0.6	54 ± 21

TABLE III: Rate Constant Data for Isolated *p*-Fluorotoluene

E, cm^{-1}	Assignments	τ_F, nsec	Φ_F	k_R, 10^7 sec^{-1}	k_{NR}, 10^7 sec^{-1}
36,860	e	18.4	0.65	3.6 ± 0.3	1.9 ± 0.3
37,665	e + 794	11.8	0.38	3.2 ± 0.3	5.3 ± 0.4
38,070	e + 1194 e + 794 + 398	9.7	0.30	3.1 ± 0.3	7.2 ± 0.6
38,471	e + 2 × 794 e + 794 + 2 × 398 e + 1194 + 398	8.8	0.27	3.0 ± 0.3	8.3 ± 0.7
38,869	e + 794 + 1194 e + 2 × 794 + 398 e + 1194 + 2 × 398	6.6	0.23	3.5 ± 0.5	11.6 ± 1.2
39,277	e + 1229 + 2 × 584	6.4	0.20	3.1 ± 0.4	12.6 ± 1.2
39,668	e + 2 × 794 + 1194 e + 2 × 1194 + 398	6.3	0.161	2.6 ± 0.4	13.3 ± 1.3
40,057	e + 4 × 794 e + 2 × 1194 + 794	5.7	0.134	2.4 ± 0.4	15.2 ± 1.6
40,460	e + 3 × 794 + 1194 e + 3 × 794 + 1229	5.0	0.108	2.2 ± 0.4	17.8 ± 2.1
40,850	e + 5 × 794 e + 2 × 1194 + 2 × 794	4.7	0.081	1.7 ± 0.3	19.6 ± 2.4
41,252	e + 4 × 794 + 1194	4.4	0.051	1.2 ± 0.2	21.6 ± 2.8
41,642	e + 6 × 794	3.9	0.041	1.1 ± 0.2	24.6 ± 3.7

tioned, however, that the free-running N_2 flash lamp still has some line structure in the spectral output when operating at a pressure of 25 psi. Therefore, excitation radiation with a 10-Å bandpass for this system cannot be regarded as uniformly distributed about the median excitation wavelengths listed in Tables I–VIII. The accuracy of the excitation monochromator, a Bausch and Lomb high-intensity monochromator, with uv grating blazed at 300 nm, was ±2 Å and the precision was ±2 Å. The fluorescence decay curves were convoluted from the scattered lamp flash with a reproducibility of ±0.16 nsec. Calibrations of the system carried out with acetone at 280 nm[5] (τ = 1.7 nsec) and toluene at 264 nm[6] (τ = 54 nsec) corresponded to the literature values to within +10% for acetone and ±5% for toluene under identical conditions. The accuracy for acetone was below average because the lifetime was only about ⅔ that of the natural decay of the N_2 lamp flash (2.8 nsec). The precision of the lifetime values was at least ±0.325 nsec for lifetimes longer than 16 nsec and approached the convolution accuracy for lifetimes down to 5 nsec. All lifetimes were measured at a pressure of aromatic molecule of 0.25 ± 0.04 Torr. At this pressure, less than 4% of the molecules suffer collisions during a fluorescence lifetime of 16 nsec, assuming a collision diameter for the excited state equal to that of the ground state, which may not be valid.

Quantum yields at an excitation bandpass of 10 Å were measured with a standard T-shaped cell, Bausch and

TABLE IV: Rate Constant Data for Isolated *o*-Fluorobenzotrifluoride

E, cm^{-1}	Assignments	τ_F, nsec	Φ_F	k_R, 10^7 sec^{-1}	k_{NR}, 10^7 sec^{-1}
37,395	None available	6.5	0.30	4.6 ± 0.6	10.8 ± 1.2
37,735		5.8	0.22	3.9 ± 0.6	13.4 ± 1.4
38,335		5.0	0.191	3.8 ± 0.7	16.2 ± 2.0
38,665		4.4	0.165	3.8 ± 0.7	19.0 ± 2.6
38,985		4.0	0.139	3.5 ± 0.7	22 ± 3
39,335		3.7	0.106	2.9 ± 0.6	24 ± 4
39,935		3.0	0.079	2.6 ± 0.7	31 ± 6
40,735		2.1	0.033	1.6 ± 0.6	46 ± 14

Lomb grating monochromator, with uv grating blazed at 300 nm, RCA 935 phototube, RCA 1P28 photomultiplier tube, and 500-W xenon lamp combination. The xenon lamp was controlled by a current-stabilized power supply giving a 5-hr drift of 1% and short-term fluctuations less than 0.2%. Because of the stability of the lamp and the high extinction coefficients of the molecules studied, the amount of light absorbed was measured by feeding the output of the RCA 935 phototube into an electrometer and displaying the output of the electrometer directly on a stripchart recorder. Thus no approximations such as the assumption of Beer–Lambert laws were needed or used. The monochromator was calibrated using the 450.1-nm xenon line and was precise and accurate to within 2 Å. Corrections were made for the RCA 935 phototube spectral response using a salicylate plate calibration curve. The photomultiplier spectral response was not corrected for, as it was assumed that the small correction due to the shift in the mean frequency of the fluorescence spectra of these molecules would be negligible. Allowances for long term changes in the photomultiplier gain were made by running a benzene calibrant every 7 hr during experimentation. Day to day precision of quantum yield values was better than ±5% of the values.

The quantum yield of fluorescence ϕ_f is defined as the average fraction of a photon emitted per photon absorbed. Thus, by comparison of the ratio of emitted to absorbed light intensity for the sample with the same ratio for a standard of known quantum yield of fluorescence, relative fluorescence quantum yields could be estimated.

Plots of emitted intensity (E)/absorbed intensity (I) were made as a function of optical density for each wavelength listed in Tables I–VIII. From this plot, the value of E/I at a pressure of 0.25 Torr was determined and compared with that of benzene at an equivalent optical density excited at 2537 Å with the 10-Å bandpass xenon continuum. Benzene was defined to have a quantum yield of 0.18[7,8] between 2 and 10 Torr and E/I values for optical densities beyond that range were obtained by extrapolation. It is, however, well known that the quantum yield of fluorescence of benzene at pressures below 0.1 Torr shows a dramatic increase.[9] Therefore, the accuracy of the quantum yields reported in this paper depends upon the assumption that benzene has a constant quantum yield between 2 and 10 Torr.

The assumption is made in this study that for all molecules a pressure of 0.25 Torr is low enough such that no collisions occur during the radiative lifetime of the excited singlet state, *i.e.*, the molecules are "isolated." This seems reasonable in all cases when measured decay times are compared with those of benzene and fluorobenzene, but the point was further checked using *p*-fluorotoluene as a test case. For excitation to the zero-point level (λ 271.2 nm) some slight decrease in fluorescence decay time is observed over a fourfold pressure range from 2 (15.9 nsec) to 8 Torr of PFT (13.6 nsec), indicating that at these pressures collisional effects are of importance. Over a fourfold pressure range from 0.13 to 0.5 Torr, however, the variation is within experimental error, being 18.0 ± 0.3 (0.13 Torr), 18.4 ± 0.3 (0.25 Torr), and 17.8 ± 0.3 (0.5 Torr). It seems therefore reasonable to make the assumption that for all measured decay times shorter than ~20 nsec, 0.25 Torr is a pressure sufficiently low that isolated molecules are being observed.

Benzene was BDH Chromatoquality of purity better than 99.9%. All fluorocompounds were obtained pure and puriss grade from Flurochem Ltd. and the purity was checked on Carbowax 20M and OVI columns. Preparative glc purification was made in some cases and after vacuum distillation, all compounds were better than 99.6% pure.

All pressures were measured on a mercury and grease free vacuum line with limiting pressure of 5×10^{-1} Torr using an Edwards 0–20-Torr capsule dial gauge. For pressures below 2 Torr expansion procedures were used. The capsule gauge was calibrated against a column of di-*n*-butyl phthalate, and measured pressures shown to be accurate to 5%.

The low-resolution spectra given for reference in Figures 1–8 were recorded on a Unicam SP700 scanning spectrometer accurate to ±15 cm^{-1}[11] and precise to ±5 cm^{-1}. Samples at a pressure of *ca.* 2.0 Torr were run in a 5.5-cm quartz cell at 27°. The energies listed in Tables I–VIII refer to peak positions indicated on the spectra while the assignments, where available, are derived from the literature. The apparent inconsistency reflects the inherent inaccuracy and low resolution of the SP700 on which the spectra were recorded. However, since the precision of the excitation monochromators in the lifetime and quantum yield systems was no better than 30 cm^{-1} the errors in band positions recorded are of lesser importance.

Results and Discussion

The absorption spectrum of o-fluorotoluene (OFT) has been discussed[10] and tentative assignments along with relevant fluorescence quantum yields and lifetimes are listed in Table I. The spectra of *m*-fluorotoluene (MFT), *p*-fluorotoluene (PFT), *m*-fluorobenzotrifluoride (MFBTF), and *p*-fluorobenzotrifluoride (PFBTF) have been more completely analyzed by Cave and Thompson[10] as has the spectrum of 1,4-bis(trifluoromethyl)benzene (HFPX).[11] Given the limited accuracy of the SP700 absorption spectrometer used for these spectra, a tentative assignment has also been suggested for the absorption spectrum of 1,3-bis(trifluoromethyl)benzene (HFMX). The recorded band maxima and literature assignments, where available, for these compounds are listed in Tables II–VIII along with fluorescence quantum yields, lifetimes, and evaluated rate constants. Where two prominent bands were within the bandwidth of 165 cm^{-1} of the excitation monochromators used here, the assignments of both bands have been listed. However, these assignments do not include the presence of numerous weak and diffuse bands which have not been listed in the literature. These less prominent bands preclude the possibility of truly single vibronic level studies.

Radiative Rate Constants. The absorption spectra of most of the disubstituted benzenes studied here feature strong progressions in the totally symmetric ring breath-

TABLE V: Rate Constant Data for Isolated *m*-Fluorobenzotrifluoride

E, cm^{-1}	Assignments	τ_F, nsec	Φ_F	k_R, 10^7 sec^{-1}	k_{NR}, 10^7 sec^{-1}
37,335	e	6.4	0.30	4.7 ± 0.6	11.0 ± 1.1
37,642	e + 298	5.8	0.25	4.2 ± 0.6	13.0 ± 1.5
38,301	e + 963	5.4	0.22	4.0 ± 0.6	14.5 ± 1.7
38,606	e + 963 + 298	5.2	0.186	3.6 ± 0.6	15.7 ± 1.8
38,911	e + 963 + 2 × 298	4.7	0.168	3.6 ± 0.6	17.7 ± 2.3
39,276	e + 2 × 963	4.1	0.148	3.6 ± 0.7	20.8 ± 3.1
39,545	e + 2 × 963 + 298 − 40	4.1	0.119	2.9 ± 0.6	22 ± 3
39,837	e + 2 × 963 + 2 × 298	3.7	0.095	2.6 ± 0.6	25 ± 4
40,203	e + 3 × 963	3.3	0.082	2.5 ± 0.6	28 ± 5
40,472		2.6	0.072	2.8 ± 0.9	36 ± 9
40,764		2.3	0.053	2.3 ± 0.8	41 ± 12

TABLE VI: Rate Constant Data for Isolated *p*-Fluorobenzotrifluoride

E, cm^{-1}	Assignments	τ_F, nsec	Φ_F	k_R, 10^7 sec^{-1}	k_{NR}, 10^7 sec^{-1}
37,865	e	16.2	0.127	0.78 ± 0.07	5.4 ± 0.3
38,691	e + 538 + 283	13.7	0.093	0.68 ± 0.06	6.6 ± 0.3
38,935	e + 2 × 538	12.7	0.082	0.65 ± 0.06	7.2 ± 0.3
39,196	e + 792 + 538	12.5	0.078	0.62 ± 0.06	7.4 ± 0.3
39,472	e + 2 × 792	11.3	0.068	0.60 ± 0.06	8.3 ± 0.4
39,691	e + 1030 + 792	10.9	0.061	0.56 ± 0.06	8.6 ± 0.5
39,972	e + 1030 + 792 + 283	10.7	0.055	0.51 ± 0.06	8.8 ± 0.5
40,228	e + 3 × 792	10.1	0.046	0.46 ± 0.04	9.5 ± 0.5
40,472		8.5	0.040	0.47 ± 0.06	11.3 ± 0.7
40,740		8.1	0.032	0.40 ± 0.05	12.0 ± 0.8

TABLE VII: Rate Constant Data for Isolated Hexafluoro-*m*-xylene (1,3-Bis(trifluoromethyl)benzene)

E, cm^{-1}	Assignments	τ_F, nsec	Φ_F	k_R, 10^7 sec^{-1}	k_{NR}, 10^7 sec^{-1}
37,606	e	20.4	0.176	0.86 ± 0.08	4.0 ± 0.2
37,879	e + 273	19.1	0.148	0.77 ± 0.07	4.5 ± 0.2
38,223	e + 617	17.6	0.131	0.74 ± 0.08	4.9 ± 0.3
38,569	e + 963	17.0	0.128	0.75 ± 0.07	5.1 ± 0.3
38,837	e + 1231	15.7	0.105	0.67 ± 0.07	5.7 ± 0.3
39,150	e + 963 + 617	14.2	0.087	0.61 ± 0.07	6.4 ± 0.4
39,513	e + 2 × 963	12.3	0.067	0.54 ± 0.07	7.6 ± 0.5
40,130	e + 2 × 963 + 617	8.2	0.031	0.38 ± 0.06	11.8 ± 1.2

TABLE VIII: Rate Constant Data for Isolated Hexafluoro-*p*-xylene (1,4-Bis(trifluoromethyl)benzene)

E, cm^{-1}	Assignments	τ_F, nsec	Φ_F	k_R, 10^7 sec^{-1}	k_{NR}, 10^7 sec^{-1}
37,471	e	8.6	0.21	2.5 ± 0.2	9.2 ± 0.7
37,662	e + 210	8.2	0.194	2.4 ± 0.3	9.8 ± 0.8
37,906	e + 2 × 210	7.6	0.157	2.1 ± 0.3	11.1 ± 0.9
38,252	e + 770	7.2	0.156	2.2 ± 0.3	11.7 ± 1.0
38,469	e + 1020 e + 770 + 210	7.0	0.143	2.0 ± 0.3	12.2 ± 1.1
38,698	e + 1020 + 210	6.4	0.130	2.0 ± 0.3	13.6 ± 1.3
38,928	e + 2 × 770(?) e + 1020 + 2 × 210	5.9	0.108	1.8 ± 0.3	15.1 ± 1.5
39,228	e + 1020 + 770 e + 2 × 770 + 210	5.4	0.090	1.7 ± 0.3	16.9 ± 1.8
39,462	e + 1020 + 770 + 210	4.6	0.073	1.6 ± 0.3	20.2 ± 2.5
39,679	e + 2 × 1020 + 210	4.3	0.060	1.4 ± 0.3	21.9 ± 2.9
39,935		3.7	0.041	1.1 ± 0.2	25.9 ± 4.1
40,435		2.9	0.024	0.8 ± 0.2	34 ± 7

ing frequencies, the value of the frequency being dependent almost entirely on the position rather than on the nature of the two substituents. It is reasonable that the absorption spectra should show such progressions and that the most prominent low-energy band would be the 0,0 band, since disubstitution in the ortho, meta, and para positions immediately lowers the overall symmetry of the benzene ring. Thus, while the effect of the substituents is not large enough to give full allowedness to the transition, they do lift the symmetry restriction on the transition corresponding to the $^1B_{2u} \leftarrow {}^1A_{1g}$ transition in benzene. Therefore, since the electronic wave functions are now of correct symmetry to make the transition dipole moment matrix elements positive and of overall symmetry A_1, vibrations which do not destroy the symmetry will be expected to be most important in the 2600 Å of these disubstituted benzenes. Since the substituents introduce allowedness to this system, the oscillator strengths should also be correspondingly greater than those of benzene. The experimental values for the oscillator strengths of the compounds studied here have been tabulated and matched by first- and second-order perturbation theory results by Pe-

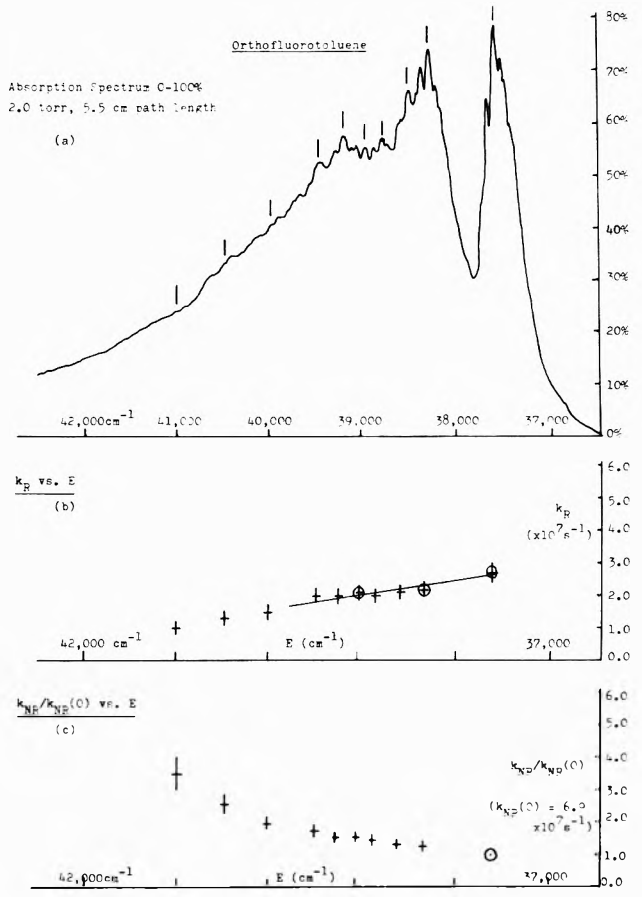

Figure 1. Absorption spectrum (a), k_R (b), and $k_{NR}(m)/k_{NR}(0)$ (c) as a function of excitation energy for o-fluorotoluene. Points marked ↓ show excitation wavelengths. Circled data points in b identify excitation of ν_1 sequence.

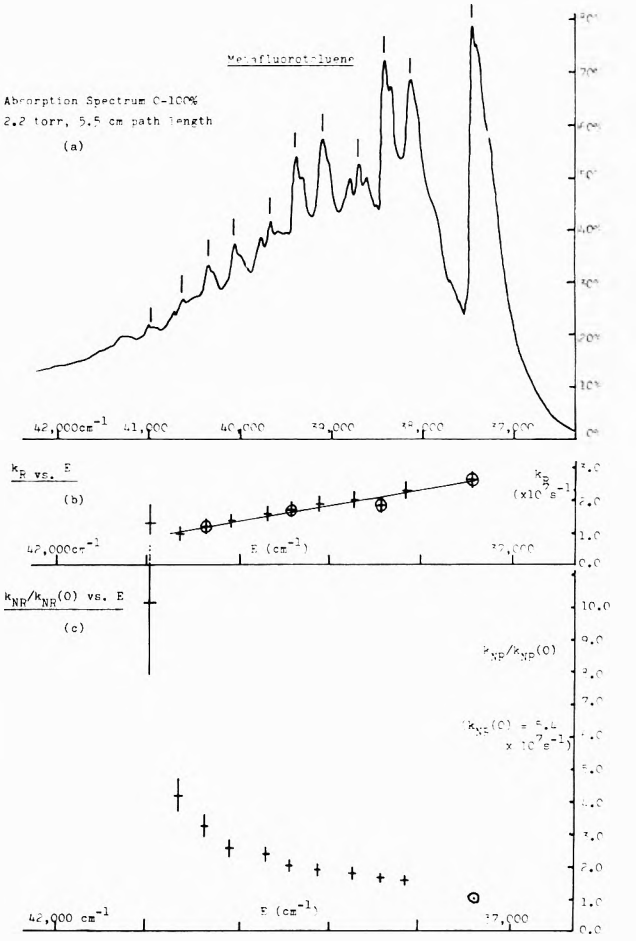

Figure 2. Absorption spectrum (a), k_R (b), and $k_{NR}(m)/k_{NR}(0)$ (c) as a function of excitation energy for *m*-fluorotoluene. See caption to Figure 1.

truska.[12] There are no outstanding variations between these tabulated oscillator strengths and the radiative rate constants listed in Tables I–VIII.

The variation in k_R for these molecules with excess vibrational energy is of interest. Both k_R and k_{NR} were obtained from the fluorescence lifetimes and the fluorescence quantum yields by use of the equations

$$\phi_F = k_R/(k_R + k_{NR}) = k_R\tau_F \quad (1a)$$

$$k_R = \phi_F/\tau_F \quad (1b)$$

$$k_{NR} = (1 - \phi_F)/\tau_F \quad (1c)$$

Lin, *et al.*,[13] have shown that for molecules of this kind for excitation in a particular progression, the radiative rate constant $k_R(n)$ would be expected to vary linearly with number of quanta n of the vibration excited, for both symmetry allowed and forbidden transitions, *i.e.*, is of the form

$$k_R(n) = k_R(0) + k'n \quad (2)$$

The theory assumes the harmonic oscillator approximation and also that intramolecular vibrational redistribution in the isolated molecule is absent, *i.e.*, the radiative properties are those of the single vibronic level initially populated. This behavior might thus be expected to be observed for small excess energies. Values of k_R for progressions in the ν_1 vibration in the substituted benzenes are identified in Figures 1–8, from which it can be observed that eq 1 is approximately obeyed for all molecules for excess energies up to about 3000 cm^{-1}. The slopes of the lines in these plots are linearly related to the frequency differences between vibrational modes in the upper and lower states.[13] In all cases a negative slope is observed, indicating that the frequency of the vibration is lower in the excited state than the ground state as is known to be the case.[10] In the case of hexafluoro-*m*-xylene and *p*-fluorobenzotrifluoride the slope is smaller but real. The oscillator strength for the transition is contained in the theoretical expression for the slope in these plots and since in these two compounds the oscillator strength is low, the smaller slope is not surprising. Excitation of a promoting mode would give rise to an increase in k_R with increasing quanta and we may thus also conclude that in these molecules, we are not exciting a promoting mode for the radiative transition. For *p*-fluorotoluene above 3000 cm^{-1} excess energy the value of k_R deviates from the straight line. This may be due to the effects of anharmonicity which can greatly influence Franck–Condon factors.[13,14] In an earlier paper[15] it was suggested that anharmonicity induced vibrational redistribution from the optical mode into isoenergetic vibrational modes might also lead to a reduction in Franck–Condon factors for the radiative transition thus causing a decrease in k_R. Freed[16] has pointed out that for this process to occur, the average energy spacing of all vibrational levels must be less than the line width of the optically pumped transition. The latter is given simply by the Heisenberg uncertainty principle and thus in order to observe vibrational redistribution

$$\tau_F/\rho\hbar < 1 \quad (3)$$

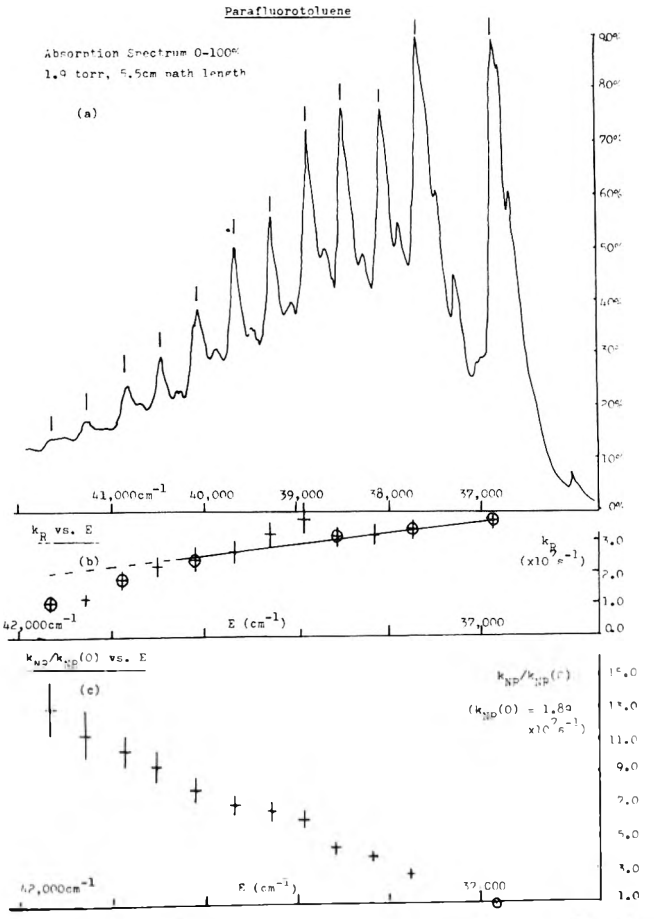

Figure 3. Absorption spectrum (a), k_R (b), and $k_{NR}(m)/k_{NR}(0)$ (c) as a function of excitation energy for *p*-fluorotoluene. See caption to Figure 1.

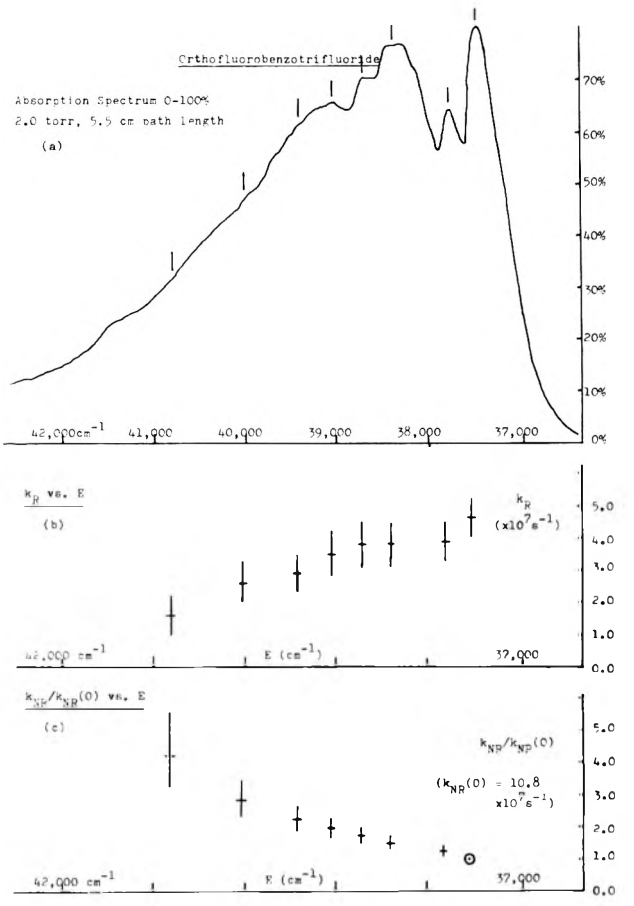

Figure 4. Absorption spectrum (a), k_R (b), and $k_{NR}(m)/k_{NR}(0)$ (c) as a function of excitation energy for *o*-fluorobenzotrifluoride. See caption to Figure 1.

where τ_F is the fluorescence lifetime of the excited state and ρ is the density of vibrational levels in the excited singlet manifold. The method of Haarhoff[17] can be used to estimate ρ as a function of excess energy above the zero-point energy. Two different approximations have been used for the rough calculations of ρ. The first assumes that the average value of the vibrational frequency for all modes in *p*-fluorotoluene is 1000 cm^{-1}. In the second more rigorous calculation, the values of all available frequencies were used. Figure 9 shows plots of the function $\tau_F/\rho\hbar$ against excess energy ΔE obtained. It may be seen that certainly for excess energies above 3000 cm^{-1} where $\tau_F/\rho\hbar < 0.1$ the redistribution process becomes possible in theory, and thus deviations in values of k_R from values expected on the basis of Lin's approach may be attributable to this phenomenon. The more rigorous calculation of ρ shows that redistribution effects may be observable for excess energies of a little as 1500 cm^{-1}, and it is thus possible that for most of the initially populated levels in this study fast vibrational redistribution may already have occurred before emission. Under these circumstances the radiative rate constant observed will be the microcanonical average rate constant, and Lin, *et al.*,[13] have shown this *also* to be linearly dependent upon excess energy above the zero-point level.[13] Spectroscopic studies are presently being carried out to determine the extent of vibrational redistribution in these and other molecules. In view of the theoretical linear dependence of k_R with excess energy for both single vibronic level and the redistributed levels, it would appear that the derivations from linearity observed here in PFT for excitation above 3000 cm^{-1} can only be due to anharmonicity.

Nonradiative Rate Constants. Heller, Freed, and Gelbart[3] have provided an excellent theoretical basis for a quantitative understanding in the case of benzene of the variation in relative nonradiative rate constants as a function of number of quanta of excitation in the optically pumped mode. It is important to stress that the nonradiative decay is assumed to be exclusively an intersystem crossing to the triplet manifold in this treatment. In the theory, the available energy, which is the difference in energies between the optically pumped state and the zero-point energy of the triplet state less the energy of the promoting vibration, is partitioned in the triplet state between the optical mode and other totally symmetric modes termed accepting modes. The absolute value of k_{NR} is very sensitive to choice of promoting mode frequency, which is generally unknown, but relative rates for excitation in a sequence are insensitive to the particular value chosen. With the assumption that the optical mode frequency was equal in the singlet and triplet states, qualitative agreement between the experimental results of Spears and Rice[1] and calculated values was obtained. This agreement could be made quantitive if it were assumed that the optical mode frequency changed by +25 cm^{-1} in the triplet state.

The theoretical treatment outlined by Heller, Freed, and Gelbart can be used to gain a qualitative understanding of the molecules studied here, again making the assumption that the observed nonradiative decay is exclu-

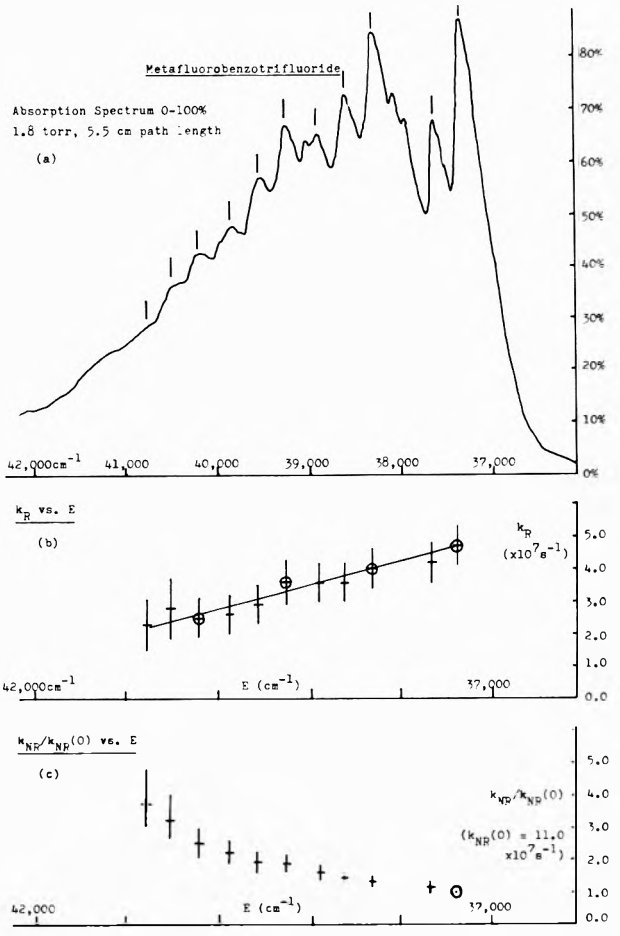

Figure 5. Absorption spectrum (a), k_R (b), and $k_{NR}(m)/k_{NR}(0)$ (c) as a function of excitation energy for *m*-fluorobenzotrifluoride. See caption to Figure 1.

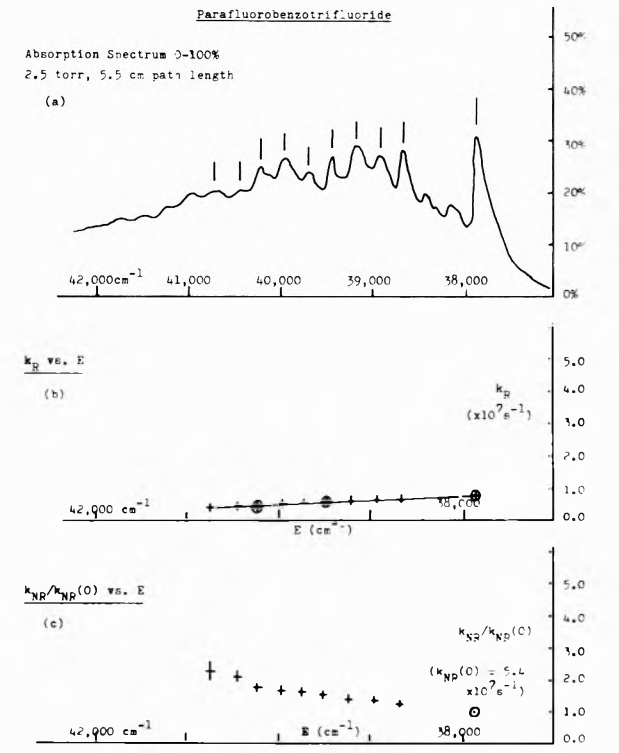

Figure 6. Absorption spectrum (a), k_R (b), and $k_{NR}(m)/k_{NR}(0)$ (c) as a function of excitation energy for *p*-fluorobenzotrifluoride. See caption to Figure 1.

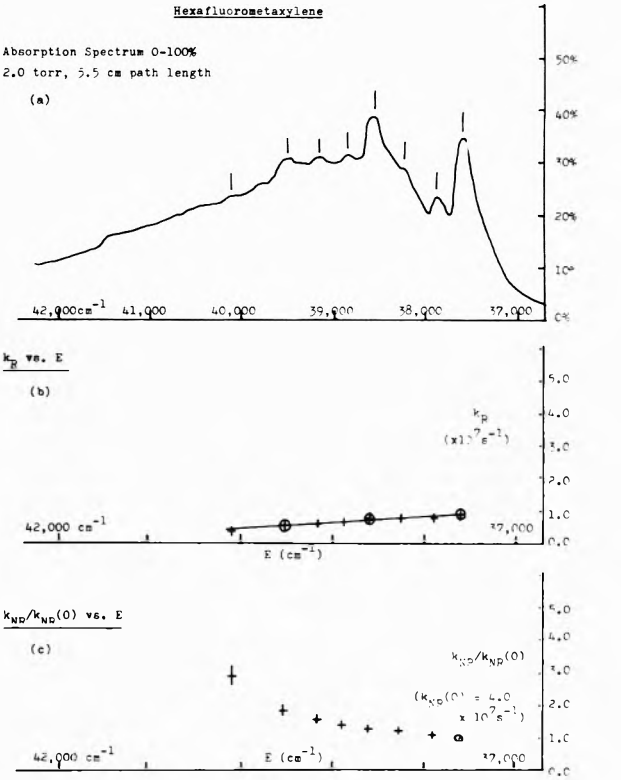

Figure 7. Absorption spectrum (a), k_R (b), and $k_{NR}(m)/k_{NR}(0)$ (c) as a function of excitation energy for hexafluoro-*m*-xylene. See caption to Figure 1.

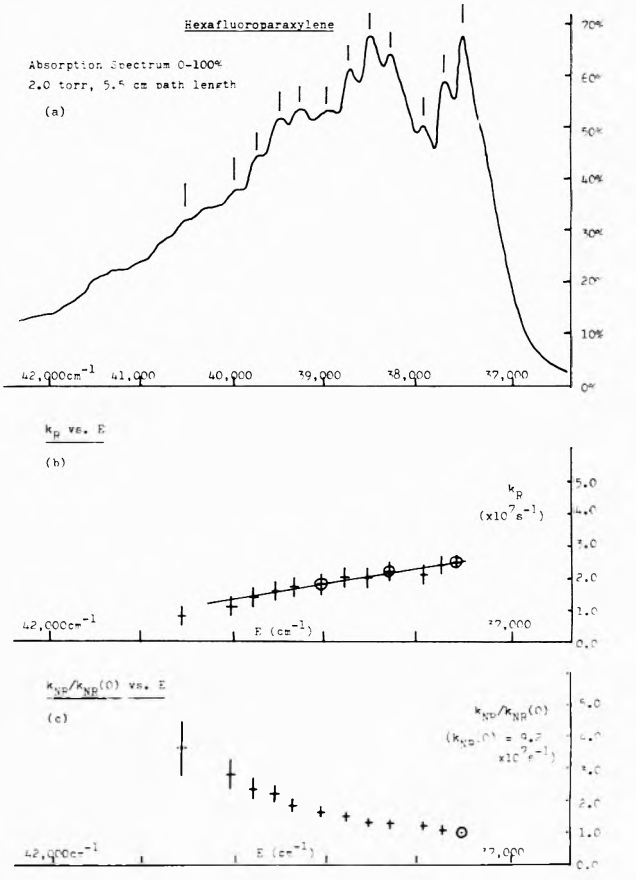

Figure 8. Absorption spectrum (a), k_R (b), and $k_{NR}(m)/k_{NR}(0)$ (c) as a function of excitation energy for hexafluoro-*p*-xylene. See caption to Figure 1.

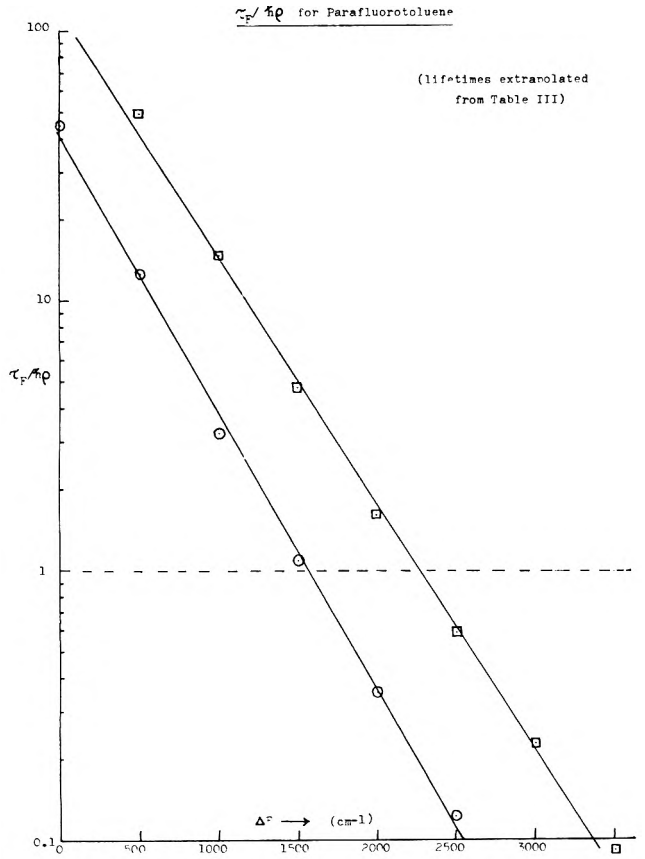

Figure 9. Variation in values of function $\tau_F/\hbar\rho$ for *p*-fluorotoluene with excess energy. ρ (density of states) calculated by method of Haarhoff assuming (□) all ν_i = 1000 cm^{-1} and (○) including assigned modes and assuming all other modes = 1000 cm^{-1}.

sively an intersystem crossing to the triplet manifold in each case. In Table IX we have listed the available data for excitation of the C–C symmetric skeletal breathing frequency (ν_1) in each compound, and compared this with that available for excitation of benzene.

Disubstitution of the benzene ring provides extra totally symmetric C–H high-frequency accepting modes for the fluoro, methyl, and CF_3 substituted benzenes studied here. From the theory[3] this would mean that the lower frequency optical modes in the triplet state would be less efficient in competing for the excess vibrational energy. Therefore, one would expect the change in relative nonradiative rates to be smaller than that for benzene for these compounds, as has been observed in fluorobenzene.[2] Unfortunately, the experimental errors for this work are large enough that this observation can only be positively attributed to *p*-fluorobenzotrifluoride. With the exception of MFT and PFT, the trend for other compounds lies fairly close to the values for benzene. The similarity of the results suggest that the hexafluoroxylenes and the fluorobenzotrifluorides have a positive frequency change for the totally symmetric optical mode between the singlet and triplet states. This must be approximately the same as that for benzene, +25 cm^{-1}, or slightly larger to account for the observed results. A similar result was indicated for fluorobenzene.[3] The data indicate that low-frequency C–F vibrations do not play a significant role as accepting modes.

The fluorotoluenes show somewhat different behavior from that of the other disubstituted benzenes in that

TABLE IX: Variation in Nonradiative Decay Rate with Excitation in ν_1 Vibration

No. of ν_1[a] quanta optically excited	Frequency of ν_1, cm^{-1}	$k_{NR}(m)/k_{NR}(0)$[b]	$k_{NR}(0)$, 10^7 sec^{-1}
PFT			
0	794	(1.0)	1.9 ± 0.3
1		2.78	
2		4.41	
3			
4		8.04	
5		10.4	
6		13.0	
MFT			
0	965	(1.0)	5.4 ± 0.4
1		1.61	
2		2.00	
3		3.20	
OFT[c]			
0	707	(1.0)	6.9 ± 0.5
1		1.25	
2		1.57	
PFBTF			
0	792	(1.0)	5.4 ± 0.3
1			
2		1.53	
3		2.22	
MFBTF			
0	963	(1.0)	11.0 ± 1.1
1		1.32	
2		1.89	
3		2.55	
HFPX			
0	770	(1.0)	9.2 ± 0.7
1		1.27	
2(?)		1.64	
HFMX[c]			
0	963	(1.0)	4.0 ± 0.2
1		1.28	
2		1.90	
Benzene[3]			
0	923	(1.0)	
1		1.22	
2		1.73	
3		2.42	

[a] C–C symmetric skeletal vibration. [b] Rate constant for nonradiative decay relative to that for zero-point level for successive quanta *m* of ν_1 vibration. [c] Assignments tentative.

apart from the ortho derivative, a much stronger variation in $k_{NR}(m)/k_{NR}(0)$ than that observed in benzene is seen. There are three possible explanations for these results.

(a) There is a large change in optical mode frequency between the singlet and triplet states. This explanation has been given[3] to account for the results of Schlag and Von Weyssenhoff[18] on β-naphthylamine. Using benzene as the model, the changes in sensitivity for MFT and PFT would suggest an optical mode frequency shift of ≅+50 and ≅+80 cm^{-1}, respectively.

(b) A contribution of the methyl C–H vibrations in the optical mode. Because of the congestion in the absorption spectrum of these compounds this cannot be discounted as a possibility. The net result of a and b would be to place the methyl-substituted benzenes in the strong coupling limit with respect to one or more of their modes, *i.e.*, these optical modes have large geometry and/or frequency changes between the two electronic states involved in the radiationless transition. While OFT remains somewhat of an anomaly in its unexpected similarity of relative nonradiative rate variation to that of benzene, it seems feasible that the fluorotoluenes should have some modes

(involving methyl vibrations) for which the strong coupling limit is applicable.

(c) That the promoting mode itself is being excited. This may lead to large variations in $k_{NR}(m)/k_{NR}(0)$ with excess energy.[16] The fluorotoluenes are of low enough symmetry that this could be the case with these molecules. Nominally however it is the totally symmetric ν_1 mode which is being excited, and thus c seems unlikely as the explanation of the present results.

In the above discussion it has been assumed that there is no great difference in energies between zero-point levels of the singlet and triplet manifolds from compound to compound. This is essentially valid.[19]

Although experimental errors are fairly large, one can, in the compounds studied here, observe a noticeable trend in the sensitivity of the relative rates of nonradiative decay to the frequency of the optical mode. From the theory[3] it would be expected that the greater the frequency of the optical mode the more effective this mode would be in competing for the net available energy with the high-frequency symmetrical modes in the triplet state. Thus one would expect the relative rates to be more sensitive to higher quanta of ν_1 vibrations with increasing frequency of these symmetrical modes in the singlet state. From Table IX, it can be seen that for OFT (ν_1 = 707 cm^{-1}), PFBTF (ν_1 = 792 cm^{-1}), and HFPX (ν_1 = 770 cm^{-1}) the values of $k_{NR}/k_{NR}(0)$ for increasing quanta of the ν_1 vibration are always less than the comparable values for benzene (ν_1 = 923 cm^{-1}). However, for MFT (ν_1 = 965 cm^{-1}), MFBTF (ν_1 = 963 cm^{-1}), and HFMX (ν_1 = 963 cm^{-1}) the relative values of $k_{NR}/k_{NR}(0)$ are always greater than the corresponding ratios for benzene. Although too much quantitive significance is not justified for these results, the qualitative trends indicate excellent agreement between theory and experiment in these cases.

Channel 3 Process. For benzene, excitation to vibrational levels with excess energy greater than 3100 cm^{-1} is thought to introduce a new nonradiative decay channel (channel 3) which results in a dramatic increase in k_{NR}.[20] For the compounds studied here, even with excess energies of 5000 cm^{-1} in the case of *p*-fluorotoluene and in most cases for excess energies greater than 3000 cm^{-1} (with the dubious exception of *m*-fluorotoluene where experimental errors in the region of interest are large), no corresponding large increase in the nonradiative rate constant is observed. Nevertheless, studies at higher pressure indicate that for many of these molecules excitation to higher vibrational levels produces significantly less detectable triplet state concentrations than those produced upon excitation near the zero-point level.[19] The implication of these results is therefore that for excitation up to the excess energies in these studies either nonradiative decay produces short-lived triplet states which are not detectable by conventional chemical trapping techniques, or that the channel 3 process does occur, but is not characterized by a threshold energy, having instead a rate constant which increases smoothly with excess singlet energy. The fact that our results can be interpreted satisfactorily in terms of the theory of Heller, Freed, and Gelbart,[3] which assumes that nonradiative decay is exclusively intersystem crossing to the triplet manifold, and that in benzene the channel 3 decay process is characterized by an energy threshold, with a corresponding discontinuity in the value of k_{NR} as a function of excess energy above this threshold which is absent in the molecules studied here, indicates that the former explanation is more acceptable.

Acknowledgments. We are grateful to the Science Research Council and the Royal Society for equipment grants, and one of us (M. G. Rockley) is grateful to The University of Southampton for a Research Studentship. We gratefully acknowledge helpful discussions of our results with Professor Karl Freed, University of Chicago.

References and Notes

(1) K. G. Spears and S. A. Rice, *J. Chem. Phys.*, **55**, 5561 (1971).
(2) A. S. Abramson, K. G. Spears, and S. A. Rice, *J. Chem. Phys.*, **56**, 2291 (1972).
(3) D. F. Heller, K. F. Freed, and W. M. Gelbart, *J. Chem. Phys.*, **56**, 2309 (1972).
(4) G. M. Breuer, P. A. Hackett, D. Phillips, and M. G. Rockley, *J. Chem. Soc., Faraday Trans. 2*, **68**, 1995 (1972).
(5) G. M. Breuer and E. K. C. Lee, *J. Phys. Chem.*, **75**, 983 (1971).
(6) G. M. Breuer and E. K. C. Lee, *Chem. Phys. Lett.*, **14**, 404 (1972).
(7) *Cf.* discussion of W. A. Noyes, Jr., D. Harter, and W. A. Mulac, *J. Chem. Phys.*, **44**, 2100 (1966).
(8) H. Ishikawa and W. A. Noyes, Jr., *J. Chem. Phys.*, **37**, 583 (1962).
(9) C. S. Parmenter and A. H. White, *J. Chem. Phys.*, **50**, 1631 (1969).
(10) W. T. Cave and H. W. Thompson, *Discuss. Faraday Soc.*, **9**, 35 (1950).
(11) C. D. Cooper and F. W. Noegel, *J. Chem. Phys.*, **20**, 1303 (1952).
(12) J. Petruska, *J. Chem. Phys.*, **34**, 1120 (1961).
(13) G. R. Fleming, O. L. J. Gijzeman, and S. H. Lin, *Chem. Phys. Lett.*, **21**, 527 (1973).
(14) W. Siebrand and D. F. Williams, *J. Chem. Phys.*, **49**, 1860 (1960); B. R. Henry and W. Siebrand, *ibid.*, **49**, 5369 (1968).
(15) M. G. Rockley and D. Phillips, *Chem. Phys. Lett.*, **21**, 181 (1973).
(16) K. Freed, private communication.
(17) P. C. Haarhoff, *Mol. Phys.*, **7**, 101 (1963).
(18) E. W. Schlag and H. Von Weyssenhoff, *J. Chem. Phys.*, **51**, 2505 (1969).
(19) D. Phillips, *J. Photochem.*, **1**, 97 (1972).
(20) J. H. Callomon, J. E. Parkin, and R. Lopez-Delgado, *Chem. Phys. Lett.*, **13**, 125 (1972).

The External Heavy-Atom Effect on the Photoisomerization of Cyanine Dyes

W. Cooper* and K. A. Rome[1]

Research Laboratories, Eastman Kodak Company, Rochester, New York 14650 *(Received August 10, 1973)*

Publication costs assisted by the Eastman Kodak Company

The photoisomerization of 3,3′-diethyl-9-methylthiacarbocyanine has been studied at −125° in EPA (ethyl ether, isopentane, and ethyl alcohol, 5:5:2 by volume) and in matrices consisting of various combinations of EPA and ethyl halides. The rates of photoconversion of geometrical isomers of the dye were found to be proportional to the spin–orbit coupling factor of the heavy atom. It is concluded that the photoisomerization of the dye, cis ⇌ trans, occurs primarily *via* a triplet-state mechanism. Measurements of relative quantum yields of fluorescence and phosphorescence and decreases in the triplet-state lifetimes with the addition of heavy atoms substantiate the proposed mechanism. The effects of solvent matrices on the distribution of isomers are also discussed. An activation energy of 8.5 ± 0.5 kcal was found for the trans → cis isomerization in EPA.

Introduction

In a study of the spectroscopic properties of alcoholic solutions of cyanine dyes, West, Pearce, and Grum[2a] reported that thiacarbocyanines containing alkyl substituents in the meso position of the methine bridge exhibited visual absorption spectra that were resolved into two component bands at low temperature. Photochemical experiments showed that the two bands could be assigned to cis and trans geometrical isomers of the *meso*-alkylthiacarbocyanines and were readily interconvertible. Nearly pure forms of the stereoisomers were obtained by irradiation at wavelengths near the cis and trans band maxima.

Since the previous investigation concerned itself with the phenomenon and not the finer details of the mechanism of the photoisomerization, we have initiated studies to determine whether the molecular isomerization takes place from lowest-lying singlet states, or intermediate electronic states are involved in the interconversion reactions. The consideration of lower-lying electronic states being involved in the reaction pathway immediately suggested ways of altering the intersystem crossing rate between the first excited-singlet state and the lowest-lying triplet level of the dye molecule. The intersystem conversion is known to occur through spin–orbit coupling, which can be enhanced by heavy-atom solvents,[2b,3,4] and we have employed this method in our study of the photochemical reaction of 3,3′-diethyl-9-methylthiacarbocyanine bromide. Recently, Cowan and Drisko,[5] in a study of the photodimerization of acenaphthylene, have reported a direct correlation of relative yields of trans dimer with the square of the spin–orbit coupling parameters of heavy-atom solvents and concluded that it was a result of spin–orbit coupling. In this report we will present evidence to document the heavy-atom solvent effect on the photoisomerization of a typical thiacarbocyanine dye and to show that the enhancement of the conversion of geometrical isomers is related to the spin–orbit coupling factor of the solvent molecule. The addition of heavy atoms to the solvent matrix will be shown to have a significant effect on the luminescence properties of the dye, providing further substantiation of a triplet-state mechanism for the phototransformation.

Experimental Section

The apparatus used in this study for the photoisomerization reactions was similar to that of West, Pearce, and Grum.[2a] Absorption spectra were measured with a Cary Model 14 automatic spectrophotometer. A small heating coil containing the absorption cell was placed in a quartz dewar flask under a helium atmosphere and sealed. The dewar was equipped with four plane windows for observing the sample and liquid nitrogen was used as a coolant. Temperatures were measured with a copper–constantan thermocouple whose probes were placed in the absorption cell just above the sample. It is estimated that the temperature could be maintained within ±1.5° over long periods of time. The principal solvent matrix, EPA, a mixture composed of five parts ethyl ether, five parts isopentane, and two parts ethyl alcohol, by volume, was fluorometric grade, manufactured by Hartman-Leddon and purchased from the American Instrument Co. Iodomethane, bromoethane (ether-free), and chloroethane were Eastman reagent grade. All solvents were used without further purification and absorption spectra were not corrected for changes in effective concentration caused by contraction of the solvent at low temperatures.

Interconversion of geometrical isomers was brought about at low temperatures by irradiation with light of the appropriate wavelengths corresponding to the maxima of the cis and trans configurations. Interference filters of half bandwidth, 10 nm, combined with a Kodak Wratten filter No. 12 to absorb blue and ultraviolet radiation were used to isolate the 540- and 560-nm wavelengths characteristic of the cis and trans maxima, respectively. A Corning No. 4600 heat filter was also incorporated in the light path to prevent heating effects on the sample from the focused emission of a PEK X-75 high-intensity xenon point source. Resultant changes in absorptivities of the electronic transitions assigned to the isomers were measured spectrophotometrically immediately after irradiation. The dye sample, which was the bromide, was analytically pure and electrochromatography at room temperature showed no impurity bands. All dye samples were at a concentration of 6×10^{-6} *M* unless otherwise specified.

Measurements of the luminescence spectra of the dye solutions have been reported in detail elsewhere[6] and are

similar for this study except that a 1000-W quartz-iodine source was used for irradiation of the dye samples. Triplet-state lifetimes were obtained by taking the output of the photomultiplier at the appropriate wavelength and coupling it to an oscilloscope in the usual fashion.

Results and Discussion

Before studying the effect of heavy-atom solvents on the photoisomerization of the thiacarbocyanine dye it was of interest to survey a number of solvent matrices as a means of determining the one most appropriate for conducting the photoconversion reactions. The equilibrium distribution of the cis and trans isomers of 3,3′-diethyl-9-methylthiacarbocyanine is highly solvent dependent, especially at low temperatures, corroborating previous observations of isomer distribution of dye molecules at room temperature.[7,8] In this study we have observed that the trans isomer of the dye, with absorption maximum centered at about 560 nm, appears to dominate in solvent matrices that are essentially aprotic and nonpolar. For example, the absorption intensity of the trans geometrical isomer is larger in EPA than the cis form at −125°, as shown in Figure 1. However, in more protic solvents, such as Alphanol 79, a mixture of heptanol:octanol:nonanol (45:43:12 by volume), 3-A alcohol, and mixtures of alcohol and water, the cis configuration with maximum at 540–545 nm is dominant, as is likewise shown. A highly polar solvent, such as butyronitrile, gives essentially the all-cis structure of the dye and little evidence of the trans isomer at −88°. The higher temperature had to be utilized for this polar matrix because of "cracking," or crystallization of the matrix at lower temperatures.

The curves also show that the allowed transition centered at 508 nm and associated with a dimeric state of the dye molecule is very prominent in the spectrum of the dye in the EPA matrix. A forbidden transition of the dimer, unresolved and of relatively low intensity, is found at about 590 nm. Other subtle differences in the dye spectrum for the various matrices are obvious, and include the slight dependency of the transition maxima as a function of the refractive index of the medium. However, these changes are negligible and not germane to the primary study.

The results of the study of the dependency of the equilibrium distribution of the geometrical isomers of 3,3′-diethyl-9-methylthiacarbocyanine as a function of solvent suggest that the bulk properties of the solvent matrix may play a dominant role in determining the equilibrium distributions of the isomers since it is found that the cis geometrical isomer dominates, not only in polar-protic solvent systems, but also in polar-aprotic matrices. Brooker and coworkers[7] showed that in aromatic hydrocarbons the trans, or extended forms, of the chromophoric chain of the cyanine dyes were favored, and in more polar solvents the cis, or bent form, was favored, consistent with the proposed diminished repulsion between charged atoms of the heterocyclic nuclei in media of relatively high dielectric constant. Our experimental observations generally corroborate these published data.

Although the EPA matrix had the disadvantage of promoting dimer formation at low temperatures, it was decided to utilize the matrix for the study of the photoisomerization of 3,3′-diethyl-9-methylthiacarbocyanine based upon the rather rapid photoconversion obtained in the matrix at convenient temperatures. Figure 2 shows the

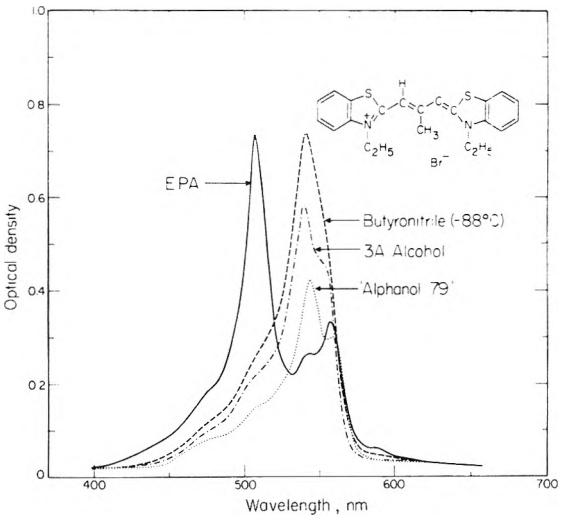

Figure 1. Absorption spectra of 3,3′-diethyl-9-methylthiacarbocyanine bromide in various solvent matrices at −125°: concentration = 6×10^{-6} *M*.

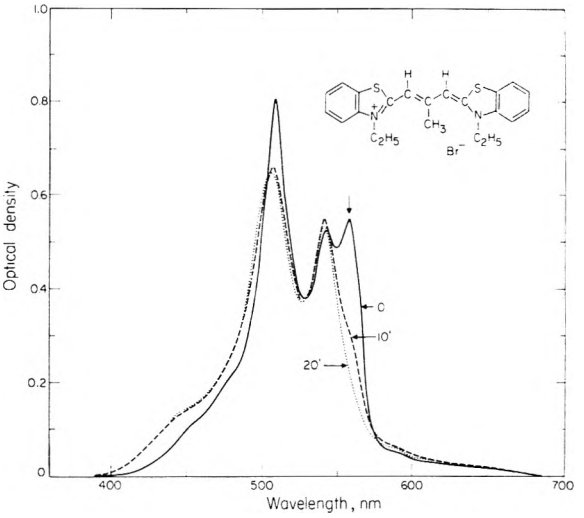

Figure 2. Photoisomerization (trans → cis) of 3,3′-diethyl-9-methylthiacarbocyanine bromide as a function of exposure time in EPA solution at −125°: concentration = 6×10^{-6} *M*. Arrow indicates excitation of the trans geometrical isomer at 560 nm.

phototropic changes in the dye at −125°, brought about by irradiation in the trans geometrical isomer with monochromatic light of 560 nm at various times of exposure. Within a period of 20 min, or less, the intensity of the band assigned to the trans isomer has become negligible, if not near zero. Only a slight increase in the intensity of the cis isomer centered at about 524 nm is noticed, and this is partially attributed to the decrease in molar absorption coefficient of that geometrical isomer compared to that of the more thermodynamically stable trans configuration.[2a] After irradiation in the trans form of the dye, a rather significant decrease occurs in the relative intensity of the allowed transition of the dimer, accompanied by a broadening of the band and increased absorption at shorter wavelengths due to the formation of higher states of aggregation of the dye.[9] The overall integrated intensities of the curves at zero irradiation time and after 20 min of exposure are essentially the same, the latter being only about 3% less. The small loss of intensity suggests that in the relatively "soft" EPA matrix, density loss in absorption due to bleaching of the dye is insignificant. Compari-

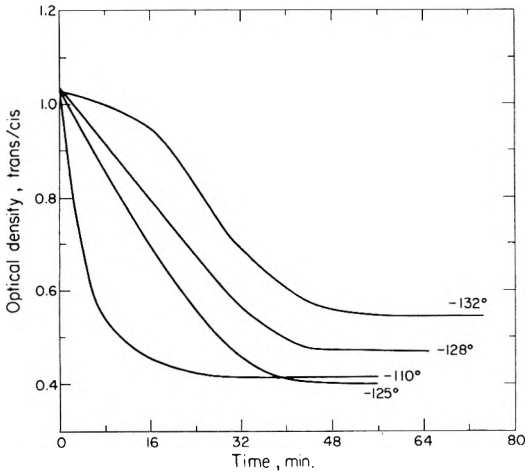

Figure 3. Effect of temperature on the rate of the trans → cis photoisomerization of 3,3′-diethyl-9-methylthiacarbocyanine bromide in EPA solution: concentration = 6 × 10^{-6} *M*. Excitation is at 560 nm.

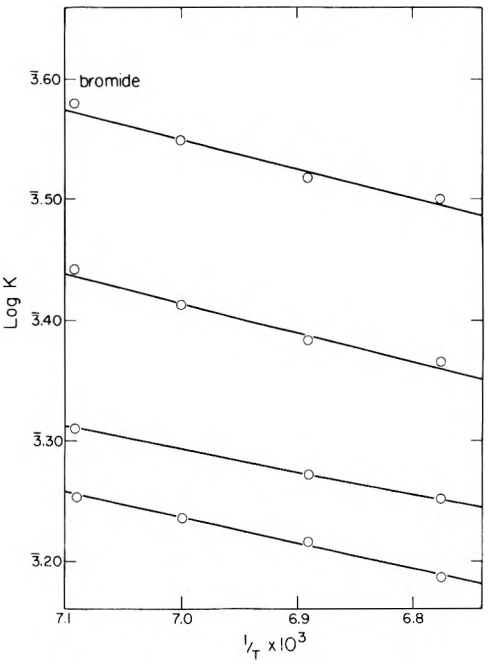

Figure 4. Arrhenius plots of the temperature dependence of the rate of trans → cis photoisomerization of 3,3′-diethyl-9-methylthiacarbocyanine bromide in EPA solution: concentration = 6 × 10^{-6} *M*.

son of the room-temperature absorption spectra of the dye, before and after exposure at the low temperature, corroborates the low bleaching loss since on regeneration of the unresolved isomers at room temperature, the optical density of the dye approximates that measured at zero excitation time.

The rates of the photochemical conversion of the isomers were determined at various temperatures by plotting the ratio of the optical densities of isomers as a function of time of excitation. Some of these data are shown in Figure 3. And, as would be anticipated for a reaction involving rotation around an essential double bond, an activation energy is associated with the reaction as indicated by the temperature dependency. Not only is the greatest slope, or change in the optical density of the cis compared to the trans, found at the highest temperature, but the time required to establish a photostationary concentration of isomers is shortest. As the temperature is lowered, a rapid decrease is observed in the transformation of the excited trans configuration of the dye into primarily its cis isomer, and secondarily into higher states of dye aggregation, as previously mentioned. It is recognized that the solvent matrix undergoes an increase in viscosity as the temperature is lowered,[10] and therefore the barrier to reaction appears to be a combination of temperature and viscosity effects.

Although viscosity of solvent mixtures tends to have a more pronounced effect on bimolecular reactions, such as second-order triplet decay, nevertheless for monomolecular reactions, such as photoinduced molecular rearrangements, the effects of high viscosities are less prominent. It has been reported[11] that the internal rearrangement of merocyanines, produced by irradiation of the appropriate spiropyrans, is reduced sharply in hydrocarbon glasses, apparently by the combined effect of low temperature and high viscosity. These reported data provide supplemental substantiation of our observations of the photoinduced isomerization of a cyanine dye. Furthermore, at the lowest temperature studied (−132°) an induction period is initially observed as shown in Figure 3. The photostationary state for the isomeric mixture not only requires a much longer time to attain equilibrium, but the concentration of trans to cis at equilibrium is larger than that observed at the higher temperatures. The apparent dependency of the trans/cis equilibrium on the temperature may be attributed to differences in trans → cis and cis → trans activation energies. It would be expected that the more stable trans geometrical isomer would require a larger activation energy to convert it into the cis isomer than the reverse process.

The steady state, or photostationary state, achieved by irradiation in the band assigned to the trans isomer of the dye describes the isomerization more dramatically than irradiation in the band ascribed to the cis isomer. For at the photostationary state, one would anticipate a high cis-isomer population reflected in part by the larger extinction coefficient of the trans isomer. This generalization tends to prevail in our study, for it has been observed that much larger changes in the optical densities of the isomers occur for the trans → cis conversion than for the opposite reaction. Also, at high concentrations of the cis isomer, the optical density at 560 nm may include the tail of the electronic transition of the cis geometrical isomer.

It is reasonable to assume that the photorearrangement is a first-order process, and therefore rate constants have been calculated from the first-order relationship, $k = 1/t \ln (OD)_0/[(OD)_0 - (OD)_t]$, where $(OD)_0$ is the initial optical density of the isomer to be irradiated, and $(OD)_t$ is the optical density at time t. The first-order rate constants have been calculated as a function of the temperature for the photochemical trans → cis reaction. From the usual Arrhenius plots, log k *vs.* $1/T$, as shown in Figure 4 for a series of reactions, an activation energy of 8.5 kcal/mol is found. The value compares favorably with the observations of Dörr and coworkers,[12] who reported activation energies ranging from 9 to 16 kcal/mol, depending upon the viscosity of the solvent matrix, in a flash-photolysis study of the reversible photoisomerism of several simple polymethine cyanines. Solvents of relatively high viscosity presented a larger barrier to the isomerization than those of relatively low viscosity. A similar situation has

been observed in this study, as indicated by the limited temperature range at which the activation energy of the photoisomerization could be studied. Significant increases of the viscosity of EPA at the lower temperatures place practical experimental limitations on the study.

Intuitively, it would appear that since the lifetime of the first excited-singlet state of *trans*-3,3′-diethyl-9-methylthiacarbocyanine should be of the order of 10^{-9} sec,[13] the probability of a molecular rotation of a bulky dye molecule occurring within this time is very small. To a first approximation calculations of the potential energy necessary for twisting around an essential double bond indicate a high probability of a triplet intermediate for the photoconversion.[14] Therefore, it does not appear that the molecular isomerization can take place from the first excited-singlet state of the dye molecule attained by optical excitation. Buettner,[15] however, in a flash-photolytic study of 3,3′-diethylthiacarbocyanine in methanol and polyvinyl alcohol (PVA) film at room temperature, observed that the quantum yield of isomer production in methanol is about eight times the quantum yield of triplet production in PVA. He has suggested that the isomer was produced from the singlet state.

The preceding considerations led us to question the nature of the one or more intermediate states that might be involved in the photoisomerization. The effect of various electronic states on the interconversion rate could be best determined by altering the distribution and population of excited dye molecules in the various electronic levels available. It is well known that the singlet-triplet transitions formally forbidden by the selection rule prohibiting transitions between states of different multiplicity can be relaxed by the presence of heavy atoms. The process is known as spin-orbit coupling and arises owing to interaction of the electron spin with the nucleus of the heavy atom.[16,17]

In this study we have used heavy-atom solvents to alter the forbiddenness of the intercombinational, nonradiative population of the triplet state *via* enhanced spin-orbit interaction of the first excited-singlet state with the triplet state of the dye molecule. Figure 5 shows the effect of heavy-atom solvents on the rate of photoisomerization; in this case the conversion of the trans form into the cis by photochemical means is shown. The curves represent plots of the ratio of optical density of trans to cis *vs.* excitation time at −125° in EPA. The absorption characteristics of the dye are essentially unaltered in the presence of the ethyl halides, *i.e.*, no evidence of transitions associated with charge-transfer bands or iodine-dye complexes were observed.

The data show that although the photostationary state shows a slight dependency on solvent matrix composition, the rate of conversion increases in the presence of the heavy-atom solvent at concentration 2.5 *M*. The initial rates increase in the following order with respect to solvent composition: EPA + EtI > EPA + EtBr > EPA + EtCl > EPA. The rate is approximately 40% greater in the presence of ethyl chloride and almost three times as great with bromide as the heavy-atom component of the solvent matrix. Although an accurate measurement of the initial slope was difficult to obtain with the ethyl iodide owing to the rapidity of the reaction, the rate is believed to be at least four times that in the pure solvent matrix alone. The rate of photoconversion of isomers is also found to be dependent upon the concentration of the added

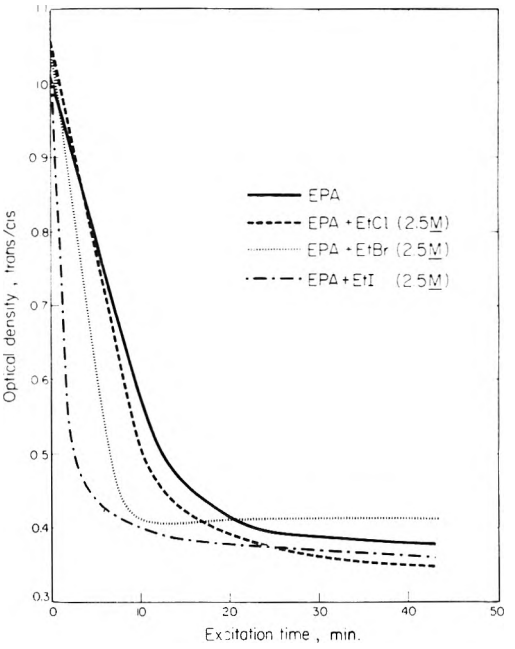

Figure 5. Effect of external heavy atoms (2.5 *M*) on the rate of trans → cis photoisomerization of 3,3′-diethyl-9-methylthiacarbocyanine bromide in EPA at −125°: concentration = 6×10^{-6} *M*. Excitation is at 560 nm.

heavy-atom solvent. Undoubtedly, at the higher concentrations of heavy atoms the probability of spin-orbit coupling is enhanced by the closer approach of iodine atoms to the chromophore, resulting in an increase in the rate of conversion. The rate of photoisomerization of the cyanine dye is found to increase with increasing number of electrons of the heavy atom incorporated in the ethyl halide solvent. Apparently, with increased spin-orbit coupling factor of the atom, the rate of intersystem crossover from the excited-singlet to the triplet level is correspondingly increased. And as a result of the enhancement of the trans → cis conversion, it can be concluded that the photoisomerization of 3,3′-diethyl-9-methylthiacarbocyanine must proceed essentially through a triplet state.

Further evidence to support a reaction mechanism requiring population of the triplet state is provided by the observation that the 3,3′-diethyl-9-methylselenacarbocyanine dye in EPA under similar experimental conditions undergoes a very rapid conversion from trans to cis, in fact, so fast that within 15 min or less excitation time, the absorption band assigned to the trans isomer of the dye is completely bleached. The rapid rate of photoconversion is attributed to the intramolecular heavy-atom contribution of the selenium atom. In contrast, the oxacarbocyanine analog shows little or no evidence of isomer resolution at low temperature. For example, after extended periods of irradiation at −125° in a band reputedly ascribed to a geometrical isomer of the 3,3′-diethyl-9-methyloxacarbocyanine,[2a] followed by rapid cooling to −196°, no suggestion of either increased or decreased band absorption could be found that might be a manifestation of a photoisomerization. With respect to the oxa, thia, and selena derivatives of the dye, a direct correlation exists between the spin-orbit coupling factor and the ease of photoisomerization. The order of rates is as follows: selena > thia > oxa. Furthermore, a study[18] of the triplet-state lifetimes and relative quantum efficiencies of the fluorescence and phosphorescence shows explicitly the operation of an in-

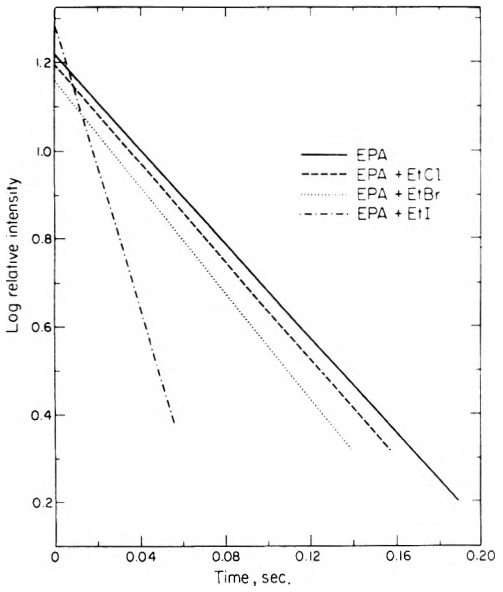

Figure 6. Decay of triplet states of 3,3′-diethyl-9-methylthiacarbocyanine bromide in EPA solution at −196° as a function of external heavy atoms (2.5 *M*): dye concentration = 6 × 10^{-6} *M*.

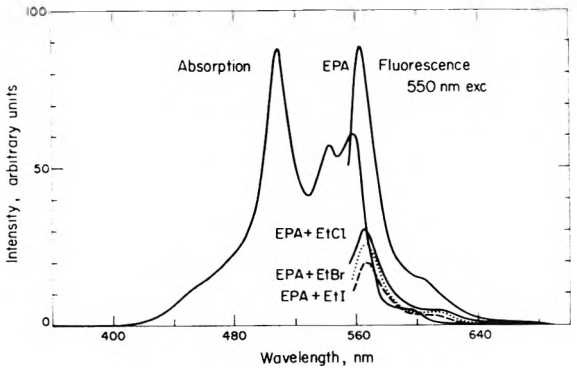

Figure 7. Absorption and total emission (fluorescence) spectra of 3,3′-diethyl-9-methylthiacarbocyanine bromide in EPA solution at −196° as a function of external heavy atoms (2.5 *M*): dye concentration = 6 × 10^{-6} *M*.

tramolecular heavy-atom effect. For example, the relative quantum yield of fluorescence decreases in going from oxa, thia, to selena derivatives of the dye. The opposite relationship exists with respect to the phosphorescence quantum yields, and it is verified by a measure of the mean phosphorescence lifetimes of the dyes, *i.e.*, the heavier the atom the greater the phosphorescence yield relative to the fluorescence, and the shorter the triplet-state lifetime of the dye.

The phosphorescence decay rates of 3,3′-diethyl-9-methylthiacarbocyanine in EPA and the heavy-atom solvents were measured and found to be exponential and followed first-order decay kinetics as shown in Figure 6, where the log (relative intensity) is plotted as a function of time. The data show that the slopes, and consequently lifetimes, of the triplet state of the dye vary significantly only in the presence of ethyl iodide, 2.5 *M*. The presence of ethyl chloride or ethyl bromide at 2.5 *M* in the solvent matrix appears to have little effect upon the decay rate when compared to the control (dye in EPA). The presence of iodide as a heavy-atom addition to the matrix greatly influences both the intersystem crossover rate and the

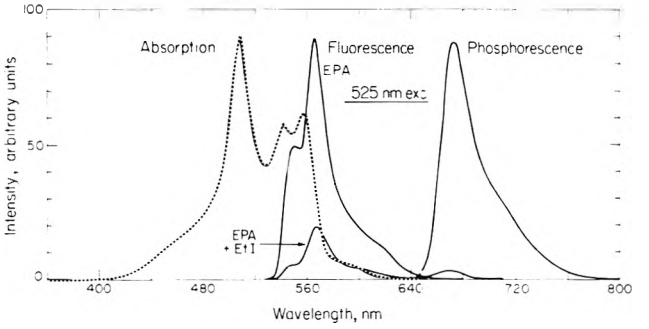

Figure 8. Absorption, fluorescence, and phosphorescence spectra of 3,3′-diethyl-9-methylthiacarbocyanine bromide in EPA solution at −196° in the presence of ethyl iodide at 2.5 *M* concentration: dye concentration = 6 × 10^{-6} *M*. Evidence of triplet emission is seen in the fluorescence spectrum due to effective spin–orbit coupling of the iodide.

triplet-state lifetime. This behavior is in contrast to that of chloride and bromide, which seemingly affect only the crossover rate. This anomaly may be attributable to the varying effects of the heavy atoms on the radiationless process. These effects are not well known for the systems studied.

However, the fluorescence quantum yields are affected in all cases as shown in Figures 7 and 8 for excitations at two different wavelengths. For 550-nm excitation, ethyl chloride and ethyl bromide appear almost as effective in quenching the fluorescence as ethyl iodide. In the presence of chloride the fluorescence intensity at peak emission wavelength is shown to be decreased by about one-third of the intensity in EPA alone. Further decreases occur on the addition of ethyl bromide to the solvent, and for the iodide the fluorescence intensity of the most intense emission band decreases to less than one-quarter the intensity observed in EPA alone. A similar situation prevails in the presence of ethyl iodide for the excitation at 525 nm, which induces (Figure 8) the emission bands characteristic of the geometrical isomers situated at 550 and 566 nm, respectively, for the cis and trans isomers. Of greater significance in the total emission (fluorescence) is evidence of emission assigned to the triplet state, as shown by the relatively low intensity unresolved band with center at about 670 nm, which coincides with the position of the phosphorescence. This result unequivocally illustrates the ability of iodide to increase the population of the triplet manifold and provides further proof for the proposed mechanism of photoisomerization occurring primarily *via* a triplet state.

Further substantiation of the triplet state as the dominant intermediate in the photoisomerization is provided by experiments wherein a known triplet sensitizer, benzophenone, was added to an oxygen-free 2-methyltetrahydrofuran solution of 3,3′-diethyl-9-methylthiacarbocyanine bromide. The concentration of the sensitizer was 2 × 10^{-2} *M* and that of dye was 6 × 10^{-6} *M*. The solution, cooled to −90°, was exposed for 2.5 min to the light of a 900-W xenon arc source transmitted through a water filter to eliminate undesirable infrared radiation, plus a Kodak Wratten filter No. 18-A. This arrangement permitted excitation of the solution with wavelengths primarily from 340 to 380 nm, a region of the spectrum where the dye is transparent, but the benzophenone absorbs yielding n–π^* states. After excitation the solution was rapidly cooled to −196° and the emission and excitation spectra were studied. In comparison to controls, the ratio of cis to trans iso-

TABLE I: Manifestations of Heavy-Atom Solvent (2.5 *M*) on 3,3′-Diethyl-9-methylthiacarbocyanine Bromide at −196° [a]

Solvent	Heavy-atom spin-orbit coupling factor, ζ, cm^{-1}	$\zeta(cm^{-1})^2 \times 10^{-6}$	Rate of photoisomerization[b] (t → c) × 10^3	Relative yield[c] φ_{ph}/φ_F	Triplet lifetime, τ_{ph}, sec
EPA	188[d]	0.04	4.5	0.005	0.081
EPA + EtCl	587	0.35	6.3	0.012	0.079
EPA + EtBr	2460	6.1	12.5	0.019	0.070
EPA + EtI	5060	25.6	18.0	0.101	0.003

[a] $C = 6 \times 10^{-4}$ *M*. [b] Data taken at −125°. [c] Corrected for slit widths and spectral response of photomultiplier. [d] Coupling factor for intramolecular sulfur atom of the dye according to B. W. N. Lo, K. M. S. Saxena, and S. Fraga, *Theor. Chim. Acta*, **25**, 97 (1972).

mers in the triplet sensitized solution was found to have increased about 300%, as measured by the fluorescence emission, suggesting that the benzophenone triplet couples primarily with the ground-state trans-geometrical isomer to yield ground-state sensitizer and the triplet state of the isomer. On relaxation the trans isomer is converted to the cis and the low temperature equilibrium distribution is now altered to give more cis than that found in the absence of triplet sensitizer.

Since the probability of spin-orbit coupling is related to the square of the spin-orbit coupling constant of the heavy atom,[19,20] we can correlate to a rough approximation the relationships existing between the heavy-atom spin-orbit coupling factor, rates of photoisomerization as measured by initial slopes, triplet-state lifetimes, and relative quantum yields of fluorescence and phosphorescence. These data are summarized in Table I. The intramolecular heavy-atom effect exerted by the sulfur heteroatom is approximately twice or more that of an external heavy atom, and thus the change in the rate of isomerization in the presence of ethyl chloride is not dramatically different. However, the data illustrate that although the relative rate of photoisomerization of *trans*-3,3′-diethyl-9-methylthiacarbocyanine into its cis configuration compares favorably with the calculated probability of spin-orbit coupling only for the pure solvent and the ethyl chloride matrix, a progressive increase in rate of molecular rearrangement is found to parallel increases in relative quantum yields of phosphorescence and spin-orbit coupling of the solvent. Changes in solvent viscosity on addition of bromide and iodide atoms may be involved in suppressing the reaction rates below those anticipated based primarily upon the spin-orbit coupling factors of the heavy atoms. Also, the efficiency of the electronic coupling of the excited-singlet state of the dye molecules with solvent molecules may vary, and subsequently alter the expected relationship between spin-orbit coupling parameters and rates of trans to cis isomerization. Studies of the intramolecular heavy-atom effect on the photochemical isomerization are planned as a means of obviating solvent viscosity effects and possibly improving the correlation between theory and experiment for the heavier atoms.

The heavy-atom effect, which is a commonly used tool in spectroscopy, is shown to be applicable to experimental problems of cyanine dyes. In this specific instance the rate of photoconversion of geometrical isomers resolved at low temperature can be increased by the effect.

References and Notes

(1) Deceased.
(2) (a) W. West, S. Pearce, and F. Grum, *J. Phys. Chem.*, **71**, 1316 (1967); (b) S. P. McGlynn, R. Sunseri, and N. J. Christodouleas, *J. Chem. Phys.*, **37**, 1818 (1962).
(3) M. Kasha, *J. Chem. Phys.*, **20**, 71 (1952).
(4) S. P. McGlynn, T. Azumi, and M. Kasha, *J. Chem. Phys.*, **40**, 507 (1964).
(5) D. O. Cowan and R. L. E. Drisko, *J. Amer. Chem. Soc.*, **92**, 6281 (1970).
(6) W. Cooper, S. P. Lovell, and W. West, *Photogr. Sci. Eng.*, **14**, 184 (1970).
(7) L. G. S. Brooker, G. H. Keyes, and D. W. Heseltine *J. Amer. Chem. Soc.*, **73**, 5350 (1951); **87**, 2443 (1965).
(8) E. M. Kosower, *J. Amer. Chem. Soc.*, **80**, 3253 (1958).
(9) W. West and S. Pearce, *J. Phys. Chem.*, **69**, 1894 (1965).
(10) H. Greenspan and E. Fischer, *J. Phys. Chem.*, **69**, 2466 (1965).
(11) R. Heiligman-Rim, Y. Hirshberg, and E. Fischer, *J. Phys. Chem.*, **66**, 2470 (1962).
(12) F. Dorr, J. Kotschy, and H. Kausen, *Ber. Bunsenges. Phys. Chem.*, **69**, 11 (1965).
(13) J. Q. Umberger, *Photogr. Sci. Eng.*, **11**, 392 (1967).
(14) J. N. Murrell, "The Theory of the Electronic Spectra of Organic Molecules," Chapman and Hall Ltd., London, 1963, p 54.
(15) A. V. Buettner, private communication.
(16) W. Kauzman, "Quantum Chemistry," Academic Press, New York, N. Y., 1957, p 349.
(17) D. S. McClure, *J. Chem. Phys.*, **17**, 905 (1949).
(18) W. Cooper, unpublished data.
(19) S. K. Lower and M. A. El-Sayed, *Chem. Rev.*, **66**, 199 (1966).
(20) S. P. McGlynn, T. Azumi, and M. Kinoshita, "The Triplet State," Prentice-Hall, Englewood Cliffs, N. J., 1969, Chapter 5.

Excited State Production by Nonionic Processes in the Pulse Radiolysis of Gaseous Systems Containing Naphthalene[1]

Myran C. Sauer, Jr.,* and William A. Mulac

Chemistry Division, Argonne National Laboratory, Argonne, Illinois 60439 *(Received June 14, 1973)*

Publication costs assisted by Argonne National Laboratory

The emission yield (relative) from the first excited singlet state of naphthalene and the yield of the lowest triplet state of naphthalene have been determined in the gas phase as a function of the concentrations of naphthalene, argon, and *n*-hexane in samples containing SF_6, which is known to eliminate the formation of these excited states by ionic processes. The conclusion is reached that in argon systems, an important mechanism for production of the lowest excited singlet of naphthalene is direct excitation by low-energy electrons which lose energy to argon with a much lower efficiency than to naphthalene. In *n*-hexane systems, the results indicate that a major part of the singlet emission is a result of energy transfer from an excited state of *n*-hexane. In the case of the triplet state yields, arguments are presented which indicate that intersystem crossing from a highly vibrationally excited level of the first excited singlet is responsible for a large part of the triplet yield, and that this cross over occurs before vibrational deactivation can occur, even at the relatively high pressures used.

I. Introduction

The experimental determination of energy partitioning (with respect to excited state formation) in the radiolysis of gaseous mixtures, and of yields of excited states in pure gases as well as in mixtures is a subject which is still in its infancy. In the present work, the techniques of pulse radiolysis are applied to this important problem, and the information presented, it is hoped, will stimulate further experiments on this subject.

The subject of energy partitioning in the radiolysis of gaseous mixtures has been investigated by Klots in the case of total ionization yields, by precise measurements of W values of mixtures.[2-5] The conclusion reached is that the fractional energy adsorption (leading to ion production) due to a molecule in a mixture can be related to a parameter, Z', for that molecule, which is independent of the nature of other molecules in the mixture. (Z' may be considered as an effective atomic number.) For example, in the case of a mixture of molecules i and j

$$\epsilon_i = Z_i'C_i/(Z_i'C_i + Z_j'C_j) \quad (1)$$

where ϵ_i is the fraction of energy absorbed from the radiation field by species i, and C represents concentration. The quantity ϵ_i can therefore be thought of as an effective electron fraction. If G^0_{im} represents the 100-eV yield of any states, m, leading to ionization when $C_j = 0$, then the G for ionization in the mixture is given by

$$G_{im} = G^0_{im}\epsilon_i \quad (2)$$

Although the aforementioned investigations have resulted in a set of Z' values for a series of gaseous molecules which allow one to accurately calculate the G for ionization in mixtures of these molecules, the applicability of these Z' values in the case of excitation to levels below the ionization potential is largely an untested extrapolation.[4,6] Information bearing on the latter problem is presented in this paper, where the lowest excited singlet and triplet states of naphthalene are observed in mixtures with argon or *n*-hexane. Some of the results are found to be incompatible with Z' values expected on the basis of the W value measurements of Klots.

II. Experimental Section

General aspects of the pulse radiolysis apparatus, as well as details of the sample vessels and sample preparation, have been given previously.[7] Samples were sealed off in 16 cm long, 4 cm i.d. cylindrical vessels and irradiated with electron pulses of from 10 nsec to 1 μsec duration and of approximately 13-MeV energy. Currents of about 10 A were used with the shorter duration pulses (10-40 nsec), and 1.5 A with the 1-μsec pulse. Although the detection system previously described,[7] which has a rise time of about 15 nsec, was used for most of the experiments, a Tektronix 7904 oscilloscope was used in experiments where a faster response was needed, the rise time then being limited by the photomultiplier to a few nsec.

The argon (99.999% stated purity), *n*-hexane (Phillips Research Grade), naphthalene (zone refined, James Hinton Co.), and SF_6 (Matheson) were used without purification.

III. Results

The yields of N^1 (used to designate the levels of the first excited singlet[8] state of naphthalene which produce the observed emission of light in the region of 313-378 nm) were determined from the emission decay curves obtained with 10-A, 40-nsec pulses. Because of the nature of the decay, the relative yields could be determined either by measuring the emission signal at a fixed time after the pulse, or by extrapolating the emission decay curve to the end of the pulse and in making a small correction for decay during the pulse. The latter method was slightly preferable, because of possible small changes in the emission decay rate due to temperature variations. The emission decay at 120° was first order over three half-times with a half-time of 78 nsec, which was independent of the pressures of various components in the mixtures studied. The half-time changed with temperature, however, being 55 nsec at 200° and 106 nsec at 25°. The emission spec-

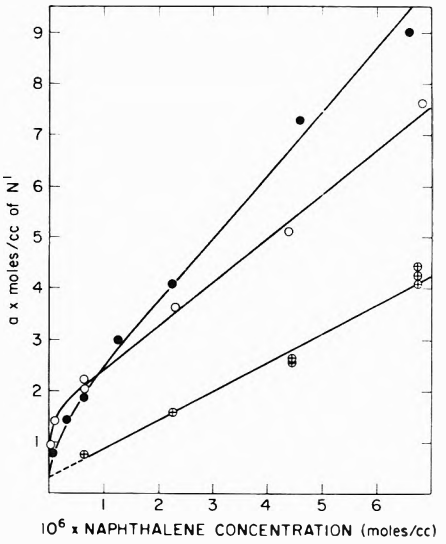

Figure 1. Yields of N^1 *vs.* concentration of naphthalene. All samples contained 3 × 10^{-7} mol/cc of SF_6; 200°: ⊕, no additives; O, 2.62 × 10^{-5} mol/cc of argon; ●, 1.46 × 10^{-5} mol/cc of *n*-hexane.

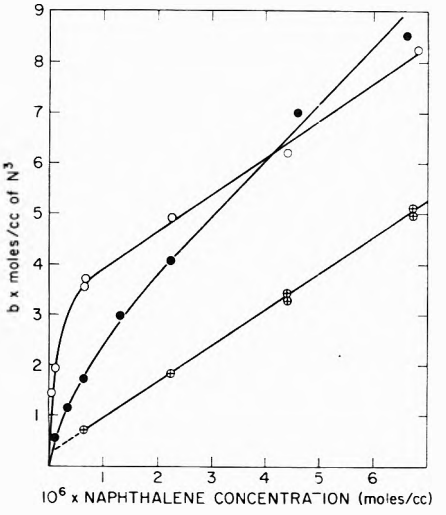

Figure 2. Yields of N^3 *vs.* concentration of naphthalene. All samples contained 3 × 10^{-7} mol/cc of SF_6; 200°: ⊕, no additives; O, 2.62 × 10^{-5} mol/cc of argon; ●, 1.46 × 10^{-5} mol/cc of *n*-hexane.

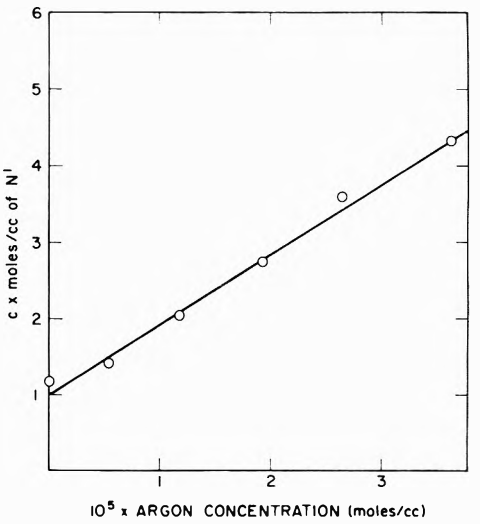

Figure 3. Yield of N^1 *vs.* concentration of argon. All samples contained 6.7 × 10^{-7} mol/cc of naphthalene and 3 × 10^{-7} mol/cc of SF_6; 135°.

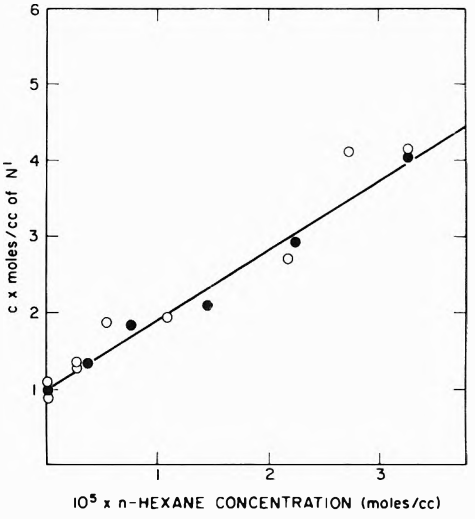

Figure 4. Yields of N^1 *vs.* concentration of *n*-hexane. All samples contained 6.7 × 10^{-7} mol/cc of naphthalene and 3 × 10^{-7} mol/cc of SF_6; 135°. Each point represents a separate sample, and the two sets of points represent two separate series of experiments.

trum, which is reported elsewhere,[10] was likewise independent of the pressures, except that at wavelengths below about 324 nm the spectrum was distorted due to absorption by ground-state naphthalene. Therefore, in studying the N^1 yields as a function of naphthalene concentration, the emission was observed at 348 nm (band pass 5 nm). When the naphthalene concentration was constant, a wavelength of 328 nm was used. Examination of the spectrum in various mixtures showed no evidence of interference from impurity emissions. The relatively large concentrations of naphthalene used should inhibit the production of excited states of any trace impurities, such as N_2 and H_2O, which might be present.

The yields of N^3 (used to designate the lowest triplet state of naphthalene) were determined using 1.5-A, 1-μsec pulses, the larger pulse being used to obtain enough N^3 absorption to make the analysis feasible. The 397-nm absorption of N^3 in the vapor phase has been determined[11] to follow Beer's law. Under all conditions, the first half-life of the N^3 decay was greater than 10 μsec, so an accurate initial yield could be obtained. The initial yield was obtained by extrapolating the triplet decay curve to the end of the pulse and making a small approximate correction for decay during the pulse. A correction for a small underlying absorption was made by subtracting the absorbance at 388 nm (where N^3 absorbs only weakly) from that at the absorption maximum (397 nm).

The results of the N^1 and N^3 yield measurements are shown in Figures 1–6. The yields are given in arbitrary units, and are proportional to the concentration of the N^1 or N^3 produced by a pulse. The proportionality constants are designated by the letters *a*, *b*, *c*, and *d* in the labels of the ordinates in order to indicate in which figures the yield scales are identical.

Although the analysis of the results is done in terms of these relative yields, the *G* value for N^3 was estimated in one sample by integrating the absorption spectrum, shown in Figure 7, to obtain the concentration of N^3 produced by

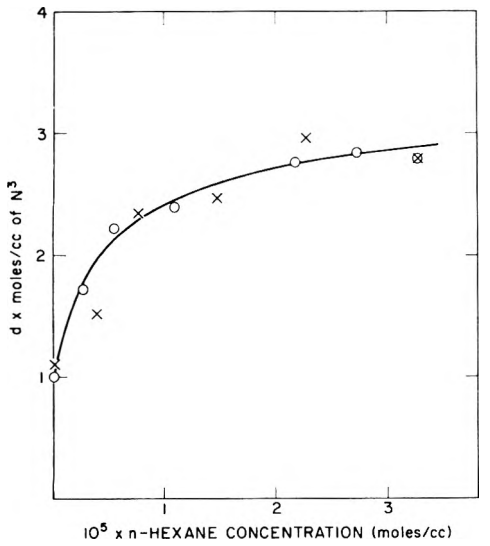

Figure 5. Yield of N^3 *vs.* concentration of *n*-hexane. All samples contained 6.7 × 10^{-7} mol/cc of naphthalene and 3 × 10^{-7} mol/cc of SF_6; 135°. Each point represents a separate sample, and the two sets of points represent two separate series of experiments.

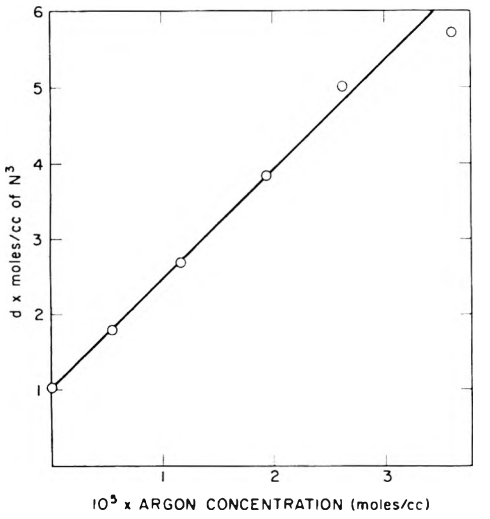

Figure 6. Yield of N^3 *vs.* concentration of argon. All samples contained 6.7 × 10^{-7} mol/cc of naphthalene and 3 × 10^{-7} mol/cc of SF_6; 135°.

a pulse, using the value of 0.12[12] for the oscillator strength in the region 348–414 nm. The relationship used[13] is

$$C = (3.48 \times 10^{-8}/fl) \int_{E_1}^{E_2} D \, dE$$

where C is the concentration in moles/cc, f is the oscillator strength, l is the optical path length in cm, D is the absorbance, and E is energy in eV. In integrating the N^3 spectrum, the absorption indicated by the ×'s in Figure 7 was subtracted from the curve through the open circles. That this subtraction should be made is indicated by the effect of oxygen on the absorption spectrum and the fact that in the sample without oxygen, nearly the same background absorbance is obtained (not shown) if a long-lived component of the decay curves is plotted. This background absorbance is probably due to a radical species. The observed effect of oxygen in increasing the triplet decay rate is in qualitative agreement with a previous

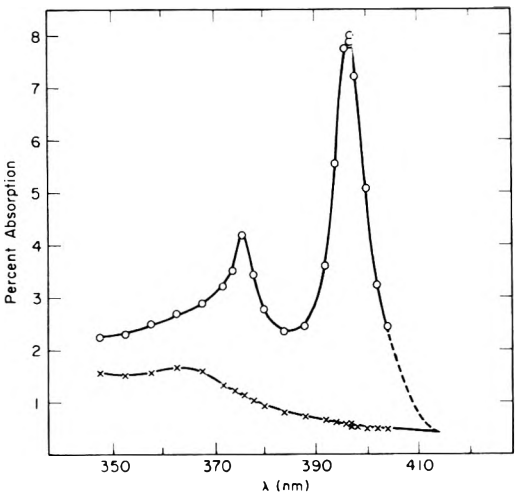

Figure 7. Absorption spectra of N^3. The samples contained 7.4 × 10^{-6} mol/cc of naphthalene and 6 × 10^{-7} mol/cc of SF_6 at 195 ± 5°. The band pass was 2.5 nm: O, % absorption corrected for decay during pulse; ×, 6 × 10^{-7} mol/cc of O_2 added, half-time of N^3 decay 3.5 μsec, per cent absorption measured at 15 μsec after pulse.

study of this reaction in the vapor phase.[11] The dosimetry method (O_3 formation in O_2-containing SF_6) has been described elsewhere.[7,10] Using the measured dose, and the concentration obtained from the above integration, a G value for N^3 of 1.5 is obtained.

IV. Discussion

At the outset of this discussion, the evidence indicating that SF_6 eliminates the production of N^1 and N^3 by ionic processes must be cited. A thorough study has been made of the temporal behavior of the N^1 emission following an electron pulse.[10] In samples without SF_6, semilog plots of the emission decay curves are "S-shaped," but when SF_6 is added, the semilog plot of the decay is linear, with the slope independent of dose per pulse. Analysis of the dependence of the S-shaped decays on dose per pulse confirms the conclusion that in the absence of SF_6, an important fraction of the N^1 is formed *via* ion recombination, and the rate constant for the reaction of the electron with the naphthalene positive ion is determined as (2.4 ± 0.6) × 10^{18} cc mol^{-1} sec^{-1}. At the SF_6 concentrations used in the present work (about 3 × 10^{-7} mol/cc), SF_6 should capture electrons before recombination occurs, because of the large rate constant of this capture reaction[14] (1.3 × 10^{17} cc mol^{-1} sec^{-1}), and the fact that the ion concentrations are in the range of 10^{-11} mol/cc. The possibility that, in samples containing SF_6, part of the N^1 arises from a fast geminate recombination between SF_6^- (or the electron) and the naphthalene positive ion can be ruled out by the following arguments. A thermal electron will diffuse,[15] on the average, a certain distance before being captured by SF_6. This distance, at the SF_6 concentration used, is greater than the calculated distance between primary electron tracks, and it is therefore likely that the distribution of ions is fortuitously homogeneous. The tendency toward homogeneity is enhanced by the fact that the electrons are not initially at thermal energy. Inhomogeneous recombination has been observed[16] in electron capturing gases at ion concentrations about five orders of magnitude lower than those used in the present work, where track overlapping is not expected to lead to a homogeneous distribution. However, there is no evidence to

suggest that there is geminate recombination of the free electron with positive ions. Conceptually, such a process would be indistinguishable from direct production of neutral fragments or excited states.

Concerning the formation of N^3 by ionic reactions, 1 mol % SF_6 was observed[17] to reduce the N^3 yield by 95% in 3.7×10^{-5} mol/cc cyclohexane containing 0.2 mol % naphthalene, which shows that the production of N^3 by ionic reactions is negligible in samples containing SF_6, especially since the remaining 5% can be explained on the basis of nonionic mechanisms. Therefore, because all of the systems to be discussed contained SF_6, we need only consider the production of excited states of naphthalene *via* direct excitation by energetic electrons, or by energy transfer processes.

The yields of N^1 and N^3 as a function of naphthalene concentration are shown in Figures 1 and 2, respectively. In the absence of added argon or *n*-hexane, the observed linear increases in yields are reasonable, because the absorption of energy from the beam is expected to be linear with stopping power over the range of naphthalene concentration covered.[7] However, the nonzero intercepts are bothersome, and are apparently due to excitation processes which are not related to absorption of energy from the electron beam as it passes through the gas, and which are "saturated" at low naphthalene concentration. Cerenkov emission from the Suprasil cell window was shown to be responsible, in part, by experiments in which a Suprasil disk was inserted in front of the cell window. In the normal cell, absorption of Cerenkov radiation is responsible for about 15% of the N^1 at 6.7×10^{-7} mol/cc, and about 6% at ten times higher concentration of naphthalene. Since this effect can explain less than half of the nonzero intercept, absorption of energy from relatively low-energy electrons, originating from the passage of the primary beam through the vessel window, is suggested as an additional process which can be imagined to saturate at low naphthalene concentration. Obviously, this situation introduces uncertainty to the interpretation of the results; however, it is clear that the changes in the N^1 and N^3 yields caused by variation of the argon, *n*-hexane, and naphthalene concentrations are predominantly due to other processes, and that these "window yields" do not obscure the interesting qualitative conclusions which can be drawn from the results.

A. N^1 Production in Argon Systems. Figure 3 shows the yield of N^1 as a function of C_{Ar}. The straight line is drawn through the points only to indicate the approximately linear increase, and has no basis in theory, although approximately linear behavior can be obtained, as is seen in the following.

The significance of these data lies in their implications with respect to the application of equations analogous to (1) and (2) to this system. Applying these to the production of N^1 in argon–naphthalene mixtures, we obtain

$$G(N^1) = G^0(N^1)(1 + Z_{Ar}'C_{Ar}/Z_N'C_N)^{-1} \quad (3)$$

Equation 3 can be converted to a yield basis ($Y(N^1)$ for comparison with Figure 1 using the relationship $Y(N^1) \propto G(N^1)(S_{Ar}C_{Ar} + S_NC_N)$, where $Y(N^1)$ is the concentration of N^1 produced for a given pulse length and current, which leads to

$$Y(N^1) = Y^0(N^1)(1 + Z_{Ar}'C_{Ar}/Z_N'C_N)^{-1} \times (1 + S_{Ar}C_{Ar}/S_NC_N) \quad (4)$$

where $Y^0(N^1)$ refers to $C_{Ar} = 0$. The stopping power ratio is estimated as $S_{Ar}/S_N = 0.232$ on the basis of atomic stopping powers.[18] One can readily show that there is no value of Z_{Ar}'/Z_N' which allows a fit with the data of Figure 3, even if allowance is made for the fact that 40% of $Y^0(N^1)$ may be due to the "window yield" of N^1, which would not be expected to increase with increasing C_{Ar}. However, a fit can be obtained if, in addition to the window yield, two processes, each being described by an equation such as 4, are responsible for N^1 production. One process must have a Z_{Ar}'/Z_N' value of about 0.1, and the other a value of approximately 0.006, and the $Y^0(N^1)$ values for the processes must be approximately equal.[19] A Z' ratio of 0.1 would be expected on the basis of Klot's studies.[3,4] The significance of the requirement of a process with a much smaller Z' ratio is that a variation of Z' with electron energy is implied, and accordingly, the two Z' ratios may represent average values for high ($Z_{Ar}'/Z_N' = 0.1$) and low ($Z_{Ar}'/Z_N' = 0.006$) energy electrons. This does not seem unlikely, because a considerable part of the oscillator strength of naphthalene[9] is at lower energy than in the case of argon, and, of course, subexcitation electrons (<11.6 eV) would lose energy almost entirely to naphthalene.

This interpretation in terms of two Z' values can also be shown to be qualitatively consistent with the results in Figure 1 showing the yield of N^1 as a function of naphthalene concentration at a constant C_{Ar}, *i.e.*, a rapid initial rise[20] is expected, corresponding to the process with low Z_{Ar}'/Z_N', after which the slower increase in the N^1 yield approximately follows the slope obtained with naphthalene alone, and is due to a combination of the two processes.

An important question with respect to the above interpretation is whether energy transfer can be responsible for the observed increase in N^1 yield with increasing argon pressure. Mathematically, it is possible to obtain a fit on this basis, but energy transfer appears to be ruled out by the nature of the N^1 emission decay curves observed in argon (3×10^{-5} mol/cc) containing SF_6 (6×10^{-8} mol/cc), and as little as 1.3×10^{-8} mol/cc of naphthalene. Using a 10-nsec pulse width, and a detection system with an overall risetime of no more than 3 nsec, the decay of N^1 was observed to be exponential after the pulse (with the same decay constant as obtained at 100 times greater naphthalene concentration). Therefore, there was no indication of any process producing N^1 after the pulse. Production of N^1 by collision of naphthalene with excited argon should have proceeded with a rate (see below) slow enough that a distortion of the exponential decay of the N^1 emission would have been observed. Such a distortion would be expected to be in the form of a "flat" portion just after the pulse, or a smaller decay $t_{1/2}$ than observed at 100 times greater naphthalene concentration. Reaction of $Ar(^3P_2)$ with naphthalene can be predicted to proceed with a collisional efficiency of about unity on the basis of measured rate constants for reaction of $Ar(^3P_2)$ with other reactants.[21] The other excited states of argon at about 11.6 eV, *i.e.*, $^3P_0$, $^3P_1$, and $^1P_1$, are likely to react with comparable efficiencies. Although the $^3P_2$ and $^3P_0$ states are metastable and the $^3P_1$ and $^1P_1$ states are radiatively allowed, all of these states were observed[22,23] to decay with the same half-time (about 0.2 μsec) at argon concentrations of about 3×10^{-5} mol/cc, and the decay was slower at lower pressures. This situation has been dis-

cussed in terms of radiation imprisonment and collisionally induced transitions among the above states.[23] Hence, the lifetimes of these states should be sufficiently long that energy transfer to naphthalene should have been observable under the conditions of our experiment if this were an important source of N^1. The deactivation of these excited states of argon by three body reactions (to form Ar_2 excited dimers) will proceed much slower than the energy transfer, on the basis of the rate constant[24] of 2.2 $\times 10^{15}$ cc^2 mol^{-2} sec^{-1} for Ar($^3P_2$). Therefore, the reaction of these excited states of argon, which are about 3.5 eV above the ionization potential of naphthalene, with naphthalene must result predominantly in ionization, bond breakage, or production of triplet states of naphthalene, or alternatively, these excited states are not produced in significant concentrations, possibly because of quenching by naphthalene of higher (precursor) excited states.

B. N^1 Production in n-Hexane Systems. The dependence of the N^1 yield on the *n*-hexane concentration is shown in Figure 4, and, as in the case of argon, the increase is approximately linear. However, the explanation cannot be analogous, because if the assumption (which is of doubtful validity in this case) is made that the Z' ratio for hexane to naphthalene is very small for part of the electron energy spectrum, which would allow an explanation analogous to that given for the argon system, then the results in Figure 1 for constant *n*-hexane concentration cannot be explained. A curve with a sharp initial rise and a general similarity to the curve in Figure 1 for constant argon concentration is predicted if a low Z' ratio applies. Computer simulations show that the N^1 yields in hexane (Figures 1 and 4) can be explained if energy transfer from an excited state of *n*-hexane is important. A natural lifetime of about 10^{-9} sec is required, assuming a collisional efficiency of unity for the energy transfer. Excited states with comparable lifetimes have been found to be important in alkane liquids.[25-27]

C. N^3 Production in n-Hexane Systems. The levelling off of the N^3 yield at higher *n*-hexane concentrations (Figure 5) is an important qualitative difference in comparison with the other results on the N^1 and N^3 yields as a function of argon or *n*-hexane concentration. From the shape of the curve in Figure 5 and the approximately linear increase in Figure 4, the fraction of N^3 which is produced by cross over from the lowest excited singlet state, N^1, in the absence of added hexane can be no greater than 0.15 to 0.2. The remainder of the N^3 could be formed by direct excitation of the naphthalene by electrons with energies near the threshold energies for the production of various naphthalene triplet states, the cross sections for such processes being negligible otherwise.[28] The use of an equation analogous to (4), with $S_{hexane}/S_N = 0.754$[18] and with a Z' ratio for hexane to naphthalene of about 0.2 enables a fit with the experimental data to be obtained. However, our observed G value of 1.5 for N^3 in naphthalene, and the fact that cross over from the N^1 levels which produce the observed emission is not responsible for a major part of the N^3 even though the cross-over efficiency is greater than 80%,[29] argue against the latter explanation for N^3 formation. This can be seen as follows. The G value of the emitting levels of N^1 would be only *ca* 0.3, and the G value of N^3 produced by direct excitation would be about 1.3. Such a high yield of N^3 from direct excitation is unlikely, because the triplets can only be produced by electrons near threshold, whereas the excitation of singlet states is contributed to by electrons of all energies above threshold. Therefore, the production of singlet states by direct excitation should be favored over direct production of triplet states. (An estimate of the G value for all states below the ionization potential on the basis of the optical approximation is $G = 0.6$.[30])

A more likely source of the major part of the N^3 is cross over from N^1 containing a large excess of vibrational energy. That this process can be important is supported by the following evidence. The absorption spectrum[31] and electron energy loss spectroscopy[9] of naphthalene vapor show that the oscillator strength in the energy region[32] corresponding to the third excited singlet state (5.7-6.4 eV) is 1.3 compared to 0.11 for lower energies; hence production of the lower excited singlet states by electron impact is not favorable relative to deposition of energy at 5.7-6.4 eV. Internal conversion of the third excited singlet to vibrationally excited levels of the first excited singlet has been found by Lim and Uy[29] to proceed before other processes can occur. Combining their fluorescence quantum yield measurements with the lifetime studies of Laor and Ludwig,[33] they have found the rate constant for nonradiative decay of the vibrationally excited first excited singlet (k_{nr}) to increase exponentially with increasing vibrational energy beginning at about 5.3-eV total energy. (The radiative rate constant also increases, but it is considerably smaller and increases much less rapidly.) Also, Lim and Uy conclude that this nonradiative decay channel at energies above 5.3 eV is intersystem crossing to the first triplet state, and, from the lifetime studies of Laor and Ludwig, the value of k_{nr} corresponding to an excitation energy (6 eV) in the region of the maximum absorption intensity of the third excited singlet is nearly 10^9 sec^{-1}. Therefore, the cross over to N^3 could occur before collisional processes are able to remove appreciable vibrational energy from the highly vibrationally excited N^1, and as a result, most of the N^3 could result from excitation in the singlet manifold. If this explanation is correct, the results in Figure 5 can be fit, using an equation analogous to (4), again with $S_{hexane}/S_N = 0.754$ and a Z' ratio for hexane to naphthalene of about 0.2. In this case, the Z' ratio refers to the process of absorption of energy by naphthalene to produce the third excited singlet state. A Z' ratio (hexane/naphthalene) of about 0.6 is predicted on the basis of Klot's studies;[3,4] therefore the value of 0.2 is a further indication that Z' ratios for excited state production are not generally the same as those for ion production.

The results on the N^3 yield as a function of naphthalene concentration (Figure 2) at constant hexane concentration can be fit equally well using either of the mechanisms which have been discussed. Therefore, one can only say that these results are consistent with those obtained as a function of *n*-hexane concentration.

D. N^3 Production in Argon Systems. In the case of argon systems, there is no tendency for the N^3 yield to level off at higher argon concentrations (Figure 6). In section C, the conclusion was reached that no more than 0.15 to 0.2 of the N^3, in a sample without added hexane or argon, could be formed by cross over from the lowest excited singlet state, N^1. On the basis of this and the observed nature of the increases in N^1 and N^3 with increasing argon pressure, one can also rule out cross over from N^1 as being responsible for a major fraction of the N^3

yield in the argon system. On the basis of the above discussion of the N^3 yield in *n*-hexane systems, the production of N^3 in argon by cross over from vibrationally excited N^1 is the most likely process. In order to obtain the observed approximately linear increase in yield (Figure 6), the Z' ratio for production of the third excited singlet state must be approximately 0.006 (argon/naphthalene) as in the case of the N^1 yield in argon. However, two other processes cannot be ruled out as contributing to the N^3 yield in argon, because they would also result in an approximately linear increase in N^3 yield with increasing argon concentration. N^3 could be produced by direct excitation by subexcitation electrons, but the G value argument presented in the discussion of N^3 in *n*-hexane probably precludes this process from being the major source of N^3. The production of N^3 by energy transfer from excited argon cannot be ruled out because the N^3 absorption could not be looked at with sufficiently good time resolution. It is possible then, that all three of the above processes contribute to the N^3 yield. The results (Figure 2) on the N^3 yield as a function of naphthalene concentration at constant argon concentration can readily be fit on the basis of the above mechanisms. The rapid initial increase followed by a linear increase with the same slope as obtained in the case of naphthalene alone is expected on the basis of the production of N^3 by a process with a low Z' ratio, or by an energy transfer process which is very efficient.

In spite of the complexities in the processes occurring in excited naphthalene, the results and discussion presented here offer some insight into the production of excited states *via* nonionic processes. Concerning possible future experiments, a direct measurement of the G values for singlet states of naphthalene would be valuable. It is not clear whether the methods used for determining $G(N^1)$ in a study of liquid naphthalene[30] can be applied to the gas phase, since the processes of eximer formation and collisional removal of vibrational energy may result in qualitatively different behavior in the liquid phases. The results of the latter work are not expected to be directly comparable with the present study, because in addition to the phase difference, the G values for excited states from ionic and nonionic processes could not be separated. However, it is interesting that the liquid phase values of $G(N^3) = 3.8$ and $G(N^1) = 2.4$ show that the yield of the lowest excited singlet state of naphthalene is more important relative to N^3 than is indicated by the gas-phase results presented here, where values of $G(N^3) \simeq 1.3$ and $G(N^1) \simeq 0.3$ are suggested by the analysis (section C) for the excited state yields produced in naphthalene vapor by direct excitation.

Acknowledgment. We thank Dr. R. H. Huebner for enlightening discussions bearing on many aspects of this paper.

References and Notes

(1) Work performed under the auspices of the U. S. Atomic Energy Commission.
(2) C. E. Klots, *J. Chem. Phys.*, **39**, 1571 (1963).
(3) C. E. Klots, *J. Chem. Phys.*, **44**, 2715 (1966).
(4) C. E. Klots, *J. Chem. Phys.*, **46**, 3468 (1967).
(5) C. E. Klots, "Fundamental Processes in Radiation Chemistry," P. Ausloos, Ed., interscience, New York, N. Y., 1968, p 2.
(6) C. E. Klots, *Proc. Tenth Czech. Annu. Meet. Radiat. Chem., 10th*, **1**, 120 (1970).
(7) M. C. Sauer, Jr., and W. A. Mulac, *J. Chem. Phys.*, **56**, 4995 (1972).
(8) A recent summary of the spectral features of naphthalene vapor is given in ref 9.
(9) R. H. Huebner, S. R. Mielczarek, and C. E. Kuyatt, *Chem. Phys. Lett.*, **16**, 464 (1972).
(10) M. C. Sauer, Jr., and W. A. Mulac, *Int. J. Radiat. Phys. Chem.*, in press.
(11) G. Porter and P. West, *Proc. Roy. Soc., Ser. A*, **279**, 302 (1964).
(12) D. Lavalette, R. Bensasson, B. Amand, and E. J. Land, *Chem. Phys. Lett.*, **10**, 331 (1971).
(13) S. P. McGlynn, L. G. Vanquickenborne, M. Kinoshita, and D. G. Carroll, "Introduction to Applied Quantum Chemistry," Holt, Rinehart and Winston, New York, N. Y., 1972, pp 300–301.
(14) F. C. Fehsenfeld, *J. Chem. Phys.*, **53**, 2000 (1970).
(15) S. McGowan, *Can. J. Phys.*, **45**, 439 (1967).
(16) L. B. Loeb, "Basic Processes of Gaseous Electronics," University of California Press, Berkeley, Calif., 1960, p 201.
(17) G. R. A. Johnson and M. C. Sauer, Jr., *J. Chem. Phys.* **51**, **496** (1969).
(18) D. W. Huyton and T. W. Woodward, *Radiat. Res. Rev.*, **2**, 205 (1970).
(19) Although a series of computations was carried out to reach these conclusions, the quantitative aspects should not be emphasized because of the uncertainties introduced by the "window yield" and by the nature of this fitting procedure. In fact, various mechanisms for excited state formation were tested, for all of the systems studied, in a series of computer simulations. However, it became clear that the results could be used mainly in a qualitative sense, as has been done in this discussion.
(20) The initial rise would be expected to be even more rapid if the presence of SF_6 were not required, because SF_6 undoubtedly is effective in absorbing energy from the electron flux at the lowest naphthalene concentration.
(21) M. Bourene and J. LeCalve, *J. Chem. Phys.*, **58**, 1452 (1973).
(22) S. Arai and R. F. Firestone, *J. Chem. Phys.*, **50**, 4575 (1969).
(23) R. F. Firestone and L. M. Dorfman, *Actions Chim. Biol. Radiat.*, **15**, 8 (1971).
(24) J. LeCalve and M. Bourene, *J. Chem. Phys.*, **58**, 1446 (1973).
(25) M. S. Henry and W. P. Helman, *J. Chem. Phys.*, **56**, 5734 (1972).
(26) G. Beck and J. K. Thomas, *J. Phys. Chem.*, **76**, 3856 (1972).
(27) W. Rothman, F. Hirayama, and S. Lipsky, *J. Chem. Phys.*, **58**, 1300 (1973).
(28) J. B. Birks, L. G. Christophorou, and R. H. Huebner, *Nature (London)*, **217**, 809 (1968).
(29) E. C. Lim and J. O. Uy, *J. Chem. Phys.*, **56**, 3374 (1972).
(30) R. A. Holroyd and C. Capellos, *J. Phys. Chem.*, **76**, 2485 (1972).
(31) C. A. George and G. C. Morris, *J. Mol. Spectrosc.*, **26**, 67 (1968).
(32) We will, for convenience, designate this energy region as the third excited singlet; possible states in this region are discussed in ref 9.
(33) U. Laor and P. K. Ludwig, *J. Chem. Phys.*, **54**, 1054 (1971).

Radiolysis of Liquid Nitrous Oxide[1]

T. E. M. Sambrook and G. R. Freeman*

Chemistry Department, University of Alberta, Edmonton, Canada T6G 2G2 *(Received July 11, 1973)*

The product yields from the γ radiolysis of liquid nitrous oxide at 183 K were $G(N_2) = 13.1 \pm 0.2$, $G(O_2)$ 2.7 ± 0.1, and $G(NO_2) = 5.6 \pm 0.2$. Addition of nitrogen dioxide (dinitrogen tetroxide) to the liquid decreased the oxygen yield to zero and the nitrogen yield to an extrapolated limit of 5 ± 1 units. Nitrogen dioxide scavenges electrons and probably positive charge and oxygen atoms in liquid nitrous oxide. Carbon dioxide has no effect on the product yields from nitrous oxide. Sulfur hexafluoride decreases the oxygen yield to zero and the nitrogen yield to 10 ± 1 units. Sulfur hexafluoride scavenges electrons and possibly oxygen atoms in liquid nitrous oxide.

Introduction

The electron-scavenging properties of nitrous oxide are well recognized[2-12] and have been exploited in liquid-phase radiation chemistry.[2,3,7-10] However, the radiolysis of liquid nitrous oxide itself has only been investigated briefly,[13] and the correction to apply for the direct radiolysis of nitrous oxide in liquid systems is uncertain.[12] It is therefore desirable to make an extended study of the radiolysis of liquid nitrous oxide. Additionally, the radiolysis of inorganic liquids other than water have received scant attention, so an investigation of liquid nitrous oxide has merit in itself.

Experimental Section

Materials. Research grade nitrous oxide (Matheson Co.) was initially bubbled through two concentrated potassium hydroxide solutions to remove carbon dioxide and nitrogen dioxide, and dried through three 60-cm columns of Drierite. It was further purified by freeze-pump-thaw and distillation cycles under vacuum and then stored in a reservoir. Sulfur hexafluoride and carbon dioxide, both supplied by Matheson Co., were thoroughly degassed and introduced into 1-l. storage bulbs.

Nitrogen dioxide (Matheson Co.) contained traces of nitric oxide; this was removed by trap-to-trap distillation at 195 K using a Dry Ice and acetone slush bath. The purified nitrogen dioxide was retained in a reservoir until used. Prolonged use of nitrogen dioxide caused corrosion in the vacuum system and required the replacement of valves and mercury manometers.

Sample Preparation and Irradiation. The liquid samples ($\sim$1.5 ml) were prepared by conventional vacuum techniques in Pyrex bulbs of 2.5-ml capacity, and extreme care was taken to ensure removal of nitrogen and oxygen. Hoke stainless steel needle valves with Teflon seats were used in the nitrous oxide purification, storage, and sample-filling line. Ground glass joints were greased very lightly with Apiezon N, the grease being confined to a band around the bottom half of the joint. The mercury manometer was isolated from the sample preparation line during the filling of the cells. Care was taken at all times to prevent mercury condensation in the line.

Most samples were maintained at 183 K by a methanol slush bath while being irradiated in a ^{60}Co Gammacell-220 (Atomic Energy of Canada Ltd.). Samples containing nitrogen dioxide were irradiated at a temperature of 228 K using a chlorobenzene slush, and solutions of nitrous oxide and carbon dioxide were irradiated at 226 K using a *m*-xylene slush. These higher irradiation temperatures were used because both additives appeared insoluble in liquid nitrous oxide at 183 K. The dose rate, determined by the Fricke dosimeter and corrected for the relative electron densities, was 2.5×10^{17} eV/min g_{N_2O} and the dose was 2.5×10^{18} eV/g_{N_2O}.

Product Analysis. Nitrogen and oxygen were extracted by vacuum distillation through two traps at 77 K, then collected and measured in a McLeod-Toepler apparatus, followed by gas chromatography analysis. A 2.5-m Linde Molecular Sieve 5A column was used at 298 K with helium carrier gas and a Gow Mac thermal conductivity detector.

Nitrogen dioxide was determined through conversion to nitrite.[14]

$$2NO_2 + 2OH^- \longrightarrow NO_2^- + NO_3^- + H_2O \qquad (1)$$

A cell containing the frozen sample was allowed to warm and explode in 20 ml of 0.025 *M* sodium hydroxide solution contained in a partially evacuated, 1-l., thick-walled bottle. After agitation on a mechanical shaker for 0.5 hr to ensure complete absorption of the nitrogen dioxide, the resultant solution was filtered through a sintered glass crucible (10–20 μ porosity) into a 100-ml volumetric flask. Subsequently, 10 ml of sulfanilic acid solution (8 g of acid in 270 ml of glacial acetic acid diluted to 1 l. with water) and 10 ml of α-naphthylamine reagent (freshly prepared, 5 g of amine in 270 ml of glacial acetic acid, diluted to 1 l.) were added to the flask. This solution was diluted to 100 ml, mixed, and set aside. After 30 min, aliquots were pipetted into 1-cm optical cells and the nitrite concentration measured spectrophotometrically at 520 nm. Unirradiated samples were processed through the above stages and used as blanks. Calibrations were made with standard nitrite solutions.

Results

Pure Nitrous Oxide. The yields of nitrogen, oxygen, and nitrogen dioxide obtained from the radiolysis of liquid nitrous oxide at 183 K were $G(N_2) = 13.1 \pm 0.2$, $G(O_2) = 2.7 \pm 0.1$, and $G(NO_2) = 5.6 \pm 0.2$. These results agree satisfactorily with those reported earlier for 185 K, namely, $G(N_2) = 12.9 \pm 0.2$, $G(O_2) = 2.6 \pm 0.1$, and $G(NO_2) = 5.0 \pm 0.2$.[13]

Effects of Additives. The product yields from solutions are expressed both as G values, based upon the total energy absorbed by the solution, and as g values, based upon the energy initially absorbed in the solvent only: $g = G/$(electron fraction of solvent). The latter (g) is usually the more convenient to use in kinetic analysis of results from concentrated solutions.

Addition of nitrogen dioxide decreased the oxygen yield to zero, but only reduced that of nitrogen to about half of the value in pure nitrous oxide (Figure 1). The magnitude of a g value is always greater than that of the corresponding G at solute concentrations >0, but for the oxygen yields in Figure 1 the two types of yield are the same within the resolution of the graph.

Radiolysis of pure liquid nitrogen dioxide, or dinitrogen tetroxide, at 273 K gave $G(N_2) < 0.1$ and $G(O_2) < 0.1$.

Addition of up to 37 mol % of carbon dioxide had little or no effect upon either $g(N_2)$ or $g(O_2)$, as shown in Figure 2. The decrease in $G(N_2)$ and $G(O_2)$ were simply due to dilution of the nitrous oxide by the carbon dioxide.

Sulfur hexafluoride reduced the oxygen yield to zero, but had relatively little effect upon $g(N_2)$ (Figure 3). The nitrogen yields at 183 and 228 K were the same, within the experimental uncertainty, thereby indicating that the solute was completely dissolved at both temperatures.

The relative magnitudes of the effects of the solutes on the nitrous oxide product yields were in the order $NO_2 > SF_6 > CO_2$ = zero.

Discussion

The previously suggested mechanism[13] would require only slight modification if recent information about gas-phase reactions[15] could be extrapolated to the liquid phase. In particular, Parks could not detect a long-lived N_2O^- ion, and at high nitrous oxide pressures O^- ions reacted rapidly to form $N_2O_2^-$.[15] The corresponding liquid-phase mechanism might be as follows (mechanism I).

$$N_2O \longrightarrow N_2O^+ + e^- \quad (2)$$

$$N_2O \longrightarrow N_2O^* \quad (3)$$

$$e^- + N_2O \longrightarrow N_2O^- \quad (4)$$

$$N_2O^- \longrightarrow N_2O + O^- \quad (5)$$

$$O^- + N_2O \xrightarrow{N_2O} N_2O_2^- \quad (6)$$

$$N_2O^+ + N_2O_2^- \longrightarrow N_2O^* + 2NO \quad (7)$$

$$N_2O^+ + N_2O_2^- \longrightarrow N_2O^* + N_2 + O_2 \quad (8)$$

$$N_2O^* \longrightarrow N_2 + O \quad (9)$$

$$O + O + M \longrightarrow O_2 + M \quad (10)$$

$$2NO + O_2 \longrightarrow 2NO_2 \quad (11)$$

The oxygen atoms in reactions 9 and 10 are assumed to be in the ground, triplet state.[13]

The $N_2O_2^-$ ions observed in the gas phase were formed in a third-order reaction,[15] which might indicate that they were ion-dipole "clusters" of O^- with N_2O, rather than single-molecule ions such as $ONNO^-$. A gas-phase $O^- \cdot N_2O$ cluster extrapolated to the liquid-phase becomes O^-_{solv}. For simplicity the subscript solv may be dropped, because all of the ions in the liquid are solvated. A possible variant of mechanism I is therefore to replace reactions 6-8 by (12) and (13), giving mechanism II.

$$N_2O^+ + O^- \longrightarrow 2NO \quad (12)$$

$$N_2O^+ + O^- \longrightarrow N_2 + O_2 \quad (13)$$

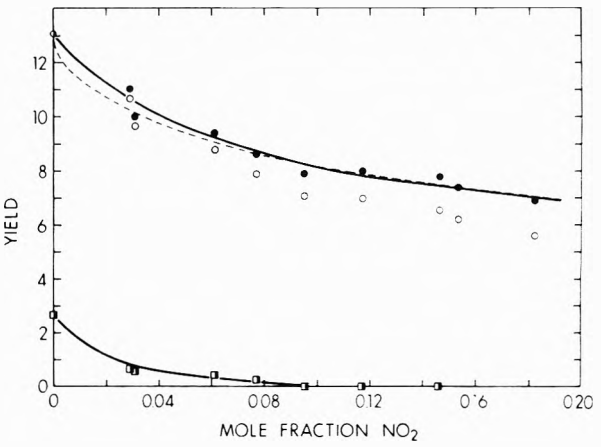

Figure 1. Effect of nitrogen dioxide on the nitrogen and oxygen yields from the radiolysis of nitrous oxide at 228 K: ○, $G(N_2)$; ●, $g(N_2) = G(N_2)/$(electron fraction of N_2O); ◨, $G(O_2)$ and $g(O_2)$. The full curve through $g(N_2)$ was calculated using eq 19; the dashed curve was calculated using eq 20.

A third version of the mechanism must be considered. Model[16] calculations indicate that about 99% of the radiolytic ions in liquid nitrous oxide undergo geminate neutralization (dielectric constant = 1.97 at 183 K;[17] assume the average secondary electron range to be ≲100 Å because the molecule contains π bonds[18]). Thus most of the ions have neutralization times $<10^{-9}$ sec.[16] There is indirect evidence[5,19-22] that N_2O^- might be sufficiently long-lived to participate in geminate neutralization, in which case reactions 5-8 would be replaced by (14) and (15) (mechanism III).

$$N_2O^+ + N_2O^- \longrightarrow 2NO + N_2 \quad (14)$$

$$N_2O^+ + N_2O^- \longrightarrow 2N_2 + O_2 \quad (15)$$

Mechanisms I-III differ only in the importance assigned to reactions 5 and 6, with consequent adjustments made to the neutralization reactions.

Effect of Added Nitrogen Dioxide. For the sake of simplicity equilibrium 16 will be ignored, because the relative reactivities of NO_2 and N_2O_4 are not known.

$$2NO_2 \rightleftharpoons N_2O_4 \quad (16)$$

Although the values of the electron affinities are uncertain, that of NO_2 (90 kcal/mol,[23] <60 kcal/mol[24]) is probably greater than that of N_2O (≥11 kcal/mol[21]). Furthermore, the ionization potential of NO_2 (9.78 eV[25]) is lower than that of N_2O (12.89 eV[25]). Thus reaction 17 can compete with (4), and (18) with the neutralization reactions 7 and 8 or 12 and 13 or 14 and 15.

$$e^- + NO_2 \longrightarrow NO_2^- \quad (17)$$

$$N_2O^+ + NO_2 \longrightarrow N_2O + NO_2^+ \quad (18)$$

Both solute and solvent are electron scavengers, so the competition between reactions 4 and 17 is governed by the homogeneous kinetics equation

$$\frac{1}{g(NO_2^-)} = \frac{1}{g(\text{ionization})}\left(1 + \frac{k_4[N_2O]}{k_{17}[NO_2]}\right) \quad (19)$$

Reaction 18 competes with geminate neutralization and is governed by the nonhomogeneous kinetics equation[26]

$$g(NO_2^+) = g(\text{ionization}) \int_0^\infty F(y)\Phi_0\, dy \quad (20)$$

where $F(y)\,dy$ is the fraction of thermalized electron-ion

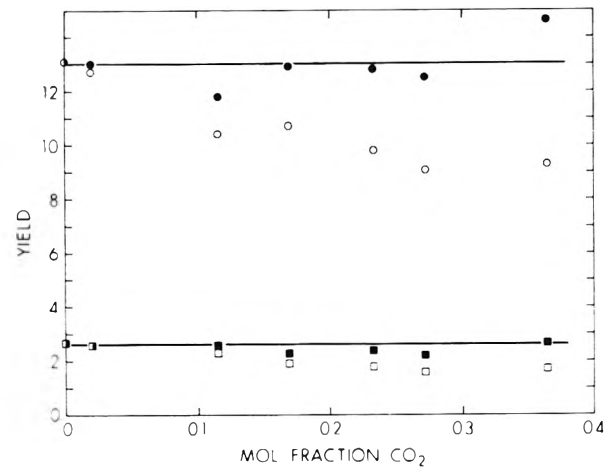

Figure 2. Effect of carbon dioxide on the nitrogen and oxygen yields from the radiolysis of nitrous oxide at 226 K: O, $G(N_2)$; ●, $g(N_2)$; □, $G(O_2)$; ■, $g(O_2)$.

pairs that have initial intrapair distances between y and $y + dy$

$$\Phi_y = \phi_y^{fi} + (1 - \phi_y^{fi})[1 - (1 - fN_s)^{1.4 \times 10^7 y^3 \beta}] \quad (21)$$

$$\phi_y^{fi} = \exp(-\xi^2/\epsilon k T y) \quad (22)$$

f is the encounter efficiency of the scavenging reaction, N_s is the mole fraction of scavenger in the solution, ϵ is the dielectric constant of the liquid, β is an adjustable parameter, ξ is the electronic charge, k is Boltzmann's constant, and T is the absolute temperature.

The complete scavenging of all of the electrons and positive ions by NO_2 would decrease the nitrogen yield by an amount $\Delta g(N_2)_{max}$. The radiolysis of pure NO_2 yields no nitrogen, so it can be assumed that the neutralization of NO_2^+ by NO_2^- does not lead to nitrogen formation.

$$NO_2^+ + NO_2^- \longrightarrow \text{no } N_2 \quad (23)$$

$\Delta g(N_2)_{max}$ therefore corresponds to the amount of nitrogen formed by reactions of charged species in pure nitrous oxide.

The simple shape of the $g(N_2)$ curve in Figure 1 indicates one of two possible things: (a) $\Delta g(N_2)_{max}$ can be achieved by scavenging only one type of species, *i.e.*, only electrons or only ions; or (b) the efficiency of scavenging electrons is similar to that of scavenging ions. The latter seems to be more credible.

Approximate values of k_4/k_{17} and $g(N_2)_{max}$ can be obtained by assuming $\Delta g(N_2) \propto g(NO_2^-)$ and plotting $1/\Delta g(N_2)$ against $[N_2O]/[NO_2]$ (Figure 4). One obtains $k_4/k_{17} = 0.07 \pm 0.02$ and $\Delta g(N_2)_{max} = 8 \pm 1$.

Conversely, by assuming $\Delta g(N_2) \propto g(NO_2^+)$ and doing iterative calculations with eq 20 one may estimate the ion scavenging efficiency and $\Delta g(N_2)_{max}$. As a rough approximation the distribution function $F(y)$ was taken as (24),

$$F(y) = 1800y^{-3} \quad y \geq 30 \text{ Å}$$
$$F(y) = 0 \quad y < 30 \text{ Å} \quad (24)$$

which gives $\phi_{fi} = \int_0^\infty F(y)\,\phi_y^{fi}\,dy = 0.01$ for $\epsilon = 1.97$ and $T = 183$ K. The dashed curve in Figure 1 was calculated using $\Delta g(N_2)_{max} = 8$ and $\beta = 4 \times 10^{12}$ V/cm^2.

It appears that $\Delta g(N_2)_{max} = 8 \pm 1$, independent of the above choice of mechanisms. The "unscavengeable" yield of nitrogen $g(N_2)_{unsc} = 5 \pm 1$ is attributed to reactions 3 and 9.

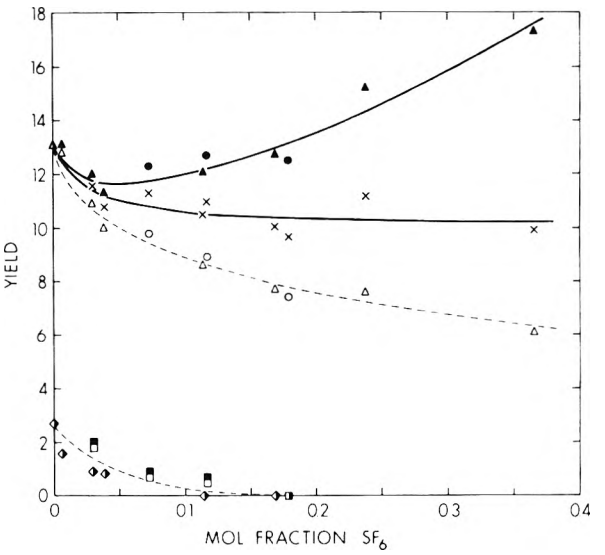

Figure 3. Effect of sulfur hexafluroide on the nitrogen and oxygen yields from the radiolysis of nitrous oxide at 183 (triangles and diamonds) and 228 K (circles and squares): △ and ○, $G(N_2)$; ▲ and ●, $g(N_2)$; ◆ $G(O_2)$ and $g(O_2)$; □, $G(O_2)$; ■, $g(O_2)$; ×, $g(N_2)_{corr}$. The full lines were calculated from eq 29 and 30.

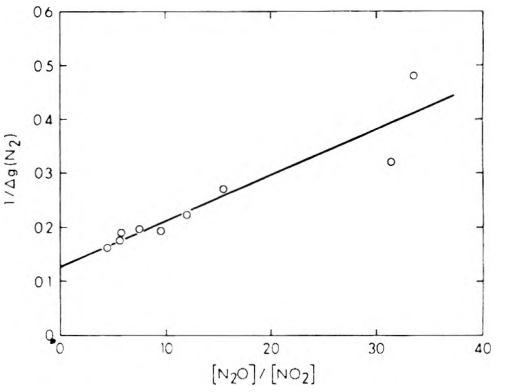

Figure 4. A plot of the nitrogen yields from N_2O/NO_2 solutions according to eq 19.

One can determine from a material balance that the ionization yield required to give $\Delta g(N_2)_{max} = 8 \pm 1$ for mechanism I would be $g(\text{ionization}) = 3.6 \pm 0.4$, whereas it would be 5.5 ± 0.5 for either mechanism II or III. By comparison, in the gas phase, $g(\text{ionization})_{gas} = 3.0$.[27,28]

The oxygen yield is reduced to zero by NO_2 (Figure 1), which may be attributed to

$$O + NO_2 \longrightarrow NO_3 \quad (25)$$

Effect of Added Carbon Dioxide. Carbon dioxide has a negligible effect on the nitrous oxide product yields (Figure 2). Scavenging of positive charge by carbon dioxide would not occur because its ionization potential (13.79 eV[25]) is greater than that of nitrous oxide. Furthermore, the lack of effect on the product yields indicates that the electron affinity of carbon dioxide is lower than that of nitrous oxide. Electrons initially captured by carbon dioxide may be transferred to nitrous oxide.

Effect of Added Sulfur Hexafluoride. The value of $g(N_2)$ decreases slightly with increasing sulfur hexafluoride concentration up to about 5 mol %, then increases at higher concentrations (Figure 3).

The initial decrease can be attributed to electron scavenging by the additive.[29,30]

$$e^- + SF_6 \longrightarrow SF_6^- \quad (26)$$

The competition between reactions 26 and 4 would be governed by an equation analogous to (19).

The increase in $g(N_2)$ at high sulfur hexafluoride concentrations is attributed to charge transfer to N_2O from SF_6^+ ions created by direct radiolysis of sulfur hexafluoride

$$SF_6^+ + N_2O \longrightarrow SF_6 + N_2O^+ \quad (27)$$

$$N_2O^+ + SF_6^- \longrightarrow N_2 + \text{products} \quad (28)$$

The ionization potential of sulfur hexafluoride is 19.3 eV,[25] much larger than that of nitrous oxide, 12.89 eV, so reaction 27 is exothermic.

The values of $g(N_2)$ in Figure 3 were corrected for nitrogen produced by reactions 27 and 28, assuming that $g(\text{ionization})_{SF_6} = 4$ in the liquid phase and that the amount of energy absorbed by the solute was proportional to the electron fraction of the solute in the solution. The gas-phase ionization yield in SF_6 is 2.9[31] and there is evidence that ionization potentials are lower in the condensed phases than in the gas phase,[32-35] so $g(\text{ionization})_{SF_6} = 4$ is not unreasonable for the liquid. Analysis of the corrected yields by an equation analogous to (19) gave $\Delta g(N_2)_{max} = 3 \pm 1$, and $k_4/k_{26} = 0.03 \pm 0.015$.

The lines of Figure 3 were calculated from equations 29 and 30

$$g(N_2)_{cor} = 13.1 - 3\left(1 + \frac{[N_2O]}{40[SF_6]}\right)^{-1} \quad (29)$$

$$g(N_2) = g(N_2)_{cor} + 4(\epsilon_{SF_6}/\epsilon_{N_2O}) \quad (30)$$

where ϵ_{SF_6} and ϵ_{N_2O} are the electron fractions of the respective substances in the solution.

Inclusion of reactions 26-28 in mechanism I, and using the value $g(\text{ionization})_{N_2O\ liq} = 3.6$ estimated from the nitrogen dioxide solution results, leads to the prediction that $\Delta g(N_2)_{max} = 4.5$ for the sulfur hexafluoride solutions. Similar treatments of mechanisms II and III using the value $g(\text{ionization})_{N_2O\ liq} = 5.5$, required by the nitrogen dioxide solution results, lead to the predicted value $\Delta g(N_2)_{max} = 2.8$ for both mechanisms. The observed value $\Delta g(N_2)_{max} = 3 \pm 1$ slightly favors mechanism II or III over I.

The fact that the oxygen yield is reduced to zero (Figure 3) indicates that sulfur hexafluoride reacts either with oxygen atoms or their precursor.

References and Notes

(1) Assisted financially by the National Research Council of Canada.
(2) F. S. Dainton and D. B. Peterson, *Nature (London)*, **186**, 878 (1960).
(3) G. Scholes and M. Simic, *Nature (London)*, **202**, 895 (1964).
(4) G. R. A. Johnson and J. M. Warman, *Trans. Faraday Soc.*, **61**, 1709 (1965).
(5) W. J. Holtslander and G. R. Freeman, *Can. J. Chem.*, **45**, 1661 (1967).
(6) G. R. A. Johnson and M. Simic, *J. Phys. Chem.*, **71**, 118 (1967).
(7) M. G. Robinson and G. R. Freeman, *J. Chem. Phys.*, **48**, 983 (1968).
(8) J. M. Warman, K.-D. Asmus, and R. H. Schuler, *Advan. Chem. Ser.*, **No. 82**, 25 (1968).
(9) K. N. Jha and G. R. Freeman, *J. Chem. Phys.*, **51**, 2839, 2846 (1969).
(10) M. G. Robinson and G. R. Freeman, *J. Chem. Phys.*, **55**, 5644 (1971).
(11) S. Takao, Y. Hatano, and S. Shida, *J. Phys. Chem.*, **75**, 3178 (1971).
(12) Y. Hatano, K. Takeuchi, and S. Takao, *J. Phys. Chem.*, **77**, 586 (1973).
(13) M. G. Robinson and G. R. Freeman, *J. Phys. Chem.*, **72**, 1394 (1968).
(14) J. C. Gage, N. Stafford, and R. Truhaut, "Methods for the Determination of Toxic Substances in Air," International Union of Pure and Applied Chemistry, Butterworths, London, 1959, p 16.1.
(15) D. A. Parks, *J. Chem. Soc., Faraday Trans. 1*, **68**, 2103 (1972).
(16) G. R. Freeman and J. M. Fayadh, *J. Chem. Phys.*, **43**, 86 (1965).
(17) A. A. Maryott and E. R. Smith, *Nat. Bur. Stand. U. S., Circ.*, **No. 514**, 3 (1951).
(18) J.-P. Dodelet, K. Shinsaka, U. Kortsch, and G. R. Freeman, *J. Chem. Phys.*, **59**, 2376 (1973).
(19) J. F. Paulson, *Advan. Chem. Ser.*, **No. 58**, 28 (1966).
(20) P. J. Chantry, *J. Chem. Phys.*, **51**, 3380 (1969).
(21) J. F. Paulson, *J. Chem. Phys.*, **52**, 959 (1970).
(22) F. S. Dainton, P. O'Neil, and G. A. Salmon, *Chem. Commun.*, 1001 (1972).
(23) S. Tsuda and W. H. Hamill, *Advan. Mass Spectrosc.*, **3**, 249 (1966).
(24) E. E. Ferguson, D. B. Dunkin, and F. C. Fehsenfeld, *J. Chem. Phys.*, **57**, 1459 (1972).
(25) R. W. Kiser, "Introduction to Mass Spectrometry and Its Applications," Prentice-Hall, Englewood Cliffs, N. J., 1965.
(26) G. R. Freeman, *J. Chem. Phys.*, **46**, 2822 (1967).
(27) G. G. Meisels, *J. Chem. Phys.*, **41**, 51 (1964).
(28) R. Cooper and R. M. Mooring, *Aust. J. Chem.*, **21**, 2417 (1968).
(29) R. W. Fessenden and K. M. Bansal, *J. Chem. Phys.*, **53**, 3468 (1970).
(30) A. V. Phelps and R. E. Vorshall, *J. Chem. Phys.*, **49**, 3246 (1968).
(31) D. W. Huyton and T. W. Woodward, *Trans. Faraday Soc.*, **66**, 1648 (1970).
(32) C. Vermeil, M. Matheson, S. Leach, and F. Muller, *J. Chim. Phys.*, **61**, 598 (1964).
(33) N. Geacintov, M. Pope, and H. Kallmann, *J. Chem. Phys.*, **45**, 2639 (1966).
(34) J. Moan, *Chem. Phys. Lett.*, **18**, 447 (1973).
(35) M. G. Robinson and G. R. Freeman, *Can. J. Chem.*, **51**, 641 (1973).

Radiolysis of Liquid Nitrous Oxide. Hydrocarbon Additives[1]

T. E. M. Sambrook and G. R. Freeman*

Chemistry Department, University of Alberta, Edmonton, Canada, T6G 2G2 *(Received July 11, 1973)*

Sixteen different hydrocarbons were added over wide concentration ranges to liquid nitrous oxide at 183 K. The oxygen and nitrogen dioxide yields were reduced from their initial G values of 2.7 and 5.6, respectively, to zero by 8 mol % hydrocarbon, while the water yield increased from zero to a maximum value of 11. The nitrogen yield decreased from 13.1 to about 11 over the same concentration region, but continued to decrease as the nitrous oxide was progressively diluted by the hydrocarbon. Kinetic analysis of the results led to the following observations. (a) G(total ionization) = 5.5 ± 0.5 in liquid nitrous oxide, nearly double the gas-phase yield. (b) Reactions of the charged species are precursors of all the NO_2 and 8 ± 1 G units of N_2. (c) The G value of N_2O^* formed by direct excitation is 5 ± 1, and the decomposition of N_2O^* is not inhibited by hydrocarbons. (d) Hydrocarbons inhibit nitrogen formation by reaction with N_2O^+, probably by charge transfer.

Introduction

Nitrous oxide has been extensively used as an electron scavenger in studies of the kinetics and mechanism of radiolysis reactions in liquid hydrocarbons.[2-11] The yield of nitrogen from an irradiated solution is generally taken to be proportional to the yield of electrons scavenged by nitrous oxide,[11] but it is not yet certain whether the proportionality factor is 1.0 or whether it is slightly greater. Electron scavenging in alkanes by nitrous oxide decreases the hydrogen yield, but the decrease in hydrogen yield $\Delta g(H_2)$ is always smaller than the yield of nitrogen $g(N_2)$.[6,8,9,11] This has often been interpreted to mean that more than one nitrogen molecule results from the initial reaction of one electron with a nitrous oxide molecule, the "excess" nitrogen being attributed to secondary reactions of O^- or some other intermediate. Another possibility is that, on the average, less than one hydrogen results from the reaction of each electron in the absence of nitrous oxide.[12]

A major difficulty in the interpretation of results from nitrous oxide solutions has been the uncertainty about the magnitude of the yield of nitrogen from the direct radiolysis of the nitrous oxide in the solutions. The present work was done to solve the problem by measuring the yields of products from liquid nitrous oxide in the presence and absence of hydrocarbons.

Experimental Section

Materials and Techniques. The materials and procedures were the same as those reported earlier,[13] with the following exceptions.

Toluene was obtained from Fisher Scientific Co. All the other hydrocarbons were Phillips Research Grade.

Traces of olefins were removed from the liquid alkanes by shaking for 1 day with concentrated sulfuric acid. The alkanes were then washed with water, dried over anhydrous magnesium sulfate and distilled from lithium aluminum hydride. The liquids were then introduced into a vacuum system and thoroughly degassed.

Alkanes that were gaseous at STP were purified by freeze–pump–thaw and distillation cycles under vacuum.

Both liquid and gaseous alkenes were degassed and introduced into storage bulbs until ready for use.

The 1.7-cm^3 samples were prepared in 2.5-cm^3 Pyrex cells using conventional vacuum techniques. Care was taken to ensure that the liquid nitrous oxide and additive were completely mixed at 183 K, the irradiation temperature.

The irradiation dose rate was 2.5×10^{17} eV/g min (5.1×10^{15} eV/cm^3 sec) and the doses used were $2\text{–}9 \times 10^{18}$ eV/g.

The product water was measured with the aid of a special irradiation cell (Figure 1A). After irradiation, the cell was glassblown into the analysis line that is shown schematically in Figure 1B, while keeping the sample cooled to 183 K. The tubing on both sides of the cell was then evacuated, BS1 being warmed to allow all adventitious water to be pumped out of the tubing. The entire cell was then cooled to 183 K, up to the level of B1 in Figure 1B, breakseal BS1 was broken, and the nitrous oxide was pumped away, leaving the water. The cell was then isolated from the pump by closing valve H2; the sidearm below H1 was warmed and evacuated to remove adventitious water. Helium carrier gas, dried through a tube containing Molecular Sieve 5A, was then introduced through H1, 25 μl of absolute ethanol was injected through septum S to flush the product water through the analysis line, breakseal BS2 was broken and the gas stream passed through H3 onto the gas chromatography column (6 ft × 3/16 in. copper tubing containing Porapak Q at 190°). Just before breaking BS2 the cell and tubing leading to the gas chromatography column were raised to 190° with a heating tape. The detector cell was from Gow-Mac Instrument Co. and contained W2 filaments. Unirradiated samples were analyzed in the same way to serve as blanks. Calibrations were done both by putting water into sample cells and by putting water through the septum S just before injecting the ethanol "chaser."

Alcohol products were analyzed by the same technique as that used for water, except that a 9 in. × 3/16 in. Porapak Q column was used and different alcohols (methanol, ethanol, propanol, etc.) were used as chasers.

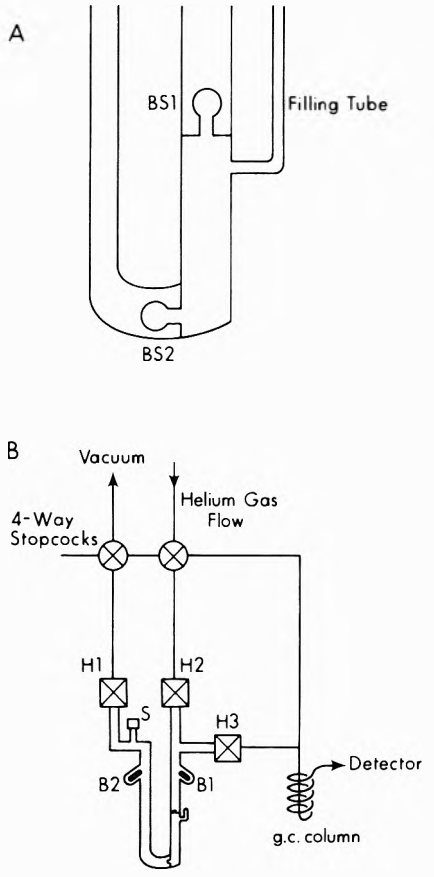

Figure 1. (A) Sample cell used when water was to be measured: made of Pyrex; BS1 and BS2 are breakseals; volume ≈ 3 cm^3. (B) Water analysis apparatus: H1, H2, and H3 are stainless steel Hoke needle valves with Teflon seats; S is a septum for injection of ethanol; B1 and B2 are pieces of iron, manipulated by a U magnet, used to break the breakseals.

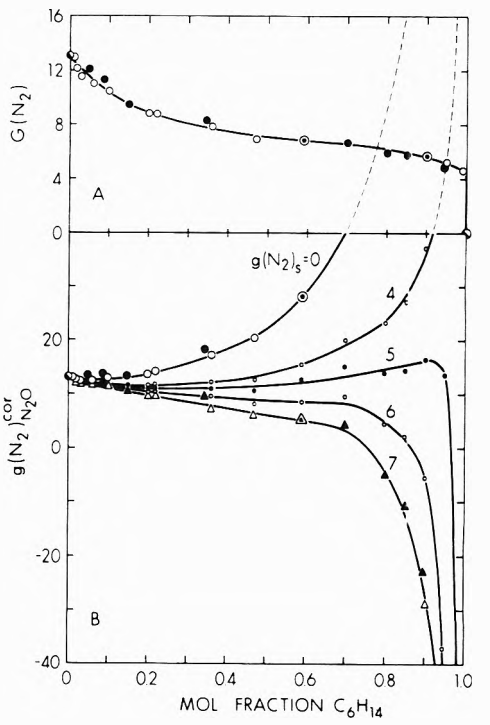

Figure 2. (A) $G(N_2)$ from solutions of *n*-hexane (○) or neohexane (●) in nitrous oxide at 183 K. The half-filled points refer to pure nitrous oxide or pure hydrocarbon. (B) Values of $g(N_2)_{N_2O}^{cor}$ calculated from the results in Figure 2A, using eq 1 and assuming $g(N_2)_s$ = 0, 4, 5, 6, and 7.

Results

Nitrogen Yields. In the following the symbol $G(N_2)$ represents the number of molecules of nitrogen formed per 100 eV absorbed by the solution, while $g(N_2)$ represents the number of molecules of nitrogen formed per 100 eV absorbed by the solvent (nitrous oxide) only: $g(N_2) = G(N_2)/\epsilon_{N_2O}$, where ϵ_{N_2O} is the electron fraction of nitrous oxide in the solution. Some nitrogen also results from energy absorbed initially in the solute hydrocarbon; for example, electrons generated in the hydrocarbon can be scavenged by the nitrous oxide and lead to nitrogen formation. Yields that have been corrected for energy absorbed in the solute are symbolized by $g(N_2)_{N_2O}^{cor}$

$$g(N_2)_{N_2O}^{cor} = [G(N_2) - g(N_2)_s\epsilon_s]/\epsilon_{N_2O} \quad (1)$$

where $g(N_2)_s$ is the number of molecules of nitrogen formed as a result of 100 eV absorbed initially by the solute and ϵ_s is the electron fraction of solute in the solution.

The nitrogen yields from *n*-hexane and neohexane solution will be used to illustrate the difference between $G(N_2)$ and $g(N_2)_{N_2O}^{cor}$. It will then suffice to report $g(N_2)_{N_2O}^{cor}$ values for the rest of the solutions.

When *n*-hexane is added to liquid nitrous oxide, $G(N_2)$ decreases gradually from 13.1 in pure nitrous oxide to 4.6 in 99 mol % hydrocarbon (Figure 2A). The decrease is partly a dilution effect. Less nitrogen is formed from 100 eV initially absorbed in the hydrocarbon than from 100 eV initially absorbed in the nitrous oxide. If one were to assume that no nitrogen resulted from energy absorption in the hydrocarbon, *i.e.*, that $g(N_2)_s = 0$, one would obtain the corresponding curve shown in Figure 2B. The yields along this curve increase with hydrocarbon concentration, which implies that some nitrogen is formed as a result of energy absorption in the solute. If one assumes that $g(N_2)_s = 4$, the curve for $g(N_2)_{N_2O}^{cor}$ also increases with solute concentration (Figure 2B). This implies that the true value of $g(N_2)_s$ is greater than 4. By contrast, values of $g(N_2)_{N_2O}^{cor}$ obtained with $g(N_2)_s = 6$ and 7 decrease with increasing hexane concentration (Figure 2B). The curve with $g(N_2)_s = 5$ has a shallow minimum at about 30 mol % and decreases sharply beyond 95 mol % hexane. The conclusion, to be discussed later, is that the best value of $g(N_2)_s$ for *n*-hexane is 5.5 ± 0.3.

It might be helpful to mention at this point that the sharp decrease in the best $g(N_2)_{N_2O}^{cor}$ curve at very high hydrocarbon concentrations is due to loss of electrons through geminate neutralization in the hydrocarbon. For the alkanes used in the present work this process is only significant at >90 mol % alkane.[4-6,9]

The "plateau" value of $g(N_2)_{N_2O}^{cor}$, $g(N_2)_{N_2O}^{plat}$ = 10.6, corresponds to a decrease $\Delta g(N_2)_{N_2O}^{plat} = 2.5$.

Results from neohexane solutions were the same, within experimental error, as those from the *n*-hexane solutions (Figure 2). The best value of $g(N_2)_s$ for neohexane is also 5.5 ± 0.3 and $\Delta g(N_2)_{N_2O}^{plat} = 2.0$.

The value $g(N_2)_s = 5.5 \pm 0.5$ can also be obtained by extrapolation of $G(N_2)$ against ϵ_s to the pure hexane axis (Figure 3). Extrapolation to the pure nitrous oxide axis indicates that the hexanes can inhibit nitrogen formation in nitrous oxide radiolysis to the extent of $\Delta G(N_2) = (13.1 - 10.8 \pm 0.5) = 2.3 \pm 0.5$.

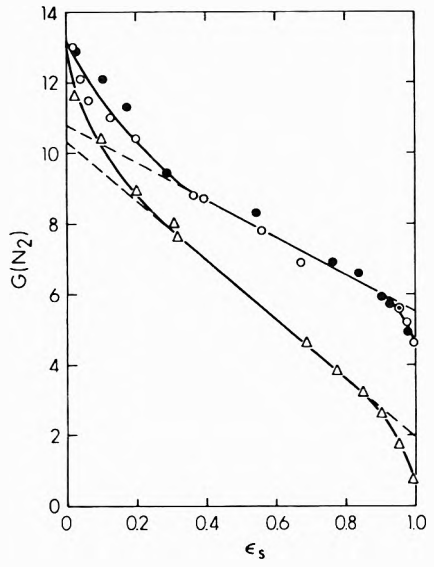

Figure 3. $G(N_2)$ as a function of electron fraction ϵ_S of solute at 183 K: solute O, *n*-hexane; ●, neohexane; Δ, 1,3-butadiene.

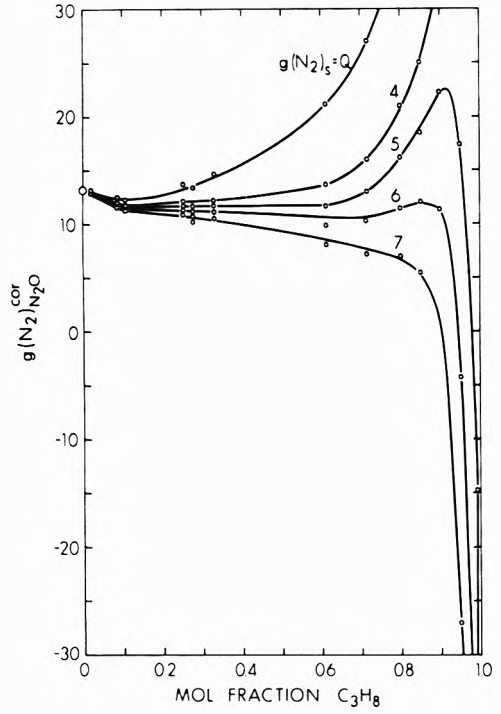

Figure 4. $g(N_2)_{N_2O}^{cor}$ from propane solutions in nitrous oxide at 183 K, assuming $g(N_2)_S$ = 0, 4, 5, 6, and 7.

Figure 3 is perhaps easier to understand superficially than is Figure 2, but the extrapolations and interpretations of the simple plots seem more subjective than the conclusions drawn from the more complex treatment.

(*1*) *Effects of Other Alkanes and Cycloalkanes.* The behavior of $g(N_2)_{N_2O}^{cor}$ from propane solutions is shown in Figure 4 for assumed values of $g(N_2)_S$ = 0, 4, 5, 6, and 7. In this case the best value of $g(N_2)_S$ is 6.

The value of $g(N_2)_{N_2O}^{cor}$ decreased for all values of $g(N_2)_S$ when low concentrations of propane were added. For the best value of $g(N_2)_S$, $g(N_2)_{N_2O}^{cor}$ decreased until about 10 mol % propane had been added, then remained relatively constant up to much higher propane concentrations. The decrease in nitrogen yield was $\Delta g(N_2)_{N_2O}^{plat}$ = 2.

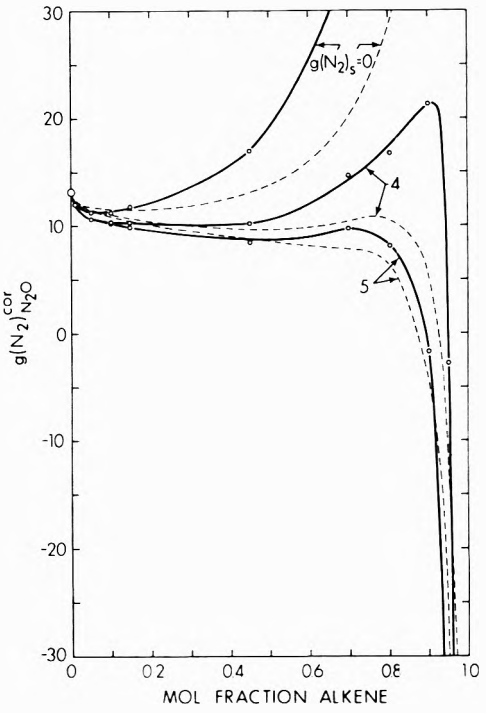

Figure 5. $g(N_2)_{N_2O}^{cor}$ from alkene solutions in nitrous oxide at 183 K, assuming $g(N_2)_S$ = 0, 4, and 5: full lines, 1-hexene; dashed lines, propene.

The effects of ethane, *n*-butane, cyclopropane, and cyclopentane were also measured. All gave results similar to those displayed for the hexanes and propane in Figures 2-4. The best values of $g(N_2)_S$ and $\Delta g(N_2)_{N_2O}^{plat}$ are listed in Table I. For all of the saturated hydrocarbons the best values are $g(N_2)_S = 5.5 \pm 0.5$ and $\Delta g(N_2)_{N_2O}^{plat} = 2.5 \pm 0.5$.

(*2*) *Effects of Alkenes and Cycloalkenes.* Ethene, propene, 1-butene, 1-hexene, and cyclopentene were added separately to nitrous oxide and the nitrogen yields measured. Results from the propene and 1-hexene solutions are shown in Figure 5 to illustrate the behavior. The best values of $g(N_2)_S$ and $g(N_2)_{N_2O}^{plat}$ are given in Table I. It appears that $g(N_2)_S = 4.5 \pm 0.5$ and $\Delta g(N_2)_{N_2O}^{plat} = 3.0 \pm 0.5$.

(*3*) *Effects of Alkynes and Other Hydrocarbons.* Acetylene and propyne gave as best values $g(N_2)_S \approx 5$ and $\Delta g(N_2)_{N_2O}^{plat} \approx 2$ (Figure 6 and Table I). Toluene behaved similarly (Figure 7 and Table I).

Although 1,3-butadiene gave $\Delta g(N_2)_{N_2O}^{plat} \approx 2.8$ similar to other hydrocarbons, the apparent best value of $g(N_2)_S \approx 1.9$ was unusually low (Figures 3 and 7 and Table I).

Yields of Oxygen-Containing Products. The yields of oxygen and nitrogen dioxide were reduced to zero by the addition of each of the hydrocarbons (Figure 8). In the absence of hydrocarbon $g(O_2)_{N_2O} = 2.7$ and $g(NO_2)_{N_2O} = 5.6$.

The only detectable oxygen-containing product that resulted from the scavenging reactions of *n*-butane and 1-butene was water, the yields of which are displayed in Figure 9. Difficulties of water calibration and analysis make the values uncertain by about 10%. The water yields are presented as gross *G* values for the sake of simplicity.

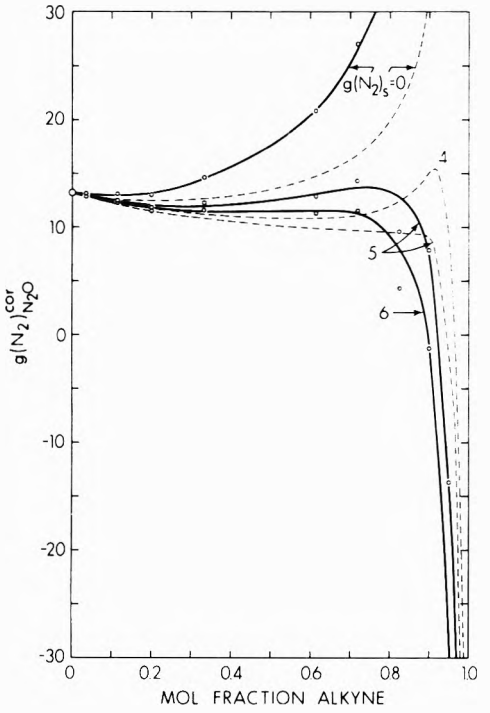

Figure 6. $g(N_2)_{N_2O}^{cor}$ from alkyne solutions in nitrous oxide at 183 K, assuming $g(N_2)_s$ = 0, 4, 5, and 6: full lines, propyne; dashed lines, acetylene.

TABLE I: Best Values of $g(N_2)_s$ and $\Delta g(N_2)_{N_2O}^{plat}$ for Hydrocarbon Solutions in Nitrous Oxide at 183 K

Solute	$g(N_2)_s$	$\Delta g(N_2)_{N_2O}^{plat}$
Alkanes and Cycloalkanes		
C_2H_6	5	2.5
C_3H_8	6	2.0
n-C_4H_{10}	5.5	2.5
n-C_6H_{14}	5.5	2.5
neo-C_6H_{14}	5.5	2.0
c-C_3H_6	5.5	3.0
c-C_5H_{10}	5.5	2.5
Alkenes and Cycloalkene		
C_2H_4	4.5	3.0
C_3H_6-1	4.0	3.0
C_4H_8-1	4.5	2.8
C_6H_{12}-1	4.5	3.5
c-C_6H_8	5.0	2.5
Alkynes		
C_2H_2	4.5	2.5
C_3H_4	5.5	1.5
Miscellaneous		
1,3-C_4H_6	1.9	2.8
$C_6H_5CH_3$	4.5	~1.5

[a] Estimated error is ±0.5 units.

Alcohols were sought in the n-butane and 1-butene solutions and it was concluded that G(ethanol) < 0.01, G(propanols) < 0.1 and G(butanols) < 0.3.

Discussion

Addition of 10 mol % of a hydrocarbon to nitrous oxide prevents the formation of oxygen and nitrogen dioxide, but water is formed in their stead. The yield of nitrogen is reduced by only about 3 g units. These results have been used to test mechanisms I–III of the preceding article.[13]

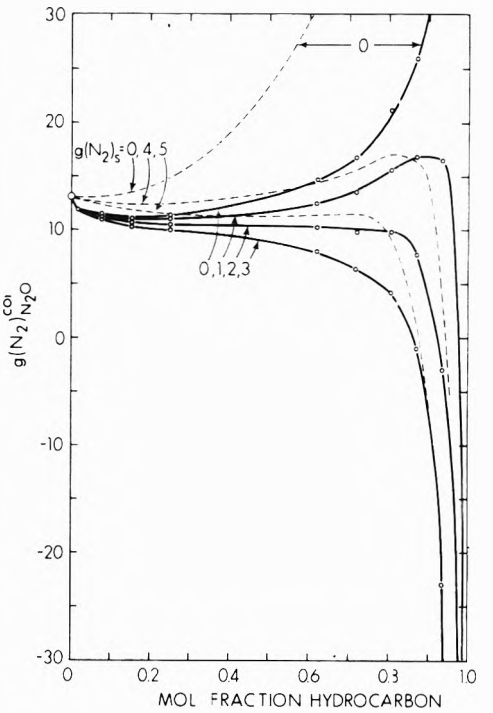

Figure 7. $g(N_2)_{N_2O}^{cor}$ from 1,3-butadiene (full lines) and toluene (dashed lines) solutions in nitrous oxide at 183 K. The assumed values of $g(N_2)_s$ are indicated in the figure.

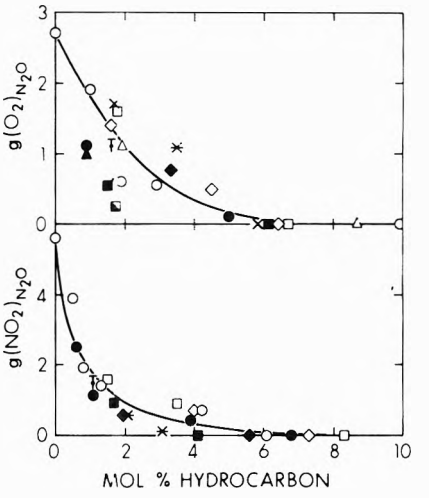

Figure 8. Effects of hydrocarbons on the oxygen and nitrogen dioxide yields from nitrous oxide at 183 K: O, n-hexane; □, n-butane; Δ, propane; ◇, ethane; ●, 1-hexene; ■, 1-butene; ▲, propene; ◆, ethene; ◪, 1,3-butadiene; ×, acetylene, * propyne; T, toluene. The oxygen yield curve was calculated using homogeneous kinetics and $k_{22}/k_{10} = 4 \times 10^{-9}$; the nitrogen dioxide yield curve was calculated using nonhomogeneous kinetics and distribution (25), with $\beta = 5 \times 10^{13}$ V/cm^2.

The same reaction numbering for 2-15 is used here for convenience.

$$N_2O \longrightarrow N_2O^+ + e^- \quad (2)$$

$$N_2O \longrightarrow N_2O^* \quad (3)$$

$$e^- + N_2O \longrightarrow N_2O^- \quad (4)$$

$$N_2O^* \longrightarrow N_2 + O \quad (9)$$

$$O + O + M \longrightarrow O_2 + M \quad (10)$$

$$2NO + O_2 \longrightarrow 2NO_2 \quad (11)$$

The mechanisms differ in the proposed reactions of the ions. In mechanism I

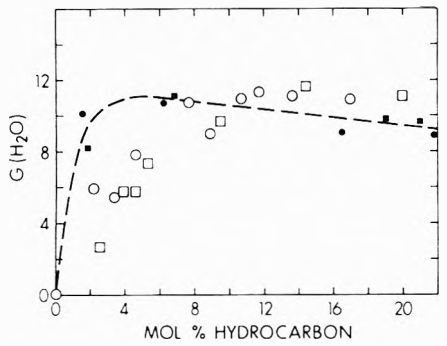

Figure 9. Water yields from solutions of *n*-butane (□) and 1-butene (○) in nitrous oxide at 183 K. The dashed curve and the small, filled points represent $[G(N_2) - 2G(O_2) - 1.5G(NO_2)]$.

$$N_2O^- \longrightarrow N_2 + O^- \quad (5)$$

$$O^- + N_2O \xrightarrow{N_2O} N_2O_2^- \quad (6)$$

$$N_2O^+ + N_2O_2^- \longrightarrow N_2O^* + 2NO \quad (7)$$

$$N_2O^+ + N_2O_2^- \longrightarrow N_2O^* + N_2 + O_2 \quad (8)$$

In mechanism II

$$N_2O^- \longrightarrow N_2 + O^- \quad (5)$$

$$N_2O^+ + O^- \longrightarrow 2NO \quad (12)$$

$$N_2O^+ + O^- \longrightarrow N_2 + O_2 \quad (13)$$

In mechanism III

$$N_2O^+ + N_2O^- \longrightarrow 2NO + N_2 \quad (14)$$

$$N_2O^+ + N_2O^- \longrightarrow 2N_2 + O_2 \quad (15)$$

The material balances for mechanisms I-III indicated by the previous electron and ion scavenging results[13] are summarized in Table II.

The values of $\Delta g(N_2)_{N_2O}^{plat}$ recorded in Table I are much smaller than the yield of N_2O^*, which would be $g(N_2O^*)_{N_2O}^{cor} = 8.7$ in mechanism I or 4.9 in II or III. It appears that hydrocarbons do not prevent the decomposition of N_2O^*. The reduction of the nitrogen yield therefore involves the ionic reactions.

Inhibition of Mechanism I. None of the present hydrocarbons, with the possible exception of 1,3-butadiene, would scavenge electrons in liquid nitrous oxide. However, all of them would scavenge the anion O^-.

$$O^- + RH \longrightarrow OH^- + R \quad (16)$$

If (16) were followed by (17) the nitrogen yield would be reduced by $\Delta g(N_2)_{N_2O}^{plat} = 0.9$, which is much less than the value 2.7 ± 0.5 observed. On the other hand, if the neutralization reaction did not produce a nitrous oxide molecule that was excited enough to decompose, (18), $\Delta g(N_2)_{N_2O}^{plat}$ would be 4.5, which is much more than observed. Reaction 18 seems much less probable than (17) in any case.

$$N_2O^+ + OH^- \longrightarrow N_2O^* + OH \quad (17)$$

$$N_2O^+ + OH^- \longrightarrow N_2O + OH \quad (18)$$

Charge transfer from the cation N_2O^+ to the hydrocarbons, (19), is possible because the ionization potentials of all the hydrocarbons are lower than that of nitrous oxide. The ionization potentials of the hydrocarbons range from 8.82 eV for toluene to 11.65 eV for ethane,[14] while that of nitrous oxide is 12.89 eV.[14] However, (16) is almost certain to occur, and (19) followed by neutralization (20) would give the excessive value $\Delta g(N_2)_{N_2O}^{plat} = 4.5$ in mechanism I.

$$N_2O^+ + RH \longrightarrow N_2O + RH^+ \quad (19)$$

$$RH^+ + OH^- \longrightarrow R + H_2O \quad (20)$$

Mechanism I is not favored.

Inhibition of Mechanism II. Mechanism II could be inhibited by (16) and (19). Reaction 16 followed by 17 would tend to *increase* $g(N_2)$ toward 15.9 and *decrease* $g(NO_2)$ toward zero. The observed *decrease* in nitrogen yield would require (19). Saturation occurrence of reactions 16, 19, and 20 would give a net decrease of 2.8 units in the nitrogen yield, consistent with observation (Table II).

Inhibition of Mechanism III. This mechanism would be inhibited by (19) followed by (21). The value of $\Delta g(N_2)_{N_2O}^{plat}$ would be 2.8, in satisfactory agreement with experiment (Table II).

$$RH^+ + N_2O^- \longrightarrow RH + N_2O^* \text{ (or } R + N_2 + OH) \quad (21)$$

Conclusions from Material Balance. Mechanisms II and III are consistent with the results, but I is not. The detailed material balances of II and III have many points in common (Table II), which allow the following conclusions to be drawn. (a) G(total ionization) = 5.5 ± 0.5 in liquid nitrous oxide, nearly double the gas-phase yield of 3.0.[15,16] (b) Reactions of the charged species are precursors of all the NO_2 and 8 ± 1 G units of N_2. (c) Direct formation of N_2O^* in reaction 3 has a yield of $G_3 = 5 \pm 1$. (d) Hydrocarbons inhibit nitrogen formation by reaction with N_2O^+, probably by charge transfer (19).

Yields of Oxygen-Containing Products. The amounts of oxygen and nitric oxide formed by the ionic reactions 12 and 13 or 14 and 15 consume each other in the formation of nitrogen dioxide by (11). From the material balance alone one might suggest that NO_2 is formed directly by the ionic reactions, but it is difficult to conceive such a reaction that appears reasonable.

The net amount of oxygen observed in the final products corresponds essentially to that formed in (10). Reduction of the observed oxygen yield therefore corresponds to the inhibition of (10), presumably by (22) and (23)

$$O + RH \longrightarrow OH + R \quad (22)$$

$$O + R \text{ (or OH)} \longrightarrow R' \text{ (or } HO_2) \quad (23)$$

TABLE II: Material Balance for N_2O Radiolysis

	G (reaction step)			
Reaction	Mechanism I	Mechanism II	Mechanism III	Measured
2	3.6	5.5	5.5	
3	5.1	4.9	4.9	
4	3.6	5.5	5.5	
5	3.6	5.5		
6	3.6			
7	2.7			
8	0.9			
9	8.7	4.9	4.9	
10	4.4	2.5	2.5	
11	2.7	2.7	2.7	
12		2.7		
13		2.8		
14			2.7	
15			2.8	
$g(N_2)$	13.2	13.2	13.2	13.1 ± 0.2
$g(O_2)$	2.6	2.6	2.6	2.7 ± 0.1
$g(NO_2)$	5.4	5.4	5.4	5.6 ± 0.2
$\Delta g(N_2)^{plat}$	0.9 or 4.5	2.8	2.8	2.7 ± 0.5

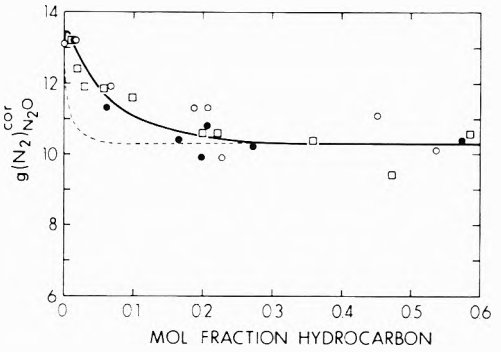

Figure 10. $g(N_2)_{N_2O}^{cor}$ as functions of the concentration of *n*-hexane (□, $g(N_2)_s$ = 5.5), *n*-butane (○, $g(N_2)_s$ = 5.5), and 1-butene (●, $g(N_2)_s$ = 4.5). The curves were calculated using nonhomogeneous kinetics and distribution (25): ----- β_- = 0, $\beta_+ = 5 \times 10^{13}$ V/cm²; —— $\beta_- = 5 \times 10^{13}$, $\beta_+ = 1.2 \times 10^{13}$ V/cm².

$$2 \text{ monoradicals} \longrightarrow \text{products} \qquad (24)$$

where R and R′ are free radicals. Steady-state treatment of reactions 2, 9, 10, and 22-24 and numerical analysis of the results in Figure 8, assuming $k_{10} \approx k_{23} \approx k_{24}$, indicates that $k_{22}/k_{10} \approx 4 \times 10^{-9}$. If reactions 16 and 17 are also important (see later) one obtains $k_{22}/k_{10} \approx 6 \times 10^{-9}$. Assuming $k_{10} \approx 10^{10}$ M^{-1} sec^{-1}, this gives $k_{22} \approx$ 40–60 M^{-1} sec^{-1}. By comparison, the gas-phase rate constant for reaction of methoxy radicals with propane,[17] extrapolated to 183 K, is 100 M^{-1} sec^{-1}. The bond dissociation energies of ·O–H (→ triplet ground state O) and CH_3O–H are both 102 kcal/mol,[18] so it is not unreasonable that the hydrogen atom abstraction rate constants of O (triplet ground state) and CH_3O should be of the same order of magnitude. The results imply that the oxygen atoms taking part in reaction 10 are in the triplet ground state. Such atoms may be generated directly in (9) or by deactivation of excited atoms that might be formed in (9).

It is demonstrated in the next section that the observed reduction in nitrogen dioxide yield is not due to reaction 19, because if it were the relative rates of decrease of the nitrogen and nitrogen dioxide yields should be the same. Reaction 16 is, however, consistent with the observed nitrogen dioxide yields. The neutralization reactions 12, 13, etc., occur nearly exclusively in spurs because the dielectric constant of liquid nitrous oxide is low,[19] being 1.97 at 183 K.[20] Nonhomogeneous kinetics[21] would therefore govern the competition between the scavenging reaction 16 and neutralization reactions 12 and 13. The relevant equations are given in the adjacent article.[13] The NO_2 curve in Figure 8 was calculated using the electron-ion separation distribution (25),[13,22] the scavenging parameter $\beta = 5 \times 10^{13}$ V/cm² and an encounter efficiency of unity. The efficiency of hydrocarbons in reducing the NO_2 yield in liquid nitrous oxide is 80% of the efficiency of scavenging electrons by nitrous oxide in cyclohexane.[22]

$$\begin{aligned} F(y) &= 1800y^{-3} \qquad y \geq 30 \text{ Å} \\ F(y) &= 0 \qquad\qquad y < 30 \text{ Å} \end{aligned} \qquad (25)$$

If water were the ultimate product of all of the scavenged oxygen-containing intermediates the yield of water should equal $[G(N_2) - 2g(O_2) - 1.5G(NO_2)]$; this quantity is represented by the dashed line in Figure 9. Water appears to be the only major oxygen-containing product when more than 6 mol % of hydrocarbon is present. At these concentrations oxygen atoms apparently react exclusively by (22) and the OH radicals are consumed by (26). At lower RH concentrations reactions 23 and 24 may lead to oxygenated products other than water. The other products do not include appreciable amounts of the lower alcohols.

$$OH + RH \longrightarrow H_2O + R \qquad (26)$$

Calculation of the Nitrogen Yield Curve. Reduction of the nitrogen yield is due to scavenging of N_2O^+ in reaction 19. If inhibition of nitrogen dioxide formation were also due to (19), rather than to (16), the value of the scavenging parameter $\beta = 5 \times 10^{13}$ V/cm² obtained from the nitrogen dioxide results (Figure 8) should also apply to the nitrogen yields. However, this value is tenfold too large (Figure 10). It is concluded that inhibition of nitrogen dioxide formation is not due to (19).

On the other hand, if reduction of the nitrogen dioxide yield were due mainly to (16), the value $\beta = 5 \times 10^{13}$ V/cm² would correspond to competition between the O^- reactions 12 plus 13 and 16 and would be designated β_-. A different value would be obtained for the parameter β_+ for scavenging N_2O^+. Reaction 16 followed by (17) and (9) would tend to *increase* $g(N_2)$ by an amount equal to half the *decrease* in $g(NO_2)$

$$\Delta g(N_2)_{O^-_{sc}} = -(1/2)\Delta g(NO_2) \qquad (27)$$

Reaction 19 followed by (20) would decrease the nitrogen yield by an amount equal to $\Delta g(N_2)_{N_2O^+_{sc}}$

$$\Delta g(N_2)_{N_2O^+_{sc}} = \frac{-g(N_2O^+)_{sc}}{5.5}(2.8 + \Delta g(N_2)_{O^-_{sc}}) \qquad (28)$$

where 5.5 is the total ionization yield.

The solid curve in Figure 10 was calculated using $\beta_- = 5 \times 10^{13}$ V/cm² and $\beta_+ = 1.2 \times 10^{13}$ V/cm². It agrees satisfactorily with the results.

Although further attempts to refine the yield measurements will be necessary, the totality of the present results indicates that both reactions 16 and 19 occur, and therefore tends to favor mechanism II over III.

The oxygen-containing intermediates are completely scavenged by 10% hydrocarbon in nitrous oxide. Secondary reactions involving O^- do not, therefore, produce nitrogen in solutions containing >10% hydrocarbon.

References and Notes

(1) Assisted financially by the National Research Council of Canada.
(2) G. Scholes and M. Simic, *Nature (London)*, **202**, 895 (1964).
(3) R. Blackburn and A. Charlesby, *Nature (London)*, **210**, 1036 (1966).
(4) N. H. Sagert and A. S. Blair, *Can. J. Chem.*, **45**, 1351 (1967).
(5) M. G. Robinson and G. R. Freeman, *J. Chem. Phys.*, **48**, 983 (1968).
(6) E. D. Stover and G. R. Freeman, *J. Chem. Phys.*, **48**, 3902 (1968).
(7) R. Schutte and G. R. Freeman, *J. Amer. Chem. Soc.*, **91**, 3715 (1969).
(8) K. Horacek and G. R. Freeman, *J. Chem. Phys.*, **53**, 4486 (1970).
(9) M. G. Robinson and G. R. Freeman, *J. Chem. Phys.*, **55**, 5644 (1971).
(10) F. S. Dainton, P. O'Neill, and G. A. Salmon, *Chem. Commun.*, 1001 (1972).
(11) Y. Hatano, K. Takeuchi, and S. Takao, *J. Phys. Chem.*, **77**, 586 (1973).
(12) G. R. Freeman and E. D. Stover, *Can. J. Chem.*, **46**, 3235 (1968).
(13) T. E. M. Sambrook and G. R. Freeman, *J. Phys. Chem.*, **78**, 28 (1974).
(14) R. W. Kiser, "Introduction to Mass Spectrometry and its Applications," Prentice-Hall, Englewood Cliffs, N. J., 1965, Appendix IV.
(15) G. G. Meisels, *J. Chem. Phys.*, **41**, 51 (1964).
(16) R. Cooper and R. M. Mooring, *Aust. J. Chem.*, **21**, 2417 (1968).
(17) A. F. Trotman-Dickenson, *Advan. Free Radical Chem.*, **1**, 1 (1965).
(18) S. W. Benson, *J. Chem. Educ.*, **42**, 502 (1965).
(19) G. R. Freeman and J. M. Fayadh, *J. Chem. Phys.*, **43**, 86 (1965).
(20) A. A. Maryott and E. R. Smith, *Nat. Bur. Stand. U.S., Circular*, **No. 514**, 3 (1951).
(21) G. R. Freeman, *J. Chem. Phys.*, **43**, 93 (1965); **46**, 2822 (1967).
(22) J.-P. Dodelet and G. R. Freeman, *Can. J. Chem.*, **49**, 2643 (1971).

Carbon-13 Nuclear Magnetic Resonance Spectroscopy of Molecules Adsorbed on Silica

Ian D. Gay

Department of Chemistry, Simon Fraser University, Burnaby 2, British Columbia, Canada *(Received August 21, 1973)*

Publication costs assisted by the National Research Council of Canada

^{13}C nuclear magnetic resonance spectra have been obtained for CO_2, C_2H_4, $C_2H_4Cl_2$, C_2H_5OH, $(CH_3)_2CO$, *cis*- and *trans*-C_4H_8, $(C_2H_5)_2O$, c-C_6H_{12}, and toluene, adsorbed on a high area silica gel. Coverages in the range of 0.1 to 1.1 statistical monolayers were used. Chemical shifts, line widths, and C–H coupling constants are reported for the above adsorbed molecules. For adsorbed *trans*-2-C_4H_8 and $(CH_3)_2CO$, spin–lattice relaxation times were also obtained. An interpretation of the results in terms of structure and motion of the adsorbed molecules is attempted.

Introduction

^{13}C nmr spectroscopy possesses several advantages over ^1H spectroscopy for the study of molecules adsorbed on surfaces. These comprise chiefly a much wider variation of chemical shifts, for given changes in molecular environment, and, for most relaxation processes, narrower lines due to the smaller nuclear magnetic moment. This small nuclear moment, together with the low natural abundance of ^{13}C, leads to a severe signal-to-noise problem for low concentration studies. However, use of fourier transform spectroscopy makes it possible to obtain natural abundance ^{13}C spectra of submonolayer quantities of adsorbed species on high area solids. In spite of the potential advantages of C spectroscopy, the literature of surface studies by this technique consists only of the two studies by Geschke[1] and Michel[2] of hydrocarbons sorbed in zeolites. We report in this paper the results of ^{13}C spectroscopy of several molecules adsorbed on a high area silica gel, at coverages of 0.2 to 1.0 monolayer.

Experimental Section

Nmr measurements were performed at 15 MHz on the pulse spectrometer described by Collins, *et al.*[3] This instrument has since been fitted with a field-frequency lock system[4] operating from an external H_2O lock sample, which typically maintained a long-term field stability of 1 part in 10^7. Spectra were obtained by applying 50-μsec radiofrequency pulses (approximately $\pi/3$ pulses) at repetition frequencies of 2 to 5 Hz. The resulting free induction decays were signal averaged, and the final average fourier transformed, using a Nicolet 1082 computer. Typically, 10^4–10^5 free induction decays had to be averaged to obtain an adequate signal-to-noise ratio in the spectrum. Samples were sealed in 12-mm o.d. Pyrex tubing and were not spun. Under these conditions, magnetic field inhomogeneities contributed approximately 7 Hz to the line width.

Chemical shifts were measured relative to external samples of the same substance in the pure liquid state, except for CO_2 and C_2H_4, in which case a liquid benzene reference was used and comparison made with the pure gas using the data given in ref 5. We estimate our uncertainty in chemical shifts to be ±5 Hz, (±0.3 ppm) arising from small field drifts, and from uncertainties in locating the center of the fairly broad peaks found for adsorbed molecules. Since proton decoupling was not available on the spectrometer, the spectra show multiplet structure due to direct bonded C–H spin coupling. The coupling constants J_{C-H} for the adsorbed molecules were obtained with an uncertainty of ±5 Hz.

Adsorption was carried out by exposing the evacuated SiO_2 samples to vapor-phase adsorbate. The amount adsorbed was determined from the decrease in adsorbate pressure and the known system volume. Initial pressures of adsorbate were always less than one-half of the saturated vapor pressures. The quantities adsorbed on the various samples are shown in Table I. Overall concentrations of equivalent carbons in the sample region range from 0.44 M for CO_2 at $\theta = 0.10$ to 9.9 M for c-C_6H_{12} at $\theta = 0.74$. The concentration of adsorbed phase in the sample region always exceeded the gas-phase concentration by a large factor, ranging from 30 for C_2H_4 at $\theta = 0.14$ to 3×10^4 for C_2H_5OH at $\theta = 0.74$.

The area of the adsorbent was obtained by BET measurement using N_2 with an assumed area of 16.2 Å^2 per molecule. Fractional coverages for adsorbed molecules were calculated by deriving an effective radius from the liquid density on the assumption of spherical shape. While this is a rather crude estimation, it does lead to a monolayer coverage of reasonable magnitude.[6] Silica samples were degassed for 4–16 hr at 250° under a vacuum of 10^{-5} Torr before adsorption. In the case of acetone adsorption, other outgassing treatments were used, as noted below.

Materials. The silica gel used was 60–80 mesh chromatographic grade material from Matheson Coleman and Bell, Ltd. It had a surface area of 650 m^2/g and a bulk density of 0.8 g/cm^3. The adsorbates were reagent grade liquids from various suppliers, or CP grade gases from Matheson of Canada, Ltd. They were degassed and/or distilled *in vacuo* before use.

Results

A typical spectrum (of diethyl ether) is shown in Figure 1. For comparison, the ^1H spectrum (recorded at 100 MHz on a Varian XL100) of the same sample is shown in Figure 2. The expectations mentioned in the introduction are well illustrated by these spectra. Thus, the CH_3 and CH_2 groups are completely resolved in the ^{13}C spectrum, but grossly overlapping in the ^1H spectrum. This arises from

TABLE I: ^{13}C Spectral Parameters of Adsorbed Molecules

Molecule	Amount[a] adsorbed	Coverage[b]	C atom	Chemical[c] shift	J_{C-H}[d]	Width[e]
CO_2	8.4×10^{-7}	0.10		1.5		31
C_2H_4	1.10×10^{-6}	0.14		0.7	147	25
$Cl-CH_2-CH_2-Cl$	2.48×10^{-6}	0.48		0.5	152	37
CH_3-CH_2-OH	4.87×10^{-6}	0.74	CH_3	1.5	122[g]	50[g]
			CH_2	−1.0	126[g]	94[g]
$CH_3-CO-CH_3$	1.23×10^{-6}	0.22	CH_3	+1.1	125[g]	65[g]
			CO	−10.5		43
	2.64×10^{-6}	0.47	CH_3	1.0	124	48
			CO	−9.2		37
	4.52×10^{-6}	0.82	CH_3	0.3	127	50
			CO	−7.1		41
t-2-C_4H_8	1.03×10^{-6}	0.29	CH_3	1.0	118	53
			CH	−2.1	148[g]	78[g]
	1.61×10^{-6}	0.45	CH_3	1.0	120	53
			CH	−1.8	150	64
	2.70×10^{-6}	0.75	CH_3	0.7	125	31
			CH	−1.2	150	41
	3.93×10^{-6}	1.10	CH_3	0.8	122	35
			CH	−0.9	151	44
c-2-C_4H_8	3.29×10^{-6}	0.91	CH_3	0.5	126	37
			CH	−1.9	153	45
$(C_2H_5)_2O$	2.99×10^{-6}	0.68	CH_3	1.4	122[g]	44[g]
			CH_2	−0.3	128[g]	92[g]
c-C_6H_{12}	1.06×10^{-6}	0.24		0.4	127	54
	2.11×10^{-6}	0.48		0.8	128	43
	3.16×10^{-6}	0.74		−0.3	127	45
$C_6H_5-CH_3$	2.06×10^{-6}	0.49	CH_3	1.5	132	43
			ring 1	−0.8		*f*
			ring 2, 4 (unresolved)	+0.1	161	*f*

[a] In moles per m^2. [b] In monolayers, using liquid density. [c] In ppm relative to external liquid, except CO_2, C_2H_4 calculated relative to external gas, ±0.3 ppm. [d] In Hz ±5 Hz. [e] Full width at half-maximum height. Corrected for contribution of magnetic field inhomogeneity and exponetial smoothing used in data reduction. ±5 Hz. [f] Unobtainable due to overlapping of peaks. [g] Obtained by computer fitting.

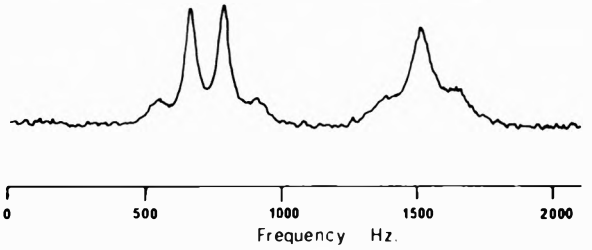

Figure 1. ^{13}C nmr spectrum of diethyl ether on silica gel at θ = 0.68. Fourier transform of 4×10^4 averaged free induction decays at 15.0 MHz.

the different range of chemical shifts, 53 ppm (800 Hz) for ^{13}C as opposed to 2.2 ppm (220 Hz) for ^1H, together with narrower lines in the case of ^{13}C. Graphical resolution gives a full width at half-maximum of 220 Hz for the ^1H methyl peak, as compared with 55 Hz for the uncorrected ^{13}C peaks. Some further ^{13}C spectra are shown in Figures 3–5.

^{13}C spectra were recorded for several molecules adsorbed on SiO_2 and the results are collected in Table I. The chemical shifts shown are relative to external liquid samples of the same substance, except for CO_2 and C_2H_4, where they are relative to the gas. Corrections for diamagnetic susceptibility of the environment have not been applied to these data. If the volume susceptibility of SiO_2 were calculated from the molecular susceptibility together with the observed bulk density, and used to apply such corrections, the indicated chemical shifts would be reduced by 0.2 to 0.4 ppm, which is scarcely significant, given the experimental uncertainty of ±0.3 ppm. The line widths indicated in Table I have been obtained by applying to the observed line widths a correction of 7 Hz for the effect of magnetic field inhomogeneities and 2 to 5 Hz for the effect of exponential smoothing used in data reduction. In cases where components of a multiplet overlapped significantly, line widths and coupling constants were obtained by least-squares computer fitting, assuming Lorentzian line shapes.

Since acetone showed the largest chemical shift change on adsorption, further measurements were done in which the effects of different outgassing treatments were studied. These results are shown in Table II. The data collected by Davydov, *et al.*,[7] show that the surface OH content of SiO_2 is determined primarily by the degassing conditions and is largely independent of the source of the material. These concentrations are also given in Table II. The work of Fripiat and Uytterhoeven[8] shows that a sample degassed at 150° should have the same OH concentration as a 250° sample, and in addition about 0.8 μmol/m^2 of adsorbed H_2O.

For two of the samples studied, spin-lattice relaxation times (T_1) were measured by applying a π, τ, $\pi/2$ pulse sequence, with accumulation and subsequent fourier transformation of the free induction decay following the $\pi/2$ pulse. Variation of τ enabled T_1 to be obtained in the usual manner.[9] The results are given in Table III. This table also shows values of T_2, the transverse relaxation time, derived from the corrected line widths.

Discussion

Chemical Shifts. The data in Table I establish two trends of chemical shift behavior. First, methyl group chemical shifts are invariably upfield of those in the pure liquid; second, carbons adjacent to a probable hydrogen

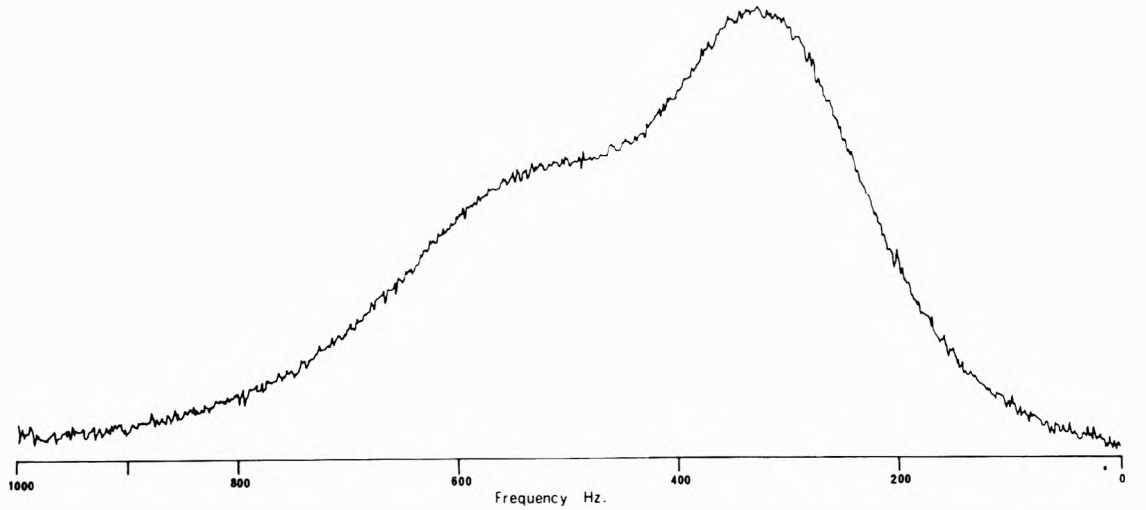

Figure 2. ^{1}H nmr spectrum of same sample as Figure 1. Single scan at 100 MHz.

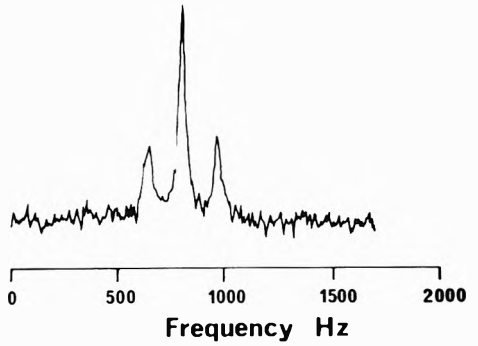

Figure 3. ^{13}C nmr spectrum of ethylene on silica gel at θ = 0.14. Fourier transform of 3.5 × 10^4 free induction decays.

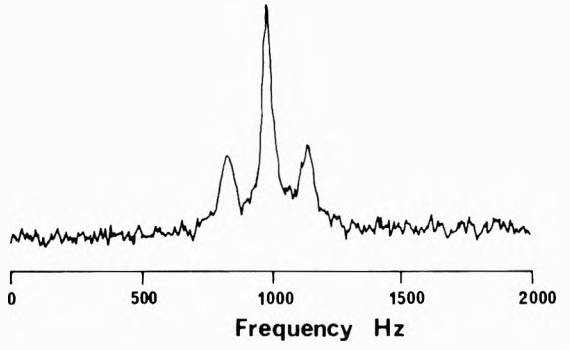

Figure 4. ^{13}C nmr spectrum of $ClCH_2CH_2Cl$ on silica gel at θ = 0.48. Fourier transform of 1.6 × 10^4 free induction decays.

bonding site (=C< in C_4H_8, $-CH_2-O-$ in C_2H_5OH and $(C_2H_5)_2O$, and >C=O in acetone) all suffer downfield shifts compared to the liquid. The first of these is probably an effect of steric crowding, since it is known[10] that CH_3 groups which are sterically hindered have shifts upfield of what would otherwise be expected. It is quite reasonable to suppose that molecules in an adsorbed layer are crowded or deformed relative to the same molecules in the liquid state. The second effect is probably due to withdrawal of electrons through formation of a hydrogen bond to the surface, and consequent deshielding of adjacent carbons. This effect is particularly marked in the case of the >C=O resonance of acetone, in keeping with the large shifts observed when acetone is dissolved in hydrogen-bonding solvents.[11] There

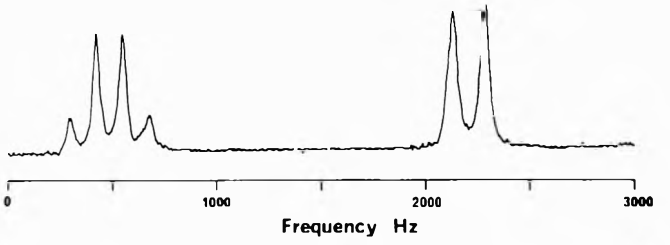

Figure 5. ^{13}C nmr spectrum of *cis*-2-C_4H_8 on silica gel at θ = 0.91. Fourier transform of 1.5 × 10^5 free induction decays.

TABLE II: Effect of Outgassing Conditions on Spectrum of Adsorbed Acetone

Outgassing procedure	Coverage[a]	Chemical shift		Surface OH[c] concn
		Methyl[b]	Carbonyl[b]	
2 hr 150°	0.83	0.3	−7.4	7[d]
16 hr 250°	0.82	0.3	−7.1	7
16 hr 450°	0.80	1.6	−3.9	4
16 hr 650°	0.81	0.7	−1.7	2.5

[a] In monolayers. [b] In ppm, relative to external liquid. ±0.3 ppm. [c] In μmol/m².[6] [d] Plus 0.8 μmol/m² H_2O.[7]

TABLE III: Relaxation Times

Adsorbate	Coverage	C atom	T_1, sec	T_2, sec
t-2-C_4H_8	1.10	CH_3	0.33 ± 0.06	0.09 ± 0.01
		CH	0.16 ± 0.03	0.07 ± 0.01
$(CH_3)_2CO$	0.83	CH_3	0.15 ± 0.02	0.07 ± 0.01
		CO	0.09 ± 0.02	0.07 ± 0.01

is clearly a coverage dependence of the second effect for acetone, and probably for *trans*-2-butene, although in the latter case, smaller shifts make this dependence less certain, in view of our experimental uncertainty.

The wide range of shifts for the CO resonance of acetone suggest that this might be a convenient way of studying surface hydroxylation. Thus, within our experimental error, the dependence of chemical shift on hydroxyl concentration is linear, using the values given in ref 7 for (OH) concentration. This is readily understandable if acetone moves sufficiently rapidly on the surface to average the chemical shifts due to bare and hydroxylated ad-

sorption sites. It would be desirable to check the existence of such a linear relation using samples for which OH concentration had been directly measured, since the data in ref 7 show a fair amount of scatter. Should such a relationship be confirmed, nmr measurements would comprise one of the simpler experimental methods of determining surface OH concentration.

The coverage dependence of CO chemical shift on 250° samples is also linear within experimental error. The shift extrapolates to −11.9 ppm at zero coverage. This does not appear to be consistent with hydrogen bonding of each acetone molecule to a single OH site. If such were the case, an essentially constant chemical shift might be expected while acetone concentration was less than OH concentration, with a decline in shift at higher acetone coverages, due to motional averaging. All of the acetone concentrations used (Table I) are less than the OH concentration, but the chemical shift is clearly not constant. This seems to imply that at low coverages a greater shift can be produced by simultaneous hydrogen bonding to two or more surface hydroxyls, since the concentration of suitably oriented OH pairs is quite likely to be small compared to both acetone and total OH concentrations.

Relaxation and Line Widths. The measured T_1 values (Table III) are much smaller than those found for the same molecules in the liquid state, which are typically of the order of tens of seconds. Such increased efficiency of relaxation could reasonably be attributed to increased efficiency of dipole–dipole relaxation, due to slowing of molecular motion on adsorption, or to interaction with paramagnetic impurities in the silica. T_2 values calculated from line widths are not necessarily reliable, since a component of the line width may result from unresolved long-range C–H coupling, from variations of chemical shift at different surface sites, or from other forms of inhomogeneous broadening. If the T_2 values in Table III are taken at face value, their ratios to T_1 imply[12] that motional correlation times are near the values which give T_1 its minimum value, and hence that dipole–dipole relaxation might be relatively efficient.

It is, however, impossible to attribute all relaxation to a dipole–dipole mechanism. Thus, the >C=O carbon of acetone is quite efficiently relaxed, in spite of the absence of a directly bonded H atom. Intramolecular dipole relaxation as a sole mechanism is ruled out by comparison of ^{13}C and ^{1}H line widths at low coverage. For example, with ethylene, where C–H and H–H vectors almost certainly have the same correlation times, the relative ^{13}C and ^{1}H relaxation rates due to intramolecular dipole effects can be calculated from the γ^2 and r^{-6} terms.[12] Such a calculation in the case of ethylene indicated that the ^{13}C line width should exceed the ^{1}H line width, because of the shortness of the C–H bond relative to the nearest H–H distance, and corresponding dominance of the r^{-6} term over the γ^2 term. Measurement of the ^{1}H line width on our ethylene sample gives 155 Hz, as compared with 25 Hz (Table I) for the ^{13}C line width; thus intramolecular dipole relaxation is ruled out as the sole mechanism. Similarly, intermolecular dipole interaction with neighboring adsorbed molecules is unlikely at low coverages. Dehydroxylation of the surface has little effect on ^{13}C line widths of acetone, so that interaction with surface protons is probably not important.

In the case of paramagnetic impurities, one might expect average distances of C and H from the impurity to be about the same, and hence ^{1}H line widths to be about 16 times the ^{13}C line widths because of the γ^2 term. For those samples (C_2H_4, C_2H_5OH, $(C_2H_5)_2O$, and $CH_3C_6H_5$) where we have measured ^{1}H spectra as well as ^{13}C, the ^{1}H line widths are 4 to 6 times those of ^{13}C in the same sample. The existence of sufficient paramagnetic impurities in commercial silicas to cause significant relaxation of ^{1}H resonances has been demonstrated by other workers.[13,14] While the present relaxation measurements are not sufficient unambiguously to define the overall relaxation process, it is clear that a combination of dipole–dipole and paramagnetic relaxation will account for the present results. The possibility of paramagnetic impurities in the surface region of our samples is supported by the observation that our butene samples undergo a catalytic cis–trans isomerization over a period of a few weeks. This may reasonably be attributed to surface impurities.[15] It would be of considerable interest to perform more detailed relaxation measurements, particularly using a surface free of paramagnetic impurities. The observed differences of T_1 and line width for different atoms in the same molecule indicate the possibility of determining differences in the motion of the relevant atoms in the adsorbed state.

Coupling Constants. None of the C–H coupling constants in Table I differ from those in the pure liquid by more than our experimental uncertainty, with the exception of those for the CH_2 groups of C_2H_5OH and $(C_2H_5)_2O$. For the pure liquids, these are 139 and 138 Hz, respectively. The general lack of difference is not surprising, since these coupling constants are determined mainly by the amount of s character in the C–H bond.[16] The two anomalous examples are both, unfortunately, cases in which computer fitting of an unresolved multiplet was required to derive the value of J. It might, therefore, be thought that errors may be larger than estimated, although the least-squares standard deviations for these constants are 2.7 and 3.2 Hz respectively for C_2H_5OH and $(C_2H_5)_2O$. Since these two cases are those in which the adsorbate suffers the strongest interaction with the surface, the effect may well be real, but the present data do not seem sufficiently secure to warrant speculations as to the cause of any effect.

Conclusion

The present results indicate that ^{13}C nmr spectroscopy has considerable potential for the study of adsorbed molecules, in that chemical shift changes on adsorption and relaxation rates of different molecular constituents are readily measured. The former are obtained with difficulty in ^{1}H spectra, and the latter have not yet been reported in literature.

The present instrumentation is somewhat less than ideal for these studies. The experimental conditions cited above required a few hours for the recording of a spectrum. With a 23-kG spectrometer incorporation proton decoupling, an order of magnitude increase in sensitivity should be achieved, and the present information, apart from coupling constants, could be obtained in a few minutes per sample. Alternatively, measurements could be extended to samples of less than 100 m^2/cm^3 surface to volume ratio.

Acknowledgment. The author is indebted to Dr. T. P. Higgs and Dr. E. J. Wells for much practical help and useful discussions at many points in this investigation.

Financial support was provided by the National Research Council of Canada.

References and Notes

(1) D. Geschke, *Z. Phys. Chem.*, **249**, 125 (1972).
(2) D. Michel, *Z. Phys. Chem.*, **252**, 263 (1973).
(3) T. R. Collins, Z. Starčuk, A. H. Burr, and E. J. Wells, *J. Amer. Chem. Soc.*, **95**, 1649 (1973).
(4) A. Brooke, T. P. Higgs, and E. J. Wells, unpublished results.
(5) G. C. Levy and G. L. Nelson, "C-13 NMR for Organic Chemists," Wiley-Interscience, New York, N. Y., 1972.
(6) R. T. Davis, Jr., T. W. De Witt, and P. H. Emmett, *J. Phys. Chem.*, **51**, 1232 (1947).
(7) V. Ya. Davydov, A. V. Kiselev, and L. T. Zhuravlev, *Trans. Faraday Soc.*, **60**, 2254 (1964).
(8) J. J. Fripiat and J. Uytterhoeven, *J. Phys. Chem.*, **66**, 800 (1962).
(9) T. C. Farrar and E. D. Becker, "Pulse and Fourier Transform NMR," Academic Press, New York, N. Y., 1971.
(10) D. M. Grant and B. V. Cheney, *J. Amer. Chem. Soc.*, **89**, 5315 (1967).
(11) G. E. Maciel and J. J. Natterstad, *J. Chem. Phys.*, **42**, 2752 (1965).
(12) H. Pfeifer, *Nucl. Magn. Resonance*, **7**, 53 (1972).
(13) D. Michel, *Z. Naturforsch. A*, **22**, 1751 (1967).
(14) D. Geschke, *Z. Naturforsch. A*, **23**, 689 (1968).
(15) P. B. West, G. L. Haller, and R. L. Burwell, Jr., *J. Catal.*, **29**, 486 (1973).
(16) W. McFarlane, *Quart. Rev., Chem. Soc.*, **23**, 187 (1969).

Role of Interlayer Cations in the Formation of Acrylonitrile–Montmorillonite Complexes

S. Yamanaka,* [1] F. Kanamaru, and M. Koizumi

The Institute of Scientific and Industrial Research, Osaka University, Suita, Osaka 565, Japan *(Received June 29, 1973)*

The adsorption of acrylonitrile on montmorillonites containing various interlayer cations has been investigated by the measurement of infrared spectra and sorption isotherms. The CN stretching band of adsorbed acrylonitrile undergoes a systematic shift toward higher frequency, the amount of the shift varying linearly with the polarizing power of the interlayer cations. The shapes of sorption isotherms differ considerably from each other depending upon the kind of cation present. In the case of Ca, Mg, Co, Ni, and Cu montmorillonites, four acrylonitrile molecules per divalent cation are so strongly chemisorbed that they cannot be removed even by continuous evacuation. The strength of the interaction between acrylonitrile and the various montmorillonites is interpreted in terms of the polarizing power of the interlayer cations.

Introduction

It is well known that polar organic molecules penetrate into the interlayer spaces of montmorillonite, forming organo-clay complexes. The nature of this interesting chemical bonding between the inorganic compound and organic molecules has been studied by many scientists. Although the recent development of spectroscopic techniques[2,3] has produced experimental evidence which indicates that interlayer cations play an important role in the formation of organo-clay complexes, the mechanism of the bonding is not yet fully understood.

In an effort to better understand the bonding mechanism, we have studied the adsorption of acrylonitrile (AN) on montmorillonites containing a variety of interlayer cations by the measurement of infrared spectra and sorption isotherms. This isothermal study, in combination with infrared spectroscopy, provides important quantitative information concerning the stability of the complexes.

Since AN is a readily polymerizable monomer, we expect that the present study will be extended to investigation of interlayer polymerization.

Experimental Section

The clay mineral used in this study was a montmorillonite from Kambara in Niigata, Japan, and was supplied by Nihon Chikagaku-sha Ltd. The <2-μ particle size fraction was separated by floatation and converted to the Li^+, Na^+, K^+, Ca^{2+}, Mg^{2+}, Ba^{2+}, Cu^{2+}, Co^{2+}, Ni^{2+}, and NH_4^+ forms by washing several times with the respective chloride solutions. The converted materials were washed with distilled water until chloride free and then dried at room temperature. The cation exchange capacity was determined to be 67 mequiv per 100 g of clay. Thin, self-supporting films (2–4 mg/cm^2) of the various montmorillonites were prepared by spreading the gels, together with an appropriate amount of water, on aluminum foil using a spatula. These could be readily separated from the aluminum surfaces after drying. In the preparation of oriented films of the Co, Ni, and Cu forms, polyethylene was used, because these materials reacted with aluminum. Films prepared in this way were utilized in the measurement of sorption isotherms as well as infrared spectra.

AN was purified by distillation at atmospheric pressure after refluxing with P_2O_5 for 5 hr. This was followed by distillation in a vacuum line through a P_2O_5 tube.

Sorption isotherms were measured using a tungsten spring. The measurements were carried out on thin films in an aluminum basket. After drying at 50° under vacuum (10^{-3} Torr), the films were equilibrated at 18° with a certain pressure of AN vapor which had been carefully degassed just before use. Although the sorption equilibrium was established after only 0.5-hr contact, isotherm points were determined at intervals of 2 hr to ensure thermal equilibration.

The infrared spectra of the thin self-supporting films were measured in an evacuable glass cell with NaCl windows, using a Hitachi-Perkin-Elmer EPI-2G spectrometer. After the film was placed within the cell and dried under vacuum at room temperature, its infrared spectrum was recorded to determine the extent of dehydration. It was

allowed to react with AN by exposure to the vapor (72 Torr/18°). In order to protect the complexes from atmospheric moisture, their spectra were recorded while the sample remained in the cell. Prior to running the spectra, excess AN vapor was removed from the cell by evacuation. In the case of K, Na, NH_4, Li, and Ba montmorillonites, spectral measurements were carried out in the presence of a very small amount of AN vapor (*ca.* 1 Torr), because adsorbed AN on these montmorillonites was easily degassed by evacuation.

Results and Discussion

Isotherm. The adsorption-desorption isotherms for AN on montmorillonites are shown in Figure 1. All belong to type II in Brunauer's classification, but their shapes differ considerably according to the kind of cations existing in the interlayer space. The rapid increase in the amount of adsorption in the very low vapor pressure region indicates that AN is strongly chemisorbed to the montmorillonites. The amount of adsorption increases markedly as the relative vapor pressure (P/P_0) approaches one, due to the condensation of multilayers and capillary liquid.

In the case of Mg, Ca, Cu, Co and Ni montmorillonites, *ca.* 0.1 g of AN per 1 g of clay was still adsorbed after P/P_0 was reduced to zero in a desorption process, even after 6 hr of continuous evacuation using a rotary vacuum pump. The amount of adsorption so retained is indicated by an arrow in Figure 1. The amount was 0.066–0.069 g/g for the above five montmorillonites, which corresponds to 3.8–4.1 molecules of adsorbed AN per divalent cation. These retention complexes again adsorbed AN up to 0.1 g/g upon re-exposure to the vapor. This fact suggests that 0.1 g of AN/g contains the molecules four times as much as the exchangeable cation (chemisorbed) and that the remainder is weakly bound in the interlayer space (physically sorbed). The isotherm of Cu montmorillonite was different from those of Mg, Ca, Co, and Ni montmorillonites in that it adsorbed only half as much AN in the very low pressure region. Adsorption isotherms of Na, K, and NH_4 montmorillonites do not show the large increases in the low pressure region exhibited by the Ca, Mg, Co, and Ni complexes. In the desorption process, *ca.* 0.06 g of AN/g remained under a reduced pressure, but most of this amount was removable by evacuation. Isotherms for Li and Ba montmorillonites are similar in shape to those of Na, K, and NH_4 montmorillonites, but adsorbed molecules on the former could not be removed as easily by evacuation as those on the latter. The amount of AN adsorbed on Li and Ba montmorillonite decreased gradually on evacuation, approaching zero, while in the case of Mg, Ca, Cu, Co, and Ni montmorillonites, the AN retained after evacuation for 6 hr could not be removed by further evacuation. From the results, it is concluded that the strength of the interaction between montmorillonites and AN decreases in the following order depending on the cation present: Mg, Ni, Cu, Co, and Ca > Li and Ba > Na, K, and NH_4.

Infrared Spectrum. The characteristic CN stretching vibration can be easily recognized in the wave number region of 2230 to 2290 cm^{-1}. In the case of liquid AN, a very strong band at 2230 cm^{-1} and a shoulder at 2280 cm^{-1} are observed in this region. They were assigned to ν_4 (the CN stretching) and to the combination vibration of ν_6 (the CH_2 deformation) + ν_{11} (the C–C stretching), respectively.[4] The very strong band of the CN group of the adsorbed AN was also accompanied by a higher frequency

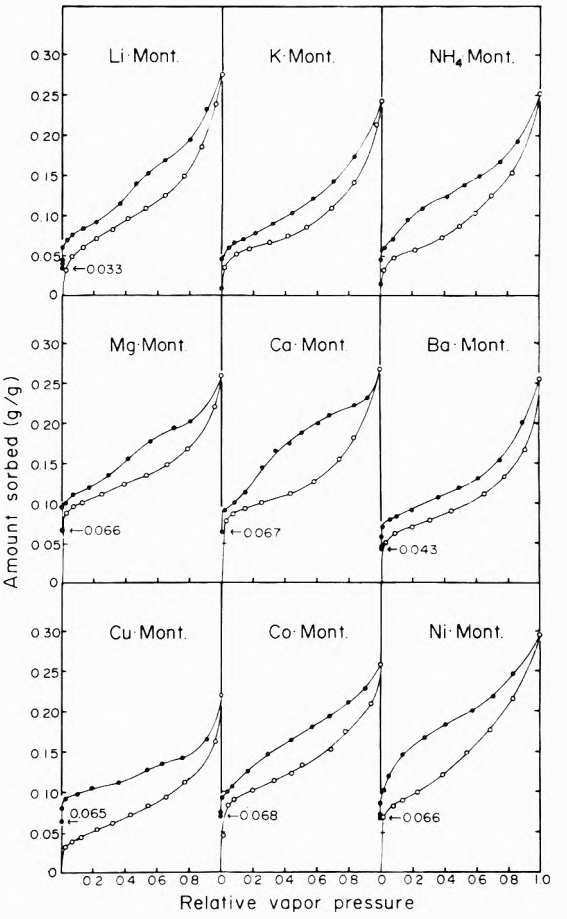

Figure 1. Adsorption–desorption isotherms for AN on montmorillonites: O, adsorption; ●, desorption. The values indicated with arrows (←) are the amount of retained AN after the evacuation for 6 hr.

shoulder. Both of them exhibited a systematic shift toward the higher frequency with respect to those of liquid AN, and there exists a linear relation between the magnitude of the shift and the polarizing power of the interlayer cations as shown in Figure 2. The precise CN frequencies of montmorillonite–AN complexes are listed in Table I together with the polarizing power of the interlayer cations.

Polarizing power (Z/R) is defined as a ratio of the charge of the cation (Z) to its ionic radius (R), and is directly related to the strength of the electrostatic field around the cation. Even if the CN frequency is plotted against another polarizing function such as Z/R^2, there is a similar relation between them. Therefore, the importance of the linear relation is not in its good linearity itself, but in the strong correlation between the CN frequency and the polarizing power.

In order to differentiate the absorptions arising from physically sorbed AN and chemisorbed AN on the infrared spectra, the samples were subjected to the spectral measurement in the presence of various amounts of AN vapor. Unlike liquid and adsorbed AN, vapor AN has very weak absorptions in the CN stretching region (2238, 2280 cm^{-1}). Therefore, the vapor remaining in the cell does not interfere with the measurement of the absorption of the adsorbed AN in this region, as long as the amount is not too large. Even in the case of the samples containing only the chemisorbed AN, the same shoulder band as that mentioned above was always observed. As the vapor pres-

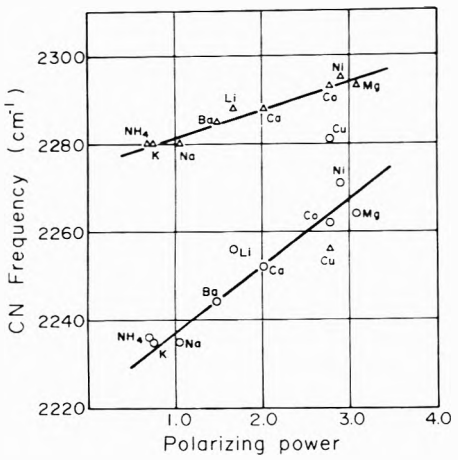

Figure 2. Linear relationship between polarizing power of interlayer cations and CN frequency of montmorillonite–AN complexes: O, main absorption band; Δ, shoulder band.

TABLE I: Infrared CN Stretching Frequency of Adsorbed AN and the Polarizing Power of the Interlayer Cation

Interlayer cation	Ionic radius (R), Å	Charge (Z)	Polarizing power (Z/R)	CN frequency, cm^{-1}	
				Main	Shoulder
Li	0.60	+1	1.67	2256	2288
Na	0.95	+1	1.05	2235	2280
K	1.33	+1	0.75	2235	2280
NH_4	1.48	+1	0.68	2236	2280
Mg	0.65	+2	3.08	2264	2293
Ca	0.99	+2	2.02	2252	2288
Ba	1.35	+2	1.48	2244	2285
Cu	0.72	+2	2.78	2281	2256
Co	0.72	+2	2.78	2262	2293
Ni	0.69	+2	2.90	2271	2295

sure increases, new weak shoulders appeared, but they could not be distinguished from the bands arising from the vapor AN present in the cell. Thus, the spectral measurement could not differentiate the two levels of bonding.

These findings are interpreted as follows. The CN group is polarized in the electrostatic field surrounding the interlayer cation, and the CN band undergoes a shift to higher frequency. The shoulder band can be assigned to the combination band of $\nu_6 + \nu_{11}$. Since the C–C bond is perturbed by the polarized CN group, the combination band which consists of ν_{11} (the C–C stretching) also exhibits a shift. As mentioned before, physically adsorbed molecules were not distinguished from vapor AN on the infrared spectra. The result can be explained in terms of the effect of cation polarizing power on the molecules. That is, the molecules physically adsorbed outside the primary shell of four chemisorbed molecules are less polarized by the center cations in comparison with those being in contact with Na, K, and NH_4 cations. As shown in Figure 1 even the AN adsorbed on Na, K, and NH_4 montmorillonites is hardly distinguished from vapor AN on infrared spectra, much less the molecules adsorbed outside the primary shell.

Numerous coordination compounds containing AN as ligand molecules have been studied previously;[5-10] and it is a well established fact that AN molecules can coordinate to transition metals in two different ways: through the N atom of the CN group, and through the π electrons of the C=C double bond. In the former complexes the CN band undergoes a shift to higher frequency, while the C=C band near 1610 cm^{-1} is not shifted. In the latter, however, the CN band shifts to lower frequencies and the band near 1610 cm^{-1} cannot be observed. Thus, in the case of montmorillonite–AN complexes, it is obvious that AN is bonded to interlayer cations through the CN group because we observed a characteristic C=C band at 1602 cm^{-1} and a shift of the CN band toward higher frequencies.

An infrared study of benzonitrile sorbed on Mg, Ca, and Ba montmorillonites has been performed by Serratosa.[11] He reported that the CN band of benzonitrile was shifted toward higher frequencies depending on the interlayer cations present. We found that the frequencies measured by him also showed a similar linear relation *vs.* the polarizing power introduced in this study. The bonding mechanism between montmorillonite and AN can be thought of as very similar to that between montmorillonite and benzonitrile, which may be explained in terms of the conjugated π-electron systems of AN and benzonitrile.

The CN frequency of the Cu montmorillonite complex deviated from the linear relation and the intensity of the higher frequency band at 2281 cm^{-1} was much stronger than that of the lower one at 2256 cm^{-1}. This relationship of intensity of the two bands is the inverse of the usual one. This seems to indicate that a different mode of bonding exists in this complex. The characteristic properties of Cu montmorillonite–AN complex are of great interest. However, it is necessary that further discussion is preceded by data from other measurements which are concerned with the electron system such as esr and uv spectroscopies.[12,13]

On the basis of the present study, it is possible to draw the following general conclusions. The interlayer cations play an important role in the formation of montmorillonite–AN complexes. The CN group is polarized by the electrostatic field surrounding the interlayer cation, and the induced dipole of AN is strongly attracted by the cation located at the center. The results of the sorption study are also interpretable from the standpoint of polarizing power as follows. Since the cation with stronger polarizing power attracts AN molecules more tightly, the stability of the complexes against evacuation decreases in the following order: Mg, Ni, Cu, Co, Ca > Li, Ba > Na, K, NH_4 montmorillonite–AN complexes.

Acknowledgment. The authors wish to express their gratitude to Professor M. M. Mortland for reading the manuscript. The expense of this study was defrayed by a Grant in Aid for Special Research Project from the Ministry of Education.

References and Notes

(1) Present address: Department of Applied Chemistry, University of Osaka Prefecture, Sakai, Osaka 591, Japan.
(2) J. M. Serratosa, *Clays Clay Miner.*, **14**, 385 (1967).
(3) V. C. Farmer, *Clay Miner.*, 7, 373 (1968).
(4) F. Halverson, R. F. Stamm, and J. J. Whalen, *J. Chem. Phys.*, **16**, 808 (1948).
(5) H. J. Coerver and C. Curran, *J. Amer. Chem. Soc.*, **80**, 3522 (1958).
(6) G. N. Schrauzer, *J. Amer. Chem. Soc.*, **81**, 5310 (1959).
(7) A. R. Luxmoore and M. R. Truter, *Proc. Chem. Soc.*, 466 (1961).
(8) J. C. Evans and G. Y.-S. Lo, *Spectrochim. Acta*, **21**, 1033 (1965).
(9) M. Kubota and D. L. Johnston, *J. Inorg. Nucl. Chem.*, **29**, 769 (1967).
(10) K. Nakamoto, "Infrared Spectra of Inorganic and Coordination Compounds," 2nd ed, Wiley, New York, N. Y., p 186.
(11) J. M. Serratosa, *Amer. Mineral.*, **53**, 1244 (1968).
(12) T. J. Pinnavaia and M. M. Mortland, *J. Phys. Chem.*, **75**, 3957 (1971).
(13) D. M. Clementz, T. J. Pinnavaia, and M. M. Mortland, *J. Phys. Chem.*, **77**, 196 (1973).

Electron Spin Resonance Spectra of Manganese(II)-Doped Powder Samples of Hexakis(pyridine *N*-oxide)mercury(II) Perchlorate Complexes

Gerald M. Woltermann[1] and John R. Wasson*

Department of Chemistry, University of Kentucky, Lexington, Kentucky 40506 *(Received July 16, 1973)*

The electron spin resonance (esr) spectra of powdered samples of manganese(II)-doped hexakis(pyridine *N*-oxide)mercury(II) perchlorate complexes are reported. The pyridine *N*-oxides employed were pyridine, 2-methylpyridine, 3-methylpyridine, 4-methylpyridine, 4-nitropyridine, and 4-cyanopyridine *N*-oxide. The analysis of the esr spectra of polycrystalline manganese(II) complexes is discussed. The 4-methyl- and 4-nitropyridine *N*-oxide complexes exhibit rhombic symmetry while the others are axially symmetric. The electron spin-nuclear spin hyperfine coupling constants indicate Mn(II)–pyridine *N*-oxide bonding to be more covalent than Mn(II)–water bonding. Manganese–ligand covalency was also shown to be highly dependent on the substituent on the pyridine ring, covalency increasing with increasing electron-withdrawing ability.

Introduction

Recently, the electron spin resonance (esr) spectra of manganese(II)-doped hexakispyridine and substituted pyridine *N*-oxide complexes of zinc and cadmium perchlorate have been reported.[2] The esr data showed that the ring-substituted zinc complexes possess rhombic symmetry while the cadmium compounds generally exhibited axial symmetry. In all of the complexes the zero-field splitting was surprisingly large in view of what might be expected from steric considerations. Furthermore, variation in the zero-field splitting with substituents on pyridine *N*-oxide could not be rationalized using geometric arguments alone. Byers, *et al.*,[3] have noted that cobalt(II) and nickel(II) pyridine *N*-oxide complexes exhibit unusually large axial distortion even in their electronic spectra. They noted that the effective symmetry of a complex is dependent on the electronic symmetry, governed by metal ion–ligand wave function interaction, as well as the geometry of the surrounding ligands. Variation in zero-field splitting in manganese(II)-doped zinc and cadmium pyridine *N*-oxide complexes[2] required postulation of covalency effects, which infrared and electronic spectral data[4-7] showed to increase with increasing electron-withdrawing ability of the ring substituents, opposite in sign to contributions from the point charge crystalline field. This effect had previously been shown to be present in manganese(II)-doped zinc chloride by Sharma, *et al.*[8]

Very recently the crystal structure of hexakis(pyridine *N*-oxide)mercury(II) perchlorate has been described.[9] The crystals belong to space group $R\bar{3}$ and have one molecule per unit cell. The mercury has regular octahedral coordination, Hg–O = 2.35 Å and the Hg–O–N angle is 114°. Carlin, *et al.*,[10] had previously shown that the six-coordinate mercury complex was isomorphous with the corresponding nickel(II) and cobalt(II) complexes. They[10] attributed the ability to pyridine *N*-oxide to form a six-coordinate complex with mercury to be due to minimal steric interactions between the ligands. In view of our previous work[2] and the preceding results we undertook a study of the esr spectra of manganese(II)-doped hexakis(pyridine *N*-oxide)mercury(II) perchlorate. Several additional hexakis substituted pyridine *N*-oxide complexes were prepared and characterized and doped with manganese(II) in order to observe the change in zero-field splitting with substituent variation and to compare the trends in zero-field splitting with those observed[2] for the corresponding zinc and cadmium complexes.

Experimental Section

Pyridine *N*-oxides were purchased from Aldrich Chemical Co., Milwaukee, Wis., and metal perchlorates were obtained from Alfa Inorganics, Beverly, Mass. Carbon, hydrogen, and nitrogen analyses were performed by Chemalytics, Inc., Tempe, Ariz.

Hexakis complexes of pyridine *N*-oxide and its derivatives with mercury(II) perchlorate were prepared by mixing ethanolic solutions of mercury(II) perchlorate hexahydrate and the appropriate ligand. Precipitation of the complex occurred immediately upon mixing and the solids were collected by suction filtration, washed with ethanol and ether, and air dried. The complexes were subsequently recrystallized from absolute ethanol. In the preparation of the 4-nitro- and 4-cyanopyridine *N*-oxide complexes the ethanolic solutions of the ligands were heated in order for dissolution to occur. The manganese(II)-doped complexes were prepared by adding small (2%) amounts of manganese(II) perchlorate hexahydrate to hydrated mercury perchlorate and then dissolving the mixture in ethanol before addition of the ligand. C, H, and N analyses of previously uncharacterized mercury(II) pyridine *N*-oxide complexes are listed in Table I.

Esr spectra were measured with a Magnion MVR-12X X-band spectrometer (O. S. Walker Co., Worcester, Mass.) operating at about 9.4 GHz using 6-kHz field modulation and a 12-in. electromagnet. The frequency was monitored with a calibrated absorption wavemeter incorporated in the microwave unit. Field calibration was checked using diphenylpicrylhydrazyl (DPPH) free radical for which g = 2.0036. Quartz sample tubes were employed. Reproducibility of spectra from sample to sample and at different levels of Mn(II) doping was excellent. Infrared spectra (4000–200 cm^{-1}) were measured with a Perkin-Elmer 621 recording spectrometer using Nujol mulls on CsI plates.

TABLE I: Elemental Analysis of $Hg(R\text{-}C_5H_4N \rightarrow O)_6(ClO_4)_2$

Substituent R	Calculated			Found		
	% C	% H	% N	% C	% H	% N
2-Methyl	41.17	3.65	8.00	40.91	3.73	7.57
3-Methyl	41.17	3.65	8.00	40.68	3.81	7.76
4-Methyl	41.17	3.65	8.00	40.92	3.85	7.78
4-Nitro	29.15	1.63	13.60	29.08	1.66	13.23
4-Cyano	38.74	1.81	15.06	38.60	2.06	14.83

Theory

The spin Hamiltonian for a Mn(II) ion surrounded by an axially symmetric crystalline field is given by[11]

$$H = g\beta H\cdot S + D(S_z^2 - S(S+1)/3) + AS\cdot I \quad (1)$$

when the quartic terms in a and F are ignored. These two terms produce only small splitting of the fine lines and in a powder spectrum contributions from these terms are effectively averaged to zero. Using eq 1 the fine line field positions for an arbitrary orientation of the crystal in the applied magnetic field can be shown[2] to be

$$H_{M_s} = H_0 - (M_s - 1/2)[3\cos^2\theta - 1]D + (13 - 12M_s(M_s - 1))(\sin^2\theta\cos^2\theta\, D^2/H_0) - (29 - 12M_s(M_s - 1))D^2\sin^4\theta/(16H_0) \quad (2)$$

where $H_0 = h\nu/g\beta$ and θ is the angle between the crystalline z axis and the applied field direction. In a powder sample crystallites are present at all orientations and it might be expected that the fine lines which show a first-order dependence would spread out onto broad structureless humps. This would leave only the central $\Delta M_s = 1$ ($-1/2 \leftrightarrow 1/2$) fine line clearly resolved. However, sharp lines in the esr spectra of powdered solids are obtained only at preferred orientations of the individual crystallites. These orientations represent singularities in the theoretical powder pattern and are of two kinds, that is, either absorption edges or infinities. Infinities bring about esr signals substantially more intense than absorption edges and in axial symmetry absorption edges are often not observed. For axial symmetry infinities occur[2] at orientations such that $\theta = 90°$ for the ΔM_s $\pm5/2 \leftrightarrow \pm3/2$ and $\pm3/2 \leftrightarrow \pm1/2$ fine lines while absorption edges occur for the same transitions at $\theta = 0°$. The central ΔM_s $-1/2 \leftrightarrow +1/2$ fine line is split due to its second-order dependence on θ. Infinities occur for this transition at an orientation such that $\theta = 90°$ and $\tan^2\theta = 0.8$. Using eq 2 the D value can be easily derived from the observed fine lines in the esr spectrum. Each of these fine lines will, of course, be split into six hyperfine lines and the position of an individual fine line is measured at the center of the two central hyperfine lines in the hyperfine sextet. When $\theta = 90°$, the lines due to the $\pm5/2 \leftrightarrow \pm3/2$ transitions should be separated by $4D$ while the $\pm3/2 \leftrightarrow \pm1/2$ transitions will be separated by an amount $2D$ where D is expressed in gauss. Furthermore, the central fine line will be split by an amount $5.6D^2/H_0$. Hence, three independent methods of determining D are available from an esr spectrum of a powdered complex, resolution permitting. Once D is determined, eq 2 can be employed to calculate H_0 for the complex. The g value of the complex can be determined by measuring the field separation between H_0 and H_0 for DPPH and using the expression

$$g = g_s(h\nu/\beta)/[(\Delta H)g_s + (h\nu/\beta)] \quad (3)$$

where $g_s = 2.0036$ and ΔH is negative for a low field displacement of the resonance signal of the complex with respect to DPPH. The electron spin-nuclear spin hyperfine coupling constant, A, is determined by measuring the field separation between the two central hyperfine lines of the central ΔM_s $+1/2 \leftrightarrow -1/2$ fine line for which second-order contributions are minimal.

When the manganese(II) ion is surrounded by a crystalline field having rhombic symmetry, the spin Hamiltonian is given by

$$H = g\beta H\cdot S + D(S_z^2 - S(S+1)/3) + E(S_x^2 - S_y^2) + AS\cdot I \quad (4)$$

The fine line positions for an arbitrary orientation of the applied field with respect to the symmetry axis of the crystal are given by

$$H_{M_s} = H_0(M_s - 1/2)(D(3\cos^2\theta - 1) - 3E\cos^2\theta\sin^2\theta) + (13 - 12M_s(M_s - 1)/H_0)[(D - E\cos 2\phi)^2\sin^2\theta\cos^2\theta + (E\sin 2\phi)^2\sin^2\theta) - (29 - 12M_s(M_s - 1)/(16H_0)[D\sin^2\theta + E\cos 2\phi \times (1 + \cos\theta\sin 2\phi)]^2 \quad (5)$$

where θ is the angle the applied field makes with the z axis and ϕ is the angle between the x axis and the projection of the field in the xy plane. The x spectrum is often buried under the strong central transitions. The splitting of the central fine line is complex in rhombic symmetry and dependent on the relative sizes of D and E. Burns[12] has noted that the rhombic spin Hamiltonian is the same as the quadrupole Hamiltonian employed in nmr spectroscopy when an asymmetry parameter, η, is present, if one replaces $3[4I(2I-1)]^{-1}e^2Qq$ by D when the symmetry is axial and η by 3 (E/D) when the symmetry is rhombic. Strauss[13] has calculated how the central lines will split for various values of $3(E/D)$ and application to esr spectra is straightforward. Once D and E have been determined from the outer lines, the central line positions can be calculated and compared to experiment. D and E zero-field splitting parameters are determined from the outer fine lines with the aid of eq 5. The ΔM_s $\pm5/2 \leftrightarrow \pm3/2$ fine lines are separated by an amount $8D$ when the field is directed along the z axis and by an amount $4D + 12E$ when the field is directed along the y axis. The ΔM_s $\pm3/2 \leftrightarrow \pm1/2$ fine lines are separated by an amount $4D$ when H is parallel to the z axis and by an amount $2D + 6E$ when the field is along the y axis. Figure 1 shows the esr spectrum and fine line assignments for an axially symmetric manganese(II) complex while Figure 2 gives the spectrum and assignments for a Mn(II) ion surrounded by a rhombic field.

Results and Discussion

Infrared Spectra. The ν(N-O) stretching frequencies of pyridine *N*-oxide complexes are reasonably sensitive probes of the extent of metal-ligand covalency. The crystallographic study of $Hg(C_5H_5NO)_6(ClO_4)_2$ by Kepert, *et al.*,[9] showed that the perchlorate anion has C_{3v} symmetry and bands at 938, 1127, 1077, 629, and 621 cm^{-1} were assigned to the perchlorate anion. Table II lists the N-O stretching frequencies, bands associated with the perchlorate anion, and compares changes in ν(N-O) for the mercury(II) and related iron(III) complexes.[14] Since iron(III) is, like Mn(II), an S-state ion with a half-filled d shell, its complexes should be comparable to those of Mn(II) with pyridine *N*-oxide. The absence of crystal field stabilization energies in high-spin iron(III) and mercury(II) com-

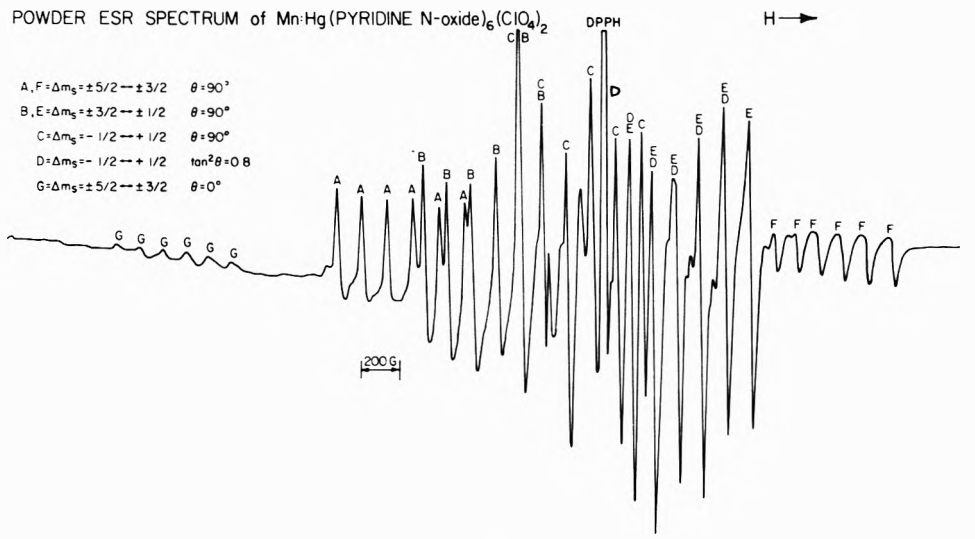

Figure 1. Esr spectrum of hexakis(pyridine *N*-oxide)manganese perchlorate doped into the corresponding mercury(II) complex. The transitions are as indicated.

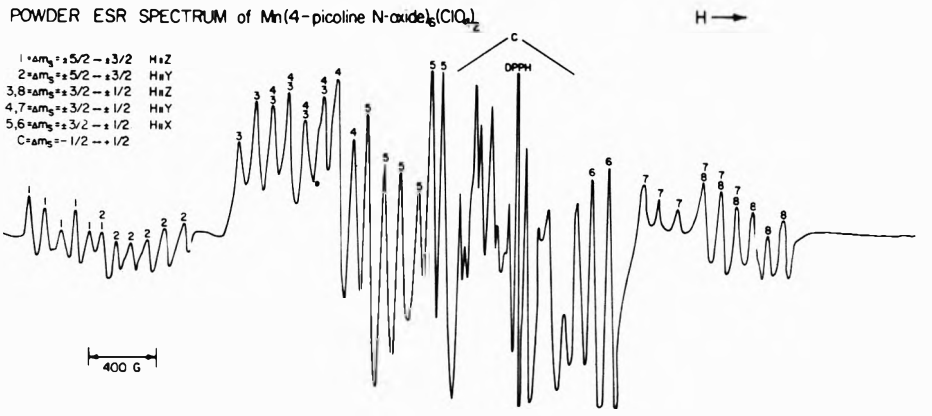

Figure 2. Esr spectrum of hexakis(4-picoline *N*-oxide)manganese perchlorate doped into the corresponding mercury(II) complex. The transitions are as indicated.

TABLE II: Infrared Spectral Data for $Hg(R\text{–}C_5H_4N \rightarrow O)_6(ClO_4)_2$

Substituent R	Mp (uncor), °C	Ligand ν(N–O), cm^{-1}	Hg complex $\Delta\nu$(N–O), cm^{-1}	Hg complex[a] $\Delta\nu$(N–O), cm^{-1}	Fe(III) complex[b] $\Delta\nu$(N–O), cm^{-1}	Hg complex ClO_4^- bands, cm^{-1}
Hydrogen	161	1246	1242	−4	−38	1082, 1123, 934, 623, 630
2-Methyl	144	1230	1230	0	−30	1080, 1125, 938, 623, 630
3-Methyl	158	1270	1270	0	−15	1085, 938, 629 635
4-Methyl	169	1228	1225	−3	−20	1087, 934, 623, 630
4-Nitro	190	1273	1218	−55	−58	1070, 1115, 934, 623, 625
4-Cyano	191	1280	1220	−60	−58	1082, 1118, 932, 621

[a] $\Delta\nu(N\text{–}O) = \nu(N\text{–}O)_{ligand} - \nu(N\text{–}O)_{complex}$. [b] Reference 14.

plexes suggests that the differences in the N–O stretching frequencies, $\nu(NO)_{Fe} - \nu(NO)_{Hg}$, might be associated with transition metal–pyridine *N*-oxide oxygen covalency and be correlated with the Mn(II) nuclear hyperfine coupling constants, *A*, which are well known[15] to reflect metal–ligand covalency.[15] Inspection of the data in Tables II and III shows that the greater the $\nu(NO)_{Fe} - \nu(NO)_{Hg}$ difference, the larger *A* value for the corresponding Mn(II) complex, the only exception being the 4-methylpyridine *N*-oxide complex. For the methyl-substituted mercury complexes, reduction in ν(N–O) is zero or almost zero whereas pronounced shifts occur for the 4-nitro- and 4-cyanopyridine *N*-oxide complexes. In the iron(III) hexakis complexes[14] substantial reduction in ν(N–O) occurs in all cases with the largest shifts occurring when the ring substituent is an electron-withdrawing group. The reduction of ν(N–O) for the iron(III) complexes closely parallels the Mn(II) *A* values as a qualitative indication of the metal–ligand covalency present in these complexes. Only the 2- and 3-methyl derivatives deviate from this trend.

TABLE III: Electron Spin Resonance Parameters for Mn(II)-Doped Hg(R-$C_5H_4N \rightarrow O)_6(ClO_4)_2$[a]

Substituent R	$g(+0.033)$	D, G ($\times 10^4$ cm^{-1})[b]	E, G ($\times 10^4$ cm^{-1})	$-A$, G ($\times 10^4$ cm^{-1})
Hydrogen	2.009	445 (415)		94 (88)
2-Methyl	2.010	240 (225)		93 (87)
3-Methyl	2.010	530 (497)		93 (87)
4-Methyl	2.003	720 (673)	165 (154)	95 (89)
4-Cyano	2.011	235 (221)		90 (84)
4-Nitro	2.012	500 (469)	~20	90 (84)

[a] Spectra of powdered solids. [b] Values in parentheses are in cm^{-1} units.

This suggests that reduction in ν(N-O) is not as sensitive to metal-ligand covalency as A values are and that subtle differences in Mn-O and Fe-O bonding could account for the observed deviations. The data (Table II) indicate that back-bonding is important in these complexes. Both metal → ligand back-bonding and ligand → metal donation are expected to be present to some extent in all of the complexes. Strong metal → ligand back-bonding could account for the much larger ν(N-O) shifts in the 4-nitro- and 4-cyanopyridine *N*-oxide compounds. The ability of electron-withdrawing substituents to bring about metal → ligand back-bonding was employed by Herlocker, *et al.*,[5] in their interpretation of infrared data for 4-substituted pyridine *N*-oxide complexes with nickel(II). The covalency trends indicated by ν(N-O) for the nickel(II) complexes is in qualitative agreement with the present data. The infrared spectra (4000-200 cm^{-1}) of the mercury(II) complexes showed no bands which could be attributed to metal-oxygen stretching. The bands attributable to the perchlorate ions indicate that all the Hg(II) complexes probably have very closely related structures.[9]

Esr spectra. Table III lists the esr parameters found for Mn(II)-doped pyridine *N*-oxide complexes of mercury(II). The results are unusual in several respects. The large magnitude of the zero-field splitting even for the unsubstituted pyridine *N*-oxide is surprising in view of its crystal structure.[9] Since the oxygens surrounding the central metal ion are arranged in a regular octahedron with the overall symmetry of the complex cation being C_{3v}, this complex invites comparison with the six coordinate complex of Mn(II) with antipyrine. In the latter complex the steric interaction between the ligands is larger than in the pyridine *N*-oxide complexes but the immediate surroundings of the Mn(II) ion are similar.[16] Single crystal esr studies[17] of the Mn(II) antipyrine complex in a variety of corresponding diamagnetic host lattices have shown the zero-field splitting to be quite small and to decrease regularly with increasing size of the host metal ion. Apparently, more than steric considerations are required to explain the zero-field splitting in the pyridine *N*-oxide complex.

Sharma, *et al.*,[8] have shown that overlap and covalency can contribute substantially to the magnitude of D and E and these contributions can be opposite in sign to the contributions expected from the point charge crystalline field. Byers, *et al.*,[3] noted that the metal ion-ligand wave function is also critical to the effective symmetry of a complex. These considerations coupled with the slightly higher position of pyridine *N*-oxide with respect to antipyrine in the spectrochemical series might explain the wide variation in the magnitudes of their zero-field splitting. More surprising is the manner in which the zero-field splitting varies on changing the host metal ion size. The experimental data of Title,[18] Kikuchi,[19] and Woltermann[17] would lead to the prediction that for a given pyridine *N*-oxide the zero-field splitting should be smaller in the mercury host lattice than in the zinc or cadmium host lattices. However, the zero-field splitting in the mercury host lattice is nearly identical with those found[2] for the pyridine *N*-oxide and 3-methyl-, 4-nitro-, and 4-cyanopyridine *N*-oxide complexes of cadmium. The magnitude of the zero-field splitting in the 4-methylpyridine *N*-oxide complexes even increases when the host lattice is changed from cadmium to mercury. Since in these pyridine *N*-oxide complexes steric crowding should be minimal,[9,10] no decrease in distortion on increasing the host metal ion size would be observed as occurred in the antipyrine series.[17] Therefore, the magnitude of D and E should be approximately the same irrespective of the size of the host metal ion. This argument does not explain the increase in zero-field splitting in the 4-methylpyridine *N*-oxide complex. Since crystal structures of hexakis(4-picoline *N*-oxide) complexes of cadmium and mercury are not known, the two may not be isomorphic. Crystal packing in the cadmium complex might be conducive to a more nearly octahedral arrangement of ligands about the central metal ion. It is apparent, however, that zero-field splitting in the pyridine *N*-oxides cannot be interpreted on the basis of steric factors alone nor is it possible from the magnitude of the zero-field splitting to make unambiguous judgements about steric distortions from octahedral geometry.

The magnitudes of the electron spin-nuclear spin hyperfine coupling constants, A, for these complexes show the Mn-O covalency to be independent of the host metal ion size and to be quite dependent on the nature of the substituent group on the pyridine ring. The linear increase in the magnitude of A with increasing Pauling ionicity[15,18] is well known for Mn(II) and the A values reported here show that pyridine *N*-oxides form Mn-O bonds more covalent than those formed by water. The metal-ligand covalency increase with electron-withdrawing substituents on the pyridine ring. The 4-nitro-and 4-cyanopyridine *N*-oxide complexes exhibit the smallest A values (largest covalency) while the 4-methyl complex exhibits the largest A value. This is in accord with infrared and electronic spectral data[5,6] on other hexakis(pyridine *N*-oxide) complexes. The infrared results[5] show that better electron-withdrawing substituents on the pyridine ring produce larger ν(N-O) shifts upon complexation. This was attributed to enhancement of metal → ligand back-bonding by the withdrawing group.

Finally, the g values observed for these complexes are near the spin-only value of 2.0023 as is expected for an S state ion such as manganese(II) in which no orbital contribution to the ground state is present to first order. A slight positive g shift on increasing the size of the host metal ion is observed, the mercury host lattices giving the higher g values. Since the g values are always close to the spin-only value for Mn(II) complexes, they are not a good source of information about electronic structures and little more can be said about them.

References and Notes

(1) Present address, School of Chemical Sciences, University of Illinois, Urbana, Ill.
(2) G. M. Woltermann and J. R. Wasson, *Inorg. Chem.*, **12**, 2366 (1973).
(3) W. Byers, A. B. P. Lever, and R. V. Parish, *Inorg. Chem.*, **7**, 1835 (1968).
(4) S. Kida, J. V. Quagliano, J. A. Walmsley, and S. Y. Tyree, *Spectrochim. Acta*, **19**, 180 (1963).

(5) D. W. Herlocker, R. S. Drago, and V. I. Meek, *Inorg. Chem.*, **5**, 2009 (1966).
(6) R. Whyman, W. E. Hatfield, and J. S. Paschal, *Inorg. Chim. Acta*, **1**, 113 (1967).
(7) D. W. Meek, R. S. Drago, and T. S. Piper, *Inorg. Chem.*, **1**, 285 (1962).
(8) R. Sharma, T. P. Das, and R. Orbach, *Phys. Rev.*, **155**, 338 (1967).
(9) D. L. Kepert, D. Taylor, and A. H. White, *J. Chem. Soc., Dalton Trans.*, 670 (1973).
(10) R. L. Carlin, J. Roitman, M. Dankleff, and J. O. Edwards, *Inorg. Chem.*, **1**, 182 (1962).
(11) B. Bleaney and D. J. E. Ingram, *Proc. Roy. Soc., Ser. A*, **205**, 336 (1951).
(12) G. Burns, *J. Appl. Phys.*, **32**, 2048 (1961).
(13) G. W. Strauss, *J. Chem. Phys.*, **40**, 1988 (1964).
(14) G. J. Long, G. M. Woltermann, and J. R. Wasson, unpublished results.
(15) O. Matamura, *J. Phys. Soc. Jap.*, **14**, 108 (1959).
(16) M. Vijayan and M. Viswamitra, *Acta Crystallogr.*, **21**, 522 (1966).
(17) G. M. Woltermann and J. R. Wasson, *J. Phys. Chem.*, **77**, 945 (1973).
(18) R. S. Title, *Phys. Rev.*, **136**, 623 (1963).
(19) C. Kikuchi and G. Azarbayejani, *J. Phys. Soc. Jap., Suppl. B-1*, 2503 (1962).

Geometry and Electronic Structure of Nitrostyrene Molecules and Anions

M. Barzaghi, A. Gamba, G. Morosi, and M. Simonetta*

C.N.R. Center for the Study of Structure/Reactivity Relations and Institute of Physical Chemistry, University of Milan, 20133 Milan, Italy *(Received May 22, 1973)*

Ultraviolet spectra and dipole moments for neutral molecules of o-, *m*-, and *p*-nitrostyrenes, and esr and uv spectra for the corresponding anion radicals, have been determined. Anion radicals were obtained by electrolytic reduction in liquid ammonia, acetonitrile, and dimethyl sulfoxide. Hfs coupling constants have been assigned through a comparison with related compounds and on the basis of calculations based on INDO and PPP methods. The dipole moments of the excited states associated to the most relevant transitions have been determined through the McRae theory of solvent shift of absorption bands. Ground- and excited-state properties have been studied by means of semiempirical (PPP and CNDO-CI) and *ab initio* (STO-3G) methods. Information on the conformations of the three isomers was obtained on the basis of a study of INDO energies *vs.* geometrical parameters.

Introduction

Following a research program on spectroscopic behavior of anion radicals containing the nitro group, we presented in recent papers[1,2] for a number of nitro compounds some experimental data including hyperfine splitting constants and electronic transition energies for anion radicals, as well as transition energies and probabilities for the parent neutral molecules. Their interpretation was substantiated by means of theoretical calculations.

In this paper the same experimental and theoretical work has been extended to nitrostyrenes, whose spectroscopic properties have scarcely been investigated.[3] The following experimental data for *o*-, *m*-, and *p*-nitrostyrenes have been investigated: uv spectra and dipole moments for neutral molecules, and uv and esr spectra for anion radicals. The related observations have been obtained by means of Pariser and Parr calculations, but for situations in which the validity of σ/π approximation seemed questionable, results have been supplemented by means of calculations based on "all valence electrons" methods. The ground state of neutral molecules has been also studied by *ab initio* MO calculations.

Owing to the lack of experimental data on the geometry, the energy dependence on the twist angle of vinyl and nitro groups around the bonds to the benzene ring has been determined by means of INDO calculations. In particular, the variation of hyperfine splitting constants with conformation has been examined. The numbering of atoms in the molecules and the corresponding ions is shown in Figure 1.

Experimental Section

Materials. 2-Nitrostyrene was prepared by decarboxilation of o-nitrocynnamic acid;[4,5,6] the product, a pale yellow oil, was purified by chromatography on silica column, using *n*-hexane as an eluent. A mass spectrum confirmed the purity of the sample. 3- and 4-Nitrostyrene were high-purity K & K Labs., Inc. products.

Solvents. Solvents were Carlo Erba commercial products for spectrophotometry. Acetonitrile (ACN) and dimethyl sulfoxide (DMS) used for radical solutions were further purified following the prescriptions given in ref 7 and 8–10, respectively. Tetraethylammonium perchlorate (TEAP) was a Carlo Erba product for polarography. Liquid ammonia was carefully purified in an *ad hoc* apparatus described in ref 11.

Anion Radical Preparation and Measurements. Anion radicals were obtained in vacuum cells by controlled potential electrolysis using as solvents ACN, DMS, and liquid ammonia. The technical details and the vacuum apparatus, when ACN and DMS have been used as solvents, were previously described.[1,12] Reduction potentials for each compound were evaluated from polarographic curves recorded at room temperature in ACN, using a saturated calomel electrode (sce) as an external reference, and the corresponding half-wave potentials are collected in Table I.

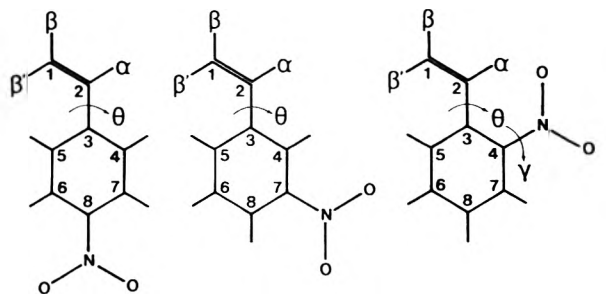

Figure 1. Topology of nitrostyrenes and numbering of atoms.

TABLE I: Half-wave Potentials Measured in ACN and Tomes Reversibility Relationship[a] for the First Polarographic Wave

Isomer	$-E_{1/2}$, V *vs.* sce	$E_{1/4} - E_{3/4}$, V
Para	1.078	0.065
Meta	1.164	0.067
Ortho	1.151	0.075

[a] J. Tomes, *Collect. Czech. Chem. Commun.*, **9**, 12, 81, 150 (1937).

The use of liquid ammonia as solvent required a particular apparatus, described in ref 11 and 13. The optimized conditions to obtain well-resolved spectra were (a) reduction potentials of −28 V, (b) temperatures ranging between −60 and −80°, and (c) concentration of the substrate *ca.* 10^{-3} *M* with an equivalent concentration of supporting electrolyte (TEAP).

Esr spectra were recorded using a Varian 4500-10A X-band spectrometer with a 100-kHz magnetic field modulation. Electronic absorption spectra were measured with a Beckman DK-2A spectrophotometer. Polarographic measurements were obtained with a multipurpose Amel Model 463 polarograph.

Neutral Molecules Measurements. The electronic uv spectra in 21 different solvents were measured with a Beckman DK-2A spectrophotometer. Recording was carried out in a purified nitrogen stream (oxygen content <0.2 ppm). The list of solvents is found in the caption of Figure 2.

Dipole moments of ground state μ_g were determined in anhydrous benzene solution at 25.0 ± 0.05°. Dielectric constants ϵ were measured with a WTW Dipolmeter Model DM 01 ($\Delta\epsilon/\epsilon = 10^{-5}$ at a frequency of 2 MHz) and the refractive indices were measured with an Abbe refractometer. The solute molar polarization P_2, extrapolated to infinite dilution, was obtained from experimental data by the simplified Guggenheim method.[14,15]

Methods of Calculation

(*a*) *Conformational Analysis.* Preliminary calculations on neutral molecules were carried out to obtain the minimum energy conformation for each isomer. The total energy was calculated by INDO method[16] as a function of two variables, that is the θ angle which represents the rotation of the vinyl group around C–C bond, and the γ angle which represents the rotation of the NO_2 fragment. The $\theta = 0°$ conformation corresponds to C_1 cis with respect to C_5 (see Figure 1) and the twist angle was taken clockwise when looking from C_3 atom. The twist angle of the nitro group (γ) was taken clockwise when looking from the ring carbon atom.

All bond lengths except one were kept fixed, that is C–C in the benzene ring = 1.397 Å, ethylenic C_1–C_2 = 1.334 Å, C–N = 1.47 Å, O–N = 1.22 Å, and all C–H equal to 1.08 Å; all bond angles were assumed equal to 120°.

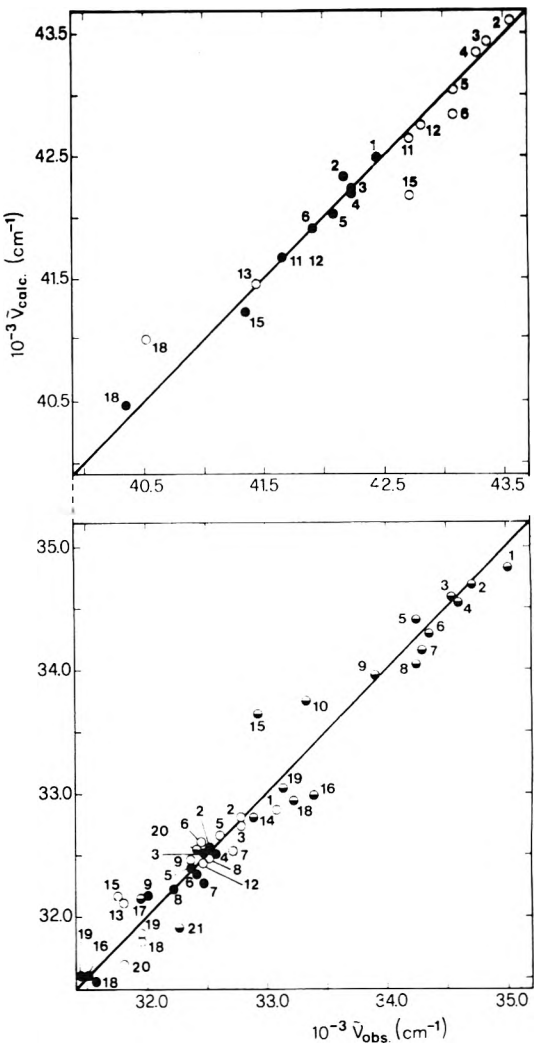

Figure 2. Calculated *vs.* observed band wave numbers of para (◒), meta (●), and ortho (O) nitrostyrenes. The frequency shifts are calculated from eq 3. Solvents: 1, *n*-pentane; 2, *n*-hexane; 3, *n*-heptane; 4, isooctane; 5, *n*-decane; 6, cyclohexane; 7, cycloheptane; 8, cyclooctane; 9, CCl_4; 10, benzene; 11, dimethoxyethane; 12, diethyl ether; 13, $CHCl_3$; 14, chlorobenzene; 15, CH_2Cl_2; 16, caprylonitrile; 17, phenylacetonitrile; 18, propionitrile; 19, acetonitrile; 20, *N,N*-dimethylformamide; 21, dimethyl sulfoxide.

For the interfragment C_2–C_3 bond length a linear dependence on cos θ was assumed in the limits: $(C_2\text{–}C_3)_{min}$ = 1.47 Å for $\theta = 0°$ and $(C_2\text{–}C_3)_{max}$ = 1.52 Å for $\theta = 90°$.

(*b*) *Electronic Transition Energies and Probabilities.* (*i*) *Neutral Molecules.* Singlet–singlet excitation energies and probabilities were evaluated by means of *standard* PPP[17] and CNDO–CI[18] methods. In the case of the former method the CI treatment includes all singly excited configurations. The parametrization used through the calculations was the same as reported in previous papers,[1,2] where starting HMO's were evaluated with the parametrization suggested by Rieger and Fraenkel[19] for the nitro group.

In the case of the CNDO–CI method the parametrization suggested by Jaffé and coworkers[20] was adopted, and electronic repulsion integrals were evaluated through Mataga's relationships.[21] The 60 lowest energy configurations were included in the configuration interaction.

In general, owing to the overlapping of bands, only the most intense transitions, among the calculated ones, can

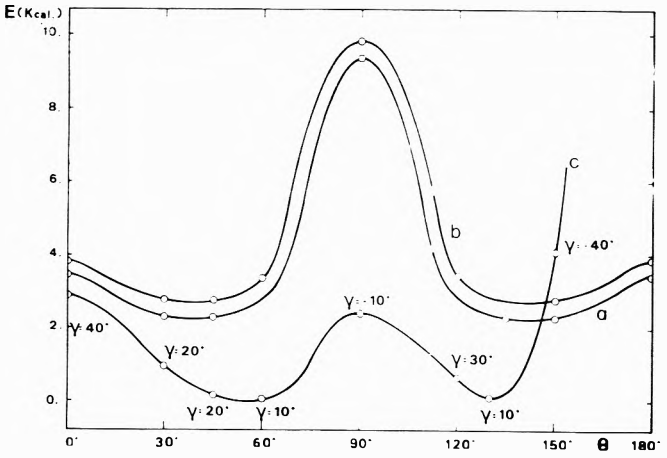

Figure 3. Total energy variation of nitrostyrenes as a function of twist angle of vinyl (θ) and nitro group (γ): (a) *p*-nitrostyrene; (b) *m*-nitrostyrene; (c) o-nitrostyrene.

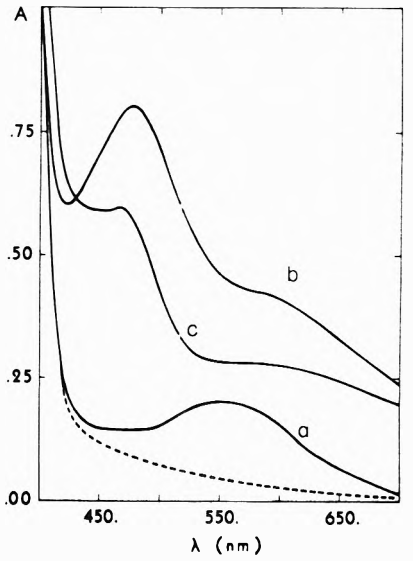

Figure 4. Electronic spectra of anion radicals in the visible region: (a) para; (b) meta; (c) ortho. Dotted line represents radicals after air exposure.

be observed. To check the overall reliability of our calculations, we tried to fit the spectrum shape by taking into account all the predicted transitions. PPP transition energies and oscillator strengths were used.

The shape of the single absorption band was assumed to be described by a Lorentz line and the whole spectrum to be the sum of Lorentz functions associated to all theoretical transitions, that is

$$\epsilon(\nu) = \sum_{j}^{\text{all transitions}} \frac{a_j}{(\nu - \nu_{j(\max)})^2 + b_j^2} \qquad (1)$$

where $\nu_{j(\max)}$ is the calculated transition energy (in cm^{-1}) and a_j and b_j are parameters to be determined, connected through the relationship

$$a_j = \frac{10^9}{4.32\pi} f_j b_j \qquad (2)$$

where f_j is the oscillator strength.

In principle, $2b_j$, which is the half-height width, could be taken from the experimental band. However, the measure of these parameters is in general not reliable or even possible owing to several factors which alter the line shape, that is overlapping of bands, vibrational structure, solvent effect, and so on. In this view b_j parameters were optimized through a least-square fitting over ϵ(calcd) − ϵ(obsd) for about 150 equally spaced wave numbers in the absorption region to obtain the best regression line between calculated and experimental spectra. (See Figure 2.)

(*ii*) *Radical Ions.* Doublet–doublet excitation energies and probabilities were evaluated by a restricted LCI–SCF method in the version given by Roothaan (R).[22] In the CI calculation interaction between ground state and all singly excited configurations of types A, B, C_α, and C_β (according to the definition reported in ref 1 and 23) was considered. Details about the calculation of energy and oscillator strength matrix elements for doublets are available in ref 1 and 23.

(c) *Ground- and Excited-State Dipole Moments.* Theoretical π electron ground- and excited-state dipole moments were obtained from the corresponding PPP wave functions. Total ground state dipole moments were also computed by an *ab initio* SCF MO calculation using a STO-3G basis set.[24]

(*d*) *Esr Spin Densities and Coupling Constants.* Spin densities (ρ) were obtained from doublet wave functions calculated by R and INDO methods. The Q_{CH}^{H} constant, which translates spin densities calculated by the R method into coupling constants a through the McConnell relationship, was optimized to give the best fit between calculated spin densities and measured hfs coupling constants. Values were obtained both in the minimum energy conformation and as average on all the conformations through the formula

$$\bar{a} = \frac{\int a(\theta) e^{-E(\theta)/kT}\, d\theta}{\int e^{-E(\theta)/kT}\, d\theta} \qquad (3)$$

Results

(*a*) *Conformation.* The results for conformational analysis of nitrostyrenes by INDO calculations are shown in Figure 3, where, owing to symmetry, only the range 0–180° of θ is reported. The nonbonded interactions between vinyl hydrogens and ortho ring hydrogens (and the nitro group in the case of o-nitrostyrene) are responsible for the deviation from planarity.

The trends of the curves for meta and para isomers are almost coincident, showing energy minima for θ = 45°, γ = 0°. Energy differences between planar and twisted (θ = 45 or 135°) conformations are about 1.0 kcal mol^{-1}. The minimum energy conformations for o-nitrostyrene are found for θ = 60°, γ = 10°, and θ = 130°, γ = 10°, respectively. Highly unstable conformations are predicted in the θ = 150–180° region, while at θ = 0 and 90° the destabilization energy with respect to the minimum is a few kilocalories (2.5–3.0 kcal mol^{-1}).

The curves in Figure 3 refer to neutral molecules, but the same calculations for the corresponding ions lead to curves of the same shape, shifted along the energy axis.

(*b*) *Uv Spectra and Dipole Moments.* Experimental and calculated transition energies and oscillator strengths for neutral molecules in the minimum energy conformations are collected in Table II, where experimental and calculated spectral data for the anion radicals are also shown. Absorption curves in the visible region for anion radicals, before and after air exposure, are shown in Figure 4. Di-

TABLE II: Electronic Transition Energies and Oscillator Strengths of Neutral Molecules and Anion Radicals

	PPP method[b]		CNDO-CI method[b]		Experimental[c]	
Isomer[a]	*E*, eV	*f*	*E*, eV	*f*	*E*, eV	*f*
Para	4.452	0.04	4.465	0.01		
	4.479	0.48	4.555	0.59	4.342	0.32
			5.560	0.07		
	5.927	0.42	5.667	0.09	5.820	0.22
	6.115	0.13	5.105	0.00[d]		
	6.193	0.33	6.291	0.12	6.269	0.52
	6.550	0.66	6.356	0.01		
	6.904	0.12	6.435	0.63		
Para′	1.999	0.02				
	2.056	0.16			2.250	
	3.292	0.02				
	4.023	0.24				
	4.255	0.03				
	4.430	0.12				
Meta	4.317	0.07	4.228	0.05	4.031	0.05
	4.735	0.06	4.963	0.13	4.861	0.34
	5.567	1.17	5.329	0.80	5.264	2.10
			5.399	0.08		
	6.086	0.17	6.077	0.06		
	6.303	0.34	6.267	0.10	6.440	0.51
	6.610	0.11	6.424	0.03		
	6.634	0.21	6.498	0.05		
Meta′	1.698	0.01			(2.083)	
	2.336	0.13			2.604	
	3.706	0.00[d]				
	3.939	0.03				
	4.413	0.05				
	4.553	0.10				
Ortho	4.381	0.11	4.312	0.08	4.101	0.07
	4.737	0.14	4.855	0.10	4.909	0.22
	5.396	0.07				
	6.007	0.78	5.260	0.28	5.398	0.57
			5.471	0.00[d]		
	6.157	0.15	5.646	0.12		
			6.021	0.01		
			6.121	0.10		
	6.589	0.67	6.347	0.16	6.490	0.41
	6.805	0.11	6.439	0.05		
Ortho′	1.939	0.01			(2.066)	
	2.392	0.13			2.637	
	3.431	0.00[d]				
	4.168	0.04				
	4.353	0.03				
	4.451	0.05				
	4.604	0.09				

[a] Anion radicals are identified by the prime. [b] In the minimum energy conformation (para and meta: $\theta = 45°$; ortho: $\theta = 60°$, $\gamma = 10°$). [c] In *n*-pentane (neutral molecules) and ACN (anion radicals). [d] 0.00 represents a value $<10^{-2}$.

pole moments calculated by the SCF STO-3G method for the ground state and by PPP method for ground and excited states involved in transitions are reported in Table III, together with experimental values.

(c) *Solvent Effect on Absorption Spectra.* Theoretical studies of the effect of solvent-solute interaction on electronic spectra have been undertaken by several authors (see, for example, McRae[25] and Longuet-Higgins and Pople[26]) by applying the perturbation theory, and an expression for the frequency shift of almost general validity has been obtained.

In order to analyze our experimental results we used McRae's approximate formula (*cf.* eq 17 in the original paper)

TABLE III: Ground-State Dipole Moments (Total and π Components), McRae's Constant *C* and Excited-State Dipole Moments (π Components)

Isomer	$\mu_{g,exptl}$, D	$\mu_{g,ab\ initio}$, D	$\mu_{g,PPP}$, D[a]
	Ground State		
Para	4.095	4.500	6.288 (6.243)
Meta	3.937	4.334	5.911 (5.990)
Ortho	3.443	4.002	5.574 (5.759)

Isomer	*C*, cm^{-1} [b]	$\mu_{e,McRae}$, D[c]	$\mu_{e,PPP}$, D[a]
	Excited States		
Para (λ 300 nm)	−2668	8.24	4.19 (3.96)
Meta (λ 310 nm)	−1682	6.65	5.74 (5.17)
(λ 240 nm)	−2864	8.56	8.39 (8.65)
Ortho (λ 310 nm)	−1508	6.23	8.21 (8.54)
(λ 230 nm)	−4010	10.85	11.49 (14.63)

[a] π-Electron dipole moments calculated as an average on different conformations (values in parentheses refer to the minimum energy conformations). [b] See text and eq 17 in McRae's paper.[25] [c] $\mu_e = \mu_g - 9.9315 \times 10^{-6} a^3 C/\mu_g$ (a in Å, C in cm^{-1}, and μ in D).

$$\nu = \nu_0 + (AL_0 + B')\frac{n_D^2 - 1}{2n_D^2 + 2} + C\frac{D - 1}{D + 2} - \frac{n_D^2 - 1}{n_D^2 + 2} \quad (4)$$

whose applicability was proved by McRae,[25] Robertson,[27] and Kubota.[28] D is the static dielectric constant of the solvent, n_D is the solvent refractive index at the frequency of the sodium D line, L_0 is the *weighted mean wavelength* at zero frequency, A, B', and C are constants characteristic of the solute, and ν_0 represents the solute frequency extrapolated in the vacuum ($n = D = 1$). Figure 2 illustrates the least-square fit of this equation on the experimental results. All points fit a full straight line with a root mean deviation of about 150 cm^{-1}, which is of the same order of magnitude as the experimental error in the determination of band frequency in solution spectra. The values of C in the McRae equation (4) were optimized by a least-squares fitting on the experimental data (see Figure 2). Being $C = (2/hca^3)(\mu_g - \mu_e)\mu_g$, the excited-state dipole moments (μ_e) were obtained. Ground- and excited-state dipole moments were assumed parallel; Onsager's reaction radius a of the solute molecule was taken equal to 4.0 Å, as suggested by other authors.[25,28]

(d) *Esr Spectra.* Esr spectra of anion radicals obtained by controlled potential electrolytical reduction were measured in liquid ammonia, DMS, and ACN. Owing to the lack of symmetry, the esr spectrum of these molecules is due to hyperfine interactions of a nitrogen and seven nonequivalent protons, but some accidental equivalences may occur.

The straightforward process for obtaining hfs coupling constants was performed through a least-squares fitting procedure[29] and the spectra of the three isomers in each solvent were fully interpreted. As an example, the spectra obtained in liquid ammonia and by the simulation process with optimized constants are shown in Figure 5.

If the nitrogen splitting is unequivocally assigned, a more difficult task is the assignment of hfs coupling constants to ring and extra ring protons. An aid for a correct assignment comes from a combined use of theoretical predictions and previous assignments on related molecules. In this view esr spectra of nitrotoluenes and chloronitrobenzenes in the same solvent (ACN)[30] were taken into consideration to assign the hfs coupling constants to ring

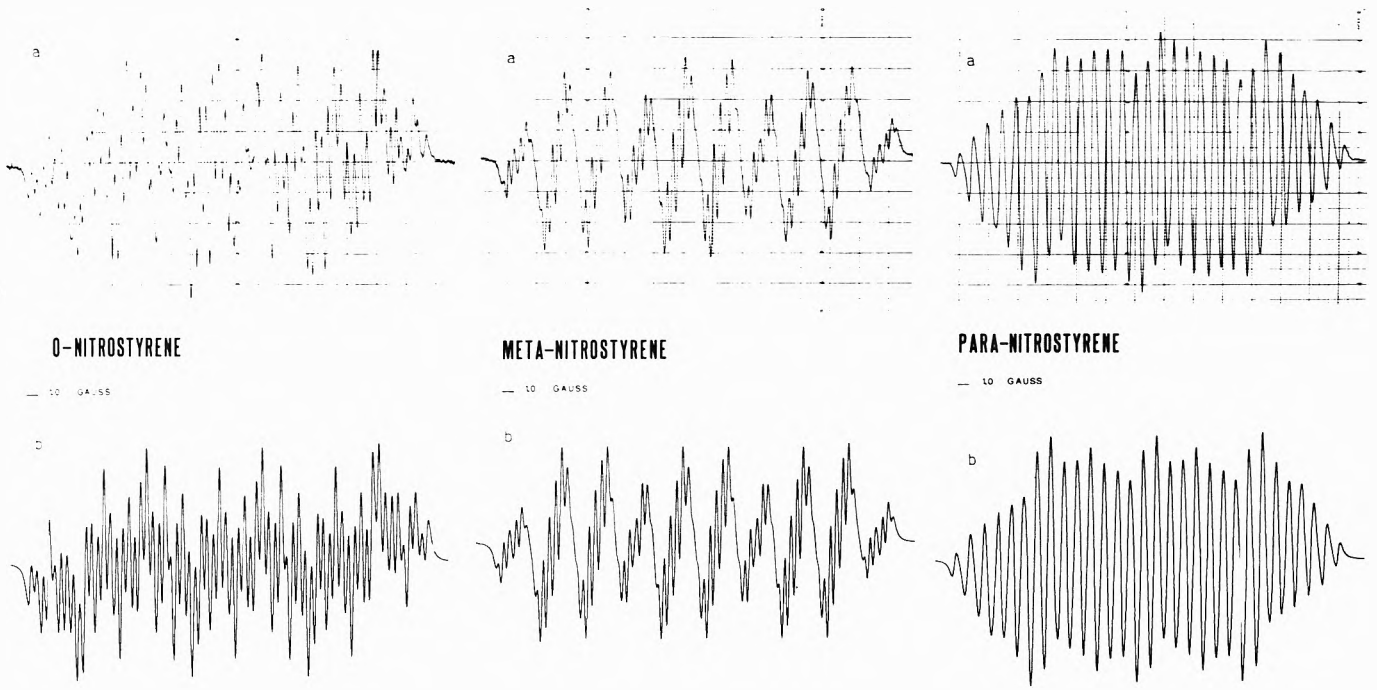

Figure 5. Esr spectra measured in liquid ammonia (a) and simulated (b).

protons: the situation is illustrated in Table IV. The coupling constants for vinyl protons can be predicted only on the basis of a comparison with calculations, and experimental and calculated results, by INDO method, for nitrostyrenes and nitrotoluenes are reported in Table V. The two series of values A and B for nitrostyrenes refer to calculations with the minimum energy conformation and with the averaging procedure previously described. For nitrotoluenes the conformations with one methyl proton in the plane of the ring and with one methyl proton in a plane perpendicular to the plane of the ring were considered, and the values for the different protons have been averaged. In Table VI spin densities and hfs coupling constants for protons of nitrostyrenes, calculated by the R method, are shown.

TABLE IV: Hyperfine Coupling Constants (G) for Nitrostyrenes and Related Compounds (X-C_6H_4-NO_2)

Isomer	Position	X: CH=CH_2			X: CH_3	X: Cl
		NH_3	DMS	ACN	ACN[30]	ACN[30]
Para	5	1.233	1.109	1.285	1.14	1.12
	6	3.289	3.180	3.226	3.31	3.42
	N	9.196	8.309	8.717	11.00	9.70
	α	1.018	1.315	1.200		
	β, β'	2.485	2.456	2.385	3.90[a]	
Meta	4	3.428	3.311	3.385	3.39	3.20
	5	3.986	3.972	3.900	3.84	4.07
	6	1.085	1.075	1.080	1.09	0.93
	8	3.428	3.311	3.385	3.39	3.20
	N	10.435	9.566	9.830	10.70	9.60
	α, β, β'	0.442	0.434	0.420	1.09[a]	
Ortho	5	1.075	1.199	1.135	1.04	1.13
	6	3.332	2.861	3.116	3.74	3.92
	7	3.119	2.830	3.053	3.32	3.30
	8	1.075	1.199	1.135	1.04	1.13
	N	10.027	9.224	9.591	11.30	9.95
	α	3.698	3.731	3.667		
	β	1.494	1.764	1.518	3.82[a]	
	β'	0.504	0.625	0.436		

[a] Methyl group protons.

Discussion

(*a*) *Conformation.* For meta and para isomers, owing to symmetry (para) or quasi symmetry (meta), there are two low-energy regions with four minima at about ±45 and ±135 for both molecules. In fact, the two curves are almost parallel. The energy barrier between the two minima in the same region is about 1.0 kcal mol^{-1}, while the energy barrier between the two regions is about 7 kcal mol^{-1}. The curve for the ortho isomer shows four minima at about 3.0 kcal mol^{-1} and two energy barriers of 2.5 kcal mol^{-1}. The region for θ = 150–210° corresponds to very high energy and is practically forbidden. According to these results in these molecules a large amplitude oscillation of the vinyl group around the bond to the ring is present. The barrier height seems too low to allow separation of geometrical isomers of the meta compound at room temperature.

(*b*) *Uv Spectra.* Uv spectra of neutral molecules recorded in *n*-pentane (Figure 6, solid line) are very similar in the case of ortho and meta isomers, for which four maxima of absorption can be localized in the region of 180–340 nm. The intensity of the first band, f = 0.07 and 0.05 for ortho and meta isomers, respectively, is low, in agreement with the values predicted by MO calculations. The second band is partly concealed by the third one, which is the strongest in this region, and again MO calculations predict the correct order of the intensities of these bands. A strong absorption starts at about 200 nm; several calculated transitions of different intensities are predicted in this region.

In the case of the para isomer the first transition of low intensity predicted by MO calculations cannot be identified in the spectrum. Probably this weak band is masked by the second one, which in the case of the para isomer is shifted toward higher wavelengths.

From Table II it appears that the agreement between the results of the Pariser and Parr method and the experimental data, both for neutral molecules and anion radicals, is very satisfactory. For the neutral molecules the

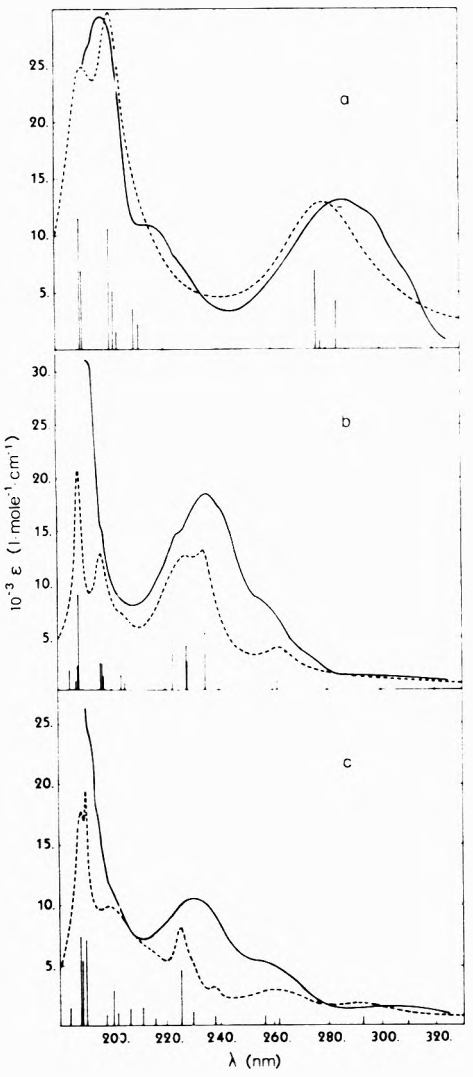

Figure 6. Stick diagrams of calculated (PPP method) transition energies (overlapping of molecular spectra in the most favored conformations) and corresponding absorption curves: experimental (—) (in *n*-pentane) and calculated (---) (see text): (a) para; (b) meta; (c) ortho.

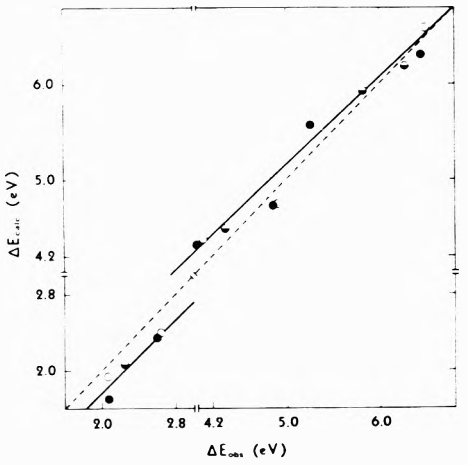

Figure 7. Regression lines (—) of theoretical *vs.* observed excitation energies for anion radicals (on the left) (r = 0.943, n = 5), and neutral molecules (on the right) (r = 0.964, n = 11). Dotted lines represent perfect agreement.

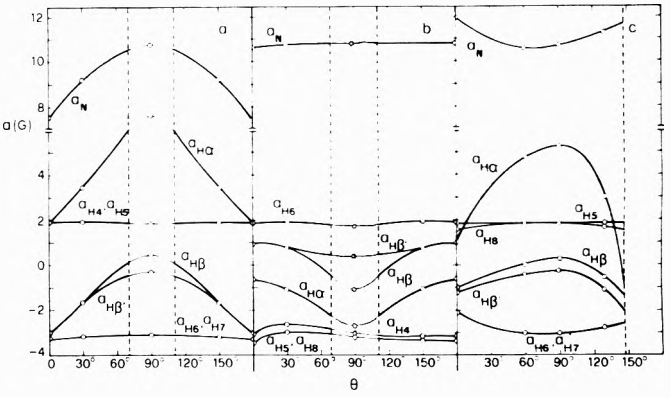

Figure 8. Hfs coupling constants for magnetic nuclei *vs.* conformation: (a) para; (b) meta; (c) ortho.

theoretical results have been supplemented by a CNDO-CI calculation and again agreement with PPP calculations and experiment was found, confirming the assignments.

PPP transition energies and probabilities have been also used to obtain calculated spectra according to the prescriptions given in the Methods of Calculation section. The results are shown in Figure 6. It is surprising and perhaps casual that not only the main features but even most of the slightest details of the experimental curves are well reproduced in our calculations.

The anion radicals show, as usual, absorption in the visible region. Again the trends of the spectra (Figure 4, solid lines) for ortho and meta isomers are similar: the maximum of absorption, at 465 and 477 nm, respectively, follows a shoulder at lower energy. In the case of the para isomer the maximum is shifted at lower energy and, as in the case of neutral molecule, may conceal a weak band, predicted by the calculation.

It is gratifying that PPP calculations with the same parametrization as for neutral molecules lead to a good prediction of positions and relative intensities of the first electronic bands in the visible region (Table II). Unfortunately, in the uv region it has not been possible to obtain spectral data owing to the presence of an unknown amount of unreduced parent molecule.

A general idea of the level of agreement, both for neutral molecules and for anion radicals, is apparent from Figure 7, which gives regression lines of theoretical excitation energies on observed ones, for the first few bands.

(c) *Dipole Moments.* Only qualitative agreement can be offered for the discussion of dipole moments. Assuming the σ part of the dipole moment unchanged upon excitation, our PPP calculations for the π part of the dipole moment correctly predict an increase upon excitation for *o*- and *m*-nitrostyrenes but fail to predict the same phenomenon in *p*-nitrostyrene.

It is gratifying that ground-state dipole moments, for which we could afford an *ab initio* calculation, are in fair agreement with experimental values: in particular the trend is correctly predicted. No experimental or theoretical data were collected for dipole moments of the corresponding ions.

(*d*) *Esr Spectra.* From Figure 5 it is clear that correct values for hfs coupling constants have been obtained from the three experimental spectra. From Tables V and VI we can see that the calculation of spin densities for minimum energy conformations and for the averaged conformations leads to the same suggestion for proton splitting constants assignments.

TABLE V: Calculated, by INDO Method, and Experimental (in ACN) Hfs Coupling Constants (G) of Nitrostyrenes and Nitrotoluenes (X-C_6H_4-NO_2)

		X: $CH=CH_2$ Theoret[a]				X: CH_3	
Isomer	Position	*A*	*B*	Exptl		Theoret[b]	Exptl
Para	4	1.740	1.75	1.285		1.666	1.14
	5	1.753	1.75	1.285			
	6	−3.217	−3.20	3.226		−3.144	3.31
	7	−3.217	−3.20	3.226			
	N[c]	8.795	9.06	8.717		10.205	11.00
	α	3.210	3.69	2.385			
	β	−1.692	−1.37	1.200	Me	4.854	3.90
	β'	−1.960	−1.50	2.385			
Meta	4	−2.722	−3.00	3.385		−3.171	3.39
	5	−3.005	−3.20	3.900		−3.102	3.84
	6	1.747	1.70	1.080		1.599	1.09
	8	−3.268	−3.20	3.385		−3.223	3.39
	N[c]	10.350	10.30	9.830		10.545	10.70
	α	−1.171	−1.46	0.420			
	β	0.602	0.44	0.420	Me	−2.261	1.09
	β'	0.523	0.58	0.420			
Ortho	5	1.683	1.60	1.135		1.674	1.04
	6	−3.075	−2.80	3.116		−3.165	3.74
	7	−3.038	−2.80	3.053		−3.171	3.32
	8	1.642	1.60	1.135		1.694	1.04
	N[c]	10.739	11.05	9.591		10.642	11.30
	α	4.511	3.71	3.667			
	β	−0.017	−0.33	0.436	Me	3.928	3.32
	β'	−0.612	−0.85	1.518			

[a] *A*, evaluated in the minimum energy conformation (para and meta: $\theta = 45°$; ortho: $\theta = 60°$, $\gamma = 10°$). *B*, average value over all the conformations (see text). [b] Average value over two conformations (see text). [c] $a_{N(NO_2)} = K_N \rho_{s_N} s_N$, where $K_N = 485.935$ has been obtained through a least-squares fitting ($\sigma = 2.01$, $r = 0.91$) of spin density of nitrogen on experimental hfs coupling constants for 16 nitro derivatives for which esr spectra were measured in the same solvent (ACN).

TABLE VI: Spin Densities and Hyperfine Coupling Constants for Protons Calculated by R Method and Experimental Values

		Theoretical[a]				
		A		*B*		
Isomer	Position	ρ_i	a_i, G[b]	ρ_i	a_i, G[c]	Exptl (in ACN)
Para	4	−0.029	0.752	−0.029	0.739	1.285
	5	−0.029	0.752	−0.029	0.739	1.285
	6	0.130	−3.394	0.130	−3.314	3.226
	7	0.124	−3.231	0.123	−3.128	3.226
	α	−0.016	0.430	−0.015	0.384	1.200
	β, β'	0.058	−1.526	0.057	−1.447	2.385
Meta	4	0.128	−3.328	0.129	−3.289	3.385
	5	0.157	−4.099	0.177	−4.512	3.900
	6	−0.036	0.942	−0.038	0.969	1.080
	8	0.138	−3.606	0.154	−3.926	3.385
	α	0.007	−0.171	0.006	−0.159	0.420
	β, β'	−0.012	0.314	−0.008	0.217	0.420
Ortho	5	−0.031	0.799	−0.029	0.752	1.135
	6	0.145	−3.790	0.137	−3.485	3.116
	7	0.122	−3.184	0.116	−2.952	3.053
	8	−0.029	0.751	−0.028	0.714	1.135
	α	−0.007	0.172	−0.010	0.242	0.436
	β	0.015	−0.394	0.024	−0.612	3.667
	β'	0.015	−0.394	0.012	−0.316	1.518

[a] *A* and *B* calculations were performed in the conformations specified in Table V. [b] $a_i^H = Q_{CH}{}^H \rho_{C_i}$ where $Q_{CH}{}^H = -26.10$ G. [c] $Q_{CH}{}^H = -25.49$ G.

When the theoretical results of Tables V and VI are compared, it appears that the general trends of assignments based on INDO or R calculations would be very similar. However, owing to the presence of the vinyl group out of the plane of the ring the use of the R method which incorporates the σ-π approximation is less reliable and we based our assignments for extra ring protons on INDO calculations. Of course there is no doubt on the assignments of the nitrogen coupling constants. For ring protons the assignment is based on the comparison with related compounds, that is chloronitrobenzenes and nitrotoluenes. The procedure is also supported by the results of our calculations for nitrotoluenes shown in Table V. We were left with the assignment of three doublets for the ortho isomer, a quartet for the meta isomer, and one doublet and one triplet for the para isomer. While, owing to degeneracy, in the meta isomer there is no problem for the assignments as proposed in Tables IV-VI, para and ortho extra

ring proton assignments are only a consequence of the results of the calculations and have no other support whatsoever. However, it is worthwhile mentioning that the values of hfs coupling constants for position 6 in o-chloronitrobenzene and o-nitrotoluene would suggest an inversion of assignments between the 6 and α positions for the corresponding nitrostyrene.

In the case of the para isomer a comparison with hfs values for *trans*-β-Br-*p*-nitrostyrene[1] is in favor of the prediction based on the R method of calculation. The $Q_{CH}{}^{H}$ values calculated on the basis of these assignments (see Table VI) are in the range of the values found for other molecules.[31]

In Figure 8 INDO hfs coupling constants for the three isomers, as function of the conformation, are shown. One can see that the variations of ring proton constants are very small in all cases, as expected. The meta isomer is the least sensitive to changes in conformation and the para isomer is the most sensitive one. However, the α proton in the ortho isomer shows the biggest variation, as can be expected, since both through space and through bond effects are large in this case.

These results suggest that an investigation of temperature influence on coupling constants might be helpful for the assignments of vinyl proton hfs coupling constants, since temperature changes might affect to a different extent the constants for protons in different positions. Of course, only a deuteration technique can give a conclusive answer.

Acknowledgments. The authors are indebted to Dr. W. J. Hehre, who made a copy of the Program GAUSSIAN 70 available, before submitting it to QCPE. They also thank Dr. V. Malatesta for a sample of o-nitrostyrene.

References and Notes

(1) A. Gamba, V. Malatesta, G. Morosi, and M. Simonetta, *J. Phys. Chem.*, **76**, 3960 (1972).
(2) A. Gamba, G. Morosi, V. Malatesta, C. Oliva, and M. Simonetta, *J. Phys. Chem.*, **77**, 2744 (1973).
(3) (a) A. Burawoy, J. P. Critchley, *Tetrahedron*, **5**, 340 (1959); (b) J. P. Durand, M. Davidson, M. Hellin, and F. Coussemant, *Bull. Chem. Soc. Chim. Fr.*, 43 (1966).
(4) C. Walling and K. B. Wolfstirn, *J. Amer. Chem. Soc.*, **69**, 852 (1947).
(5) R. H. Wiley and N. R. Smith, "Organic Syntheses," Coll. Vol. IV, Wiley, New York, N. Y., 1963, p 731.
(6) R. H. Wiley and R. N. Smith, *J. Amer. Chem. Soc.*, **72**, 5198 (1950).
(7) D. H. Geske and A. H. Maki, *J. Amer. Chem. Soc.*, **82**, 2671 (1960); **83**, 1852 (1961).
(8) E. R. Talaty and G. A. Russell, *J. Amer. Chem. Soc.*, **87**, 4867 (1965).
(9) I. Bernal and G. K. Fraenkel, *J. Amer. Chem. Soc.*, **86**, 1671 (1964).
(10) S. F. Nelsen, B. M. Trost, and D. H. Evans, *J. Amer. Chem. Soc.*, **89**, 3034 (1967).
(11) M. Ciali, Thesis, University of Milan, 1972.
(12) S. Wawzonek and M. E. Runner, *J. Electrochem. Soc.*, **99**, 457 (1952).
(13) D. H. Levy and R. J. Myers, *J. Chem. Phys.*, **41**, 1062 (1964).
(14) E. A. Guggenheim, *Trans. Faraday. Soc.*, **45**, 714 (1949).
(15) J. W. Smith, "Electric Dipole Moments," Butterworths, London, 1955.
(16) (a) J. A. Pople, D. L. Beveridge, and P. A. Dobosh, *J. Chem. Phys.*, **47**, 2026 (1967); (b) J. A. Pople, D. L. Beveridge, and P. A. Dobosh, *J. Amer. Chem. Soc.*, **90**, 4201 (1968).
(17) R. Pariser, *J. Chem. Phys.*, **24**, 250 (1956).
(18) J. Del Bene and H. H. Jaffé, *J. Chem. Phys.*, **48**, 1807 (1968).
(19) P. H. Rieger and G. K. Fraenkel, *J. Chem. Phys.*, **39**, 609 (1963).
(20) R. L. Ellis, G. Kuehnlenz, and H. H. Jaffé, *Theor. Chim. Acta*, **26**, 131 (1972).
(21) N. Mataga and K. Nishimoto, *Z. Phys. Chem. (Frankfurt am Main)*, **13**, 140 (1957).
(22) C. C. J. Roothaan, *Rev. Mod. Phys.*, **32**, 179 (1960).
(23) R. Zahradnik and P. Čársky, *J. Phys. Chem.*, **74**, 1235 (1970).
(24) W. J. Hehre, R. F. Stewart, and J. A. Pople, *J. Chem. Phys.*, **51**, 2657 (1969).
(25) E. G. McRae, *J. Phys. Chem.*, **61**, 562 (1957).
(26) H. C. Longuet-Higgins and J. A. Pople, *J. Chem. Phys.*, **27**, 192 (1957).
(27) W. W. Robertson, A. D. King, and O. E. Weigang, *J. Chem. Phys.*, **35**, 464 (1961).
(28) T. Kubota and M. Yamakawa, *Bull. Chem. Soc. Jap.*, **35**, 555 (1962); **40**, 1600 (1967); **41**, 1046 (1968).
(29) J. Heinzer, "Least-Squares Fitting of Isotropic Multiline Esr Spectra," Quantum Chemistry Program Exchange (QCPE) No. 197, Indiana University, Bloomington, Ind.
(30) T. Fujinaga, Y. Deguchi, and K. Umemoto, *Bull. Chem. Soc. Jap.*, **37**, 822 (1964).
(31) A. Carrington and A. D. McLachlan, "Introduction to Magnetic Resonance," Int. Ed., Harper, New York, N. Y., 1967, p 83.

Octahedral d^4, d^6 Ligand Field Spin–Orbit Energy Level Diagrams

E. König* and S. Kremer

Institute of Physical Chemistry II, University of Erlangen-Nurnberg, D-8520 Erlangen, West Germany *(Received March 12, 1973; Revised Manuscript Received August 27, 1973)*

The complete ligand field Coulomb-repulsion spin-orbit interaction matrices have been computed for the d^4, d^6 electron configurations in a field of octahedral symmetry. Correct energy level diagrams are presented.

Introduction

Complete octahedral ligand field spin–orbit interaction matrices for the d^4, d^6 electron configurations have been reported both by Schroeder[1] in the strong-field coupling scheme and by Dunn and Li[2] in the weak-field coupling scheme.[3-5] In the configurations d^2, c^8 and d^3, d^7, "complete" energy level diagrams have been constructed[6,7] on the basis of corresponding matrices and these have been

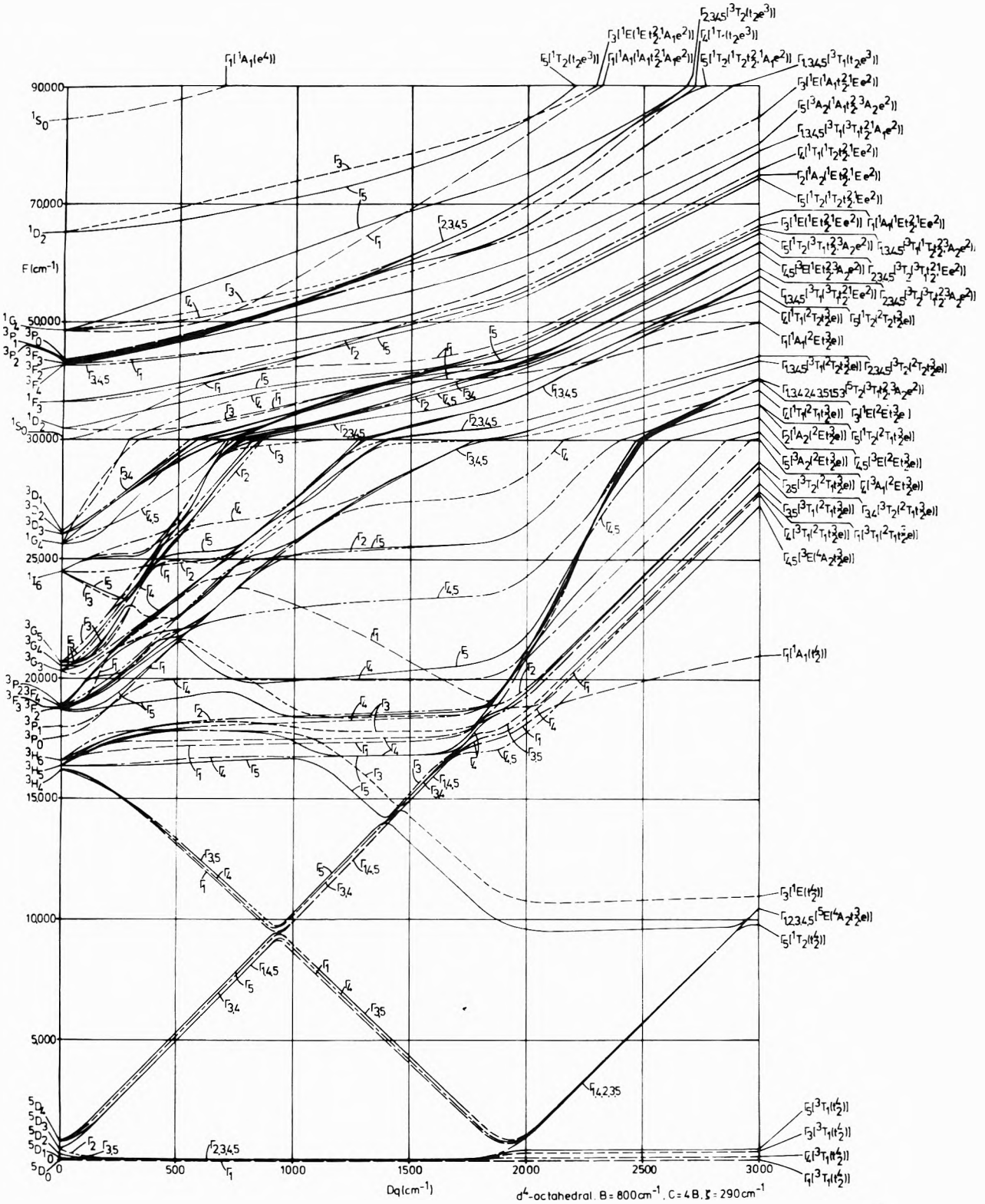

Figure 1. Energy level diagram for the d^4 configuration in an octahedral field including spin–orbit coupling $B = 800\ cm^{-1}$, $C = 4B$, $\zeta = 290\ cm^{-1}$. The designation of the terms by the strong-field configurational labels and their parent terms corresponds tc the largest contribution which is present at a Dq value assumed at the right end of the diagram. The labels have to be supplemented with g subscripts for O_h symmetry.

useful in the past to discuss the effect of the interactions and to make certain predictions of spectral transition energies. No such efforts seem to have been performed in the d^4, d^6 problem. In the present study, we have rederived all d^4, d^6 matrix elements ir. the strong-field and weak-field formalisms and, in view of their present and future utility, we present below complete energy level diagrams for these systems in octahedral symmetry.

Methods of Calculation and Results

Racah's method of irreducible tensor operators[8,9] extended to the coverage of problems in subgroups of SO(3)

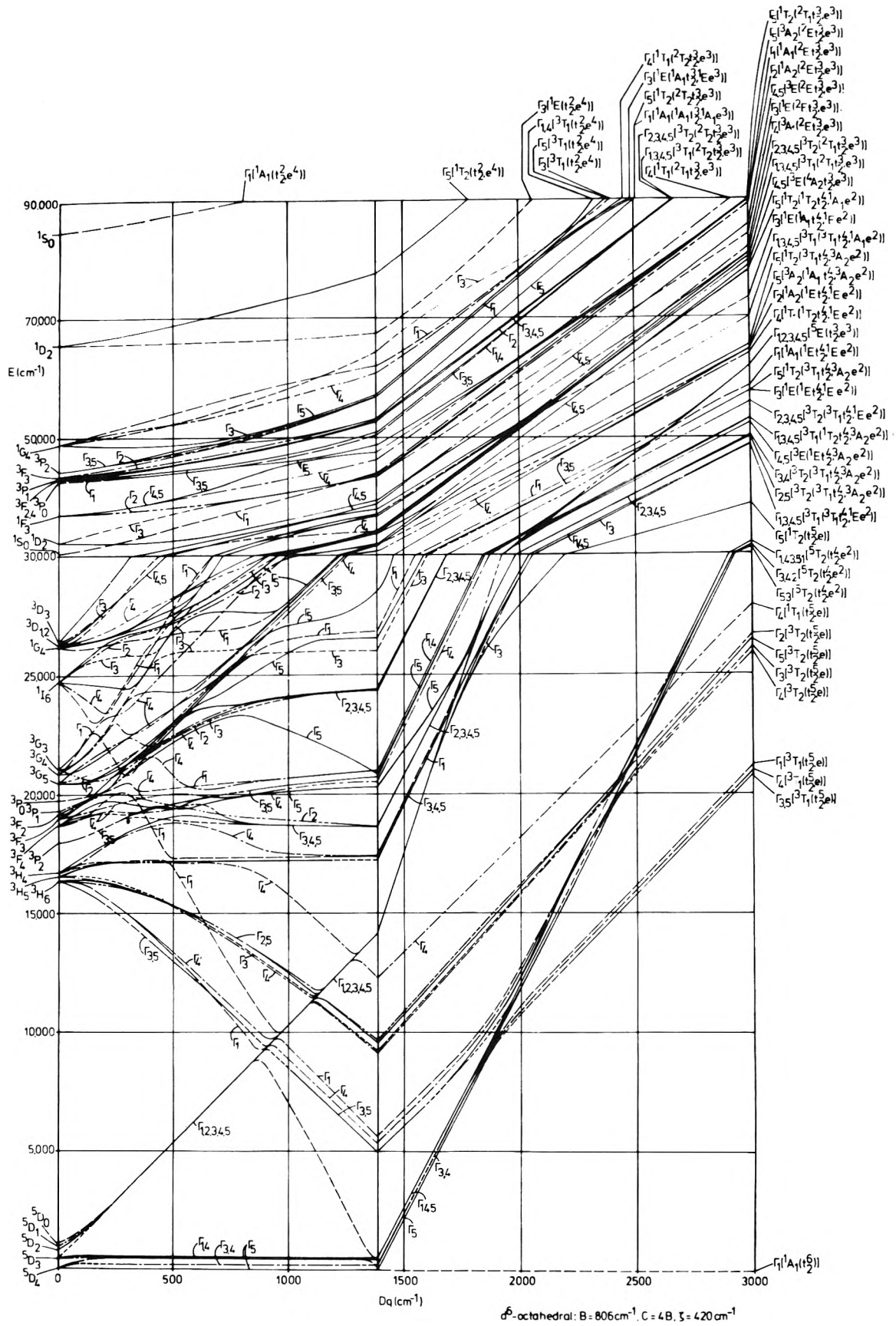

Figure 2. Energy level diagram for the d^6 configuration in an octahedral field including spin-orbit coupling: $B = 806\ cm^{-1}$, $C = 4B$, $\zeta = 420\ cm^{-1}$. Refer to caption of Figure 1 for further details.

has been applied throughout. Thus, in the weak-field coupling scheme, matrix elements of the spin-orbit interaction may be written as

$$\langle vSLJ\Gamma\gamma a|\sum_i \xi(r_i)\mathbf{s}_i\cdot\mathbf{l}_i|v'S'L'J'\Gamma'\gamma'a'\rangle = (-1)^{J+L+S'}(30)^{1/2} \begin{Bmatrix} LL'1 \\ S'SJ \end{Bmatrix} \langle vSL\|\mathbf{V}^{(11)}\|v'S'L'\rangle\delta(J,J')\delta(\Gamma,\Gamma')\delta(\gamma,\gamma')\delta(a,a')\zeta_{nd} \quad (1)$$

In eq 1, the expression in braces is a standard $6j$ symbol, $\langle vSL\|\mathbf{V}^{(11)}\|v'S'L'\rangle$ is a reduced matrix element of the double tensor operator $\mathbf{V}^{(11)}$ of Racah, and ζ_{nd} is the spin-orbit coupling parameter.

Matrix elements of the octahedral ligand field potential may be expressed according to

$$\langle vSLJ\Gamma\gamma a|V_{oct}|v'S'L'J'\Gamma'\gamma'a'\rangle = (-1)^{S+L'}3(70)^{1/2} \times [(2J+1)(2J'+1)]^{1/2} \begin{Bmatrix} JJ'4 \\ L'LS \end{Bmatrix} \langle vSL\|\mathbf{U}^{(4)}\|v'S'L'\rangle \times \sum_{MM'}(-1)^M\langle J\Gamma\gamma a|JM\rangle \left\{ \begin{pmatrix} J4J' \\ -M0M' \end{pmatrix} + \left(\frac{5}{14}\right)^{1/2} \times \left[\begin{pmatrix} J4J' \\ -M4M' \end{pmatrix} + \begin{pmatrix} J4J' \\ -M-4M' \end{pmatrix} \right] \right\} \langle J'M'|J'\Gamma'\gamma'a'\rangle \times \delta(\Gamma,\Gamma')\delta(\gamma,\gamma')\delta(S,S')Dq \quad (2)$$

In eq 2, $\langle JM|J\Gamma\gamma a\rangle$ are expansion coefficients defined by the reduction $D^J \rightarrow \Sigma a\Gamma$, γ being a component of representation Γ and a the multiplicity index.[10] In addition, $\langle vSL\|\mathbf{U}^{(4)}\|v'S'L'\rangle$ is a reduced matrix element of the unit tensor operator $\mathbf{U}^{(4)}$ of Racah and Dq is the octahedral splitting parameter of the ligand field.

Finally, matrix elements of the Coulomb interelectronic repulsion are determined by

$$\langle vSLJ\Gamma\gamma a|\sum_{i>j}\frac{e^2}{\mathbf{r}_{ij}}|v'S'L'J'\Gamma'\gamma'a'\rangle = \langle vSL\|\sum_{i>j}\frac{e^2}{\mathbf{r}_{ij}}\|v'S'L'\rangle \times \delta(J,J')\delta(\Gamma,\Gamma')\delta(\gamma,\gamma')\delta(a,a') \quad (3)$$

where the reduced matrix elements $\langle vSL\|\Sigma_{i>j}(e^2/\mathbf{r}_{ij})\|v'S'L'\rangle$ may be expressed in terms of the $\langle l\|\mathbf{C}^{(k)}\|l\rangle$ and the $F^k(nl,nl)$. Here, $\mathbf{C}^{(k)}$ are the rationalized spherical harmonic tensor operators and the F^k may be converted, for d electrons, into the Racah parameters A, B, C.

The reduced matrix elements appearing in eq 1-3 may be further reduced to coefficients of fractional parentage and other easily calculable numerical quantities like $3j$ and $6j$ symbols. Therefore, and in distinction to almost all previous treatments, all matrix elements have been completely computer generated. This procedure provides the *high degree of reliability hitherto not achieved in ligand-field calculations.* An analogous approach has been employed in the strong-field coupling scheme. Both treatments produce, upon numerical substitution, identical results, and these agree with results which were computed on the basis of the published (but corrected) matrices.[1-5]

In Figures 1 and 2 we present the complete energy level diagrams for the d^4 and d^6 electron configurations, respectively, subject to a ligand field of octahedral symmetry. The parameter values chosen for B, C, and ζ are approximately suitable for hexahydrated complex ions.[11] Since the energies are plotted *vs.* Dq, predictions for complex ions with ligands different from H_2O are possible in most cases.[12]

Hopefully, these diagrams will be useful for the spectroscopist in the same way as the corresponding diagrams in the more common d electron configurations.[6,7]

Acknowledgments. The authors appreciate financial support by the Deutsche Forschungsgemeinschaft, the Fonds der Chemischen Industrie, and the Stiftung Volkswagenwerk.

References and Notes

(1) K. A. Schroeder, *J. Chem. Phys.*, **37**, 2553 (1962).
(2) T. M. Dunn and Wai-Kee Li, *J. Chem. Phys.*, **47**, 3783 (1967).
(3) Observe that there are numerous errors in the original list of weak-field matrix elements.[4,5] An additional error has been discovered in Table IV of ref 2. It should read

$$\langle d^4,{}^4I_6|H'|d^4,{}^2G_4\rangle = 20(22)^{1/2}/11Dq$$

(4) E. R. Krausz, *J. Chem. Phys.*, **53**, 2131 (1970).
(5) T. M. Dunn and Wai-Kee Li, *J. Chem. Phys.*, **53**, 2132 (1970).
(6) A. D. Liehr and C. J. Ballhausen, *Ann. Phys.*, **6**, 134 (1959).
(7) A. D. Liehr, *J. Phys. Chem.*, **67**, 1314 (1963).
(8) B. R. Judd, "Operator Techniques in Atomic Spectroscopy," McGraw-Hill, New York, N. Y., 1963.
(9) B. G. Wybourne, "Spectroscopic Properties of Rare Earths," Interscience, New York, N. Y., 1965.
(10) E. Konig and S. Kremer, *Theor. Chim. Acta*, in press.
(11) A least-squares fit of the emission spectra of Cr^{2+} and Mn^{3+} ions gave B = 899 cm^{-1}, C = 3117 cm^{-1}, and B = 1082 cm^{-1}, C = 3916 cm^{-1}, respectively. The nephelauxetic ratio in $M(H_2O)_6^{n+}$ ions is $\beta \sim 0.88$ if $n = 2$ and $\beta \sim 0.75$ if $n = 3$. The splitting of the free ion ^5D ground term yields ζ = 228 cm^{-1} for Cr^{2+} and ζ = 348 cm^{-1} for Mn^{3+}. The values chosen are approximate averages of these data. Similarly, a least-squares fit of the emission spectrum of the Fe^{2+} ion produces B = 916 cm^{-1}, C = 3867 cm^{-1}. There are no data available for the ion Co^{3+}. The splitting of the ^5D ground term of Fe^{2+} gives ζ = 416 cm^{-1}. The parameter values were chosen as above.
(12) The designation of terms in Figures 1 and 2 does by no means imply pure configurational states. Indeed, some mixing by CI and spin-orbit interaction is often present and the notatior corresponds to the largest contribution at Dq = 3000 cm^{-1}. For the purpose of illustration, we give below the percentage content of that eigenfunction which corresponds to the term designation given for the octahedral d^6 configuration in Figure 2. **45 ± 2.5%:** $2\Gamma_5[{}^1T_2(t_2{}^4({}^3T_1)e^2({}^3A_2))]$, $\Gamma_2[{}^1E(t_2{}^3({}^2E)e^3)]$, $\Gamma_1[{}^1A_1(t_2{}^4({}^1A_1)e^2({}^1A_1))]$; **50 ± 2.5%:** Γ_2, Γ_5, $\Gamma_4[{}^3T_1(t_2{}^4({}^3T_1)e^2({}^1E))]$, $\Gamma_2[{}^1E(t_2{}^4({}^1A_1)e^2({}^1E))]$, $\Gamma_2[{}^1E(t_2{}^3({}^2E)e^3)]$; **55 ± 2.5%:** $\Gamma_1[{}^3T_1(t_2{}^4({}^3T_1)e^2({}^1E))]$; **60 ± 2.5%:** Γ_2, Γ_4, Γ_5, $\Gamma_1[{}^3T_1(t_2{}^4({}^1T_2)e^2({}^3A_2))]$, $\Gamma_2[{}^1E(t_2{}^4({}^1E)e^2({}^1E))]$, $\Gamma_5[{}^1T_2(t_2{}^3({}^2T_2)e^3)]$; **65 ± 2.5%:** $\Gamma_5[{}^1T_2(t_2{}^4({}^1T_2)e^2({}^1A_1))]$. The listing is always in the order occurring from lower to higher energies. No listing implies 70% or greater content.

Gas–Liquid Chromatography on Polymers. I. Polyisobutylene–Hydrocarbons at 25°

Yu-Kwan Leung and B. E. Eichinger*

Department of Chemistry, University of Washington, Seattle, Washington 98195 *(Received April 9, 1973; Revised Manuscript Received July 16, 1973)*

The Flory–Huggins interaction parameters at infinite dilution of C_5–C_9 *n*-alkanes, benzene, and cyclohexane in polyisobutylene have been determined by gas–liquid chromatography at 25°. Gas-phase mixed second virial coefficients for hydrocarbon and nitrogen carrier gas are obtained as a bonus. Our data for the polymer–solvent interaction are compared with the previous results of Newman and Prausnitz and of Hammers and DeLigny. The Flory–Huggins mixing parameter χ decreases smoothly with increasing chain length of *n*-alkane. Data are analyzed in terms of the solution theory of Flory, Orwoll, and Vrij; the neighbor interaction parameters X_{12} agree closely with those obtained from calorimetric enthalpies of mixing. Values of χ in the Henry's law region obtained by extrapolation of static sorption results and by glc are compared, and discrepancies between the two values that are apparent for the globular solvent molecules are discussed.

Introduction

Several different techniques are utilized to study polymer solution thermodynamics over the whole range of composition. The technique to be chosen depends upon the magnitude of the solvent activity; as the volume fraction of solvent decreases from 1 to 0, the methods of conventional osmometry, high-pressure osmometry, vapor sorption, and finally gas–liquid chromatography (glc) are successively used. Measurements of thermodynamic variables by the first three techniques are on equilibrium systems, whereas equilibrium data must be extracted from the dynamic glc measurements. This is by no means a straightforward process, as has been amply demonstrated in the work of Cruickshank, *et al.*[1,2] Great care must be exercised to ensure that dynamic influences are eliminated. The theory developed by Cruickshank, *et al.*, can be used with confidence in this regard.

Recently glc experiments on polyisobutylene,[3,4] poly(dimethyl siloxane),[5] polystyrene,[3,6] polyethylene,[6] and natural rubber[7] have been reported. The convenience of the method has doubtless encouraged its development for the study of thermodynamic properties of solvent–polymer interactions in the highly concentrated region. It has been anticipated[8-10] that investigation of the Henry's law region of polymer solutions would yield valuable information concerning the structure of the bulk polymer. This objective can be had either by means of glc alone, as Guillet has done, or a comparison can be made between the limiting activity coefficients obtained directly by glc and by extrapolation of data from concentration regions accessible by conventional methods. In this work we take the latter approach, and it proves to be interesting.

Experimental Section

Apparatus. Our glc instrument is constructed similarly to that described by Cruickshank, *et al.*[1] Of particular importance is the need for accurate temperature control, pressure measurements, and flow measurement. Our apparatus is equipped with a hydrogen-flame ionization detector; a schematic diagram is shown in Figure 1. Column temperature is controlled by a water bath using a microset thermoregulator with a sensitivity of ±0.01° (Precision Scientific Co.). Nitrogen carrier gas pressures ranging up to 130 psig are controlled upstream by a balanced pressure regulator (Veriflo PN 41200649) and downstream by a back pressure regulator (Veriflo PN 41810118). A calibrated gauge which can be read to 0.05 psi and a mercury manometer which is read against a calibrated scale with precision of ±0.2 mm are used to indicate the column inlet pressure and the pressure drop across the column, respectively. The ratio of inlet to outlet pressure can thus be controlled and measured with at least 0.4% accuracy. Flow rates, typically in the range of 13 ~ 20 ml/min, are measured at room temperature by a soap-film flowmeter[1] which is installed immediately after the inlet pressure regulator. Flow is consistently stable and can be determined with an accuracy of ±0.5%.

Instead of using the conventional microsyringe injection method, we employ a multi-port gas-sampling valve (Loenco L-206-6) with a 7 in., $^3/_{32}$ in. i.d. sample loop. Liquid is injected through a silicone rubber septum into an evacuated reservoir. A differential pressure gauge (Wallace & Tiernan FA 145) which can be read to 0.2 mm is used to indicate the solvent vapor pressure in the reservoir.

The whole system is constructed of $^3/_{32}$ in. i.d. stainless steel tubing connected with Swagelok fittings. Leakage is checked by pressurizing the system to 10 atm, and observing the decline of column pressure for a 24-hr period. No measurements are made unless this test shows negligible leakage.

Materials. Polyisobutylene (Enjay Vistanex LMMS) was fractionated from a 1% solution in benzene at 30° using methanol as the precipitant. The first fraction was discarded and the second fraction of estimated viscosity average molecular weight 4×10^4 was used for all subsequent measurements. Chromatoquality Reagent (Matheson Coleman and Bell) *n*-pentane, *n*-heptane, *n*-octane, *n*-nonane, and benzene or Spectroquality Reagent (MCB) *n*-hexane and cyclohexane were used without further purification.

Column Preparation. Polyisobutylene was coated on Chromosorb W (Supelco; mesh size 45/60) by solvent evaporation. A solution of the polymer in benzene was mixed with the solid support and solvent was removed by slow evaporation in a rotary evaporator (Büchi). The par-

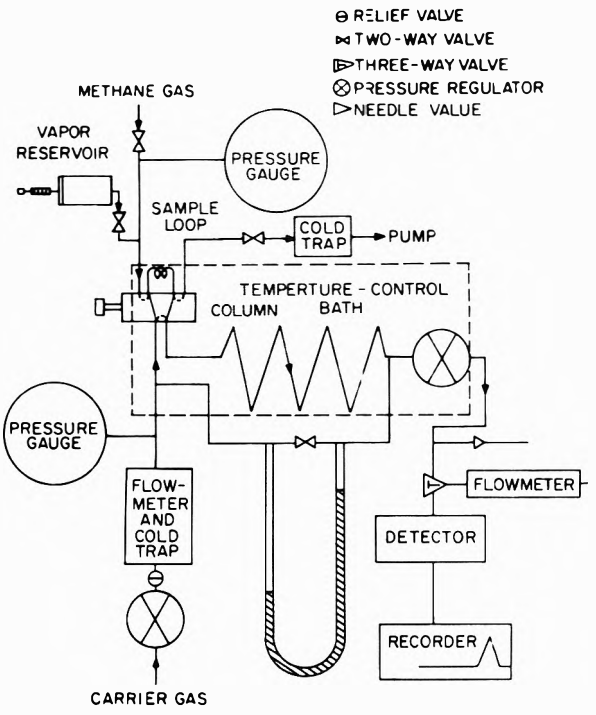

Figure 1. Gas-liquid chromatographic apparatus.

ticles were then dried under vacuum at 160° to constant weight. The weight percentage of coating was determined in duplicate by 72 hr of extraction with refluxing benzene in a Soxhlet extractor. The value determined agrees with that calculated from weighings. The coated chromosorb was then placed in a benzene-washed 8.5 ft long, 3/32 in. i.d. stainless steel tube with the aid of a mechanical vibrator. The ends of the tube were loosely plugged with steel wool. The amount of polyisobutylene was found to be 0.245 ± 0.001 g (9.45% by weight).

Measurement Procedures. Methane was injected to determine the gas hold-up (dead) volume. We found no difference between retention times for methane and *n*-hexane on uncoated columns. The retention volume was taken to be the difference between the elution volume of the solvent and the dead volume. This was converted[2] to the net retention volume by multiplication with J_3[2] (see below). The retention time at peak maximum was independent of sample size over the range 0.02-0.5 μmol but increased steadily with the sample size beyond this range. Samples of about 0.05 μmol were used for all measurements, which we consider to be equivalent to infinite dilution. Some peak asymmetry was always observed, and is commented on in the next section. For a series of measurements inlet pressures in the range 1.5-10 atm were used, but the pressure drop across the column did not exceed 1 atm in any case. For each solvent, measurements were made at three or four different column pressures. Retention volumes for at least three runs at a given pressure were averaged. Also, measurements of retention volumes of benzene and cyclohexane at varying flow rates (7-35 ml/min) and at fixed mean pressure (2.10 ± 0.05 atm) have been performed.

Results

A detailed and rigorous study of the dynamics of the gas-liquid chromatograph has been made by Everett[2] and more recently by Cruickshank, Windsor, and Young.[1] The partition coefficient k, which is defined as the ratio of solvent (component 1) concentrations in liquid and gaseous phases, is pressure dependent as well as concentration dependent. (Our indexing is not that conventionally used in chromatography. Rather it corresponds to that usual for polymer-solvent systems.) The limiting value of the partition coefficient is given[2] by

$$k = \lim_{v_1 \to 0}(C_1^l/C_1^g) = (1/\gamma_1^{\infty}{}_v p_1^0 V_1^0)[RT + B_{33}p] \quad (1)$$

A glossary of symbols will be found at the end of the paper. From their careful analysis of the thermodynamics and hydrodynamics of glc, Cruickshank, *et al.*,[1] advocate data analysis by means of the following equation

$$\ln V_N = \ln V_N^0 + \beta p_0 J_3^4 \quad (2)$$

where

$$V_N^0 = k_0 V^L \quad (3)$$

$$\beta = (2B_{13} - V_1^{\infty})/RT \quad (4)$$

and

$$J_n^m = \frac{n}{m}\left\{\frac{(p_i/p_o)^m - 1}{(p_i/p_o)^n - 1}\right\}$$

Equation 4 has been obtained by neglecting the solubility of carrier gas in the stationary phase.

If the stationary phase consists of linear chain molecules, the above glc equations may be combined with the Flory-Huggins equation[11] to give

$$\ln \gamma_1^{\infty}{}_v = (1 - 1/r) + \chi_v = \ln (RT/kV_1^0 p_1^0) - (B_{11} - V_1^0)p_1^0/RT + \beta p \quad (5)$$

where p is the carrier gas pressure; the partial pressure of solvent vapor has been previously extrapolated to zero concurrent with the limit in eq 1. The χ_v defined is dependent on carrier gas pressure. In the limit of zero pressure one obtains

$$\chi_v = \ln (RTV^L/V_1^0 p_1^0 V_N^0) - (B_{11} - V_1^0)p_1^0/RT - 1 + 1/r \quad (6)$$

Here χ_v is the interaction parameter which appears in the Flory-Huggins equation when concentrations are expressed as volume fractions, as indicated by the subscript. The magnitude of χ_v is usually on the order of 0.5-1.5; the contribution from the second term in eq 6 ranges from 10^{-2} to 10^{-3} and is significant only for highly volatile solvents; $1/r$ is *ca.* 10^{-3} for our PIB sample.

Conversion of χ from volume fractions (v) to segment fractions (s) is required for application of the Flory, Orwoll, and Vrij theory. At infinite dilution of solvent this is accomplished by

$$\chi_s - \chi_v = \ln (\tilde{v}_1/\tilde{v}_2) \quad (7)$$

(We have neglected a small, molecular weight dependent term arising from $1/r$.) The segment-fraction-based activity coefficient may be put in the form of eq 5 to give a result identical with that obtained by Patterson *et al.*[12]

The retention volume data were computer analyzed according to eq 2 to obtain V_N^0 and β by least-squares fitting. The values of B_{11} used were calculated from the McGlashan and Potter reduced equation[13] using critical constants from the A.P.I. Project 44 tables.[14] The vapor pressures p_1^0 of pure solvents were obtained from the Antoine equation with constants recommended in the A.P.I. tables. Cruickshank, Gainey, and Young[15] have estimated the error incurred in B_{13} by neglect of carrier gas dissolu-

tion for hydrocarbon–nitrogen systems to be +6 ± 6 cm^3. Since data required to estimate this term are not available for the present systems, we have not corrected our results for this effect. In calculating B_{13}, the partial molar volume $\bar{V}_1^\infty$ was estimated from $\bar{V}_1^\infty = V_1^0(1 + D\bar{v}_2/\bar{v}_1)$, which has been previously used in conjunction with the theory of Flory, Orwoll, and Vrij.[16] Here D is a constant denoting the magnitude of the excess volume of mixing. The volume changes on mixing PIB with several hydrocarbons have been investigated by Flory and coworkers.[17,18] The differences between partial molar volumes and molar volumes vary from −5 cm^3 mol^{-1} for *n*-pentane to −2.5 cm^3 mol^{-1} for *n*-nonane to +1.0 cm^3 mol^{-1} for benzene and hence are not negligible.

Our results for B_{13} and χ_s derived from the data by means of eq 4 and 6 are tabulated in Table I together with values from other sources (see below). The quoted uncertainties on χ_s and B_{13} were estimated by combining the standard deviation of the least-squares fit with estimated uncertainties for constant terms in eq 6 and 4, respectively.

Measurements of the flow rate dependence of the retention volumes of benzene and cyclohexane have also been made. Net retention volumes obtained by linear extrapolation to zero flow rate are in complete agreement with those derived by means of the previously described extrapolation method.

We have also investigated the flow rate dependence of the skewness of the elution peak (defined as the difference between relative effluent concentrations at the two inflection points).[19] Within experimental uncertainty, no consistent trend of skewness with flow rate was observed for benzene. Cruickshank, *et al.*,[20] have observed skewed elution profiles with benzene on glycerol, with relative skewness increasing with decreasing flow rate. It is interesting that we observe such a trend with cyclohexane, with which the skewness varies from 0.5 at 10 ml/min to 0.3 at 27 ml/min. That cyclohexane shows the largest deviation between the glc determined χ_s and vapor sorption χ_s may be related to this effect. However, a reasonable interpretation of such presumed peculiarities has not been obtained.

Other solvents were not investigated in detail in this respect, but all, methane included, exhibited skewness ranging from 0.3 to 0.8. Since this phenomenon is not predicted by chromatography theory, as pointed out by Cruickshank, *et al.*,[20] and since we observe it with all solvents, we believe it to be mainly instrumental in origin.

Our chromatograph, and that of Cruickshank,[1] differs from commercial instruments in that the dead volume is substantial owing to the presence of the back pressure regulator. A larger dead volume is expected to cause back mixing of the gas so as to skew the elution peak. Loss of peak symmetry is possibly the expense paid for accurate pressure control utilizing currently available instrumentation. Regardless, the fact that peak asymmetry is relatively constant from solvent to solvent gives us some confidence that results, with possible exception of data for cyclohexane, are not vitiated on this account.

Discussion

Second Virial Coefficients. The experimental mixed second virial coefficients calculated from the pressure dependence of the retention volume by means of eq 4 may be compared with those predicted from the principle of corresponding states[13] by inspection of Table I. Columns 4 and 5 contain entries calculated by use of the Hudson and McCoubrey[21] and geometric mean[13] combining rules, respectively. Column three of this table contains previous experimental results. As observed by others,[1,15,22] the experimental values of B_{13} lie between the values calculated from the alternative combining rules with exception of *n*-pentane, but are closer to those predicted by the Hudson and McCoubrey combining rule.

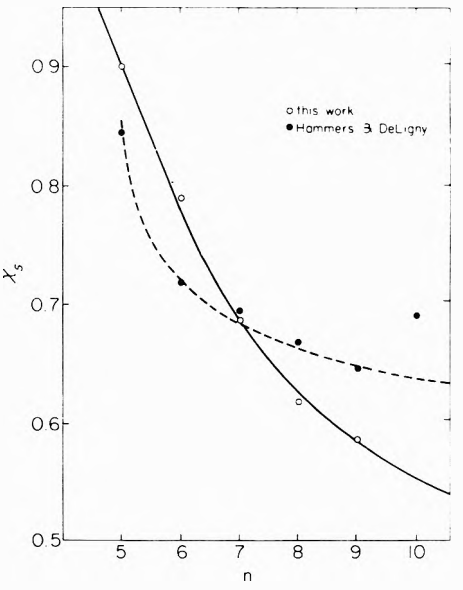

Figure 2. Flory–Huggins solution parameter χ_s for PIB with normal alkanes at 25° plotted against the number of carbons in the *n*-alkane.

Interaction Parameters. The interaction parameter χ_s was calculated from the net retention volume at zero pressure and concentration according to eq 6 and 7, and values obtained are given in Table I. Values of χ_s for *n*-alkane–polyisobutylene systems are plotted against the chain length n of the alkane in Figure 2. The interaction parameter decreases smoothly with increasing n. A similar smooth dependence on n has been reported by Young[23] with *n*-tetracosane and *n*-octadecane and by Tewari and Schreiber[7] with natural rubber as stationary phases.

Hammers and DeLigny[4] have reported glc investigations on the various hydrocarbons with PIB at temperatures above 40°. We have extrapolated their data to 25° and values of χ_s thus obtained are given in Table I and are plotted in Figure 2. Our data are in reasonably good agreement with those of Hammers and DeLigny and of Newman and Prausnitz for about half the solvents investigated, while significant differences, as large as 0.12 for χ_s for cyclohexane, are observed for the remainder.

Thermodynamic data obtained by static vapor sorption measurements for several polyisobutylene–solvent systems have been reported.[17,18] For *n*-pentane, benzene, and cyclohexane, data are available up to segment fractions of about 0.9, while for *n*-octane, measurements have been performed up to 0.5 segment fraction. Values of χ_s obtained by extrapolation of these results to infinite dilution of solvent are listed in column 9 of Table I. The extrapolated thermodynamic data agree with the glc results for PIB–*n*-pentane and PIB–*n*-octane. For benzene and cyclohexane, substantial differences between the two results are observed. We have repeated measurements on these systems many times, and all the separate measurements have yielded a consistent value of χ_s within stated accuracy. Since extrapolation of vapor sorption results on *n*-alkanes agrees with glc, it is not likely that there are systematic

TABLE I: Mixed Second Virial Coefficients and Interaction Parameters for Polyisobutylene–Hydrocarbon Systems

Solvent	$-B_{13}$, cm³ mol⁻¹ This work	$-B_{13}$, cm³ mol⁻¹ Other work	$-B_{13}$, cm³ mol⁻¹ Theory[a]	$-B_{13}$, cm³ mol⁻¹ Theory[b]	χ_s This work	χ_s Hammers and DeLigny[f]	χ_s Newman and Prausnitz[g]	χ_s Vapor sorption
n-Pentane	90 ± 10	103[c]	92	132	0.90 ± 0.02	0.85	0.87	0.88 ± 0.03[h]
n-Hexane	118 ± 10	112[c]	101	164	0.79 ± 0.02	0.72		
n-Heptane	142 ± 15	132 ± 9[d]	111	197	0.69 ± 0.02	0.69		
n-Octane	146 ± 15	143 ± 9[d]	117	229	0.63 ± 0.02	0.67		0.65 ± 0.03[i]
n-Nonane	160 ± 15		124	262	0.59 ± 0.03	0.64		
Benzene	126 ± 15	121,[e] 109[e]	111	146	0.99 ± 0.02	1.00	1.03	1.18 ± 0.03[h]
Cyclohexane	130 ± 15		109	159	0.67 ± 0.03	0.55	0.55	0.52 ± 0.03[h]

[a] Calculated using the Hudson and McCoubrey rule (ref 21). [b] Calculated using the geometric mean rule (ref 13). [c] Reference 1. [d] Reference 15, values at 35°. [e] Reference 22. [f] Reference 4, extrapolated from higher temperatures. [g] Reference 3. [h] Reference 18. [i] Reference 17, extrapolated from $\phi_2 < 0.5$.

TABLE II: Equation of State Data and Characteristic Parameters at 25°

	ρ, g cm⁻³	$\alpha \times 10^3$, deg⁻¹	γ, cal cc⁻¹ deg⁻¹	$\tilde{v}$	v_{sp}*, cm³ g⁻¹	P*, cal cm⁻³	T*, °K
PIB[a]	0.9169	0 555	0.272	1.1488	0.9493	107	7580
C_5H_{12}[b]	0.6213	1 610[c]	0.176[c]	1.3607	1.1828	97.1[c]	4158
C_6H_{14}[b]	0.6550	1 385	0.1945	1.3215	1.1554	101.2	4437
C_7H_{16}[b]	0.6793	1 253	0.205[c]	1.2973	1.1347	102.5[c]	4652
C_8H_{18}[b]	0.6983	1 159	0.212	1.2793	1.1194	103.5	4836
C_9H_{20}[b]	0.7139	1 090	0.218[c]	1.2659	1.1065	105.4[c]	4993
C_6H_6	0.8738[d]	1 223[d]	0.3017[f]	1.2917	0.8860	150.0	4709
C_6H_{12}	0.7739[e]	1.217[e]	0.2549[f]	1.2906	1.0012	126.6	4721

[a] Reference 17. [b] Reference 25. [c] Values obtained by extrapolation of data for higher homologs, *cf.* ref 17. [d] S. E. Wood and J. P. Brusie. *J. Amer. Chem. Soc.*, **65**, 1891 (1943). [e] S. E. Wood and J. A. Gray, *ibid.*, **74**, 3729 (1952). [f] G. A. Holder and E. Whalley, *Trans. Faraday Soc.*, **58**, 2095 (1962).

errors in the vapor sorption measurements. Furthermore, the fact that the difference between the χ_s values from vapor sorption and from glc is negative for cyclohexane and positive for benzene argues against systematic errors. That there is good agreement for the chain-like solvents, but not "spherical" solvents, suggests that these discrepancies arise from specific interactions, or perhaps solvent clustering, in solutions formed of linear polymers and spherical solvent molecules.

The cluster integral G_{11} for solvent molecules has been obtained by Zimm and Lundberg[24] in the form

$$G_{11}/\bar{v}_1 = -v_2(\partial\gamma_1/\partial a_1)_{T,P} - 1$$

where $\gamma_1 = a_1/v_1$. If we accept the vapor sorption and glc results as they stand, then χ_v (or γ_1) increases sharply as $a_1 \to 0$ for cyclohexane, and decreases for benzene mixtures. This implies $G_{11} > -1$ for cyclohexane, and $G_{11} < -1$ for benzene, both of course with PIB. This in turn, following the arguments of Zimm and Lundberg, means that benzene is "absorbed" on the PIB chain, whereas cyclohexane clusters in cavities, when either is present at very high dilutions.

Flory, Orwoll, and Vrij Theory. According to the Flory, Orwoll, and Vrij theory, the solution parameter χ_s can be expressed as follows

$$\chi_s = (1/RT\phi_2^2)\{P_1^*V_1^*\{3\tilde{T}_1 \ln[(\tilde{v}_1^{1/3}-1)/(\tilde{v}^{1/3}-1)] + (\tilde{v}_1^{-1}-\tilde{v}^{-1})\} + (V_1^*X_{12}/\tilde{v})\theta_2^2\} \quad (8)$$

where X_{12} is the interaction parameter denoting the energy change for the formation of contacts between species 1 and 2 in exchange for contacts between like species. In the glc region where $\phi_2 \to 1$, $\theta_2 \to 1$, and $\tilde{v} \to \tilde{v}_2$, rearrangement of eq 8 gives

$$X_{12} = RT(\tilde{v}_2/V_1^*)\chi_s - P_1^*\tilde{v}_2 \times \{3\tilde{T}_1 \ln[(\tilde{v}_1^{1/3}-1)/(\tilde{v}_2^{1/3}-1)] + (\tilde{v}_1^{-1}-\tilde{v}_2^{-1})\} \quad (9)$$

The contact interaction parameter X_{12} can be evaluated from the experimental χ_s values with use of characteristic parameters given in Table II. Values of X_{12} thus obtained are plotted against the reciprocal of the *n*-alkane chain length in Figure 3. The abscissa $1/n$ is chosen for the same reasons as those indicated by Flory and coworkers.[16] The magnitude of X_{12} for the series is small and positive as expected for mixtures of nonpolar molecules. The trend of X_{12} with $1/n$ indicates that the mixing of terminal groups of *n*-alkanes with PIB makes a larger contribution to neighbor interactions than does midchain mixing. Values of X_{12} for the *n*-alkanes as determined by glc are in remarkably close agreement with those obtained from calorimetric data.[17,26] This lends considerable support to Flory's solution theory, particularly because the X_{12}'s are obtained from opposite ends of the concentration scale. Unrealistic negative X_{12} values were reported by Ham-

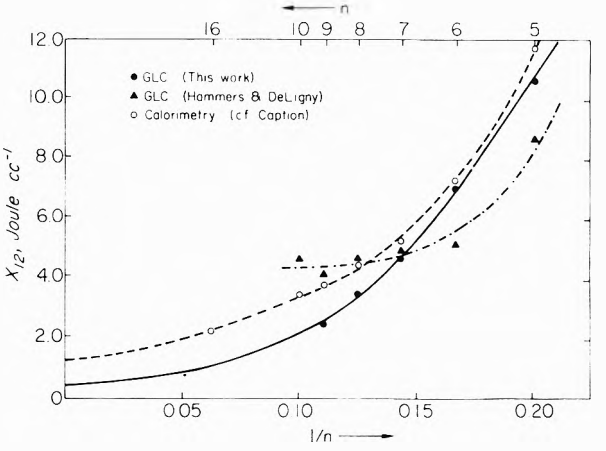

Figure 3. Contact interaction parameter X_{12} for *n*-alkane mixtures with PIB plotted against the reciprocal of the number of carbons *n*. The filled triangles have been calculated from glc data of ref 4. The open circles represent results reported by Flory and coworkers[17] from analysis of calorimetric data.

mers and DeLigny,[4,27] but re-evaluation of their data, extrapolated to 25°, using the characteristic constants specified above, reveals that positive X_{12} values are obtained. Their corrected contact interaction parameters are indicated in Figure 3. It will be noted from the figure that our results depart significantly from those of Hammers and DeLigny for short and long *n*-alkanes.

Conclusion

The Flory–Huggins mixing parameters χ_s obtained by glc agree closely with those derived by extrapolation of results from static vapor sorption and osmometry for the systems PIB–*n*-pentane and PIB–*n*-octane. Substantial discrepancies between the two are observed for the systems PIB–benzene and PIB–cyclohexane. It is not clear at this early stage whether this indicates specific interactions between solvent and polymer, including surface adsorption, or if there are large inaccuracies in the sorption data at low concentrations of solvent. As we noted above, and from consideration of the vapor sorption measurements, it does not seem likely that the latter possibility is cause for great concern. Instead, we are inclined to the view that specific interactions, or more general geometrical contraints on cavity formation, are operating in these highly concentrated solutions.

Since X_{12} values from enthalpies of mixing and from glc agree so closely for *n*-alkanes, we have further evidence for the remarkable accuracy of Flory's solution theory. However, the peculiar discrepancies between the various experimental determinations of χ and between theory and experiment[18] for benzene and cyclohexane suggest possible secondary influences on such systems that have not yet been comprehended. We are hopeful that the temperate coefficient of χ will provide further insight into the nature of such influences that appears to be manifest in the data reported here.

Acknowledgment. This work was supported, in part, by a grant from the National Science Foundation.

Glossary

1 = solvent
2 = polymer (PIB)
3 = carrier gas (N_2)
a_1 = solvent activity
B_{ij} = second virial coefficient between species i and j
C_1^g = solvent concentration in gas phase
C_1^l = solvent concentration in liquid phase
G_{11} = cluster integral of solvent
k_0 = partition coefficient at zero pressure
p_1^0 = saturated vapor pressure of solvent
p = carrier gas pressure
p_i = inlet pressure
p_o = outlet pressure
P_i^* = characteristic pressure
r = molar volume ratio of polymer and solvent
T_i^* = characteristic temperature
$\tilde{T}_i$ = reduced temperature
V_1^0 = molar volume of solvent
$\bar{V}_1^\infty$ = partial molar volume of solvent at infinite dilution
V^1 = volume of stationary liquid
V_N = net retention volume
V_N^0 = net retention volume at $p_i = p_0 = 0$
V_i^* = molar characteristic volume
v_i = volume fraction
$\tilde{v}_i$ = reduced volume of component i
$\tilde{v}$ = reduced volume of solution
v_1 = partial molecular volume of solvent
γ_1 = activity coefficient at finite concentration
$\gamma_1^{\infty,v}$ = activity coefficient at infinite dilution and finite pressure (volume fraction)
ϕ_i = segment fraction
θ_i = site fraction
χ_v = Flory–Huggins interaction parameter (volume fraction)
χ_s = Flory–Huggins interaction parameter (segment fraction)

References and Notes

(1) A. J. B. Cruickshank, M. L. Windsor, and C. L. Young, *Proc. Roy. Soc., Ser. A*, **295**, 259, 271 (1966).
(2) D. H. Everett, *Trans. Faraday Soc.*, **61**, 1637 (1965).
(3) R. D. Newman and J. M. Prausnitz, *J. Phys. Chem.*, **76**, 1492 (1972).
(4) W. E. Hammers and C. L. DeLigny, *Recl. Trav. Chim., Pays-Bas*, **90**, 912 (1971).
(5) W. R. Summers, Y. B. Tewari, and H. P. Schreiber, *Macromolecules*, **5**, 12 (1972).
(6) N. F. Brockmeier, R. W. McCoy, and J. A. Meyer, *Macromolecules*, **5**, 130 (1972); *ibid.*, **5**, 464 (1972).
(7) Y. B. Tewari and H. P. Schreiber, *Macromolecules*, **5**, 329 (1972).
(8) O. Smidsrød and J. E. Guillet, *Macromolecules*, **2**, 272 (1969); A. Lavoie and J. E. Guillet, *ibid.*, **2**, 443 (1969).
(9) J. E. Guillet and A. N. Stein, *Macromolecules*, **3**, 102 (1970).
(10) D. G. Gray and J. E. Guillet, *Macromolecules*, **5**, 316 (1972); *ibid.*, **4**, 129 (1971).
(11) P. J. Flory, "Principles of Polymer Chemistry," Cornell University Press, Ithaca, N. Y., 1953, Chapter XII.
(12) D. D. Patterson, Y. B. Tewari, H. P. Schreiber, and J. E. Guillet, *Macromolecules*, **4**, 356 (1971).
(13) M. L. McGlashan and D. J. B. Potter, *Proc. Roy. Soc., Ser. A*, **267**, 478 (1962).
(14) "Selected Values of Physical and Thermodynamic Properties of Hydrocarbons and Related Compounds," A.P.I. Project 44, Carnegie Press, Pittsburgh, Pa., 1953.
(15) A. J. B. Cruickshank, B. W. Gainey, and C. L. Young, *Trans. Faraday Soc.*, **64**, 337 (1968).
(16) P. J. Flory, R. A. Orwoll, and A. Vrij, *J. Amer. Chem. Soc.*, **86**, 3507 (1964); P. J. Flory, *ibid.*, **87**, 1833 (1965); A. Abe and P. J. Flory, *ibid.*, **87**, 1838 (1965).
(17) P. J. Flory, J. L. Ellenson, and B. E. Eichinger, *Macromolecules*, **1**, 279 (1968); B. E. Eichinger and P. J. Flory, *ibid.*, **1**, 285 (1968); P. J. Flory, B. E. Eichinger, and R. A. Orwoll, *ibid.*, **1**, 287 (1968).
(18) B. E. Eichinger and P. J. Flory, *Trans. Faraday Soc.*, **64**, 2035, (1968).
(19) O. Grubner, "Advances in Chromatography," A. Zlatkis, Ed., University of Houston, Houston, Tex., 1971, p 13.
(20) A. J. B. Cruickshank, B. W. Gainey, C. P. Hicks, T. M. Letcher, R. W. Moody, and C. L. Young, *Trans. Faraday Soc.*, **65**, 1014 (1969).
(21) G. H. Hudson and J. C. McCoubrey, *Trans. Faraday. Soc.*, **56**, 761 (1960).
(22) B. W. Gainey and C. L. Young, *Trans. Faraday. Soc.*, **64**, 349 (1968).
(23) C. L. Young, *Trans. Faraday. Soc.*, **64**, 1537 (1968).
(24) B. H. Zimm, *J. Chem. Phys.*, **21**, 934 (1953); B. H. Zimm and J. L. Lundberg, *J. Phys. Chem.*, **60**, 428 (1956).
(25) R. A. Orwoll and P. J. Flory, *J. Amer. Chem. Soc.*, **89**, 6814 (1967).
(26) G. Delmas, D. Patterson, and T. Somcynsky, *J. Polym. Sci.*, **57**, 79 (1962).
(27) W. E. Hammers and C. L. DeLigny, *J. Polym. Sci., Part C*, **39**, 273 (1972).

High-Voltage Electroosmosis. Pressure–Voltage Behavior in the System γ-Alumina–2-Propanol

A. F. Hadermann,* P. F. Waters, and J. W. Woo

Department of Chemistry, The American University, Washington, D. C. 20016 *(Received December 6, 1972; Revised Manuscript Received October 1, 1973)*

Publication costs assisted by Department of Chemistry, The American University

Relatively high electroosmotic pressures are produced when a dissociable species such as water is present in the system γ-alumina–2-propanol and potentials in the kilovolt region are applied. Pressures above 3 atm were observed in this study. A theoretical expression, based on Onsager's treatment of the dissociation field effect, is derived for the electroosmotic pressure as a function of the applied potential. The equation agrees qualitatively with the measured data.

Introduction

Nonaqueous electroosmotic systems are amenable to the study of electrokinetic phenomena in strong electric fields. This point has not been examined extensively in the past, although nonlinear pressure–voltage relationships have been observed in studies at higher voltages than can be conveniently applied to aqueous systems.

Coehn and Raydt[1] studied electrokinetic phenomena in organic systems, but it has since been thought that their results are suspect because the liquids they employed were either shaken with acids before use or were highly impure by present-day standards. Gortner[2] attempted to ascribe electrokinetic effects in nonaqueous systems to a nonionic mechanism. However, La Mer and Downes[3] and Fuoss[4] have shown that ions can exist even in pure hydrocarbon liquids. Stuetzer[5-7] has observed an electrokinetic effect, termed ion-drag pumping, in pure, low-polarity hydrocarbon liquids. Lorenz[8] studied electroosmotic pressure in the quartz–acetone system, but, unfortunately, halted the investigation at the level of electric field strengths where the relationship between the pressure and the voltage becomes strongly nonlinear. Lorenz ascribed the nonlinearity to polarization phenomena at the electrodes.

Lauffer and Gortner[9] thought that electrokinetic effects observed in systems comprised of aliphatic alcohols and alumina were due to changes derived from the liquid or the solid, but did not stress the role played by water, particularly at high field strengths. Recently, Rastogi and Jha[10] discussed the system consisting of acetone and Pyrex glass sinters in terms of an irreversible thermodynamic treatment using nonlinear coupling constants. Rastogi, Singh, and Singh[11] have discussed the methanol–quartz system in similar terms. Higher order coupling constants were used to obtain expressions which fit the experimental data.

Theory

The phenomenon of electroosmosis is assumed to be ionic in nature. Although very weak electrolytes are included in the treatment presented here, the basis of the phenomenon in γ-alumina–2-propanol systems is believed to be the selective adsorption of ionic species and the establishment of an electrokinetic potential. Water in the porous region of the electroosmotic couple is considered to be the major source of ions and this model will be used in the derivation of an electroosmotic pressure equation.

Several electric field effects have been observed in electrolyte solutions. They are of different relative importance in the γ-alumina–2-propanol–water system. Stokes' law holds up to ionic velocities of the order of 10^5 cm/sec and if we assume a field strength of 75 kV/cm and an ionic mobility of 3.62×10^{-3} (cm/sec)(V/cm) for H^+, we obtain a velocity of only 271 cm/sec. Thus, nonlinearity cannot arise from this source. Likewise, nonlinearity should not stem from the Wien effect[12] because the limit of the equivalent conductance at infinite dilution is also the limit when the Wien effect is operating. In the water–2-propanol system the free ionic content is very low and each ion may already be considered to be free of the others before the field is applied. The most important field effect in the water–2-propanol system is the dissociation field effect although it is not possible to rule out completely the development of a simple space charging by a mechanism similar to that proposed by Stuetzer. In the case of weak electrolytes the dissociation field effect may be the most important factor leading to an increase in the concentration of ions with increasing field strength.

Dissociation field effects have been observed in several nonaqueous and aqueous solutions. Onsager[13] has developed a theory to account for the dissociation field effect and a discussion of the theory can be found in Harned and Owen.[14] The purpose of the present paper is to apply this theory to γ-alumina–2-propanol–water systems and compare the theoretical result with the experimental data.

When water is present within the pore volume of the γ-alumina sample it will be considered to be a source of hydroxyl ions and solvated protons. It will be assumed that the region below the plane of shear is capable of selectivity adsorbing hydroxyl ions. Thus, the surface charge density will be a function of the applied potential and the intrinsic value of the charge density will be ignored. To simplify the treatment, it will be assumed that the intrinsic charge below the plane of shear can be safely neglected when water is present and will become manifest only in dry systems.

The application of an electric field to an electroosmotic system containing water should lead to an increase in the degree of dissociation of the water in the 2-propanol with-

in the porous region. The relationship between the degree of dissociation of the weak electrolyte in the field, α, and the degree of dissociation in the absence of the field, α_0, is given by

$$\frac{\alpha}{\alpha_0} = 1 + \frac{\bar{b}}{2} + \frac{\bar{b}^2}{24} + \cdots\cdots \quad (1)$$

for α and α_0 much smaller than unity and where

$$\bar{b} = 9.636(E/D'T^2) \quad (2)$$

for a univalent, symmetrical electrolyte. E is the field strength in volts/cm, T is the absolute temperature, and D' is the dielectric constant of the medium.

The quadratic term of eq 1 is smaller than $\bar{b}$ for typical values of D', T, and E, *e.g.*, $D' = 18.3$, $T = 298°$, and $E = 50$ kV/cm. Thus, terms higher than $\bar{b}$ may be neglected in a first approximation. However, there may be situations where this procedure would obviously be invalid, *i.e.*, in very strong fields using low polarity solvents such as dioxane.

The electroosmotic pressure[15] has the form

$$P = 2D\zeta V/(299.8)^2\pi\bar{r}^2 \quad (3)$$

where D is the dielectric constant of the medium within the double layer which may also be considered to be the dielectric constant of the medium for very dilute electrolyte systems, ζ is the electrokinetic potential in volts, V is the applied potential in volts, and $\bar{r}^2$ is the square of the mean pore radius.

If the electrokinetic potential is taken to be

$$\zeta = 4\pi\delta d/D \quad (4)$$

where d is the double layer thickness and δ is the charge density at the surface of shear, it follows from eq 3 that

$$P = 8\delta V d/299.8\bar{r}^2 \quad (5)$$

A suitable solution of the Poisson-Boltzmann equation for the direction normal to the surface of a section of a hypothetical capillary wall is

$$\frac{1}{\kappa} = \left(\frac{DkT}{\pi N_0 c}\right)^{1/2}\frac{1}{2e} \quad (6)$$

for the case of one ion dominating at the plane of shear for a 1:1 electrolyte where $1/\kappa$ is the double layer thickness, k is the Boltzmann constant, e is the electronic charge, N_0 is the Avagadro number, and c is the electrolyte concentration. Substitution of eq 6 into eq 5 leads to

$$P = \frac{4\delta V}{299.8\bar{r}^2 e}\left(\frac{DkT}{\pi N_0 c}\right)^{1/2} \quad (7)$$

where δ can be defined as

$$\delta = fN_0 c \quad (8)$$

and f is the proportionality constant, in esu cm, linking the concentration of ions in the bulk to the charge density below the plane of shear. Substituting eq 8 into eq 7 leads to

$$P = 1.334 \times 10^{-2}\frac{fV}{e\bar{r}^2}\left(\frac{N_0 kTDc}{\pi}\right)^{1/2} \quad (9)$$

It follows from eq 1 that

$$c = \alpha_0 c_0\left(1 + \frac{\bar{b}}{2} + \frac{\bar{b}^2}{24} + \cdots\cdots\right) \quad (10)$$

where c_0 is the concentration of the weak electrolyte in the fluid in the pore volume of the porous system. Substituting eq 10 into eq 9 (up to $\bar{b}$ only), together with the values of the physical constants and setting $D = 18.3$ and $T = 298°$ gives

$$P = 1.055 \times 10^{13}\omega V + 2.88 \times 10^{5}\omega\frac{V^2}{D'1} \quad (11)$$

where ω is defined as

$$\omega = f\sqrt{\alpha_0 c_0}/\bar{r}^2 \quad (12)$$

In the absence of weak electrolyte $c_0 = 0$ and the system should obey eq 3 where ζ should then be the intrinsic electrokinetic potential of the solid-liquid couple.

Experimental Section

Materials. Two sources of γ-alumina were investigated in high-voltage γ-alumina-2-propanol-water couples. These were (A) Fisher, metallographic polishing alumina, A-448, cubic crystals, type B, *ca.* 0.1 μ; and (B) Merck, reagent grade γ-alumina, 71695, for chromatography, acid washed, ground and sized, *ca.* 2 μ.

The 2-propanol was Fisher, electronic grade, A-416 with an original water content of 147 ppm prior to refluxing over and distilling out of a mixture with calcium hydride.

The calcium hydride was obtained from the Ventron Corp., lot number J-3916A, and was passed through a 40 mesh sieve.

The Karl Fischer reagent titrations were performed using Baker and Adamson absolute methanol (300 ppm water), Fisher, So-K-3 Karl Fischer reagent and So-K-5 Karl Fischer reagent diluent.

Electroosmotic Pressure Cell. A Pyrex glass apparatus was used as a sample preconditioning and electroosmotic pressure cell and it is shown in Figure 1. Ball joints were provided in order to facilitate connecting the system to an oil diffusion pump when required. A coarse glass frit was used to prevent the sample from slipping due to the high pressures generated in wet γ-alumina-2-propanol systems. The limb of the apparatus containing the sample was wrapped with a 300-W quartz Cal-Cord capable of heating up to 650° when desired. A thermocouple circuit was incorporated into the heating jacket and was placed in feedback with a Luft Model 77 controller to regulate and maintain the temperature. Evacuation pressures were monitored using an RG-21X ionization tube and a Veeco RE-75N ionization gauge. After each treatment, the final pressure was recorded. Air dried by passage through Drierite was admitted to the system prior to adding the dry 2-propanol and switching the cell over to the electroosmotic pressure mode. Access to the cell was through 20-gauge Teflon tubing. The outer leads to the platinum electrodes were potted in paraffin (in Tygon) to prevent corona discharge through the air at the very high voltages applied to the cell. The negative side of the cell was grounded to a heavy metal rack connected to the water mains.

The alumina was packed by vibrating the powder into place with a Burgess vibra-tool. The 2-propanol was introduced upward through the frit and porous plug by maintaining a hydrostatic head of 2 cm. A cathetometer was used to measure the length of the alumina sample both before and after saturation with 2-propanol and no detectable change was noted in the length. The length was also measured at the end of an electroosmotic pressure determination and remained constant for samples prepared in this manner.

The 2-propanol which was introduced to the sample within the electroosmotic pressure cell was obtained by distilling an appropriate quantity (*ca.* 15 ml) out of a continuously refluxing mixture of 50 g of calcium hydride and 500 ml of 2-propanol. The water content of the 2-propanol was always found to be less than 10 ppm when obtained directly from the refluxing system.

Power Supply. A Sola constant-voltage transformer, type CVN, was used to feed power to a powerstat connected to the primary of a Plastic Capacitors Inc. 75-kV dc power supply, HV750-152M. A 50-μA meter (Triplett Model 420) was placed in the ground circuit to permit measurement of the current flowing through the electroosmotic pressure cell. The potential difference was determined by using an RCA microammeter (battery operated) and a calibrated high-voltage probe rated at 3.84 kV/μA at the meter. Cathode ray wire was used between the corona sphere of the power supply and the hot terminal of the electroosmotic pressure cell. Although this wire was conservatively rated at 40 kV it was satisfactory up to at least 75 kV and could be manipulated with relative ease.

Karl Fischer Apparatus. An apparatus for the determination of the water content of gases, liquids, and solids was prepared by modification of some of the components of a commercial Kontes electrochemical kit. Reagents and samples were introduced to the methanol through 20-gauge Teflon tubing, whenever practical. Further construction details can be found elsewhere.[16]

Surface Area Determination and Mean Pore Radius. An Aminco-Dietz Sor-BET apparatus was used to obtain data from which the BET surface area of the Fisher metallographic γ-alumina sample was determined. A self-contained gas pump purged the sample with a binary mixture of helium and nitrogen from which the selectively adsorbed nitrogen was determined. The outgassing was performed at 200° and 10^{-4} Torr for 1 hr. The dose size was 2.096 cm^3 (STP) and the equilibration time was 3 min. The sample size was 0.9489 g. The surface area was found to be 9.75×10^5 cm^2/g. The mean pore radius was obtained by dividing twice the void volume of the sample by its surface area, based on a pore model assuming right circular cylinders.[17]

Results and Discussion

The pressure–voltage data points, as a function of the applied potential, are presented for several γ-alumina–2-propanol–water systems in Figure 2. Curve A of Figure 2 shows the P/V *vs.* V plot of a system of γ-alumina which has been activated by heating in air at 154° for 18 hr to a final water plus aluminol hydroxyl content of 3.2 wt %. The slope of the line is 3.65×10^{-3} and the intercept is 55.0. Curve B results after exposing the system used to generate curve A to a high-voltage field for an extended period. This causes the water in the plug region to migrate to the electrode compartments and the course of this process was followed by means of Karl Fischer titrations. Curve C shows the properties of a system comprising a sample of γ-alumina exposed to a thermal-vacuum treatment followed by the application of a high-voltage field to the electroosmotic couple. The curves are linear within the estimated errors of the measurements. The increasing values of the intercepts and slopes with increasing water content of the systems is in qualitative agreement with eq 11. Curve C follows eq 3. Several experimental parameters common to the systems of Figure 2 are the following: mass of the γ-alumina = 0.5000 g, volume of the plug = 0.827 cm^3 (length = 1.302 cm and diameter = 0.899 cm), volume of the γ-alumina based on a measured density of 3.7 g/cm^3 = 0.14 cm^3, void volume of the sample = 0.70 cm^3, and the mean pore radius = 2.8×10^{-6} cm.

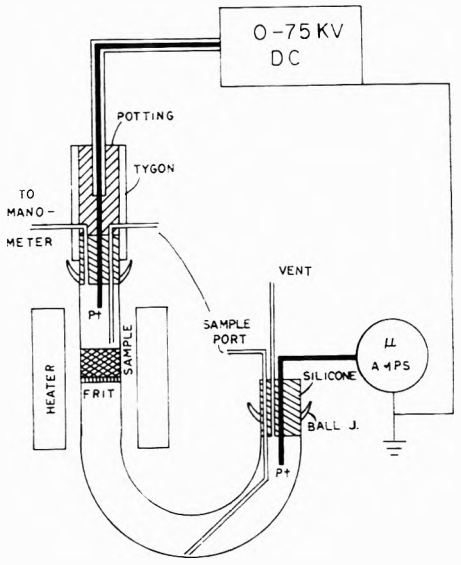

Figure 1. High-voltage electroosmosis pressure cell.

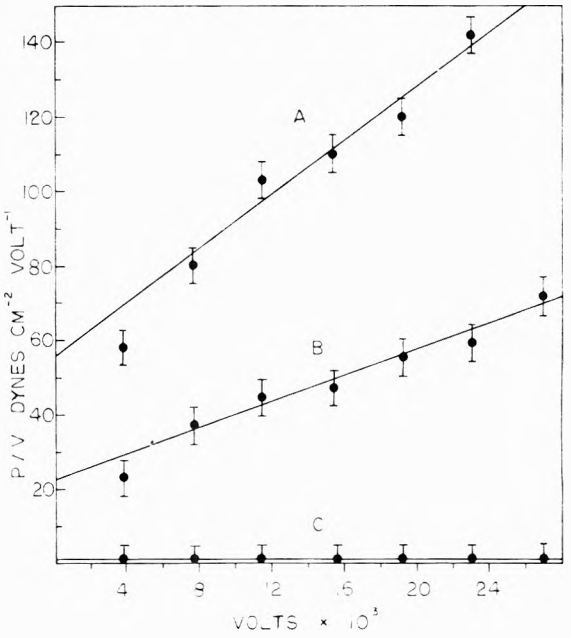

Figure 2. Pressure/voltage as a function of the applied potential in volts for several high-pressure electroosmotic couples comprised of γ-alumina and 2-propanol. The mass of the γ-alumina is 0.5000 g and the surface area is 9.75×10^5 cm^2/g. The alumina was Fisher metallographic polishing grade. The systems are defined as follows: curve A, activated by heating in air at 154° for 18 hr to a final water content of 3.2 wt %; curve B, result of subjecting the system shown in curve A to 7.68 kV for a period of 20.7 hr; curve C, sample subjected to thermal treatment at 404° for 32 hr, evacuated at 2.0×10^{-4} Torr, plus field treatment with 2-propanol at 25.9 kV for 1.6 hr.

Evaluation of Parameters

ω and D'l. These values for each of the systems of curves A and B are given in Table I.

The values of $D'l$ are lower than expected from the geometry of the cell used. This may mean that the dissociation field effect accounts for only part of the nonlinearity

TABLE I: Values of ω, $D'l$, c_0 and f for the γ-Alumina–2-Propanol–Water Systems Shown in Figure 2

Figure 2 curve	$\omega \times 10^{12}$ esu(mol/cm^3)$^{0.5}$	$D'l$, cm	$C_0 \times 10^3$ mol/cm^3	$f \times 10^{18}$ esu cm
A	5.21	0.411	1.07	76
B	2.13	0.351	0.178	
C	0.188			

observed in these experiments or it may be related to the relatively large void space of the plug and the high conductivity of the fluid in the void space relative to that of the alumina portion of the plug. This aspect of the theory is undergoing further study.

If we assume that the experimental data give reasonable values for ω we can estimate values for c_0, α_0, f, c, d, δ, and ζ.

c_0. The determination of c_0 involves estimating that portion of the titratable water plus aluminol hydroxyl which is free to be solvated by 2-propanol. A sample of Fisher γ-alumina, taken from the bottle without further treatment, assayed at 4.1 wt % water plus aluminol hydroxyl. This corresponds to 1.5 molecules/site coverage using a value of 10.8 Å/site.[18] After washing the sample with 2-propanol containing less than 10 ppm water and centrifuging it assayed at 0.9 wt % water plus aluminol hydroxyl. After five successive washings with 2-propanol the alumina assayed at 0.7 wt % water plus aluminol hydroxyl. Thus, at least 83% of the KFR titration value is derived from the water content of the sample. Another sample of this alumina was heated at 404° for 32 hr to a final pressure of 2×10^{-4} Torr after which it assayed at 0.33 wt % which is presumed to be aluminol hydroxyl. It is reasonable to expect that some of the aluminol hydroxyl reacted *via* a bimolecular process to form water which then left the surface. Thus, it would be unreasonable to use the 0.33 wt % limit for the estimation of aluminol hydroxyl in obtaining c_0 for A of Figure 2. Taking 0.8 for the water portion of the 1.60×10^{-2} g of water plus aluminol hydroxyl of A of Figure 2, $c_0 = 1.07 \times 10^{-3}$ mol/cm^3.

α_0. The degree of dissociation, α_0, of the water dissolved in the 2-propanol in the void space depends on the dielectric constant of the liquid in this region. The dissociation constant of water in a 70 wt % dioxane–water mixture is 1.396×10^{-18} at 25°.[19] The α_0 under these circumstances is 2.893×10^{-10}. Since the dielectric constant of this particular dioxane–water mixture is close to the dielectric constant of 2-propanol, it will be assumed that a reasonable value for the α_0 of water in 2-propanol is 2.89×10^{-10}. Using this value for α_0, and the equations which were presented previously, it is possible to estimate the electrostatic adsorption moment, f, for the γ-alumina–2-propanol–water system. It is 76 D.

The c_{0B} (the concentration of water in the 2-propanol in the void space of the system after sustained treatment at 7.68 kV for 20.7 hr with 2-propanol containing less than 10 ppm of water in the electrode compartments) was calculated using f = 76 D. The concentration of water in the void space was reduced to 1.8×10^{-4} mol/cm^3 by this procedure. The curve represented by curve C of Figure 2 was prepared by exhaustive drying of the alumina and P/V = 0.4 indicating that an intrinsic electrokinetic potential is involved in the γ-alumina–2-propanol couple.

Using the parameters shown in Table I and the equations which have been defined earlier it is possible to obtain all of the parameters shown in Table II. Table II illustrates the magnitudes of the field-dependent ion concentration, double layer thickness, charge density at the surface of shear, and the electrokinetic potential of each system of Figure 2 at 0 V and at 50 kV. The field-dependent and the intrinsic electrokinetic potentials are very small compared to those typically representative of aqueous systems containing strong electrolytes. Nevertheless, very high pressures, *e.g.*, up to 4 atm at 60 kV have been observed in γ-alumina–2-propanol–water systems.

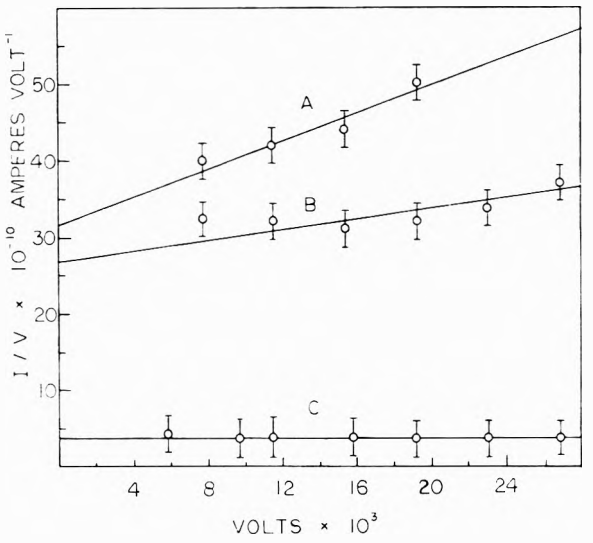

Figure 3. Current/voltage as a function of the applied potential in volts for each of the systems shown in Figure 2. Curves A, B, and C correspond to curves A, B, and C of Figure 2.

TABLE II: Double-Layer Parameters for the γ-Alumina–2-Propanol–Water Systems of Table I

Figure 2	$c \times 10^{13}$ mol/cm^3 zero volt	$c \times 10^{13}$ mol/cm^3 50 kV	d Å zero volt	d Å 50 kV	$\delta \times 10^6$ esu/cm^2 zero volt	$\delta \times 10^6$ esu/cm^2 50 kV	ζ mV zero volt	ζ mV 50 kV
A	3.1	23	12	4.3	14	106	3.4	9.4
B	0.51	4.5	29	9.8	2.3	20	1.4	4.1
C	Constant at 2.5×10^{-2}							

The concentration of the weak electrolyte, and hence the P *vs.* V function, depends on the strength and time of application of the field and the water content of the 2-propanol in the electrode compartments. In a more limited fashion, the current also depends on c_0 as is shown in Figure 3 for each of the three systems in Figure 2. However, comparing the functions in Figure 2 with the corresponding functions in Figure 3 it is apparent that the electroosmotic pressure goes through a much larger per cent decrease than does the current as the water content of the void space decreases. It must be recalled that the data shown in Figures 2 and 3 relate to applied potentials in the kilovolt range and that there is probably electronic as well as ionic conduction.

The relationship of the water content to P/V and I/V *vs.* V for Merck γ-alumina samples is shown in Figure 4. Curves A and A′ of Figure 4 were obtained after drying a 2.00-g sample in air for 2 hr at 130°. Curves B and B′ illustrate the effect of subjecting an equivalent 2.00-g sample with a 5.1 wt % water plus aluminol hydroxyl content to field treatment with dry 2-propanol (*i.e.*, containing less than 10 ppm water) at 30.7 kV for 9.4 hr. Migration of water back into the void space was minimized by collect-

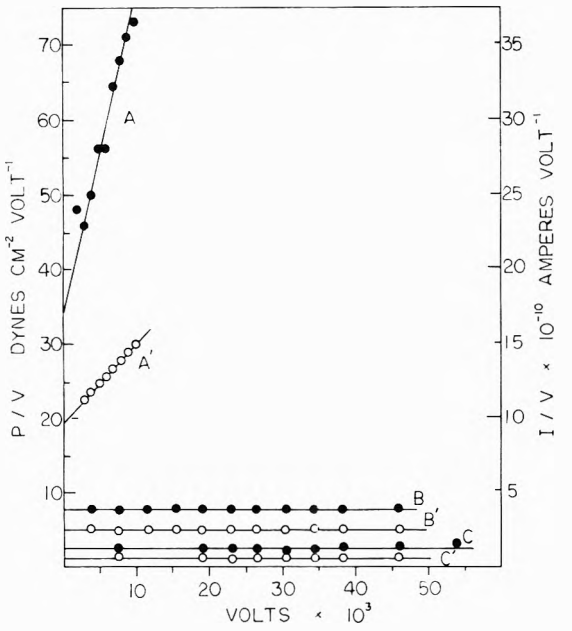

Figure 4. Pressure/voltage and current/voltage as a function of the applied potential in volts for three electroosmotic couples comprised of Merck γ-alumina and 2-propanol: pressure/voltage, ●; current/voltage, O. 2.00-g samples were used. The pretreatment water content of each sample was 5.14 wt %: curves A and A′, sample subjected to thermal activation in air for 2 hr at 130°; curves B and B′, sample (5.14 wt % water plus aluminol) subjected to field treatment at 30.7 kV for 9.4 hr; curves C and C′, sample subjected to thermal treatment for 45.5 hr at 400°, evacuated at 7×10^{-5} Torr.

ing the data by going from higher to lower voltages. Curves C and C′ are for a 2.00-g sample of the same alumina after being subjected to thermal treatment for 45.5 hr at 400° and 7×10^{-5} Torr (final pressure). The I/V curves, B′ and C′, show that Ohm's law is obeyed by both of these systems. The zero slopes associated with curves B and C suggest that c_0 is approaching zero and that the intrinsic charge density at the surface of shear can no longer be neglected from consideration. Note that curves B and B′ are for a system which has not been thermally treated or dried. Titration of the liquids in the electrode compartments with KFR shows that substantially all of the water originally present in the γ-alumina migrated to the electrode compartments when the system is subjected to the high voltage field. There it is outside the region of electroosmotic activity.

Conclusions

It is critical that traces of water be removed when the electrokinetic properties of nonaqueous systems are measured, particularly if potentials in the kilovolt region are used. The presence of a weak electrolyte such as water can lead to the development of a significant electroosmotic pressure which is nonlinear in the applied potential and follows the form of eq 11. A dry γ-alumina–2-propanol system exhibits a very small electroosmotic pressure which is linear in the applied potential in the kilovolt region. This finding is expected if the ionic content of the region of electroosmotic activity does not depend on the strength of the applied field. This will be the case only if weak electrolyte is excluded from the active region and/or a Stuetzer-type of space-charging phenomenon is absent. Electrolytes may be removed from the active region by the sustained application of potential differences in the kilovolt region.

References and Notes

(1) A. Coehn and U. Raydt, *Ann. Phys.*, **30**, 777 (1909).
(2) R. A. Gortner, *Trans. Faraday Soc.*, **36**, 63 (1940).
(3) V. K. La Mer and H. C. Downes, *Chem. Rev.*, **13**, 47 (1933).
(4) R. M. Fuoss, *Chem. Rev.*, **17**, 27 (1935).
(5) O. M. Stuetzer, *J. Appl. Phys.*, **30**, 984 (1959).
(6) O. M. Stuetzer, *J. Appl. Phys.*, **31**, 136 (1960).
(7) O. M. Stuetzer, *Phys. Fluids*, **2**, 642 (1959).
(8) P. B. Lorenz, *J. Phys. Chem.*, **57**, 430 (1953).
(9) M. A. Lauffer and R. A. Gortner, *J. Phys. Chem.*, **42**, 641 (1938).
(10) R. P. Rastogi and K. M. Jha, *Trans. Faraday Soc.*, **62**, 585 (1966).
(11) R. P. Rastogi, K. Singh, and S. Singh, *J. Phys. Chem.*, **73**, 1593 (1969).
(12) H. S. Harned and B. B. Owen, "The Physical Chemistry of Electrolytic Solutions," Reinhold, New York, N. Y., 1958 p 216.
(13) L. Onsager, *J. Chem. Phys.*, **2**, 599 (1934).
(14) Reference 12, pp 138–146.
(15) J. Perrin, *J. Chim. Phys.*, **2**, 607 (1904).
(16) A. F. Hadermann, Doctoral Dissertation, The American University, 1970.
(17) P. H. Emmett and T. W. De Witt, *J. Amer. Chem. Soc.*, **65**, 1253 (1943).
(18) H. K. Livingstone, *J. Colloid Sci.*, **4**, 447 (1949).
(19) Reference 12, p 756.

The Effect of Water–Hydrocarbon Interactions on Proton Mobility. Chronoamperometric Diffusion Coefficients in Aqueous *tert*-Butyl Alcohol[1]

J. A. Lanning,[2] M. J. Pikal,[3]* and J. Q. Chambers

Department of Chemistry, University of Tennessee, Knoxville, Tennessee 37916 *(Received July 10, 1973)*

Publication costs assisted by the Petroleum Research Fund

Chronoamperometric proton diffusion coefficients and activation energies are reported for a number of water-rich *tert*-butyl alcohol solutions. Diffusion data at 25° are reported for ethylene glycol–water mixtures, and activation energies are presented for Ag^+ ion diffusion and viscous flow in 4 mol % aqueous *tert*-butyl alcohol. Proton diffusion coefficients decrease sharply as the alcohol concentration increases, particularly at low levels of alcohol. Although it may be argued that "ice-like" structure in solution caused by *tert*-butyl alcohol should increase proton mobility, the data do not support this speculation. Rather, it is concluded that increased "solid-like" water structure caused by a hydrophobic moiety decreases the proton mobility. The Arrhenius plot for proton diffusion in 4 mol % *tert*-butyl alcohol shows a sharp change in slope around 30°, indicating that the activation energy for proton diffusion decreases by *ca.* 2.0 kcal/mol between 25 and 35°. No corresponding anomaly was observed in the Arrhenius plot for Ag^+ ion diffusion or the plot for viscous flow. It is tentatively concluded that the anomaly observed for proton diffusion is a result of both the structure enhancement in the 4 mol % system and the unique transport mechanism for proton diffusion. A theoretical model is developed which qualitatively accounts for these observations.

I. Introduction

Physical properties of aqueous alcohol solutions frequently exhibit extrema or anomalous behavior in the low alcohol content region that are normally attributed to an increase in "long-range order."[4-8] That is, the nonpolar hydrocarbon portion of the alcohol increases water–water hydrogen bonding, resulting in a water structure which is more "solid-like" (*i.e.*, "ice-like" or "clathrate-like") than the structure in pure water. This qualitative rational is, of course, not unique to alcohols, and has been applied to numerous other systems[9] where nonpolar or "hydrophobic" moieties interact with water. Compared to other commonly studied alcohols, *tert*-butyl alcohol appears to be a particularly effective "water structure promoter." It has been proposed that the degree of structure is at a maximum in the 3–6 mol % region, and at higher levels of alcohol, a deficiency of water leads to a breakdown of structure.[5]

The work presented here is an investigation of the composition and temperature dependence of proton diffusion coefficients in aqueous *tert*-butyl alcohol, with particular emphasis given to the water-rich region where presumably the long-range order or solid-like structure is at a maximum. Our primary interest was in the effect of solute-induced solid-like structure on proton mobilities. It is well known that, as a result of water–water hydrogen bonding, proton mobilities in both ice and water are much greater than would be expected by analogy to data on other ions. Moreover, the available evidence[10,11] indicates that although the activation energy for proton diffusion is about a factor of 4 greater in ice than in water, the proton diffusion coefficient is *higher in ice* by at least a factor of 2.[12] Thus, one might speculate that increased ice-like or clathrate-like structure in solution would increase both the activation energy for proton diffusion *and* the proton mobility. Speculations equivalent to the above have been advanced by other workers[10,13] in discussions of proton mobility near biological membranes.

It should be emphasized that although the mechanisms for proton diffusion in both ice and water depend on hydrogen bonding, the mechanisms apparently differ considerably in detail.[10,11] Thus, the notion that enhanced solid-like water structure will increase proton mobility assumes a rather close analogy between solute-induced water structure and the solid state. Specifically, it would seem that the following structural features are assumed: (1) the lifetime of the hydrate structure surrounding the hydrophobic moiety is long compared to the proton jump time ($\sim 10^{-12}$ sec); and (2) the dimensions of the hydrate structure are large compared to the proton jump distance (~ 3 Å). It is significant to note that, at least above 3.5 mol % where data exist,[14] proton conductivity data in aqueous methyl, ethyl, *n*-propyl, and isopropyl alcohol do not provide any evidence for unusually high proton mobilities resulting from enhanced solid-like structure. Presumably, for these alcohols, the long-range order is not sufficiently long range for the solid-state analogy to be valid.

The primary purpose of this research was to investigate aqueous solutions of a more effective structure maker, *tert*-butyl alcohol, in an effort to find evidence for solid-like proton diffusion in solution. Specifically, in the 3–6 mol % alcohol region, one might expect to find (a) anomalously high activation energies; and (b) a maximum, or at least a plateau, in a plot of proton diffusion coefficients as a function of *tert*-butyl alcohol content. Thus, chronoamperometric proton diffusion coefficients were determined at 25° for 15 *tert*-butyl alcohol–water mixtures from 0.8 to 30 mol % alcohol. Activation energies were obtained at 0, 4, 9, and 14 mol % alcohol. For purposes of comparison chronoamperometric proton diffusion coefficients were also determined at 25° in water-rich solutions of the hydrophilic solute, ethylene glycol. To aid in the interpretation of an anomaly in the activation energy data, activa-

tion energies were also determined for Ag^+ ion diffusion and for viscous flow in the 4 mol % solution.

II. Experimental Section

1. Apparatus and Materials. The electronic instrumentation and electrolysis cells were of conventional design and have been briefly described elsewhere.[15] Temperature control was within ±0.02° above 20° and within ±0.1° near 0°.

Reagent grade *tert*-butyl alcohol was further purified by refluxing for 1 hr with sodium and then distilling once using a glass packed 1.5-ft column. Fisher Certified ethylene glycol was used without further purification. Reagent grade silver nitrate was used, without further purification, as the source of silver ions. The procedure for water purification (specific conductance of 1.2×10^{-6} cm^{-1} ohm^{-1}) and the sources of sodium perchlorate and perchloric acid were the same as previously described.[15]

2. Procedures. Diffusion coefficients and viscosities were determined as previously described.[15] Briefly, diffusion coefficients were measured by chronoamperometry using the Cottrell equation as modified by Soos and Lingane[16]

$$\frac{it^{1/2}}{Ac} = \frac{n\mathfrak{F}D^{1/2}}{\pi^{1/2}}[1 + K(Dt)^{1/2}/P_0] \qquad (1)$$

where K is an empirical constant, P_0 is the radius of an unshielded planar electrode, D is the chronoamperometric diffusion coefficient, and the remaining terms have their usual meaning. We have used this equation extensively and have found that the most accurate diffusion coefficients are obtained by extrapolation of the chronoamperometric constant to zero time. The reliability of this method of correcting for nonlinear diffusion to planar electrodes has been established by reference to known diffusion coefficients of ferrocyanide, silver ion, and hydrogen ion in aqueous solutions.

Each solution investigated was 0.1 M in $NaClO_4$ and 4 mM in $HClO_4$ (or 9 mM $AgNO_3$ for Ag^+ diffusion). Thus, as discussed later, D in eq 1 is slightly less than the tracer diffusion coefficient at infinite dilution.

Determinations of D for a given solution were generally reproducible to within 1.5%. However, due to errors in solvent composition and errors in the concentration of electroactive species, the probable error in a given D value is estimated to be ±3%. Experiments in this laboratory[15] gave $8.5_9 \times 10^{-5}$ cm^2/sec (average of nine determinations) for $D(H^+)$ in aqueous 0.1 M $NaClO_4$. This value is in excellent agreement with the literature value of $8.6_3 \times 10^{-5}$ cm^2/sec.[17]

Viscosities, η, were measured using a simple Ostwald viscometer, and the relation[18]

$$\eta = A\rho t + E\rho/t^n \qquad (2)$$

where ρ is the fluid density, t is the flow time, and E, A, and n are viscometer constants evaluated by calibration with water at various temperatures. The densities were determined using 25-ml pycnometers.

III. Results

1. Proton Reduction Wave Characterization. In water-rich *tert*-butyl alcohol–water mixtures, proton reduction waves are very similar to the waves in pure water. A typical proton reduction wave in water-rich aqueous *tert*-butyl alcohol is shown in Figure 1. The cathode peak potential is −0.445 V *vs.* sce, the peak separation is 61 mV, and the ratio of anodic peak current to cathodic peak current is 1.04. The observation that addition of *tert*-butyl alcohol did not cause an appreciable shift in peak potentials from those observed in pure water indicates that any changes in proton solvation are small and that any change in liquid junction potential must also be small. A "small change," as defined by the preceding statement, refers to changes in proton solvation which result in free energy changes on the order of 0.5 kcal/mol or less.

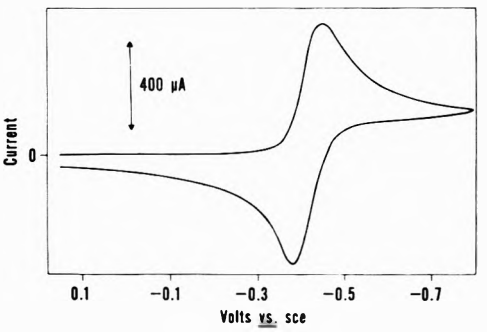

Figure 1. Cyclic voltamogram of 4.0 mM $HClO_4$ in aqueous 3.6 mol % *tert*-butyl alcohol at 25°: 0.1 M $NaClO_4$, 0.1 V sec^{-1} sweep rate, 0.223 cm^2 electrode area.

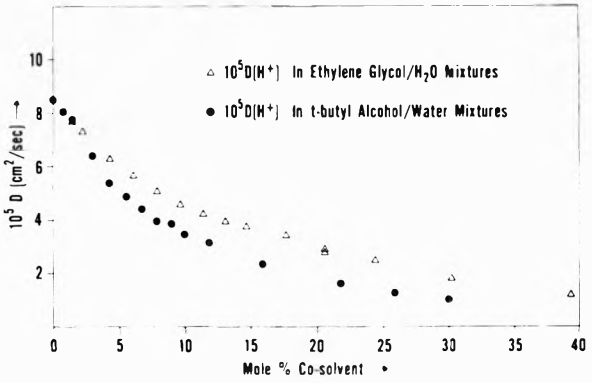

Figure 2. Chronoamperometric diffusion coefficients for protons in *tert*-butyl alcohol–water mixtures (○) and in ethylene glycol–water mixtures (△) at 25°. All solutions are 0.1 M in $NaClO_4$ and 0.004 M in $HClO_4$.

2. Proton Mobilities and Solvent Composition at 25°. Chronoamperometric proton diffusion coefficient data are shown in Figure 2 as a function of mole per cent organic cosolvent for both *tert*-butyl alcohol–water and ethylene glycol–water mixtures. All solutions are 0.1 M in $NaClO_4$ and 0.004 M in $HClO_4$, and all data are at 25°. Both sets of data are characterized by a monotonic decrease in diffusion coefficient as the solvent is made richer in organic cosolvent. At 5 mol %, the proton diffusion coefficient is *ca.* 70% that in pure water for ethylene glycol and only *ca.* 60% that in pure water for the *tert*-butyl alcohol system. The particularly rapid decrease between 2 and 4 mol % *tert*-butyl alcohol is believed to be real. However, more accurate mobility data, such as those resulting from precision conductivity measurements, would be needed to verify this result. Unfortunately, a precision conductivity bridge was not available to us.

3. Activation Energies. The effects of temperature on proton diffusion in four *tert*-butyl alcohol–water solutions are displayed in Figures 3 and 4 in the form of Arrhenius plots, and in Figure 5 where activation energies are plot-

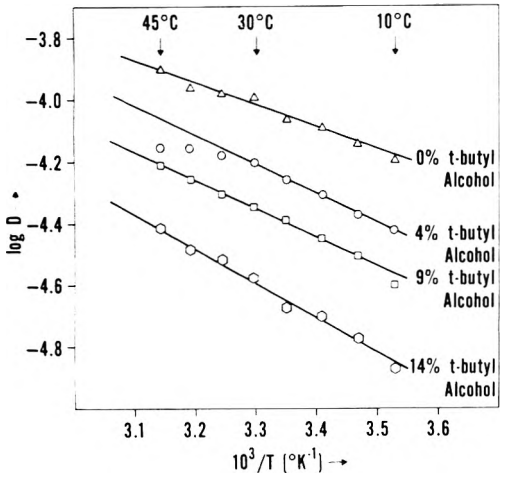

Figure 3. Arrhenius plots for proton diffusion in *tert*-butyl alcohol–water mixtures. All solutions are 0.1 *M* in $NaClO_4$ and 0.004 *M* in $HClO_4$: temperature range, 10–45°.

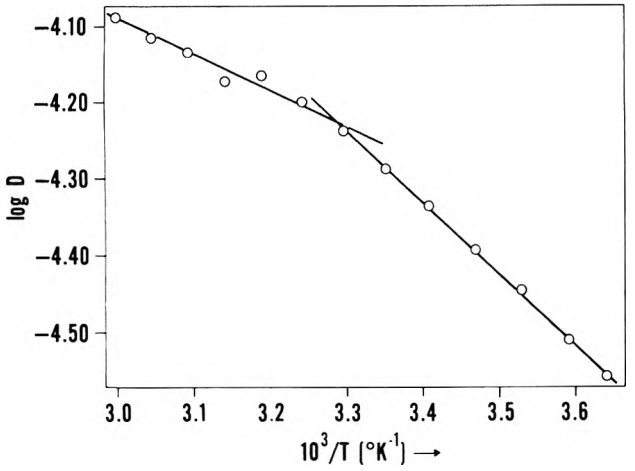

Figure 4. Arrhenius plot for proton diffusion in 4 mol % *tert*-butyl alcohol from 2 to 60°. The solution is 0.1 *M* in $NaClO_4$ and 0.004 *M* in $HClO_4$.

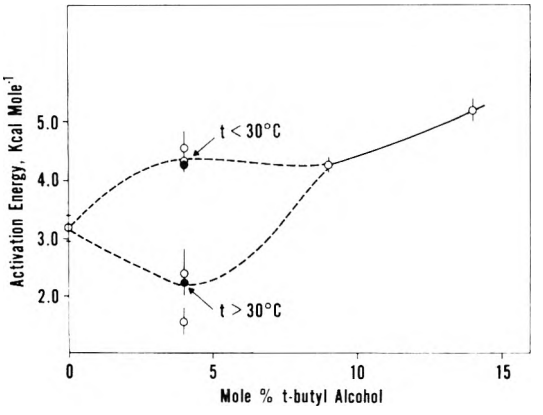

Figure 5. Activation energies, E_a, for proton diffusion in aqueous *tert*-butyl alcohol–water solutions. All solutions are 0.1 *M* in $NaClO_4$ and 0.004 *M* in $HClO_4$. The filled circles represent data resulting from the 2–60° experiment.

ted as a function of mole per cent *tert*-butyl alcohol. The activation energy, E_a, is defined by the usual expression, $D = A \exp(-E_a/RT)$, where R is the gas constant, and A is independent of temperature.

In Figure 3, it should be noted that the log D *vs.* $10^3/T$ plots are linear, within experimental error, for 0, 9, and 14

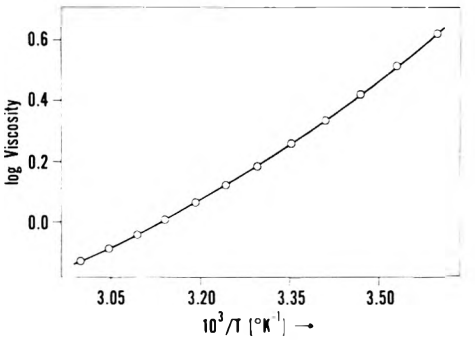

Figure 6. Arrhenius plot for viscous flow in 4 mol % *tert*-butyl alcohol 0.1 *M* in $NaClO_4$. The activation energies for viscous flow decrease smoothly as the temperature increases: 8.0 kcal/mol (5°), 5.8 kcal/mol (30°), 4.2 kcal/mol (60°).

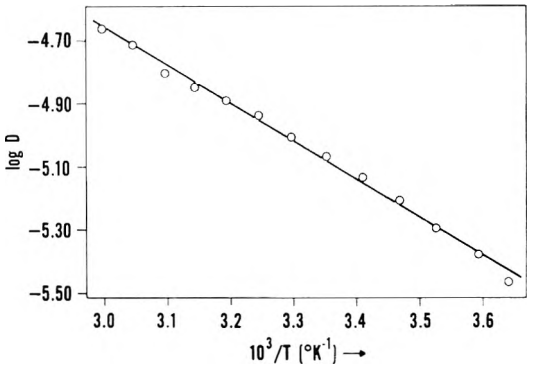

Figure 7. Arrhenius plot for Ag^+ ion diffusion in 4 mol % aqueous *tert*-butyl alcohol. The solution is 0.1 *M* in $NaClO_4$ and 0.009 *M* in $AgNO_3$: activation energy, $5.4_5 \pm 0.1_2$ kcal/mol.

mol % *tert*-butyl alcohol over the entire temperature range of 10 to 45°. However, in the plot for 4% *tert*-butyl alcohol, the high temperature points exhibit a negative deviation from the extrapolated low temperature (10–30°) linear portion. The experiments at 4% were repeated, and essentially the same results were obtained.

In an effort to study the anomaly at 4% in more detail, the following additional experiments were performed in aqueous 4 mol % *tert*-butyl alcohol containing 0.1 *M* $NaClO_4$: (a) chronoamperometric proton diffusion coefficients were measured over a wider temperature range, 2–60°; (b) viscosities were measured from 5 to 60°; and (c) chronoamperometric Ag^+ ion diffusion coefficients were measured from 2 to 61°. The results of the viscosity and Ag^+ ion diffusion experiments are given in Figures 6 and 7, respectively. The data in Figure 4 clearly show that for proton diffusion, a significant decrease in activation energy occurs over a narrow temperature range around 30°. As shown in Figure 6, the Arrhenius plot for viscous flow is not linear, but there is no evidence for a sudden decrease in activation energy. Indeed, the activation energy for viscous flow decreases *smoothly* from 8 kcal/mol at 5° to 4.2 kcal/mol at 60°.[19] The Arrhenius plot for Ag^+ ion diffusion, given in Figure 7, is linear within experimental error yielding a single activation energy of $5.4_5 \pm 0.1_2$ kcal/mol.

In view of the above observations, we conclude that the observed anomaly in 4% *tert*-butyl alcohol has physical significance and is not an experimental artifact. Moreover, the effect appears to manifest itself only for proton diffusion at *ca.* 4% *tert*-butyl alcohol. It should be noted, however, that more accurate data would most likely reveal a slight degree of curvature in all of the Arrhenius plots

considered in this research as linear. For example, our data for proton diffusion in the absence of *tert*-butyl alcohol is shown as linear in Figure 3 with an activation energy of 3.2 ± 0.2 kcal/mol. Using the more accurate H^+ ion conductivities at infinite dilution[20] to calculate diffusion coefficients at various temperatures, it is found that the Arrhenius plot exhibits some curvature-yielding an "average" activation energy of *ca.* 3.1 kcal/mol over the 10–45° range. Between 25 and 35° the activation energy decreases by 0.2 kcal/mol. However, the change in activation energy between 25 and 36° is *ca.* 2.0 kcal/mol for the 4 mol % *tert*-butyl alcohol solution.

The activation energy data for proton diffusion are summarized by Figure 5. The activation energies were determined by conventional "least-squares" analysis. The vertical bars in Figure 5 represent error limits as given by the standard deviation for the slope of a log D *vs.* $1/T$ least-squares fit. For 4 mol % *tert*-butyl alcohol, the data at the lower temperatures (30° and lower) were used to evaluate one activation energy while the high-temperature data (30° and higher) were employed in calculating a second activation energy. The experiment over the 2–60° range yielded the most accurate activation energies, and in Figure 5, these data are represented by the filled circles.

IV. Discussion

1. Effects of Electrical Migration and Ion–Ion Interactions. We now consider the contributions of ion–ion interactions and electrical migration to the composition and temperature dependence of chronoamperometric diffusion coefficients. The relationship of the chronoamperometric diffusion coefficient, D, to the tracer diffusion coefficient at infinite dilution, D^0, may be written in the form

$$D = D^0 f_m f_i \tag{3}$$

where f_m and f_i represent "corrections" for electrical migration and ion–ion interactions, respectively.

If it is assumed that all of the current is carried by the supporting electrolyte, and therefore that mass transfer of the electroactive species (*i.e.*, H^+ or Ag^+) proceeds by diffusion alone, f_m is unity, and the application of eq 1 to electrochemical raw data yields the tracer diffusion coefficient for the electroactive species in the supporting electrolyte. However, for the solutions studied in this research, about 10% of the current is carried by the electroactive species and f_m is greater than unity. Although a rigorous theoretical calculation of f_m is not available, experiments at various levels of $NaClO_4$ and $HClO_4$[19] suggest the empirical relationship[21]

$$f_m = (1 + t_+)^{(1 + t_+)} \tag{4}$$

where t_+ is the transference number of the electroactive species in the mixed electrolyte.

The effects of ion–ion interactions include both the relaxation effect,[22] a manifestation of long-range electrostatic interactions, and ion-pair formation. In pure water or in mixed solvents containing more than 90 mol % water, ion-pair formation is probably not significant,[23] and we ignore this effect. Further, we note that Onsager's theory[22] for the relaxation effect in tracer diffusion, valid for dilute electrolytes, is in surprisingly good agreement with proton diffusion data in aqueous alkali halides,[20] even at 0.1 M. Thus, as a first approximation, we may employ the Onsager theory[22] to estimate f_i.

Using the procedures outlined above for estimating f_i and f_m,[25] we find (a) the activation energies for proton

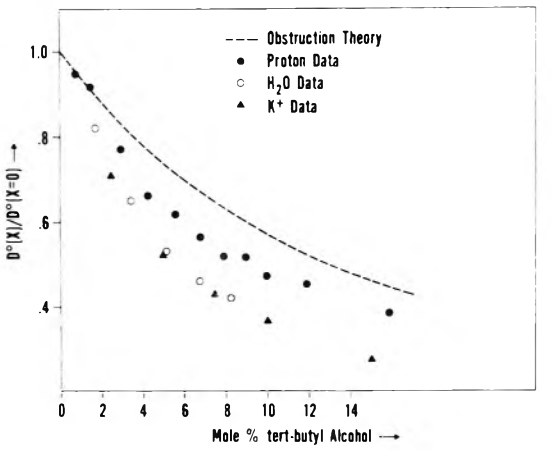

Figure 8. Comparison of tracer diffusion coefficients for protons, H_2O, and K^+ ion in aqueous *tert*-butyl alcohol at 25°.

tracer diffusion at infinite dilution are only *ca.* 0.15 kcal/mol higher than the values given in Figure 5, which were evaluated directly from chronoamperometric data; (b) the migration effect, f_m, is constant within about ±1% (= 1.1_2) over the 0 to 10 mol % alcohol or glycol composition range; (c) due primarily to a decreasing dielectric constant, f_i decreases by 15% over the 0 to 10 mol % *tert*-butyl alcohol composition range (f_i = 0.85 in pure water 0.1 M in $NaClO_4$). For glycol–water mixtures, the relative decrease in f_i over this composition range is only 4%.

Therefore, we conclude that ion–ion interactions and electrical migration have negligible effects on activation energies. Further, in aqueous *tert*-butyl alcohol, the relaxation effect causes a small, but significant, decrease in chronoamperometric diffusion coefficient as the solvent increases in *tert*-butyl alcohol content.

2. Effects of Solute Modified Water Structure. Earlier in this paper it was suggested that a plot of proton diffusion coefficients *vs.* *tert*-butyl alcohol content might exhibit a maximum, or at least a plateau region, at very low alcohol contents. This speculation was based on the notion that since proton mobility in ice is higher than in water, one might expect that increased solid-like structure in solution would increase proton mobility. Clearly the data in Figure 2 are not consistent with this speculation. Proton mobilities (*i.e.*, diffusion coefficients) decrease sharply as the level of *tert*-butyl alcohol increases, particularly in the water-rich region where high mobilities were "predicted." This behavior is similar to that shown by proton mobilities in other aqueous alcohol systems.[14] However, as demonstrated in Figure 8, the decrease in *relative* mobility is somewhat less than that found for water and other ions.

Figure 8 compares proton, water, and K^+ ion diffusion in aqueous *tert*-butyl alcohol at 25°. Although not shown in Figure 8, relative mobility curves for other ions[8] also fall below the proton curve. The quantity $D^0(X)$ represents the tracer diffusion coefficient at infinite dilution in the solvent of mole per cent X alcohol, while $D^0(X = 0)$ represents the corresponding quantity in pure water. The chronoamperometric proton data were corrected for the relaxation effect[26] and therefore represent tracer diffusion coefficients at zero electrolyte concentration. The water diffusion data were taken from the work of Goldammer and Hertz[27] while the K^+ ion data were calculated from limiting ionic conductances given by Broadwater and Kay.[8] The broken line, labeled "obstruction theory," rep-

resents the obstruction effect[20,28] which is a "nonstructural" contribution to the ratio $D^0(X)/D^0(X=0)$.

In a solution of large particles (obstructions), the large particles, here the *tert*-butyl alcohol molecules, effectively block part of the diffusion area and therefore decrease the mobility of a small diffusing species.[29] This is the so-called "obstruction effect." The obstruction effect given in Figure 8 was calculated from Prager's theory[31] using the procedure previously described.[28] The theoretical model[31] assumes that the obstructions are immobile and large compared to the solvent and diffusing species. Although the relative decrease in proton mobility is significantly less than the relative decrease shown by either water or K^+ ion, proton mobilities do decrease more than predicted by the obstruction effect, suggesting a significant "structural" contribution. In view of other evidence for structural effects in this system,[4-8] it seems likely that a significant portion of this structural contribution is a result of increased ice-like or clathrate-like water structure.

It should be noted that the structural contribution may be somewhat larger than implied by Figure 8 since the obstruction model used probably overestimates the magnitude of the obstruction effect in a molecular system such as aqueous *tert*-butyl alcohol. One would expect the theoretical model[31] to become increasingly inaccurate as the obstructing particle approaches the size and mobility of the medium and diffusing particles. Of course, in a system of particles equal in size and mobility, there can be no obstruction effect.

Activation energies of equivalent conductivity ($t \leq 25°$) for HCl in aqueous *n*-propyl and isopropyl alcohol increase smoothly as the alcohol content increases from 0 to 15 mol %.[14] Ignoring the data at 4 mol %, the activation energies for proton diffusion in aqueous *tert*-butyl alcohol increase in similar fashion. These observations appear consistent with the notion that rotation of water molecules is rate determining for proton diffusion.[32] However, at 4 mol %, the data suggest two distinct activation energies over the 0-60° temperature range. As evident from Figure 5, neither the low temperature ($t < 30°$) nor the high temperature ($t > 30°$) activation energy, 4.3 and 2.2 kcal/mol, respectively, appear to fit the general increase in activation energy established by the data at 0, 9, and 14 mol % alcohol. We note that there is significant evidence for anomalous behavior between 30 and 40° both in pure water and at water-hydrocarbon interfaces,[33] and these anomalies are most often interpreted in terms of the structural melting of ice-like water structure. In view of this evidence, it may appear reasonable to conclude that the discontinuity in activation energy is due to a structural melting of the *tert*-butyl alcohol induced solid-like structure over a narrow temperature range. Since the degree of structure is presumably a maximum near 4 mol %, structural melting yields an effect large enough to be observed as a discontinuity.

Unfortunately, the above interpretation does not appear consistent with our data for Ag^+ ion diffusion and viscosity. If structural melting causes the activation energy for proton diffusion to decrease by a factor of 2, one would also expect activation energies for Ag^+ ion diffusion and viscous flow to exhibit discontinuities at least as large. As shown by Figures 6 and 7, no evidence for such discontinuities were found. However, the continuous decrease in activation energy for viscous flow is consistent with very *gradual* structural melting. We conclude that the apparent discontinuity observed for proton diffusion is a result of *both* structure enhancement in the 4 mol % system and the unique transport mechanism for proton diffusion.

3. A Theoretical Model. With some modification, the theory of proton diffusion in water proposed by Gierer and Wirtz[34] and discussed by Eigen and DeMaeyer[10] appears capable of accounting for our observations in the 4 mol % system. The analysis by Gierer and Wirtz results in an expression for the proton diffusion coefficient in water of the form

$$D = (s^2/6) j_0 \exp(-q/RT) f_0(T,P) \tag{5}$$

where D is the diffusion coefficient; s is the average proton jump distance; j_0 is a frequency factor; q is an activation energy; and $f_0(T,P)$ is a structure factor reflecting the probability of the water structure being favorable to proton jumps.[10,34] The precise definition of these quantities depends on which step in the transport mechanism is regarded as rate determining. Two possibilities are discussed.[10,34] In both models the structure factor is roughly proportional to the fraction of water molecules present in *small* hydrogen-bonded aggregates, and it passes through a broad maximum around 50°. Eigen and DeMaeyer[10] point out that although the Gierer-Wirtz model may not be correct in detail, the form of eq 5 and the result that $f_0(T,P)$ reaches a broad maximum at some temperature in the 0-100° range are probably valid.

Assuming that in water-rich alcohol solutions the proton diffusion mechanism is essentially the same as in pure water, eq 5 is also valid for proton diffusion in the 4 mol % *tert*-butyl alcohol system, provided the structure factor and activation energy q are allowed to depend on solvent composition, denoted by X. Thus, the observed or "apparent" activation energy E_a becomes

$$E_a = q(X) - R\frac{\partial \ln f_0(T,P,X)}{\partial(1/T)} \tag{6}$$

In pure water, the temperature dependence of E_a is slight and continuous since the maximum in the structure factor is very broad; *i.e.*, the second derivative $|\partial^2 \ln f_0(T,P,X)/\partial(1/T)^2|$ is small. However, if it is assumed that the effect of small amounts of *tert*-butyl alcohol (*i.e.*, 4 mol %) is to "sharpen" this maximum, as schematically shown in Figure 9, the apparent activation energy decreases rapidly over a narrow temperature range spanning the maximum; *i.e.*, $|\partial^2 \ln f_0(T,P,X)/\partial(1/T)^2|$ is large at the maximum. Thus, an apparent discontinuity appears in E_a at the temperature corresponding to the maximum in $f_0(T,P,X)$.

As will be demonstrated shortly, a significantly larger second derivative, $|\partial^2 \ln f_0(T,P,X)/\partial(1/T)^2|$ at the structure factor maximum in 4 mol % *tert*-butyl alcohol is consistent with the notion that, at this composition, *tert*-butyl alcohol causes a particularly great enhancement of water structure. Our model assumes that the state of water favorable to proton transport is in an energy state intermediate between highly hydrogen bonded water (large clusters) and "high-energy water" such as monomer configurations. Two different interpretations for this "intermediate energy water" appear possible: (a) small clusters or aggregates, as suggested by the Gierer-Wirtz model, or (b) water of hydration as discussed in the "secondary hydration model" proposed below.

The secondary hydration model is based on the assumption that the stable form for an aqueous proton is the $H_9O_4^+$ hydrate, but for proton transfer to occur, this complex must be further hydrated. As discussed by Eigen and DeMaeyer,[10] since the $H_9O_4^+$ hydrate presumably repre-

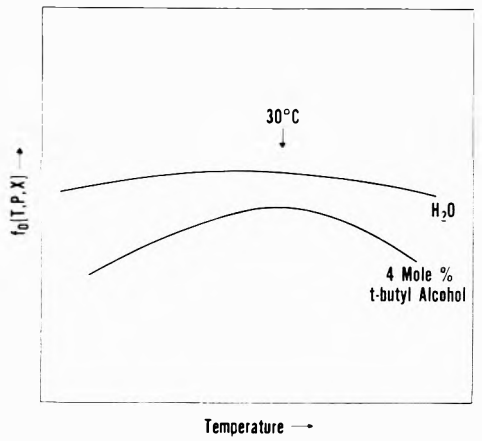

Figure 9. Conjectured variation of the structure factor, $f_0(T,P,X)$, with temperature (schematic).

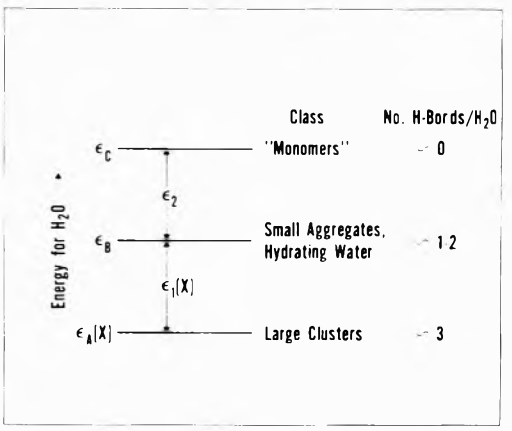

Figure 10. Energy level diagram for three energy state model of water structure (schematic).

sents the stable configuration for aqueous protons, the proton diffusion mechanism is best discussed in terms of this species. Recent quantum mechanical calculations by Newton and Ehrenson[35] support this principle and also strongly suggest that the proton diffusion rate in water is highly sensitive to secondary solvation of the "primary" $H_9O_4^+$ complex. Due to a high activation energy for the jump of a proton from the central oxygen in *isolated* (*i.e.*, gas phase) $H_9O_4^+$ to a terminal position, a hydrated state for $H_9O_4^+$ appears necessary to lower the activation energy and thus allow proton jumping at a rate consistent with the proton diffusion rate in water.[35] Thus, one might regard the aqueous proton as "trapped" in the center of the $H_9O_4^+$ complex until the complex is "suitably" hydrated by one or more water molecules hydrogen bonding to the $H_9O_4^+$ complex, where at least one of the hydrates is in thermal equilibrium. As an example, consider the following schematic sequence

$$H_9O_4^+ + H_2O \rightleftharpoons H_9O_4^+ \cdot H_2O \quad \text{(a)}$$

$$H_9O_4^+ \cdot H_2O + H_2O \rightleftharpoons H_9O_4^+ \cdot 2H_2O \quad \text{(b)}$$

$$H_9O_4^+ \cdot 2H_2O \xrightarrow[\text{slow}]{\text{proton transfer}} \quad \text{(c)}$$

The first two steps are hydration–dehydration processes where the hydrates are regarded as being in thermal equilibrium with all other possible states for water. Proton transfer (step c) is rate determining, and the activation energy refers to proton jumping within the hydrated complex. According to this general model, the structure factor is the fraction of $H_9O_4^+$ complexes which are sufficiently well hydrated to allow proton transport, and therefore, is directly proportional to the fraction of water molecules in this hydrating configuration.

To qualitatively account for the effect of temperature and solvent composition on the structure factor we adopt the simple model summarized in Figure 10. Although the model is discussed in terms of the secondary hydration model interpretation of the structure factor, the conclusions are not restricted to this model. The continuum of states available to a water molecule[36] are divided into three energy classes: (1) the high-energy form of water of energy ϵ_C characterized by ~0 hydrogen bonds per water molecule, denoted "monomer;" (2) an intermediate energy state of energy ϵ_B characterized by ~1–2 hydrogen bonds per water molecule. This state is occupied by the water molecules of small aggregates (*i.e.*, dimers, trimers, ...) and the water molecules hydrating the $H_9O_4^+$ complex; (3) the low-energy state, of energy ϵ_A, which is occupied by water molecules existing in large clusters[36] where the average number of hydrogen bonds per water molecule is ~3.

Since we assume that the effect of *tert*-butyl alcohol is to enhance ice-like or clathrate-like structure (*i.e.*, increase the fraction of large clusters), one or more of the energies ϵ_A, ϵ_B, and ϵ_C must be composition dependent. Here, we make the plausible assumption that, as a first approximation, the energy of water molecules in large clusters is composition dependent, denoted by $\epsilon_A(x)$, while ϵ_B and ϵ_C are composition independent. Thus, in 4 mol % *tert*-butyl alcohol, $\epsilon_A(x)$ is lower than in pure water, thereby increasing the fraction of large clusters. Since ϵ_B and ϵ_C are assumed composition independent, an increase in large clusters is accompanied by a decrease in the fraction of water molecules in state B, and therefore a decrease in the structure factor. Thus, an increase in structure decreases the proton diffusion rate. Moreover, since the energy level for all hydrating water and small clusters is between the large cluster and monomer levels, the fraction of water molecules in the hydrating configurations, and therefore also the structure factor, will pass through a maximum at some temperature.

Since the structure factor is proportional to the fraction of water molecules in state B, N_B/N, we may write

$$f_0(T,P,X) \propto N_B/N = g_B \exp(-\epsilon_B/kT) / \sum_{i=A,B,C} g_i \exp(-\epsilon_i/kT) \quad (7)$$

where k is Boltzmann's constant, and g_i (i = A, B, C) are the degeneracy factors for energy states A, B, and C. Differentiating eq 7, making the substitutions, $\epsilon_C - \epsilon_B = \epsilon_2$ and $\epsilon_B - \epsilon_A(X) = \epsilon_1(X)$, and using the approximation

$$[\epsilon_1(X) + \epsilon_2]/2 = \sqrt{\epsilon_1(X)\epsilon_2}$$

we find that, at the maximum in $f_0(T,P,X)$, we may write

$$\frac{\partial^2 \ln f_0(T,P,X)}{\partial(1/T)^2} = -\left(\frac{\epsilon_1(X)}{k}\right)^2 \left(\frac{N_A}{N}\right)^2 \left[4 + \frac{N_B}{N_C}\left(\frac{\epsilon_1(X) + \epsilon_2}{\epsilon_2}\right)\right] \quad (8)$$

Here, N_A, N_B, and N_C represent the number of water molecules in energy states A, B, and C, respectively. Therefore, assuming that in 4 mol % *tert*-butyl alcohol, the ice-like or clathrate-like structure is significantly enhanced over that in pure water, it follows that N_A and $\epsilon_1(X)$ are

larger. In our model, N_B/N_C is unchanged. Thus, the effect of low levels of *tert*-butyl alcohol is to increase the fraction of large water clusters which has two important consequences: (1) the ratio N_B/N decreases implying that the $H_9O_4^+$ complex is dehydrated, resulting in decreased proton mobility; and (2) the magnitude of the second derivative $|\partial^2 \ln f_0(T,P,X)/\partial(1/T)^2|$ at the structure factor maximum in increased, resulting in a sharp decrease in apparent activation energy, E_a, at this point. This decrease could well be large enough to be observed as a discontinuity since the temperature dependence of the activation energy at this point is directly proportional to $\epsilon_1(X)^2 N_A^2$.

It should be emphasized that the qualitative results contained in eq 8 do not constitute a proof of the proposed diffusion mechanism. Equation 8 may be derived from any mechanism which postulates that the structure factor is proportional to an energy state of water which is between that for large clusters (low energy) and that for monomeric water (high energy). The conclusion particularly relevant to our data is that a plausible interpretation of the proton results may be given without recourse to the "sudden structural melting" argument.

In summary, we conclude that, at least for *tert*-butyl alcohol and perhaps in general, enhanced ice-like, clathrate-like, or solid-like structure in solution *decreases* proton mobilities. In aqueous *tert*-butyl alcohol, the solid-like structure in solution is apparently not sufficiently long range for the solid-state analogy to be useful. Indeed, one might question the usefulness of this analogy when applied to the solution state in general or even the membrane–aqueous interface.[13]

Acknowledgment. Acknowledgment is made to the donors of the Petroleum Research Fund, administered by the American Chemical Society, for (partial) support of this work.

References and Notes

(1) Portions based on a dissertation by J. A. Lanning submitted to the Graduate School, University of Tennessee, in partial fulfillment of the requirements for the Ph.D. Degree, 1972.
(2) N.D.E.A. Fellow, 1970–1972, University of Tennessee.
(3) Present address, The Lilly Research Laboratories, Eli Lilly and Co., Indianapolis, Ind. 46206.
(4) F. Franks and D. J. G. Ives, *Quart. Rev., Chem. Soc.*, **20**, 1 (1966).
(5) D. N. Glew, H. D. Mak, and N. S. Rath, "Hydrogen-Bonded Solvent Systems," A. Covington and P. Jones, Ed., Taylor and Francis, London. See also, D. N. Glew, H. D. Mak, and N. S. Rath, *Chem. Commun.*, 264 (1968).
(6) M. J. Blandamer, D. E. Clark, N. J. Hidden, and M. C. R. Symons, *Chem. Commun.*, 342 (1966).
(7) E. M. Arnett and D. R. McKelvey, *J. Amer. Chem. Soc.*, **87**, 1393 (1965).
(8) T. L. Broadwater and R. L. Kay, *J. Phys. Chem.*, **74**, 3802 (1970).
(9) See, for example, (a) H. S. Frank and M. W. Evans, *J. Chem. Phys.*, **13**, 507 (1945); (b) W. Kauzman, *Advan. Protein Chem.*, **14**, 1 (1959); (c) W. Y. Wen in "Water and Aqueous Solutions," R. A. Horne, Ed., Wiley-Interscience, New York, N. Y., 1971.
(10) M. Eigen and L. DeMaeyer, *Proc. Roy. Soc., Ser. A*, **247**, 505 (1958).
(11) (a) A. von Hippel, D. B. Knoll, and W. B. Westphal, *J. Chem. Phys.*, **54**, 134 (1971); (b) A. von Hippel, *ibid.*, **54**, 145 (1971); (c) M. A Maidique, A. von Hippel, and W. B. Westphal, *ibid.*, **54**, 150 (1971).
(12) von Hippel and coworkers[11] find a factor of 2.5. Earlier work (see ref 10) indicated that the proton mobility in ice is about 20 times that in water. According to von Hippel and coworkers, this earlier work is in error.
(13) J. L. Kavanau, *Fed. Proc.*, **25**, 977 (1966).
(14) A. R. Tourky and A. A. Abdel-Hamid, *Z. Phys. Chem.*, **247**, 289 (1971); *ibid.*, **248**, 9 (1971).
(15) J. A. Lanning and J. Q. Chambers, *Anal. Chem.*, **45**, 1010 (1973).
(16) Z. G. Soos and P. J. Lingane, *J. Phys. Chem.*, **68**, 3821 (1964).
(17) M. von Stackelberg, M. Pilgram, and V. Toome, *Z. Elektrochem.*, **57**, 342 (1953).
(18) M. R. Cannon, R. E. Manning, and J. D. Bell, *Anal. Chem.*, **32**, 355 (1960).
(19) J. A. Lanning, Ph.D. Dissertation, University of Tennessee, Knoxville, Tenn., 1972.
(20) R. A. Robinson and R. H. Stokes, "Electrolyte Solutions," Butterworths, London, 1965.
(21) The relationship, $f_m = (1 + t_+)^2$, was originally suggested[15,19] as a rough approximation. However, eq 4 yields tracer diffusion coefficients which are much more consistent with both theory[22] and proton diffusion data in aqueous alkali halides.[20]
(22) L. Onsager, *Ann. N. Y. Acad. Sci.*, **46**, 241 (1945).
(23) Analysis of conductivity data[8] indicates a lack of significant ion-pair formation for alkali chlorides and bromides in mixed solvents more aqueous than 10 mol % *tert*-butyl alcohol. Since dielectric constants for water–ethylene glycol mixtures[24] are higher than for water–*tert*-butyl alcohol mixtures, one expects even less ion-pair formation in the former mixed solvent system.
(24) G. Akerlof, *J. Amer. Chem. Soc.*, **54**, 4125 (1932).
(25) Transference number data may be estimated using our proton diffusion data and ionic conductance data from ref 8. Additional data required for the calculations are either available[8,24] or may be satisfactorily estimated.
(26) The relaxation effect was calculated using Onsager's theory[22] and physical data from the literature.[25] It should be kept in mind that while this procedure is believed to be quite accurate at low *tert*-butyl alcohol levels, the data beyond 10 mol % alcohol may be subject to systematic errors as high as 5%.
(27) E. V. Goldammer and H. G. Hertz, *J. Phys. Chem.*, **74**, 3734 (1970).
(28) M. J. Pikal and G. E. Boyd, *J. Phys. Chem.*, **77**, 2918 (1973).
(29) It should be noted that while the obstruction effect decreases the mobility of a small species, the viscosity of the system is increased.[20,30] However, since the viscosity change is significantly larger in magnitude than the mobility change, the mobility–viscosity product, or Walden product, increases as the volume fraction of obstructions increases. For example, using Prager's theory[28,31] for the mobility change and the Vand equation[30] for the corresponding viscosity change, calculated Walden products for *dilute* aqueous *tert*-butyl alcohol are in semiquantitative agreement with observed Walden products.[8] Thus, the notion that changes in the Walden product with solvent composition are due only to structural effects appears to be seriously in error.
(30) V. Vand, *J. Phys. Chem.*, **52**, 277 (1948).
(31) S. Prager, *J. Chem. Phys.*, **33**, 122 (1960).
(32) B. E. Conway, J. O'M. Bockris, and H. Linton, *J. Chem. Phys.*, **24**, 834 (1956).
(33) See, for example, (a) F. S. Feates and D. J. G. Ives, *J. Chem. Soc.*, 2798 (1956); (b) F. Franks and D. J. G. Ives, *ibid.*, 741 (1960); (c) G. Salma and D. A. I. Goring, *J. Phys. Chem.*, **70**, 3838 (1966).
(34) A. Gierer and K. Wirtz, *Ann. Phys. Leipzig*, **6**, 257 (1949).
(35) M. D. Newton and S. Ehrenson, *J. Amer. Chem. Soc.*, **93**, 4971 (1971).
(36) A. T. Hagler, H. A. Scheraga, and G. Nemethy, *J. Phys. Chem.*, **76**, 3229 (1972).

Heats of Mixing and Heats of Dilution of Tetrapropylammonium Chloride. Temperature Dependence[1]

Dale D. Ensor,* Henry L. Anderson,[2] and Thomas G. Conally

Department of Chemistry, University of North Carolina at Greensboro, Greensboro, North Carolina 27412 *(Received July 20, 1973)*

Publication costs assisted by the Office of Saline Water, U. S. Department of the Interior

The heats of mixing of tetrapropylammonium chloride with LiCl, KCl, and NaCl at 0.5 *m* have been measured over a 40–80° temperature range. The heats of dilution of tetrapropylammonium chloride have been measured at 40 and 80° over the concentration range of 0.1 to 2.0 *m*. The heats of mixing show relatively little temperature dependence except near 80°. The heat of dilution decreased with increasing temperature above 0.7 *m*. The results have been interpreted in terms of the temperature effect on hydrophobic interactions of the tetrapropylammonium cation.

Introduction

The thermodynamic properties of aqueous solutions of tetraalkylammonium salts have been the subject of numerous investigations at 25°.[3] The unusually large thermal properties exhibited by the large tetraalkylammonium salts have been attributed to the ability of the cations to structure water around their relatively nonpolar surfaces. This proposal by Frank and coworkers[4-6] has been substantiated by investigations of heat capacities,[4] partial molal volumes,[7] excess free energies of mixing,[8] heats of mixing,[9] and heats of dilution.[10,11]

The tetrapropylammonium cation (n-Pr_4N^+) has been labeled a strong hydrophobic structure maker by Wen and Saito.[7] This conclusion was also reached by Kay and coworkers[12,13] and Wood and Anderson.[9] The large negative heat of mixing found by Wood and Anderson was consistent with heat of dilution measurements by Lindenbaum.[10] These two investigations have shown that the large values of the thermodynamic properties are almost entirely dependent upon the structuring properties of the n-Pr_4N^+.

Most studies concerning the tetraalkylammonium salts have been made at 25° and very few data at high temperatures exist. Recently, Lindenbaum and coworkers[14] measured the osmotic coefficients of a large number of tetraalkylammonium salts at 65°. The results were interpreted in terms of the apparent molal entropy of the solvent, $(S_1 - S_1^0)$, which is a measure of the disorder of the solvent in the presence of solutes. The values for n-Pr_4NCl showed that as the temperature increased the $(S_1 - S_1^0)$ increased, corresponding to an increase in the disorder of the solvent at 65°.

The temperature sensitivity of the hydrophobic structure around the n-Pr_4N^+ would yield information concerning the relative strength of n-Pr_4N^+ interactions. Previous studies[15,16] of the temperature dependence of the heats of mixing have been informative concerning specific ion interactions. The present research was designed to expand the knowledge of the nature of hydrophobic structure making in the temperature range 40–80° by using heat of mixing and heat of dilution measurements.

Experimental Section

Materials. All stock solutions were prepared using doubly deionized water and the solutions were stored in polyethylene bottles. The NaCl and KCl solutions were made from Mallinckrodt analytical reagent salts. The LiCl was obtained from Research Inorganic Chemicals. The stock solutions were approximately 4.0 *m* with the exact concentrations determined by standard AgCl gravimetric analysis.

The n-Pr_4NCl was prepared from n-Pr_4NI obtained from Eastman Organic Chemicals. The iodide salt was determined to be 99.9% pure by AgI gravimetric analysis. The n-Pr_4NCl was obtained by passing n-Pr_4NI through an ion exchange column containing approximately 270 g of Dowex 2-x4 resin on the Cl^- cycle. The conversion to the chloride salt was determined to be better than 99.9%.

The solutions used in the experimental work were made by diluting a known weight of stock solution with a known weight of water.

Calorimeter. All experimental measurements were made using a 250-ml Dewar calorimeter with microdegree sensitivity. The calorimeter was submerged in a constant temperature water bath. The system has been described previously.[15]

Results and Data Treatment

The experimental heats of mixing were fitted by a method of least squares to the equation.[17]

$$\Delta H_{mix}(\text{cal/kg of solvent}) = RTI^2y(1 - y)[h_0 + (1 + 2y)h_1] \quad (1)$$

where R is the gas constant, T is the temperature, I is the total ionic strength, y is the mole fraction having the largest formula weight, h_0 is the magnitude of interaction, and h_1 is the first-order skew term.

The RTh_0 and RTh_1 values obtained from eq 1 are listed in Table I.[18] A statistical F test (95% confidence level) was performed on each mixture to test the significance of h_1. In those cases where h_1 was not justified, it was set equal to zero and the data were refitted using RTh_0.

For each mixture, 10–12 experimental determinations were made between 0.0 and 0.2 and 0.8 and 1.0 mole fraction. It has been shown that this is sufficient to determine the mixing parameters.[19,20]

Since the heat of dilution going to infinite dilution, which is equal to but of opposite sign of the relative apparent molal heat content, ϕ_L, is not a measurable quan-

tity, a $\Delta\phi_L$, which is the heat evolved in going from an initial to a finite final concentration, is measured. The extended Debye-Hückel equation for 1-1 electrolytes is then used to calculate the ϕ_L of the finite final concentration going to infinite dilution.

$$\phi_L = A_H m^{1/2}[1/(1 + Am^{1/2}) - \sigma(Am^{1/2})3] + Bm + Cm^{3/2} \quad (2)$$

ϕ_L = relative apparent molal heat content, A_H = Debye-Hückel limiting slope, A = distance of closest approach, B,C = adjustable differential coefficients, m = molality, $\sigma = 3(m^{1/2})^{-3}[1 + m^{1/2} - 2 \ln (1 + m^{1/2} - 1/(1 + m^{1/2}))]$. Jongenburger and Wood[21] have established that eq 2 is valid for 1-1 electrolytes with an excess enthalpy greater than −36 cal/mol at 0.1 m.

All experimental data with an initial concentration equal to or less than 0.1 m were substituted into eq 2 and a least-squares computer program was used to obtain the best values of B and C. The results of the extrapolation are contained in Table II.[18]

The ϕ_L of n-Pr_4NCl was measured at 40 and 80° over the concentration range 0.1-2.0 m. The ϕ_L of all experimental final concentrations was evaluated by substitution of the B and C values into eq 2. This value, added to the experimentally determined $\Delta\phi_L$, yielded ϕ_L for that particular initial concentration. The experimental data, $\Delta\phi_L$, for n-Pr_4NCl at 40 and 80° and smoothed ϕ_L values are listed in Tables III and IIIA.[18] The entire extrapolation procedure and ϕ_L data treatment has been described by Ensor and Anderson.[22]

Discussion

Previous measurements of heats of mixing and heats of dilution of tetraalkylammonium salts have been interpreted using the Frank, Evans, and Wen picture of large hydrophobic structure makers. In a n-Pr_4NX-MX mixing one would expect three different kinds of like-charged pair interactions. These interactions are (1) reduction of n-Pr_4N^+-n-Pr_4N^+ overlap, (2) reduction of M^+-M^+ overlap, and (3) formation of a n-Pr_4N^+-M^+ overlap. Wood and Anderson[9] assumed that in 0.5 m solutions the large hydration sphere of the n-Pr_4N^+ must overlap with that of its nearest neighbor forming a n-Pr_4N^+-n-Pr_4N^+ cosphere. Upon mixing with the smaller cations (dilution of n-Pr_4N^+) there is considerable reduction of overlap allowing each n-Pr_4N^+ to complete its hydrophobic hydration sphere to a greater degree. This causes an increase in the total amount of structured water, thus liberating heat. The reduction of the n-Pr_4N^+ overlap was assumed to be so large that it masked all other interactions. A similar interpretation was used by Lindenbaum[10] who concluded that the heat of dilution of n-Pr_4N^+ was anion independent and the primary interaction was the reduction of the cation cosphere.

The RTh_0 values for the n-Pr_4N^+ mixings (Table I) are all large negative values and are similar in magnitude to the values reported at 25°. The smaller cations used seem to have only small effects on the size of RTh_0. The Na^+ and K^+ mixings are similar while the Li^+ values are more negative. This effect is probably due to the fact that Li^+ is a strong structure maker. The K^+ has been classified as a structure breaker and the Na^+ as a borderline case showing structure-breaking characteristics at the temperatures investigated.[16]

All mixings in the present research had significant RTh_1 values. Reilly and Wood[23] have shown that triplet interactions such as n-Pr_4N^+-n-Pr_4N^+-n-Pr_4N^+, n-Pr_4N^+-M^+-n-Pr_4N^+, M^+-M^+-M^+, and M^+-n-Pr_4N^+-M^+ contribute to the magnitude of RTh_1. Since the values of RTh_1 remain fairly constant for all mixings no matter which cation is used, it is probable that the major triplet interaction was n-Pr_4N^+-n-PrN^+-n-Pr_4N^+. The results of previous mixings of Li^+, K^+, and Na^+ [15] showed no significant RTh_1 values which supports the above hypothesis.

The nature of the hydrophobic structure-made water around tetraalkylammonium ions was proposed by Frank, Evans, and Wen[4,5] to be similar to the water structure formed around ethane and the rare gases. The water structure formed would be susceptible to thermal agitation and as the temperature increased, the hydrophobic structure would "melt off".[6] Eley[24] reported a large exothermic heat of solution for argon at 25°, but found the value decreased to near zero at 80°. Using the Frank, Evans, and Wen ideas, one would interpret the results to mean that a large number of water molecules are structured around argon at 25° but that as the temperature is increased the water structure breaks down.

The temperature dependence of RTh_0 values for the n-Pr_4N^+ mixings are rather similar in temperature dependence. Since the smaller cations used were different in size and charge density, the similarities observed may be attributed to the n-Pr_4N^+. The very definite decrease in RTh_0 between 60 and 80° indicates that there is appreciable reduction in the hydration sheath of n-Pr_4N^+ at 80°. This is consistent with previous interpretations and predictions concerning hydrophobic structure making.

The curves in Figure 1 show little, if any, temperature dependence in the range between 25 and 60°. Using the Wood and Anderson interpretation of heats of mixing for n-Pr_4N^+, this would indicate that the n-Pr_4N^+ is completing its hydration sphere to almost the same extent at 60° as it is at 25°. If the hydrophobic structured water around the n-Pr_4N^+ was similar to that around argon, one would expect the RTh_0 values should decrease gradually from 25 to 80°.

The measurements of heats of dilution of tetraalkylammonium salts at 25° have also been interpreted[10,11] as a measure of cation-cation interaction. The behavior of ϕ_L as a function of temperature should be an indication of the relative strengths of n-Pr_4N^+-n-Pr_4N^+ interactions.

Previous measurements of ϕ_L for NaCl as a function of temperature have shown that as temperature increased the magnitude of ϕ_L increased. The behavior of ϕ_L for n-Pr_4NCl as a function of temperature (Figure 2) is different. Since at dilute concentrations the n-Pr_4NCl was assumed to obey the Debye-Hückel limiting law, ϕ_L increased with increasing temperature at concentrations below 0.2 m. The family of ϕ_L curves goes through a region of scrambling but at concentrations greater than 0.7 m the ϕ_L for n-Pr_4NCl decreases with increasing temperature. This indicates that the hydrophobic interactions of the n-Pr_4NCl are not only temperature sensitive, but dependent upon the concentration as well.

Unambiguous information cannot be obtained by a direct comparison of the ΔH mix and ϕ_L data since the mixings were done at 0.5 m which falls within the region where the ϕ_L values are scrambled. A more clear-cut comparison would be possible if the mixing had been done at 1.0 m. Nevertheless, the ϕ_L values predict a gradual but

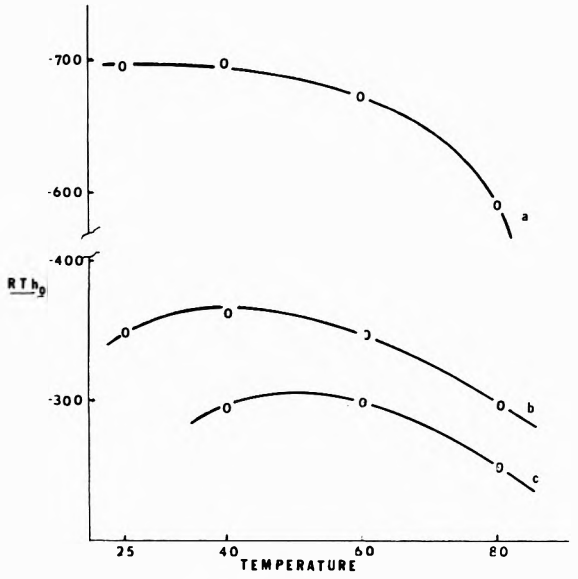

Figure 1. RTh_0 (cal mol^{-2} kg^{-1}) *vs.* temperature (°C) for (a) *n*-Pr_4NCl–LiCl; (b) *n*-Pr_4NCl–KCl; (c) *n*-Pr_4NCl–NaCl. The 40, 60, and 80° data are from this work; the 25° data are from ref 9.

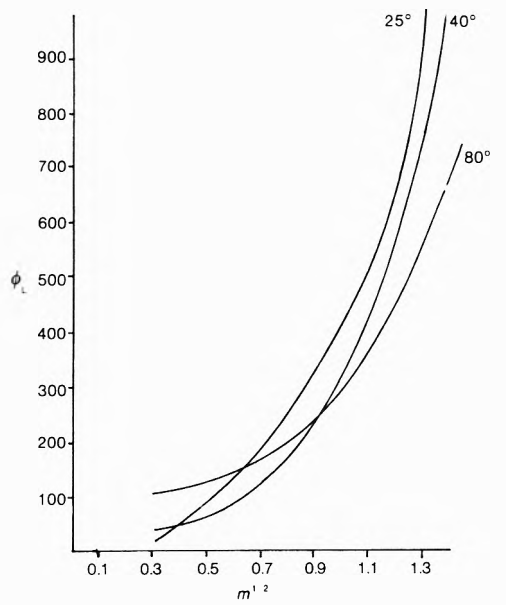

Figure 2. Relative apparent molal heat content, ϕ_L (cal/mol) *vs.* $m^{1/2}$. The 40 and 80° data are from this work; the 25° data are from ref 10.

definite decrease in the amount of *n*-Pr_4N^+–*n*-Pr_4N^+ interactions as the temperature is increased.

A study of the effect of temperature on the amount of hydrophobic interactions can lead to one possible explanation[25] for the behavior of *n*-Pr_4N^+. One would expect that as the temperature increased, the hydration sheath around *n*-Pr_4N^+ would break down. This breakdown in the structured water around the cation would increase the attraction of the hydrocarbon ends for each other. The behavior of RTh_0 as a function of temperature can be explained using the above model. As the temperature increases from 25 to 60°, the hydration sphere begins to break down; this effect would lead to a decrease in the amount of heat given off when overlapping *n*-Pr_4N^+ hydration spheres are mixed. However, the increased exposure of the hydrocarbon portions of the *n*-Pr_4N^+ allows more cospheres to overlap and this effect causes heat to be liberated upon mixing. These two opposite effects tend to balance one another so that the magnitude of RTh_0 remains relatively constant up to 60°. The decrease in RTh_0 observed between 60 and 80° indicates that at some point above 60° the solution has become saturated with *n*-Pr_4N^+–*n*-Pr_4N^+ cospheres. The breakdown of the hydration sphere then becomes the dominant effect and a reduction in the magnitude of RTh_0 is observed.

The ϕ_L data can be explained in a similar manner. The *n*-Pr_4NCl solutions above 0.7 *m* are close to being saturated with cospheres. The major effect upon dilution is the reduction in the size of the *n*-Pr_4N^+ hydration sheath and thus ϕ_L above approximately 0.7 *m* is found to decrease with increasing temperatures. For low concentration solutions there is no saturation effect and the increasing number of cosphere overlaps as the temperature is increased is more important than the decreased heat effect of each overlap. At very low concentrations, the *n*-Pr_4NCl approaches the Debye–Hückel limiting law and behaves as predicted.

It should be noted that a similar explanation of the temperature dependence of *n*-Pr_4NCl could be made using a "clathrate-like" structure proposed by Wen and Saito.[7] Organic solutes have been shown to stabilize water molecules into hydrogen-bonded cages. The alkyl chains of *n*-Pr_4N^+ could also stabilize water molecules into a structure similar to those formed around an organic solute particle.

Summary

The hydrophobic structure-made water around *n*-Pr_4N^+ is found to be temperature sensitive. As the temperature increases the size of the hydration sphere seems to decrease, but the extent of the temperature dependence is less than would have been predicted using the Frank, Evans, and Wen model of a hydrophobic structure maker. The unusual temperature dependence observed has been attributed to increased interactions of the hydrocarbon portions of the *n*-Pr_4N^+ as the temperature increases.

Acknowledgments. It is with great sorrow that we report that Henry L. Anderson was killed in an automobile accident shortly before the completion of this work. All credit for its inception should go to him.

Dale D. Ensor would like to thank John R. Jezorek and R. H. Wood for helpful suggestions and discussion concerning the completion of this work.

Supplementary Materials Available. Tables I, II, III, and IIIA will appear following these pages in the microfilm edition of this volume of the journal. Photocopies of the supplementary material from this paper only or microfiche (105 × 148 mm, 20× reduction, negatives) containing all of the supplementary material for the papers in this issue may be obtained from the Journals Department, American Chemical Society, 1155 Sixteenth St., N.W., Washington, D. C. 20036. Remit check or money order for $3.00 for photocopy or $2.00 for microfiche, referring to code number JPC-74-77.

References and Notes

(1) Presented in part before the Division of Physical Chemistry, Southeast-Southwest Regional Meeting of the American Chemical Society, New Orleans, La., December 2–4, 1970. This study was aided by a grant from the Office of Saline Water, U. S. Department of the Interior.
(2) Deceased.

(3) (a) W. Y. Wen, "Water and Aqueous Solutions, Structure, Thermodynamics and Transport Processes," R. A. Horne, Ed., Wiley-Interscience, New York, N. Y., 1971, Chapter XV. (b) H. L. Anderson and R. H. Wood, "Water Comprehensive Treatise," Vol. 3, F. Franks, Ed., Plenum Press, New York, N. Y., 1973, Chapter XIV.
(4) H. S. Frank and M. B. Evans, *J. Chem. Phys.*, **13**, 507 (1945).
(5) H. S. Frank and W. Y. Wen, *Discuss. Faraday Soc.*, **124**, 133 (1957).
(6) H. S. Frank, *Z. Phys. Chem.*, **228**, 367 (1965).
(7) W. Y. Wen and S. Saito, *J. Phys. Chem.*, **68**, 2639 (1964).
(8) W. Y. Wen, K. Miyajuma, and A. Otsuka, *J. Phys. Chem.*, **75**, 2148 (1971).
(9) R. H. Wood and H. L. Anderson, *J. Phys. Chem.*, **71**, 1871 (1967).
(10) S. Lindenbaum, *J. Phys. Chem.*, **70**, 814 (1966).
(11) R. H. Wood, H. L. Anderson, J. D. Beck, J. R. France, W. E. deVry, and L. J. Soltzberg, *J. Phys. Chem.*, **71**, 2149 (1967).
(12) R. L. Kay, T. Vituccio, C. Zawoyoki, and D. F. Evans, *J. Phys. Chem.*, **70**, 2336 (1965).
(13) R. L. Kay and D. F. Evans, *J. Phys. Chem.*, **70**, 2325 (1966).
(14) S. Lindenbaum, L. Leifer, G. E. Boyd, and J. W. Chase, *J. Phys. Chem.*, **74**, 761 (1970).
(15) H. L. Anderson and L. A. Petree, *J. Phys. Chem.*, **74**, 1455 (1970).
(16) H. L. Anderson, R. D. Wilson, and D. E. Smith, *J. Phys. Chem.*, **75**, 1125 (1971).
(17) H. L. Friedman, *J. Phys. Chem.*, **32**, 1134 (1960).
(18) See paragraph at end of text regarding supplementary material.
(19) Y. C. Wu, M. B. Smith, and T. F. Young, *J. Phys. Chem.*, **69**, 1868 (1965).
(20) R. H. Wood and R. W. Smith, *J. Phys. Chem.*, **69**, 2974 (1965).
(21) H. S. Jongenburger and R. H. Wood, *J. Phys. Chem.*, **69**, 4231 (1965).
(22) D. D. Ensor and H. L. Anderson, *J. Chem. Eng. Data*, **18**, 205 (1973).
(23) P. J. Reilly and R. H. Wood, *J. Phys. Chem.*, **73**, 4292 (1969).
(24) D. D. Eley, *Trans. Faraday Soc.*, **35**, 128 (1939).
(25) R. H. Wood, private communication.

Ultrasonic Absorption in Aqueous Solutions of Nucleotides and Nucleosides. II. Kinetics of Proton Exchange in Adenosine 5′-Monophosphate

Jacques Lang, Jean Sturm, and Raoul Zana*

C.N.R.S., Centre de Recherches sur les Macromolécules, 67083 Strasbourg-Cedex, France *(Received July 6, 1973)*

Publication costs assisted by the Centre National de la Recherche Scientifique, France

The excess ultrasonic absorption of aqueous solutions of 5′-adenosine mononucleotide (5′AMP) solutions has been measured in the frequency range 1–115 MHz and at pH 5.05 where the absorption is maximum. The relaxation spectra can be fitted by a relaxation equation with a single relaxation frequency. The excess absorption is attributed to a proton exchange between two molecules of 5′AMP in differently ionized forms coupled with the stacking of the nucleotide molecules. (In this work stacking is assumed to be limited to dimerization.) Several reaction mechanisms are proposed and discussed. The results permit us to obtain the following new information: (1) the rate constants for the proton exchange between 5′AMP molecules and for the proton transfer involving the phosphate moiety of the nucleotide molecule and (2) the dimerization constant of 5′AMP and the volume change upon dimerization. This last quantity is found to be positive, *i.e.*, of the same sign as for hydrophobic bonding.

Introduction

In the first part of this work[1] we reported ultrasonic absorption measurements on aqueous solutions of nucleosides and nucleotides showing maxima on the plots of α/f^2 (α = ultrasonic absorption coefficient, f = frequency) *vs.* pH, in the pH range 1–13. These maxima were attributed to the following two types of proton transfer equilibria: (a) hydrolysis and protolysis equilibria which appear to be responsible for the absorption maxima of small amplitude observed in the acid and/or in the alkaline range (Such equilibria have been extensively studied by means of ultrasonic methods for amino acids,[2,3] polypeptides,[4] and proteins.[3,5]) and (b) proton exchange equilibria between three differently ionized forms of the same nucleotide. These processes occur only with nucleotides which contain a nitrogen atom protonable in the acid range. Thus far ultrasonic methods have been used only for the study of proton exchange between two different molecules.[6]

The purpose of this paper is to report new experimental results which allow a quantitative study of proton exchange for adenosine 5′-monophosphate (5′AMP) around pH 5. In addition to the values of the rate constants and volume change for the proton exchange our results provide new evidence for the association of 5′AMP through base stacking.

Materials and Methods

5′AMP has been purchased from Sigma and used without further purification. All solutions were prepared with freshly deionized distilled water. The pH values were adjusted by addition of small amounts of HCl and NaOH solutions and measured using a Tacussel pH meter with a glass electrode and a standard calomel electrode. The pH meter was calibrated using Merck buffers.

A two crystal interferometer[7] was used for the ultrasonic absorption measurements at frequencies between 1 and 10 MHz, and the standard pulse technique[8] in the range 6–150 MHz.

Experimental Results

We have previously shown (in ref 1 see ref 7, Figure 5) that for aqueous solutions of 5′AMP the absorption maxi-

mum occurs at pH = pH_A = 5.05 ± 0.1, independent of concentration (in the range 0.02–0.15 *M*) and ionic strength (in the range 0–0.15 *M* KCl). As part of the present work we have also found that pH_A is independent of frequency. Within experimental error, $pH_A = (pK_{P2} + pK_N)/2$ where pK_{P2} = 6.45 and pK_N = 3.8 are the pK_a's of the secondary phosphoric acid function and of the protonable N_1 nitrogen atom of 5′AMP, respectively.

In this work ultrasonic absorption measurements have been performed in the range 1–115 MHz on four solutions of 5′AMP with concentrations 0.016, 0.05, 0.099, and 0.148 *M* at pH = pH_A and at pH >9 where the proton exchange contribution to the excess absorption of the solution is negligible.[1] The difference $\Delta\alpha/f^2$ between the values of α/f^2 at a given pH and at pH >9 can be taken as the contribution of the proton exchange reaction. In Figure 1 the value $(\Delta\alpha/f^2)_A$ of $\Delta\alpha/f^2$ at pH = pH_A, has been plotted as a function of f for four solutions of 5′AMP. (See paragraph at end of paper regarding supplementary material.)

These results obey eq 1, where f_R is the relaxation frequency and A_R the relaxation amplitude at $f \ll f_R$. The

$$(\Delta\alpha/f^2)_A = A_R/(1 + f^2/f_R^2) \qquad (1)$$

values of f_R and A_R are given in Figure 1. The variations of these two quantities as a function of the nucleotide concentration c_N are shown in Figures 2 and 3. The significant change of f_R with c_N and the nonlinear variation of A_R with c_N provide evidence that a conformational equilibrium[9] alone cannot be responsible of the observed relaxation process.

Reaction Mechanisms and Discussion

A. General Considerations. Around pH 5 the primary phosphoric acid function is completely ionized and 5′AMP molecules are essentially in four differently ionized forms

$$\begin{aligned} A &= N_1\text{—R—}PO_3^{-} \\ B &= {}^{+}HN_1\text{—R—}PO_3^{2-} \\ C &= N_1\text{—R—}PO_3H^{-} \\ D &= {}^{+}HN_1\text{—R—}PO_3H^{-} \end{aligned} \qquad (2)$$

where N_1 is the protonable nitrogen atom of the base and R the nonionized part of the molecule. Calculations carried out using the values of pK_{P2} and pK_N show that around pH 5, B exists in the solution at a concentration much smaller than A, D, and C. For this reason B is neglected in the major part of the discussion which follows.

The above expressions show that A is a proton acceptor and D a donor. According to the general reaction scheme proposed by Eigen,[10] the equilibria between these species around pH 5, may be expressed by

$$\begin{array}{ccc} & A + H^+ + C & \\ {\scriptstyle k_{31}}\swarrow\nearrow{\scriptstyle k_{13}} & & {\scriptstyle k_{32}}\swarrow\nearrow{\scriptstyle k_{23}} \\ A + D & \underset{k_{2'1}}{\overset{k_{12'}}{\rightleftharpoons}} & 2C \end{array} \qquad (3)$$

where the reactions involving H^+ can be assumed to be in the steady state. The expressions for the relaxation frequency f_R and relaxation amplitude $\Delta\alpha/f^2$ have been obtained[11] for reaction 3. They predict a maximum of absorption at pH = $(pK_{P2} + pK_N)/2 = pH_A$ in agreement with the experimental results but indicate that $(\Delta\alpha/f^2)_A$ and f_R should vary linearly with c_N while the experimental variations are not linear. Some other process must therefore be combined with reaction 3 to account for the

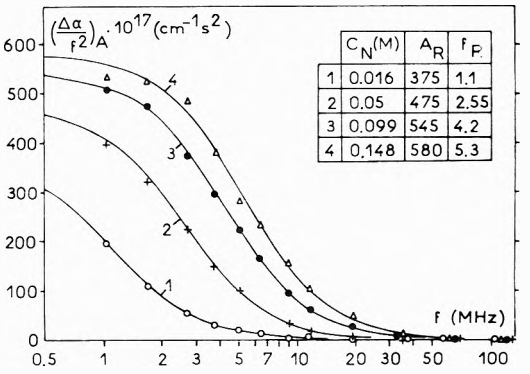

	c_N(M)	A_R	f_R
1	0.016	375	1.1
2	0.05	475	2.55
3	0.099	545	4.2
4	0.148	580	5.3

Figure 1. Ultrasonic relaxation spectra of 5′AMP in aqueous solution at pH 5.05 and 25°.

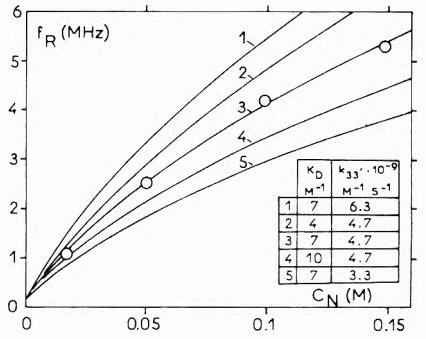

	K_D M^{-1}	$k_{33'} \cdot 10^{-9}$ M^{-1} s^{-1}
1	7	6.3
2	4	4.7
3	7	4.7
4	10	4.7
5	7	3.3

Figure 2. Variation of the relaxation frequency f_R with the nucleotide concentration c_N: (O) experimental results. The solid lines are curves calculated as explained in the text, using f_0 = 0.15 MHz and the values of $k_{33'}$ and K_D given in the figure.

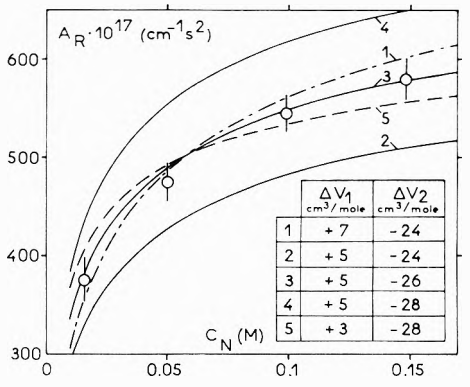

	ΔV_1 cm^3/mole	ΔV_2 cm^3/mole
1	+7	-24
2	+5	-24
3	+5	-26
4	+5	-28
5	+3	-28

Figure 3. Variation of the relaxation amplitude A_R with the nucleotide concentration c_N: (O) experimental results. The solid lines and the broken lines are curves calculated as explained in the text, using the values f_0 = 0.15 MHz, K_D = 7 M^{-1}, $k_{33'}$ = 4.76 × 10^9 M^{-1} sec^{-1}, and the values of ΔV_1 and ΔV_2 given in the figure.

experimental results of Figures 1–3. At this point it must be emphasized that taking B into account despite its very low concentration also yields relaxation frequencies and amplitudes linearly dependent on c_N. Indeed for reactions such as

$$\begin{array}{ccc} A + H^+ + A & & A + H^+ + B \\ \swarrow\nearrow & \text{or} & \swarrow\nearrow \\ A + C \underset{k_2}{\overset{k_1}{\rightleftharpoons}} A + B & & A + D \underset{k_2}{\overset{k_1}{\rightleftharpoons}} 2B \end{array} \qquad (4)$$

the corresponding relaxation frequencies can be written as

$$2\pi f_R = k_1[1] + k_2[2] + F(H^+) \quad (5)$$

where $F(H^+)$ is independent of c_N and [1] and [2] are linearly dependent on the concentrations of A, B, C, and D, which are proportional to c_N.

On the other hand, the coupling of reaction 3 with conformational equilibria[9] also yields results incompatible with the experimental observations. Indeed, if reactions such as C $\rightleftarrows$ C′, A $\rightleftarrows$ A′, or D $\rightleftarrows$ D′ are introduced into reaction mechanism 3, the expressions for the two relaxation frequencies of this system of coupled reactions predict either no variation or a linear increase with c_N (see Appendix I).

On the contrary, the coupling of reaction 3 with association equilibria of 5′AMP molecules accounts for the results of Figures 1-3 as will be seen below. Indeed, 5′AMP molecules as well as other nucleotides, nucleosides, and bases are known[12,13] to associate by means of vertical stacking of base rings.[12] A kinetic study of stacking of N_6-N_9 dimethyladenine (DMA) has been undertaken by means of ultrasonic absorption techniques.[14] The results of this study favor the isodesmic reaction model for base stacking and indicate that dimers are predominant at low concentration. The association constant of 5′AMP has been found to be (8 ± 2) M^{-1} from the results of Rossetti and Van Holde[15] using the method that these authors reported elsewhere.[16] It must be pointed out that osmotic pressure data[12] on 5′AMP disodium salt yield at low concentrations (<0.1 M) a value of the association constant in excellent agreement with that obtained from centrifugation data,[15,16] assuming dimers as the only associated species. Thus, for 5′AMP the associated constant is about 5 times smaller than for DMA.[14] Moreover the concentrations used in the present work were smaller than those reported in ref 14. For these reasons the association of 5′AMP has been assumed to be limited to dimerization in the reaction schemes which follow.

Dimerization may involve species A or D (model I), species C (model II), or appear in a more complex manner (model III).

Model I: Reaction 3 coupled with

$$2A \underset{k_d}{\overset{k_a}{\rightleftharpoons}} A_2 \quad (6)$$

or

$$2D \underset{k_d}{\overset{k_a}{\rightleftharpoons}} D_2 \quad (6')$$

Model II

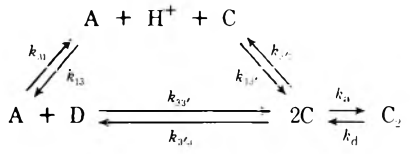

(7)

Model III

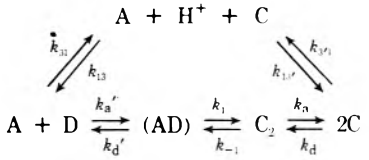

(8)

where (AD) refers to a mixed stack. In models I-III all reactions involving H^+ and (AD) are assumed to be in the steady state. The essential difference between models II and III is that stacking is a preliminary step to proton exchange in model III while these two processes may be considered as independent in model II (and I) *i.e.*, the encounter between two species C (or A or D) may result in either a proton exchange or an association.

Two relaxation frequencies characterize each of the three above models, while a single relaxation process has been observed in the frequency range investigated in this work. A similar finding has been reported by Brennan and Kustin[17] from an ultrasonic study of proton transfer in basic purine solutions. These authors concluded that proton transfers are much slower than stacking equilibria which appear to be characterized by high relaxation frequencies and small relaxation amplitudes. The results reported in ref 14 were said to support these conclusions.[17] On the other hand, a comparison of the results of ref 14 with those of Figure 1 shows that at a given concentration the relaxation frequency for stacking is at least one order of magnitude larger than for proton exchange. Also, at 50 MHz the excess absorption due to stacking in a 0.1 M DMA solution is about 13 × 10^{-17} cm^{-1} sec^2 while in a 0.1 M 5′AMP solution the excess absorption is only 5 × 10^{-17} cm^{-1} sec^2 and appears to arise only from proton exchange, within experimental error. Thus our results seem to indicate that in 5′AMP stacking may occur at much higher frequencies than in DMA and with a much smaller amplitude. This conclusion is very important since it allows us to use simplified equations for the derivation of the expressions of the relaxation frequencies and relaxation amplitudes characterizing the above models (see Appendix II).

We shall now examine each of the three reaction mechanisms in turn.

B. Reaction Mechanism I. In the case of reaction 3 coupled with reaction 6 the two relaxation frequencies have been derived as explained in Appendix II with the assumption that dimerization is much faster than proton exchange. These expressions are not given because a fit with the experimental results of Figure 2 is obtained only with values of K_D above 100 M^{-1}.

Similar calculations performed with the model where reaction 3 is coupled with reaction 6′ led to identical conclusions, *i.e.*, a fit is obtained only when values of K_D one order of magnitude larger than the experimental one[15,16] are used. For this reason the reaction mechanisms where stacking involves A or D have been discarded. The reaction mechanism where A and D self dimerize simultaneously has not been considered in detail but is expected to yield similar results.

C. Reaction Mechanism II. The rate equations for reaction 7 have been obtained using c_A and c_{C_2} as independent variables ($c_{C_2} = c_1$ and $c_A = c_2$ in eq AII,1). With the assumption that H^+ is in a steady state and dimerization is much faster than proton exchange the two relaxation frequencies are readily obtained using eq AII,2

$$2\pi f_I = k_d(1 + 4K_D\bar{c}_C) \quad (9)$$

$$2\pi f_{II} = \left(\bar{c}_A + \bar{c}_D + 4\frac{\bar{c}_C r^2}{4K_D\bar{c}_C + 1}\right)\psi \quad (10)$$

with

$$\psi = k_{33'} + \phi \quad (11)$$

where

$$\phi = \frac{k_{13}'k_{31}}{k_{13}\bar{c}_C + k_{13}'\bar{c}_A}$$

$$r^2 = K_{P2}/K_N = 2.23 \times 10^{-3} \quad (12)$$

$$\bar{c}_C = \frac{-S_H^2 + (S_H^2 + 8K_D c_N)^{1/2}}{4K_D} \quad (13)$$

$$S_H = 1 + \frac{\bar{c}_H}{K_N} + \frac{K_{P2}}{\bar{c}_H} \qquad \bar{c}_A = \bar{c}_C\frac{K_{P2}}{\bar{c}_H} \qquad \bar{c}_D = \bar{c}_C\frac{\bar{c}_H}{K_N} \quad (14)$$

where the c's refer to equilibrium concentrations and the k's to the rate constants which are defined by reaction 7.

The excess absorption is given by eq AII,3 with

$$\Delta V_I = \Delta V_1 = \bar{V}_{C_2} - 2\bar{V}_C \quad (15)$$

$$\Delta V_{II} = \frac{4K_D\bar{c}_C}{1 + 4K_D\bar{c}_C}\Delta V_1 - \Delta V_2$$

with

$$\Delta V_2 = \bar{V}_A + \bar{V}_D - 2\bar{V}_C \quad (16)$$

$$\Gamma_I = K_D\bar{c}_C^2/(1 + 4K_D\bar{c}_C) \quad (17)$$

$$\Gamma_{II} = \frac{(4K_D\bar{c}_C + 1)\bar{c}_C}{2[(4K_D\bar{c}_C + 1)r^{-1} + 2]} \quad (18)$$

D. Reaction Mechanism III. This reaction mechanism is more complicated than model II. Several assumptions have been made however which make it possible to derive the relaxation frequencies and Γ functions.

First the reactions involving H^+ and (AD) have been assumed to be in a steady state and $k_1 \gg k_a'$. This is equivalent to assuming that the proton exchange between A and D is diffusion controlled. Also, as in model II, dimerization ($2C \rightleftharpoons C_2$) is assumed to be much faster than proton exchange. This implies that dimerization is diffusion controlled.

With these assumptions the relaxation frequencies f_I' and f_{II}' for reaction mechanism III are then given by the same equations as for model II if ψ in eq 10 is replaced by ψ' given by

$$\psi' = k_a' + \phi \quad (19)$$

In deriving the expressions of f_I' and f_{II}' the quantity $k' = k_d'k_{33'}/k_{33'} = k_d'r^2$ has been neglected with respect to k_d, in accordance with the above assumptions. Also we have taken into account the fact that in the whole concentration range $k_d \gg 2r\phi c_C$. As in model II $\bar{c}_A$, $\bar{c}_C$, and $\bar{c}_D$ are given by eq 13 and 14.

The volume changes are given by (see eq AII,4)

$$\Delta V_I' = \Delta V_1' = \bar{V}_C - \bar{V}_{C_2}/2 = -\Delta V_1/2 \quad (20)$$

$$\Delta V_{II}' = \frac{2}{1 + 4K_D\bar{c}_C}\Delta V_1' - \Delta V_2' \quad (21)$$

with

$$\Delta V_2' = \bar{V}_A + \bar{V}_D - \bar{V}_{C_2} =$$
$$(\bar{V}_A + \bar{V}_D - \bar{V}_{AD}) + (\bar{V}_{AD} - \bar{V}_{C_2}) \quad (22)$$

The first term on the right side of eq 22 corresponds to the volume change for the dissociation of the mixed stack (AD) and has been assumed equal to $-\Delta V_I$ (see eq 15). With this assumption the second term on the right side of eq 22 becomes equal to ΔV_2 (see eq 16). Therefore $\Delta V_2' = -\Delta V_I + \Delta V_2$ and

$$\Delta V_{II}' = \Delta V_{II} \quad (23)$$

For the Γ functions Γ_I' an Γ_{II}' it can be easily shown that

$$\Gamma_I' = 4K_D\bar{c}_C^2/(1 + 4K_D\bar{c}_C) = 4\Gamma_I \quad (24)$$

and

$$\Gamma_{II}' = \Gamma_{II} \quad (25)$$

From an inspection of eq 9-25 it clearly appears that the excess absorption is given by the same equation for reaction mechanisms II and III if $k_{33'}$ is identified with k_a'. Therefore the calculations of the various quantities which can be obtained from the experimental results will be valid for both models. On the other hand, it is evident that a choice between the two reaction mechanisms cannot be made on the basis of ultrasonic absorption data alone. This question is examined below.

E. Calculations of the Rate Constants and Volume Changes Characterizing Reaction Mechanisms II and III. It must be first pointed out that additional evidence that the observed excess absorption cannot be due to dimerization may be found in the expression of $2\pi f_I$ at pH = pH_A, given by

$$2\pi f_I = k_d([(2r + 1)^2 + 8K_D c_N]^{1/2} - 2r) \quad (26)$$

Indeed, the results of Figure 2 cannot be represented by eq 26 whatever the values taken for k_d and K_D. On the contrary, the equations relative to proton exchange can provide an excellent representation of the experimental results of Figures 2 and 3 and also of Figure 4 ($(\Delta\alpha/f^2)_A$ *vs.* c_N at 2.82 MHz) and of Figure 5 ($\Delta\alpha/f^2$ *vs.* pH at 2.82 MHz and at different concentrations). As the calculations involve five adjustable quantities ($k_{33'}$, K_D, $k_{13'}$, ΔV_1, and ΔV_2) the way in which they were performed and the involved assumptions demand several remarks.

First we have taken a value of 3 for the ratio $k_{13'}/k_{13}$. Indeed reactions $A + H^+ \rightleftharpoons C$ and $C + H^+ \rightleftharpoons D$ are very likely diffusion controlled.[6,10] Therefore $k_{13'}$ and k_{13} can be evaluated using the Debye equation[6] for a reaction between H^+ and divalent negative ions (species A) and between H^+ and dipoles (species C), respectively. The ratio of the two recombination rate constants is then equal to the electrostatic factor in the Debye equation giving $k_{13'}$. With this assumption at pH = pH_A eq 10 becomes

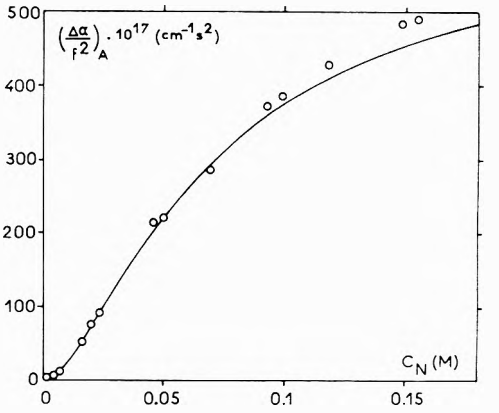

Figure 4. Variation of $(\Delta\alpha/f^2)_A$ with the nucleotide concentration c_N at 2.82 MHz: (O) experimental results: (—) curve calculated as explained in the text using the value f_0 = 0.15 MHz, K_D = 7 M^{-1}, $k_{33'}$ = 4.76 × 10^9 M^{-1} sec^{-1}, ΔV_1 = +5 cm^3/mol, and ΔV_2 = −26 cm^3/mol.

$$f_{II} = \frac{1}{\pi}\left[r + \frac{2r^2}{4K_D\bar{c}_C + 1}\right]\left[k_{33'}\bar{c}_C + \frac{k_{13'}K_N}{1 + 3r}\right] \quad (27)$$

We first looked for the values of K_D, $k_{13'}$, and $k_{33'}$ for which eq 27 gives a good representation of the experimental results of Figure 2. For this purpose eq 27 has been modified to introduce $f_0 = (f_{II})_{c_N \to 0}$ and the slope p_0 of the curve f_{II} *vs.* c_N at $c_N \to 0$. $k_{13'}$ and $k_{33'}$ are given by

$$k_{13'} = \frac{f_0\pi(1 + 3r)}{K_N r(1 + 2r)} \quad (28)$$

and

$$k_{33'} = \pi\left[\frac{p_0}{r} + \frac{8K_D f_0}{(1 + 2r)^2}\right] \quad (29)$$

This was done because the experimental results of Figure 2 give the range of values of f_0 and p_0 to be used in the curve fitting procedure while no such indications are available directly for $k_{13'}$ and $k_{33'}$. A further reduction of the range of values of f_0 was achieved by taking into account that $k_{13'}$ must be smaller than 10^{11} M^{-1} sec^{-1} which represents the calculated rate constant for the diffusion-controlled recombination[6] involving H^+ and divalent negative ions (species A) with a minimum distance of approach of 5 Å. This yields $f_0 < 0.23$ MHz. For each value of f_0, *i.e.*, of $k_{13'}$, there are a number of values of K_D and p_0, *i.e.*, of $k_{33'}$, for which a good fit is obtained with the experimental results of Figure 2. Table I summarizes the results of these calculations. In the first line of Table I are given the experimental value of K_D[15,16] and the theoretical values of $k_{13'}$ and $k_{33'}$ (or k_a') calculated assuming diffusion-controlled reactions. The value of $k_{33'}$ has been calculated using the Debye equation[6] for a reaction between a divalent negative ion (species A) and a donor with a charge +1 (species D) using for A and D the same value of the diffusion coefficient. This value has been taken as $2^{1/3}$ times the diffusion coefficient of the dimer of flavine mononucleotide[18] which is the only value of a diffusion coefficient of a nucleotide that we found in the literature.

The results of Table I have then been used to obtain ΔV_1 and ΔV_2 by curve fitting the experimental results of Figures 3-5. At the outset it must be pointed out that the literature provides no indication on volume change ΔV_1 upon stacking of 5'AMP or other nucleotides. The volume change reported by Pörschke and Eggers[14] for the stacking of N_6-N_9 dimethyladenine cannot be taken into consideration in this work because DMA differs greatly from 5'AMP and the volume change is expected to depend upon the nature of the substituents of the base. However, the fact that only one relaxation process has been observed in our work indicates that the excess absorption due to dimerization must be small, below 4×10^{-17} cm^{-1} sec^2 at 100 MHz. From this upper bound of the excess absorption and by means of eq 9, 15, 17, and 26 one obtains $|\Delta V_1| \leq 7$ cm^3/mol of dimer or $|\Delta V_1| \leq 3.5$ cm^3/mol of nucleotide. In the calculations the values $K_D = 8\ M^{-1}$, $c_N = 0.15\ M$, and $k_d = 5 \times 10^8$ sec^{-1} have been used, with this last quantity obtained by assuming that stacking of species C is diffusion controlled ($(k_a)_{calcd} = 3.7 \times 10^9\ M^{-1}$ sec^{-1}, with a minimum distance of approach equal to 7 Å).

On the other hand, ΔV_2 has been recently determined for 5'AMP and found[19] to be -26.3 cm^3/mol. For this reason we restricted ourselves to values of ΔV_2 in the range

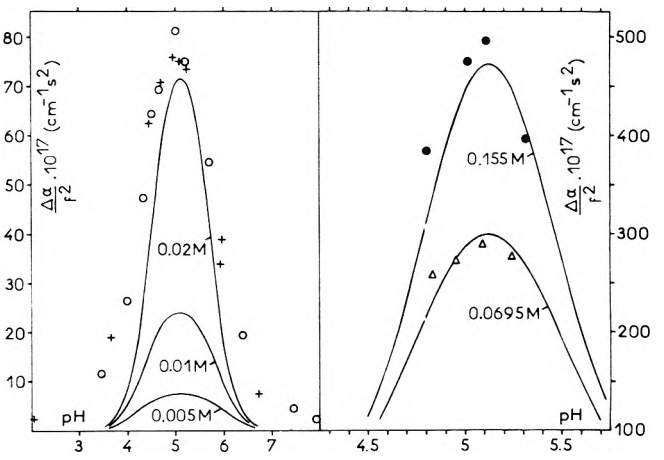

Figure 5. Variation of $\Delta\alpha/f^2$ with pH at different nucleotide concentration and $f = 2.82$ MHz. Experimental results for 5'AMP (○, ●, △) and 5'dAMP (+): (—) curves calculated as explained in the text and with the same values for f_0, K_D, $k_{33'}$, ΔV_1, and ΔV_2 as in Figure 4.

TABLE I: Values of $k_{13'}$, K_D, and $k_{33'}$ for Which the Experimental Results of Figure 2 Can Be Fitted by Eq 27[a]

f_0, MHz	$k_{13'} \times 10^{-10}$, M^{-1} sec^{-1}	K_D, M^{-1}	$k_{33'} \times 10^{-9}$, sec^{-1}
Theoretical (t)or experimental (e) values	10 (t)	8 ± 2 (e)	7.5 (t)
0.3	13.1 (2.5)	4.5 (8)	(3.6) 4.05 (4.7)
0.2	8.7 (4)	6 (10)	(4) 4.44 (5.22)
0.15	6.54 (4.5)	7 (12)	(4.13) 4.76 (5.68)
0.1	4.36 (5)	9 (15)	(4.33) 5.2 (6.2)
0.05	2.18 (6)	11.8 (22.5)	(4.52) 5.79 (7.33)

[a] The values of K_D and $k_{33'}$ in parentheses are those for which the difference between calculated and experimental values of f_R is close to the maximum experimental error. The best fit is obtained for the values which are not in parentheses.

from -23 to -29 cm^3/mol when fitting the experimental results of Figures 3-5 by means of eq 10-18.

The calculations were carried out using the values of K_D and $k_{33'}$ giving the best fit with the results of Figure 2, for each value of f_0. The results of the calculations are given in Figure 6. The solid lines give the values of ΔV_1 and ΔV_2 for which the best fit with the results of Figures 3-5 is obtained. The broken lines give the values which fit the experimental results within the maximum possible error (see Figure 3, curves 1 and 5). The results of Figure 6 allow us to obtain the most probable values of f_0, *i.e.*, of $k_{13'}$, and of K_D and $k_{33'}$ among those listed in Table I. Indeed the condition $\Delta V_1 < 3.5$ cm^3/mol of nucleotide leads to $f_0 > 0.12$ MHz. On the other hand, Table I shows that at values of $f_0 > 0.15$ MHz the calculated value of K_D giving the best fit is somewhat too small compared with the experimental value. This led us to adopt the following set of values: $f_0 = 0.15$ MHz, $k_{13'} = (6.5 \pm 1) \times 10^{10}\ M^{-1}$ sec^{-1}, $K_D = (7 \pm 1)\ M^{-1}$, $k_{33'} = (4.8 \pm 0.5) \times 10^9\ M^{-1}$ sec^{-1}, $\Delta V_1 = (5 \pm 2)$ cm^3/mol of nucleotide, and $\Delta V_2 = (-26 \pm 2)$ cm^3/mol of nucleotide.

These results demand the following remarks.

(1) The value $k_{13'}$ is close to the maximum value 10^{11} M^{-1} sec^{-1} calculated for a diffusion-controlled recombination between H^- and $-O\text{-}PO_3^{2-}$. The difference is al-

most exactly what one can expect with a steric factor 3/4 which accounts for the fact that the proton can bind on any of the three oxygen atoms of the phosphate group, the fourth being involved in the phosphate sugar linkage.

(2) The value found for $k_{33'}$ is smaller by a factor of only 1.5 than the calculated value, thus showing that the proton exchange is diffusion controlled. This result is in agreement with the prediction of Eigen's theory[10] for a proton exchange between a donor and an acceptor characterized by pK_a's differing by more than 2.5 units.

(3) The volume change ΔV_1 is small as expected for a nonionic reaction, and positive thus indicating that stacking is accompanied by an increase of volume as for reaction involving the formation of hydrophobic bonds, such as micelle formation in soap solutions[20] or association between potassium 3,5-dinitrobenzoate and 1-naphthol.[21] All of these results are at variance with those reported by Pörschke and Eggers[14] who found a negative volume change upon stacking of N_6–N_9 dimethyladenine. More experiments appear to be needed before this difference can be explained.

F. Choice between Reaction Mechanisms II and III. As pointed out above it is not possible on the basis of our ultrasonic data to choose between these two reactions mechanisms as the excess absorption is given by the same equation in both cases. Nevertheless, a choice can be made on the basis of physical differences between these two reaction mechanisms and of results of nmr studies of stacking in nucleotides. Indeed, in model III the proton is transferred from the phosphate moiety of species D to the N_1 nitrogen atom of species A by an intramolecular process within the mixed stack (AD). Such a transfer is possible only if the distance between these two sites is not too large. Schweizer, *et al.*,[12] have proposed models for the vertical stacking of bases in 5′AMP solutions. In all of these models the distance between the two sites of the dimer (AD) involved in the proton exchange appears to be too large for an internal proton transfer to occur, as shown by model building (Courtauld models). One is thus led to discard model III and to adopt model II as the most likely reaction mechanism responsible of the excess absorption of 5′AMP around pH 5.

Conclusions

The ultrasonic absorption maximum of large amplitude found in 5′AMP solutions around pH 5 has been shown to be due to proton exchange between differently ionized nucleotide molecules. The results provide evidence for the stacking of nucleotides and yield for this process a volume change of about 5 ± 2 cm³/mol of nucleotide. The increase of volume upon stacking is in line with known results of volume changes for hydrophobic association.[20,21]

The reaction mechanism II is probably also operative in solutions of cytidine and xanthosine 5′-monophosphate. Measurements on these compounds are in progress and will be reported in due course.

Proton exchange may also occur in proteins which include several protonable groups with pK_a's in the range 4–13. The possibility that such a process may be responsible for the still unexplained excess absorption of proteins at neutral pH is now being examined.

Appendix I. Relaxation Frequencies of a System where a Conformational Change is Coupled with a Proton Exchange

The reaction may be written

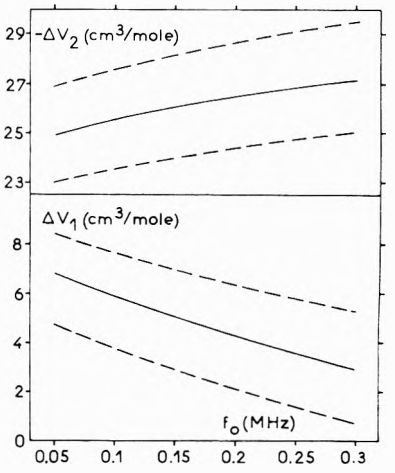

Figure 6. Ranges of possible values for ΔV_1 and ΔV_2 as a function of f_0. The solid lines correspond to values which give the best fit with the results of Figures 3–5. The broken line correspond to values for which a fit is obtained with the maximum possible error.

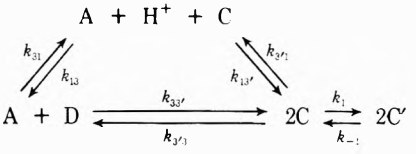

(AI,1)

If we assume that the reactions involving H^+ are in the steady state and that the conformational change equilibrates much faster than the proton exchange the two relaxation frequencies characterizing this mechanism are given by

$$2\pi f_{\mathrm{I}} = k_1 + k_{-1}$$

$$2\pi f_{\mathrm{II}} = \left(\bar{c}_{\mathrm{A}} + \bar{c}_{\mathrm{D}} + 4r\frac{1}{1 + K_1}\bar{c}_{\mathrm{C}}\right) \times \left[k_{33'} + \frac{k_{13'}k_{31}}{k_{13}\bar{c}_{\mathrm{C}} + k_{13}\bar{c}_{\mathrm{A}}}\right]$$

with $K_1 = k_{-1}/k_1$. Because of the stoichiometry of reaction AI,1 $\bar{c}_A$, $\bar{c}_D$, and $\bar{c}_C$ are proportional to c_N. Therefore $2\pi f_{II}$ increases linearly with c_N while $2\pi f_I$ is independent of concentration.

An identical conclusion would be reached if the proton exchange is assumed to equilibrate much faster than the conformational change as can be seen from the following expression of the relaxation frequencies

$$2\pi f_{\mathrm{I}} = \left(\bar{c}_{\mathrm{A}} + \bar{c}_{\mathrm{D}} + 4r\bar{c}_{\mathrm{C}}\right)\left(k_{33'} + \frac{k_{13'}k_{31}}{k_{13}\bar{c}_{\mathrm{C}} + k_{13}\bar{c}_{\mathrm{A}}}\right)$$

$$2\pi f_{\mathrm{II}} = k_{-1} + k_1\frac{\bar{c}_{\mathrm{A}} + \bar{c}_{\mathrm{D}}}{\bar{c}_{\mathrm{A}} + \bar{c}_{\mathrm{D}} + 4r\bar{c}_{\mathrm{C}}}$$

Appendix II. Relaxation Frequencies and Ultrasonic Absorption Associated with a System of Two Coupled Equilibria

The perturbation of a system of two coupled equilibria (1 and 2) results in changes of concentration (referred to as Δc's in the following). For small perturbation ($\Delta c_i \ll \bar{c}_i$, equilibrium concentration of i) the rates of change of concentration can be linearized in the neighborhood of equilibrium. By a proper choice of two independent reactants 1 and 2 associated with reactions 1 and 2, respectively, it is always possible to write the following rate

equations

$$d\Delta c_1/dt = a_{11}\Delta c_1 + a_{12}\Delta c_2$$
$$d\Delta c_2/dt = a_{21}\Delta c_1 + a_{22}\Delta c_2 \quad \text{(AII, 1)}$$

The a_{ij} can be easily obtained in terms of the rate constants and of the equilibrium concentrations of the reactants.

The general procedure outlined by Eigen and de Maeyer[6] permits us to obtain the relaxation frequencies f_I and f_{II} of the system of coupled equilibria in terms of the a_{ij}'s. Here we are interested in the case where one reaction, (1) for instance, equilibrates much faster than the other. In this case f_I and f_{II} become

$$2\pi f_I = -a_{11} = 1/\tau_1$$
$$2\pi f_{II} = -a_{22} + a_{21}(a_{12}/a_{11}) \quad \text{(AII, 2)}$$

where $1/\tau_1$ is the reciprocal of the relaxation time of reaction 1.

On the other hand, a general expression for the excess ultrasonic absorption at frequency f and 25° is given by[6]

$$\frac{\alpha}{f^2} = 1.18 \times 10^{-7}\left[\frac{\Gamma_I \tau_I \Delta V_I^2}{1 + f^2/f_I^2} + \frac{\Gamma_{II}\tau_{II}\Delta V_{II}^2}{1 + f^2/f_{II}^2}\right] \quad \text{(AII, 3)}$$

With the same assumption as above, *i.e.*, (1) faster than (2), it can be shown that

$$\Delta V_I = \Delta V_1$$
$$\Delta V_{II} = \frac{a_{12}}{a_{11}}\Delta V_1 - \Delta V_2 \quad \text{(AII, 4)}$$

where ΔV_1 and ΔV_2 are the volume changes for reactions 1 and 2, expressed respectively in cm^3/mol of 1 and cm^3/mol of 2 and with species 1 and 2 taken as products, *i.e.*, with positive stoichiometric coefficients.

$$\Gamma_I = \Gamma_1 = -RT\left[\left(\frac{\partial A_1}{\partial c_1}\right)_{c_2}\right]^{-1}$$

$$\Gamma_2 = -RT\left\{\left(\frac{a_{12}}{a_{11}}\right)^2\left(\frac{\partial A_1}{\partial c_1}\right)_{c_2} - \frac{a_{12}}{a_{11}}\left[\left(\frac{\partial A_1}{\partial c_2}\right)_{c_1} + \left(\frac{\partial A_2}{\partial c_1}\right)_{c_2}\right] + \left(\frac{\partial A_2}{\partial c_2}\right)_{c_1}\right\}^{-1} \quad \text{(AII, 5)}$$

where A_1 and A_2 are the affinities of reactions 1 and 2.

$$A_i = -RT\sum_j \nu_{ji} \log c_j$$

where the ν_j's are the stoichiometric coefficients (positive for products and negative for reactants). The above expression for Γ_2 is quite general and has never previously been given. It allows the derivation of Γ_2 in particular cases once the derivatives $\partial A_i/\partial c_j$ have been calculated, thus avoiding lengthy calculations. Extensive use of this equation has been made in this paper.

Supplementary Material Available. Value of α/f^2 at pH 5.05 and 9 and of $(\Delta\alpha/f^2)_A$ for four 5'AMP solutions will appear following these pages in the microfilm edition of this volume of the journal. Photocopies of the supplementary material from this paper only or microfiche (105 × 148 mm, 20× reduction, negatives) containing all of the supplementary material for the papers in this issue may be obtained from the Journals Department, American Chemical Society, 1155 16th St., N.W., Washington, D. C. 20036. Remit check or money order for $3.00 for photocopy or $2.00 for microfiche, referring to code number JPC-74-80.

References and Notes

(1) J. Lang, J. Sturm, and R. Zana, *J. Phys. Chem.*, **77**, 2329 (1973).
(2) K. Applegate, L. Slutsky, and C. Parker, *J. Amer. Chem. Soc.*, **90**, 6909 (1968); H. Inoue, *J. Sci. Hiroshima Univ., Ser. A-11*, **34**, 17 (1970); R. D. White, L. J. Slutsky, and S. Pattison, *J. Phys. Chem.*, **75**, 161 (1971); M. Hussey and P. D. Edmonds, *J. Acoust. Soc. Amer.*, **49**, 1309, 1907 (1971).
(3) J. Lang, C. Tondre, and R. Zana, *J. Phys. Chem.*, **75**, 374 (1971).
(4) R. Zana and C. Tondre, *J. Phys. Chem.*, **76**, 1737 (1972).
(5) H. Kanda and Y. Wada, *Rep. Progr. Polym. Phys. Jap.*, **15**, 593 (1972); R. D. White and L. Slutsky, *Biopolymers*, **11**, 1973 (1972); W. O'Brien and F. Dunn, *J. Phys. Chem.*, **76**, 528 (1972).
(6) M. Eigen and L. de Maeyer, "Technique of Organic Chemistry," Vol. VIII, Part II, S. L. Friess, E. S. Lewis and A. Weissberger, Ed., Interscience, New York, N. Y., 1963, p 895; D. Grimshaw and E. Wyn-Jones, *J. Chem. Soc., Faraday Trans. 2*, **69**, 168 (1973).
(7) R. Musa, *J. Acoust. Soc. Amer.*, **30**, 215 (1958).
(8) J. Andreae, R. Bass, E. Heasell, and J. Lamb, *Acustica*, **8**, 131 (1958).
(9) L. M. Rhodes and R. P. Schimmel, *Biochemistry*, **10**, 4426 (1971).
(10) M. Eigen, *Angew. Chem., Int. Ed. Engl.*, **3**, 1 (1964).
(11) J. Lang, J. Sturm, and R. Zana, *C. R. Acad. Sci., Ser. C*, **275**, 597 (1972).
(12) M. P. Schweizer, A. D. Broom, P. O. P. Ts'o, and D. P. Hollis, *J. Amer. Chem. Soc.*, **90**, 1042 (1968).
(13) P. O. P. Ts'o, J. S. Melvin, and A. C. Olson, *J. Amer. Chem. Soc.*, **85**, 1289 (1963); P. O. P. Ts'o and S. I. Chan, *ibid.*, **86**, 4176 (1964); M. P. Schweizer, S. I. Chan, and P. O. P. Ts'o, *ibid.*, **87**, 5241 (1965); A. D. Broom, M. P. Schweizer, and P. O. P. Ts'o, *ibid.*, **89**, 3612 (1967); P. O. P. Ts'o, N. S. Kondo, R. K. Robins, and A. D. Broom, *ibid.*, 5625 (1969).
(14) D. Porschke and F. Eggers, *Eur. J. Biochem.*, **26**, 490 (1972).
(15) G. P. Rossetti and K. E. Van Holde, *Biochem. Biophys. Res. Commun.*, **26**, 717 (1967).
(16) K. E. Van Holde and G. P. Rossetti, *Biochemistry*, **6**, 2189 (1967).
(17) M. Brennan and K. Kustin, *J. Phys. Chem.*, **76**, 2838 (1972).
(18) Q. Gibson, V. Massey, and N. Atherton, *Biochem. J.*, **85**, 369 (1962).
(19) L. Krausz, S. Fitzig, and E. Gabay, *J. Amer. Chem. Soc.*, **94**, 9194 (1972).
(20) L. Benjamin, *J. Phys. Chem.*, **70**, 3790 (1966); K. Shinodo and T. Soda, *ibid.*, **67**, 2072 (1963); J. Corkill, J. Goodman, and T. Walker, *Trans. Faraday Soc.*, **63**, 768 (1967).
(21) A. K. Colter and E. Grunwald, *J. Phys. Chem.*, **74**, 3637 (1970).

Ultrahigh Vacuum Techniques in the Measurement of Contact Angles. III. Water on Copper and Silver[1]

Malcolm E. Schrader

Naval Ship Research and Development Center, Annapolis, Maryland 21402 *(Received July 23, 1973)*

Publication costs assisted by Naval Ship Research and Development Center

Thin films of copper and silver were deposited by evaporation in an ultrahigh vacuum system capable of attaining a pressure of at least 2×10^{-10} Torr. Contact angles of oxygen-free water on the oxide-free metal surfaces were measured *in situ* and found to be 0°. Residual gas analysis with a quadrupole mass spectrometer indicated that hydrogen and often carbon monoxide were released from the surfaces upon exposure to water vapor. This apparently resulted from adsorption of water vapor to displace hydrogen and carbon monoxide previously physisorbed during completion of metal deposition. There is also the possibility that hydrogen was produced through reduction of water molecules by the active clean metal surfaces. The ability of water to displace molecules previously physisorbed to the clean copper and silver surfaces, to yield a 0° contact angle on these surfaces, and possibly to react chemically with the surfaces, all provide evidence that the clean, oxygen-free metal surfaces are decidedly hydrophilic in character.

Introduction

Girifalco and Good[2] originally proposed a method to predict interfacial tensions of liquid–liquid and liquid–solid systems through use of an interaction term involving the geometric mean of the separate surface tensions of the interacting species. Fowkes[3] proposed to separate the surface tension of each substance into additive components, so that, for example, the surface tension of water, γ, would be equal to $\gamma^d + \gamma^h$ where γ^d is a component of the surface tension of water resulting from dispersion forces and γ^h the component resulting from hydrogen bonding forces. Likewise, the surface tension of mercury was described as equal to $\gamma^d + \gamma^m$ where γ^d is the dispersion component and γ^m the so-called metallic force component. Assuming that the dispersion component, γ^d, of the surface tension of one substance would interact with only the dispersion component of the surface tension of other substances, Fowkes used the geometric mean of the dispersion components, $(\gamma_1^d\gamma_2^d)^{1/2}$, as an interaction term. By assuming $\gamma = \gamma^d$ for hydrocarbons and that water and mercury each interact with hydrocarbons only *via* the γ^d component, a γ^d for water and for mercury were calculated, by utilizing the known interfacial tensions of each against one or more hydrocarbons. Utilizing these values of γ^d for water and mercury, Fowkes then calculated an interfacial tension for the mercury–water interface on the basis of the speculative assumption that water and mercury interact with each other in the same manner that each interacts with hydrocarbons. The interfacial tension thus calculated was quite close to the experimentally measured interfacial tension of water and mercury, thus yielding the rather startling conclusion that water and mercury interact by means of dispersion forces only.

The apparent discovery that interaction at the interface of water and mercury involves only dispersion forces led Fowkes to extrapolate this principle to metal surfaces in general.[4] Previous experience with metal surfaces had shown that in the absence of a contaminating organic layer all metals are hydrophilic, *i.e.*, water will spontaneously spread on their surfaces with a zero contact angle.[5] However, the "real" metal surfaces heretofore investigated contain combined oxygen (ranging in nature from a monolayer of chemisorbed oxygen to a thick layer of surface oxide) as a result of their exposure to the atmosphere. These surface metal oxides are capable of strong hydrogen bonding interaction with water. Fowkes hypothesized that an atomically clean oxygen-free metal surface without this hydrogen bonding capability would interact by means of dispersion forces only, which would be inadequate to yield a zero contact angle. The surface of gold provided a convenient test for this hypothesis, since it is uniquely inert to oxygen and does not form a stable oxide phase. In the early and middle 1960's experimental results were reported[6,7] which seemed to indicate that water does indeed yield a finite or high contact angle on the surface of gold. These results remained controversial, however, and in 1970 reports from two different laboratories showed that the contact angle of water on gold free of organic contamination is 0°.[1,8]

It is the purpose of the present work to extend the investigation of the contact angle of water on clean metal surfaces to active metals which form surface oxides, or chemisorbed oxygen monolayers, when exposed to oxygen. In particular, the possibility is considered that clean metals do indeed interact physically with water due to dispersion forces only. To understand why this can be so despite the observed contact angle of 0° for water on gold, it should be noted that the prediction that gold will be hydrophobic really involves two assumptions. First, that water will interact with the surface of clean gold according to the geometric mean rule by means of dispersion forces only. This assumption is basic to Fowkes' approach to the wettability of high-energy surfaces. Second, that γ^d for gold is too small to give sufficient interaction with γ^d of water to cause spreading. This means that γ^d of gold must be less than 236 ergs/cm^2 if γ^d of water is taken as 21.8 ergs/cm^2. The second assumption, which is not basic to Fowkes' theory, is necessary to make gold a suitable test case. The only independent justification for this second assumption comes from a theoretical calculation by Fowkes[4] relating γ^d to the Hamaker constant (A_{12}), which in turn is calculated from data on the stability of gold sols

in aqueous solution. This procedure has been criticized by Gregory,[9] who pointed out that "most interfacial interactions will involve nonadditive effects which would not contribute to longer range forces such as those between colloidal particles." It is nevertheless of considerable interest to determine if the method is useful at least as a semiempirical approach in predicting experimental results on the wettability of clean metal surfaces. Hamaker constants for gold particles in aqueous medium are calculated by Reerink and Overbeek[10] from data by Westgren[11] and Tuorila,[12] with the calculated values of A_{12} ranging over an order of magnitude from 0.05×10^{-12} and 0.1×10^{-12} erg calculated from Westgren's data to 0.6×10^{-12} erg from Tuorila's experiments. Fowkes obtains his maximum value of 120 ergs/cm^2 for γ^d of gold from the latter value of A_{12}. More recently, however, a value of 4.1×10^{-12} erg for the Hamaker constant of gold has been reported by Derjaguin, Muller, and Rabinovich,[13] which yields a value of 464 ergs/cm^2 for γ^d. Since this latter result extends the range of calculated γ^d values for gold well over 236 ergs/cm^2, the possibility may be considered that gold yields a zero contact angle with water as a result of the γ^d interaction alone.

Now, constants representing dispersion interactions have been calculated for some elements and compounds. The calculation is performed utilizing data, for example, from atomic scattering experiments or refractive index measurements to determine parameters in London's equation which allow the calculation of the dispersion force constant. Among the elements, investigation has centered around the inert gases and alkali metals. In all cases, the dispersion or London constant increases going down any column in the periodic table. This is not surprising since the London constant is proportional to the square of the polarizability, and the latter quantity increases with increasing atomic size in any given column. Consequently, in the column copper–silver–gold, one would expect gold to have the largest London constant, silver next, and copper the least. This would also be the order of the Hamaker constants and the γ^d values for the case of gold and silver, where the atomic densities are essentially equal. The case of copper, with a larger atomic density than silver or gold, is harder to predict. However, if its London constant is sufficiently small in magnitude compared to that of silver, its γ^d will also be smaller. If γ^d of silver or copper falls below 236 erg/cm^2, a finite contact angle should be observed if the interaction is exclusively geometric mean of dispersion components.

It should be noted, in passing, that there are some values in the literature which indicate γ^d values for copper and silver considerably less than 236 ergs/cm^2. Harkins and Loeser[14] reported the values of 29 and 37 ergs/cm^2 for spreading pressures determined from adsorption isotherms of *n*-heptane on surfaces which they described as clean copper and silver, respectively. From these spreading pressures, Fowkes[4] calculated γ^d for copper equal to 60 ergs/cm^2 and for silver equal to 74 ergs/cm^2. This agreement with our hypothesis must be regarded as fortuitous, however, since even if clean surfaces were obtained in the conventional vacuum system used, despite the difficulties of obtaining and maintaining surfaces free of all contaminants in this type of vacuum, there is a strong probability of chemisorption taking place upon introduction of *n*-heptane to such active surfaces.

The present work, then, is undertaken for the general purpose of extending the investigation of the contact angle of water to clean metal surfaces other than gold, and specifically, to investigate the possibility that the zero contact angle observed with gold is characteristic only of the heavier solid metals.

Experimental Section

Deposition of Copper and Silver. The vapor transfer method of measuring the contact angles *in situ* on films[1,15] evaporated in ultrahigh vacuum has been described previously. The copper or silver, 99.99% pure, was evaporated from an electrolytically cleaned tungsten basket in a Pyrex sample chamber similar to that used for *in situ* measurements of the contact angle of water on evaporated gold.[1] Each time a glass blowing operation was performed anywhere on the manifold, precautions were taken against the remote possibility of boron contamination.[16] The system was put through three preliminary bakeout cycles each consisting of exposure to water vapor at room temperature vapor pressure followed by a short bakeout into the sorption pump. Following this, the apparatus was put through standard bakeout into the ion pump until a room temperature pressure in the 10^{-10} Torr decade was obtained. The tungsten basket and copper or silver were then degassed at low and high temperatures before deposition of the metal film. The degassing pressure produced during film deposition varied from 1×10^{-8} to as high as 1×10^{-7} Torr. Upon cessation of metal deposition, the pressure dropped slowly back to the 10^{-10} Torr decade.

Residual Gas Composition. Residual gas analysis was performed *in situ* with a Finnigan Instrument Spectra Scan 400 quadrupole residual gas analyzer. The residual gas at 10^{-10} Torr was nearly all hydrogen. Degassing during the metal deposition produced mainly carbon monoxide and additional hydrogen, with no trace of molecular oxygen at any time. The gas analyses were performed in duplicate experiments subsequent to measurement of the contact angles on copper.

Deoxygenation of Water. Extreme precautions were taken to eliminate the possible presence of dissolved oxygen in the water utilized in these experiments as follows. (1) The water was degassed into the sorption pump by momentarily opening a valve and then closing it as the top water layer started to freeze from evaporation. This operation was performed 60 times. (2) The water was exposed to a chamber evacuated to the ultrahigh vacuum region by means of the ion pump. This operation was performed seven times. The water reservoir remaining after treatment according to this and the previous step served as the original source of water vapor throughout all the experiments with copper and silver. For some of the experiments with copper, the following step was added. (3) Prior to admittance to the sample chamber for contact angle measurement, water vapor from the degassed liquid was adsorbed onto clean (oxygen-free) germanium powder in an intermediate chamber and allowed to equilibrate for at least 1 hr (in experiment 4 the germanium was in the sample chamber manifold). The germanium had been previously cleaned by heating *in vacuo* at 700°,[17] and was regenerated after each run. Clean germanium rapidly chemisorbs a monolayer of oxygen. The efficiency of the germanium powder was monitored in a separate experiment by deliberate adsorption of oxygen (after one of the 700° cleanings) which was measured by pressure difference with a thermistor pressure sensor. The amount of

oxygen chemisorbed was approximately equal to that which would have been dissolved in the entire water reservoir if it were in equilibrium with the atmosphere. Since the reservoir was actually thoroughly degassed and since, furthermore, only a small portion of it vaporizes into the vacuum chamber for contact angle measurement, the capacity of the germanium powder far exceeded that necessary to completely free the water vapor of any possible oxygen residue.

Results

Water on Copper. (a) Contact Angle Measurements. The contact angles of water on copper for the various methods of removing possible residual oxygen from the water are listed in Table I. The results one through five were obtained before the quadrupole mass spectrometer was installed in the system. The experiments were consequently run in such a fashion as to successively eliminate possibilities of introducing oxygen contamination to the copper surface. The purpose was to obtain oxygen-free introduction of water vapor with as short and uncomplicated a procedure as possible. A reproducible hydrophobic contact angle at any stage would of course indicate success in oxygen removal while simultaneously demonstrating the hydrophobicity of clean copper. On the other hand, continued zero angles would be inconclusive until the complete absence of oxygen could be independently demonstrated, at which point the hydrophilicity of clean copper would be established. It can be seen that with only one exception, the contact angle of water was 0° throughout, culminating in the experiments where clean powdered germanium, of proven efficiency, was used to getter any possible residue of oxygen. In the lone experiment where a nonzero contact angle (20°) was observed, the failure of a dose of clean oxygen to lower the angle indicated that the hydrophobicity was not due to the presence of a clean, oxygen-free surface, but rather to contamination which apparently resulted from organic ambients picked up by the recycled water during bakeout.

The sixth and seventh experiments were performed to determine if hydrogen, ubiquitous as a residual gas in metal ultrahigh vacuum systems and sometimes used to remove oxide from metal surfaces, would create a hydrophobic metal surface at elevated temperature. No such effect was found under the conditions of the experiment.

(b) Residual Gas Analysis. Upon installation of the quadrupole mass spectrometer in the vacuum system, pertinent portions of the first five experiments in Table I were repeated for the purpose of monitoring the ambients present at various stages of the experiments. The water utilized for contact angle measurements was monitored both by analyzing the atmosphere above frozen water and by leaking vapor from the liquid state. No indication of oxygen was found in the water reservoir after the 67 cycle degassing procedure, with or without additional purification with germanium powder. Exposure of the metal parts of the vacuum system, germanium powder, or evaporated copper to traces of water vapor tended to evolve hydrogen and sometimes carbon monoxide. The interaction of water vapor with deposited copper was found to produce hydrogen and carbon monoxide in varying amounts depending upon the conditions of evaporation.

Water on Silver. The results of the determination of the contact angle of water on evaporated silver are given in Table II. It can be seen that all measurements yield a zero contact angle. Analysis of the gases produced by exposure of the first deposited silver film to water vapor at saturation yielded hydrogen and carbon monoxide in approximately equal amounts. The second film, on the other hand, yielded nearly all hydrogen on exposure to water vapor.

TABLE I: Contact Angle of Water on Deposited Copper Films under Various Conditions

Experiment	Conditions	Contact angle, deg
1	H_2O thoroughly degassed	0
2	H_2O from 1 reused after frozen storage in chamber partially located in bakeout zone	20
3	O_2 admitted to drop of 2	20
4	Degassed H_2O exposed to clean Ge powder in sample chamber manifold	0
5	Degassed H_2O equilibrated with clean Ge powder in upper dosing chamber prior to admission to sample chamber manifold	0
6	H_2 admitted to drop of 5	0
7	Copper film deposited by evaporation in presence of 10^{-7} Torr of H_2	0

TABLE II: Contact Angle of Water on Deposited Silver Films

Film	Drop	Contact angle, deg
1	1	0
	2	0
2	1	0
	2	0
	3	0

Discussion

Measurements of the contact angle of water on evaporated films of copper and silver in ultrahigh vacuum fail to yield any evidence that clean, oxygen-free, metallic surfaces are hydrophobic. In fact, it remains to be determined whether water can come into contact with these active surfaces without decomposing. The exposure of clean copper or silver to even small amounts of moisture results in evolution of hydrogen. While this may be due to the displacement of weakly adsorbed hydrogen from the metal surface by water molecules, the possibility remains that the water has oxidized the surface with consequent evolution of molecular hydrogen. It is planned to utilize Auger electron spectroscopy to resolve this question.

References and Notes

(1) Part II: M. E. Schrader, *J. Phys. Chem.*, **74**, 2313 (1970).
(2) L. A. Girifalco and R. J. Good, *J. Phys. Chem.*, **61**, 904 (1957).
(3) F. M. Fowkes, *J. Phys. Chem.*, **67**, 2538 (1963).
(4) F. M. Fowkes, *Ind. Eng. Chem.*, **56**, (12), 40 (1964).
(5) H. W. Fox and W. A. Zisman, *J. Colloid Sci.*, **5**, 514 (1950).
(6) M. L. White, *J. Phys. Chem.*, **68**, 3083 (1964).
(7) R. A. Erb, *J. Phys. Chem.*, **69**, 1306 (1965).
(8) M. K. Bernett and W. A. Zisman, *J. Phys. Chem.*, **74**, 2309 (1970).
(9) J. Gregory, *Advan. Colloid Interface Sci.*, **2**, 396 (1969).
(10) H. Reerink and J. Th. Overbeek, *Discuss Faraday Soc.*, **18**, 74 (1954).
(11) Westgren, *Ark. Kemi, Min. Geol.*, **7**, No. 6 (1918).
(12) Tuorila, *Kolloidchem. Beih.* **22**, 191 (1926); **27**, 44 (1928).
(13) B. V. Derjaguin, V. M. Muller, and Ya. I. Rabinovich, *Kolloid Zh.*, **31**, 304 (1969).
(14) W. D. Harkins and E. H. Loeser, *J. Chem. Phys.*, **18**, 556 (1950).
(15) Part I: M. E. Schrader, *J. Colloid Interface Sci.*, **27**, 743 (1968).
(16) F. G. Allen, T. M. Buch, and J. T. Law, *J. Appl. Phys.*, **31**, 979 (1960).
(17) A. J. Rosenberg, P. H. Robinson, and H. C. Gatos, *J. Appl. Phys.*, **29**, 771 (1958).

COMMUNICATIONS TO THE EDITOR

An Electron Spin Resonance Study of the Effect of Electron-Releasing Groups upon the Molecular Orbitals of Substituted Cyclooctatetraene Anion Radicals

Publication costs assisted by the University of Puerto Rico

Sir: The effects of electron-releasing groups upon the molecular orbital distribution in cyclic conjugated molecules has been of much recent interest. The fact that an electron-donating group on the benzene system removes the orbital degeneracy of the two lowest antibonding orbitals has been verified by esr studies upon substituted benzene anion radicals.[1] The two nonbonding orbitals in the cyclooctatetraene (COT) system have four nodes each. Similar to the benzene system, the presence of an electron-releasing substituent is expected to split the degeneracy of these two orbitals as shown in Figure 1. Carrington and Todd[2] have generated the anion radicals of some alkyl-substituted cyclooctatetraenes, but they were unable to resolve an ambiguity in assigning the ring proton splittings. They were thus unable to verify this prediction. Further, the reduction of monodeuteriocyclooctatetraene exhibited no splitting of the nonbonding orbitals in disagreement with molecular orbital prediction.[3] Here we wish to verify one of the most significant predictions of the effect of electron-releasing substituents and give a quantitative estimate of this effect.

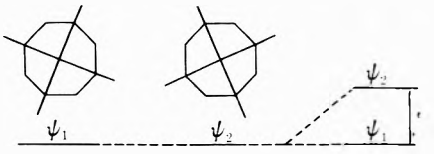

Figure 1. The two nonbonding degenerate orbitals of planar COT splitting due to the presence of an electron-releasing group.

The reduction of 1,3,5,7-tetramethylcyclooctatetraene[4] by potassium metal in hexamethylphosphoramide, using the same technique as previously described,[5] leads to the formation of an anion radical solution yielding a well-resolved esr spectrum. Figure 2. This spectrum consists of 13 equally spaced pentets due to 12 equivalent protons with a coupling constant of 6.29 ± 0.01 G and four equivalent protons with a coupling constant of 0.42 ± 0.01 G. The occupancy of the ψ_2 orbital by the odd electron is in accord with prediction. ψ_2 is strongly destabilized by the presence of the methyl groups and thus contains only the odd electron, while ψ_1 is left essentially unaffected by the presence of the methyl groups and contains two electrons. The fact that the protons in nonnodal positions possess a finite coupling constant indicates that the odd electron is not in a pure ψ_2 orbital but in a combination of the two orbitals. Describing the wave function for the odd electron with a linear combination of ψ_1 and ψ_2 we obtain $\Psi = C_1\psi_1 + C_2\psi_1$. From the esr coupling constants $C_1^2 = 6.29/(6.29 + 0.42)$ and $C_2^2 = 0.42/6.71$ ($\Psi = 0.06\psi_1 + 0.94\psi_2$). The difference in energy between ψ_1 and ψ_2 can now be obtained by the use of eq 1. Solving this expression for ϵ yields a value of 1.60 kcal/mol. Since each alkyl group contributes one fourth of this total splitting, a single alkyl group will cause a splitting of 0.4 kcal/mol.

$$C_1^2 = e^{-\epsilon/kT}/(1 + e^{-\epsilon/kT}) \qquad (1)$$

The reduction of ethylcyclooctatetraene[6] in the same manner yields a well-resolved esr pattern consisting of a quartet of 4.33 G due to three equivalent ring protons, a pentet of 1.99 G due to four equivalent ring protons, a triplet of 2.69 G due to the methylene protons, and a

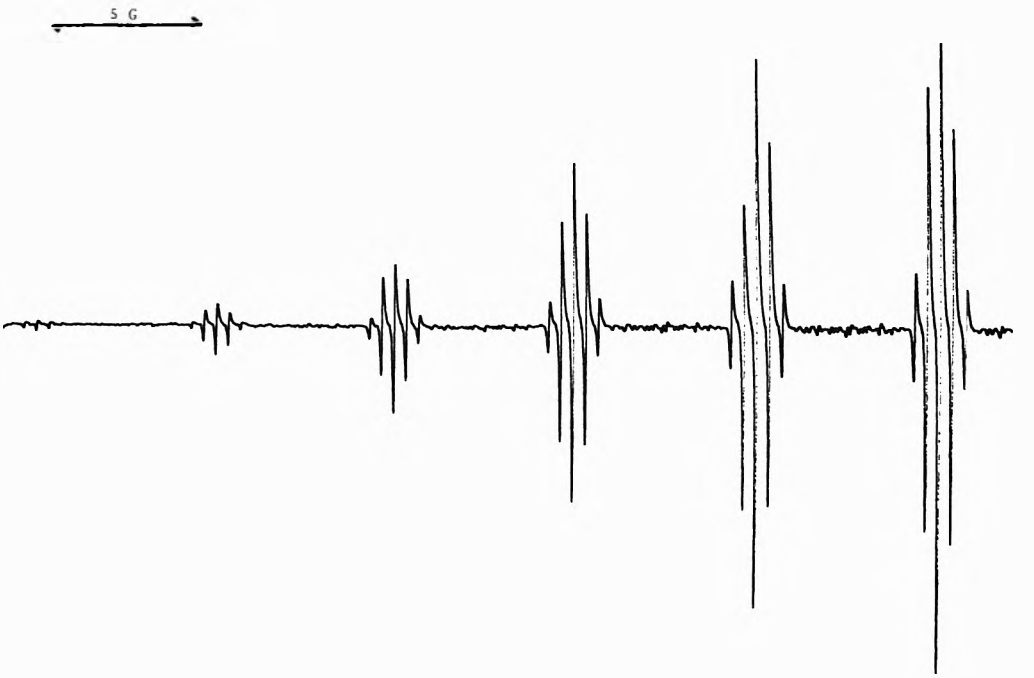

Figure 2. Low-field half of the esr spectrum for the system 1,3,5,7-tetramethylcyclooctatetraene–HMPA–K at room temperature. The first pentet is not shown and cannot be seen at this spectrum amplitude.

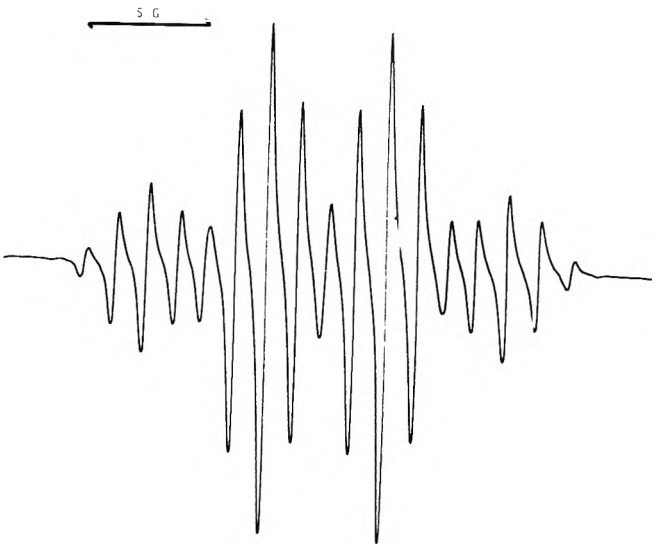

Figure 3. Esr spectrum for the system *tert*-butylcyclooctatetraene–HMPA–K at room temperature.

small quartet from the methylene protons of 0.26 G. These results are in complete agreement with those of Carrington.[2] For this system, the nodal ring proton splitting of 4.33 G and the other ring proton splitting of 1.99 G yield values for C_1^2 and C_2^2 of 0.31 and 0.69, respectively. From eq 1 the splitting of the nonbonding orbitals is found to be 0.45 kcal/mol. This is in good agreement with the value predicted from the tetrasubstituted system.

The reduction of *tert*-butoxycyclooctatetraene[7] in the same manner also yields a well-resolved esr pattern, Figure 3. This spectrum consists of a quartet of 4.89 ± 0.02 G due to three equivalent protons and a pentet of 1.30 ± 0.02 G due to four equivalent protons. For this system C_1^2 = 0.21 and C_2^2 = 0.79 and ϵ = 0.78 kcal/mol. Alkoxy groups are known to be more electron releasing in character than alkyl groups. These results indicate that the splitting of the nonbonding orbitals due to the alkoxy group is about double that for the alkyl group.

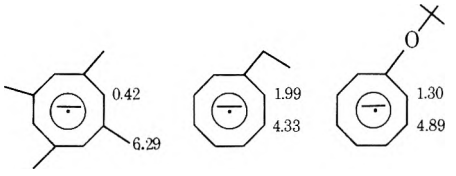

Acknowledgment. We are grateful to Research Corporation for support of this work.

References and Notes

(1) J. R. Bolton and A. Carrington, *Mol. Phys.*, **4**, 497 (1961).
(2) A. Carrington and P. F. Todd, *Mol. Phys.*, **8**, 299 (1964).
(3) R. G. Lawler, J. R. Bolton, G. K. Fraenkel, and T. H. Brown, *J. Amer. Chem. Soc.*, **86**, 520 (1964).
(4) (a) P. deMayo and R. W. Yip, *Proc. Chem. Soc.*, 84 (1964); (b) F. A. Cotton, J. W. Feller, and A. Musco, *J. Amer. Chem. Soc.*, **90**, 1438 (1968).
(5) G. R. Stevenson and J. G. Concepción, *J. Phys. Chem.*, **76**, 2176 (1972).
(6) A. C. Cope and H. O. vanOrden, *J. Amer. Chem. Soc.*, **74**, 175 (1952).
(7) A. Krebs, *Angew. Chem.*, **77**, 966 (1965).

University of Puerto Rico
Department of Chemistry
Rio Piedras, Puerto Rico 00931

Gerald R. Stevenson*
Jesus G. Concepción

Received September 10, 1973

Spin Trapping of Hydrogen Atoms in γ-Irradiated Liquid Alkanes

Publication costs assisted by Wayne State University

Sir: The only direct observation of hydrogen atoms in γ-irradiated alkanes has been in liquid[1] and solid[2] methane by electron paramagnetic resonance (epr). In other alkanes no H atoms are detected by epr either in the liquid during continuous irradiation[1] or in the solid at 4 K after irradiation.[3] Trapped H atoms have also not been detected in other organic systems, such as ethanol and methyltetrahydrofuran, after radiolysis at 4 K.[4] These results imply that thermal H atoms may not be formed in irradiated organic systems. In contrast, thermal H atoms have been indirectly implicated as intermediates in the radiolysis of higher liquid alkanes, such as *n*-pentane, by scavenging studies.[5] In this work we report the indirect observation of thermal H atoms in several organic liquids, including alkanes, by a spin trapping technique.[5]

Spin trapping involves the addition of a short-lived reactive free radical to a nitroso or nitrone function to form a stable spin adduct nitroxide that can be observed by epr to identify the original radical. We use phenyl-*tert*-butyl nitrone (PBN) as the spin trap for which the epr spectra of various spin adducts have been discussed.[6] The spin adduct of PBN with H atoms has a characteristic large β-proton splitting of ~7 G which distinguishes it from the spin adducts with other radicals.[7]

Typically, a 0.1 *M* solution of purified PBN, obtained from Dr. LeBel of this department, is made with the organic liquid of interest. Samples are degassed under vacuum and sealed in 2 mm i.d. quartz tubes. The samples are irradiated with ^{60}Co γ rays at a dose rate of 0.2 Mrad hr^{-1} at room temperature to a typical dose of 0.01 Mrad. Epr spectra are obtained at room temperature with a Varian E-4 spectrometer.

The H atom spin adduct with PBN has been observed in *n*-hexane and 3-methylpentane in the neat liquid. A typical epr spectrum from *n*-hexane is shown in Figure 1a. The prominent lines are a triplet of doublets with A^N ~ 14 G and A_β^H ~ 2 G which is characteristic of alkyl radical spin adducts with PBN. These will not be discussed further here. In addition to the six intense lines, there are six weaker lines, which are shown more clearly in Figure 1b, which comprise six of the nine lines expected for the H atom spin adduct. The other three H atom spin adduct lines are hidden under the strong lines. These weak lines can be analyzed to give A^N = 14.8 ± 0.1 G and A_β^H = 7.0 ± 0.1 G which are unambigously characteristic of the H atom spin adduct of PBN.[7] The same splittings are obtained for the H atom spin adduct observed in 3-methylpentane. Other C, H, O, N containing radicals give spin adducts with PBN with A_β^H = 1.5–4 G.

The observed H atom spin adducts could be formed in at least the two ways given by reactions 1 and 2. Reaction

$$H + PBN \longrightarrow PBNH \quad (1)$$

$$e_m^- + PBN \longrightarrow PBN^- \xrightarrow{\text{hexane}} PBNH + C_6H_{13}^- \quad (2)$$

1 seems most probable to us. In alkane glasses we have found that PBN does not act as an efficient electron scavenger. It also seems doubtful that the proton affinity of $C_6H_{13}^-$ is greater than the proton affinity of PBN^-. Finally, the radical anion of PBN would probably protonate on the oxygen and it is not clear that this adduct would

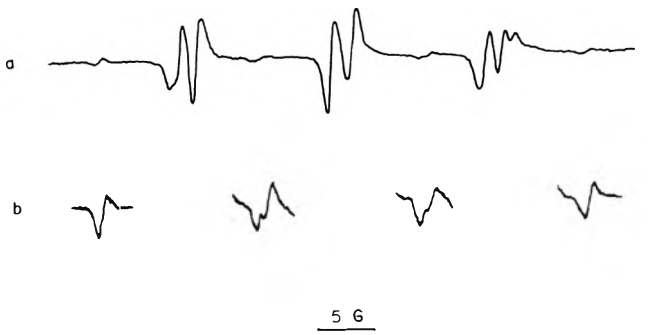

Figure 1. (a) Epr spectrum of 0.1 *M* phenyl-*tert*-butylnitrone in *n*-hexane at room temperature after 0.008 Mrad ^{60}Co γ-irradiation. (b) Weak lines of spectrum in a at tenfold higher sensitivity.

rapidly isomerize to form the observed H atom spin adduct. It should be mentioned that addition of an efficient electron scavenger such as N_2O does not unambiguously distinguish between (1) and (2) because H atoms can be formed by combination of the parent molecular cations with electrons.

Recent work suggests that PBN excited by uv irradiation in alcohols may abstract hydrogen to form the H atom spin adduct.[8] Direct excitation of 0.1 *M* PBN in alkanes by γ-irradiation is negligible because excitation is proportional to electron fraction, and there is little evidence for indirect excitation for low concentration of solutes in γ-irradiated alkanes. So H abstraction by PBN* is not expected to contribute to the observed spin adduct in this work.

Although the intensity of the H atom spin adducts is low compared to that of the other radical spin adducts, this does not necessarily imply that the H atom is low compared to other radical yields. The intensity of a certain spin adduct depends on the spin trapping efficiency, the stability of the spin adduct, and other factors. However, we can conclude that the trapped H atoms are thermal since the PBN concentration is only 0.1 *M*.

Preliminary attempts have also been made to trap H atoms in γ-irradiated solid alkanes at 77 K, but the results are inconclusive at present. In liquid alkanes the H atom spin adduct intensity is below our detection sensitivity at PBN concentrations below ~0.05 *M*. PBN concentrations of 0.1 *M* in 3-methylpentane crystallize out when the solution is rapidly frozen to 77 K. The most concentrated PBN solution that appears to freeze to give a solid solution in either 3-methylpentane or *n*-hexane is about 4×10^{-3} *M*. When this sample is γ-irradiated at 77 K and then warmed to room temperature, an epr spectrum is obtained which is identical with that from a similar sample irradiated at room temperature. Of course the PBN concentration is too low to observe the H atom spin adduct; however, it seems probable that H atoms may be spin trapped in the solid also.

Finally, we have also observed H atom spin adducts with PBN in γ-irradiated liquid methanol, and propionitrile, and in benzene solutions of succinonitrile but not in liquid benzene itself. The formation of the spin adduct in these various systems may well involve more than one mechanism. Further work is in progress.

Acknowledgment. This work was supported by the Air Force Office of Scientific Research in its early stages and by the Atomic Energy Commission in its later stages. We thank Dr. N. LeBel for providing the nitrone and Dr. E. Janzen for helpful discussions.

References and Notes

(1) R. W. Fessenden and R. H. Schuler, *J. Chem. Phys.*, **39**, 2147 (1963).
(2) W. Gordy and R. Morehouse, *Phys. Rev.*, **151**, 207 (1966).
(3) D. Timm and J. E. Willard, *J. Phys. Chem.*, **73**, 2403 (1969).
(4) D. R. Smith and J. J. Pieroni, *Can. J. Chem.*, **45**, 2723 (1967).
(5) R. A. Holroyd, *J. Phys. Chem.*, **70**, 1341 (1966).
(6) E. G. Janzen, *Accounts Chem. Res.*, **4**, 31 (1971).
(7) E. G. Janzen and B. J. Blackburn, *J. Amer. Chem. Soc.*, **91**, 4481 (1969).
(8) E. G. Janzen and D. E. Nutter, private communication.

Department of Chemistry
Wayne State University
Detroit, Michigan 48202

S. W. Mao
Larry Kevan*

Received August 10, 1973

There's nothing theoretical about the value of I&EC Process Design and Development

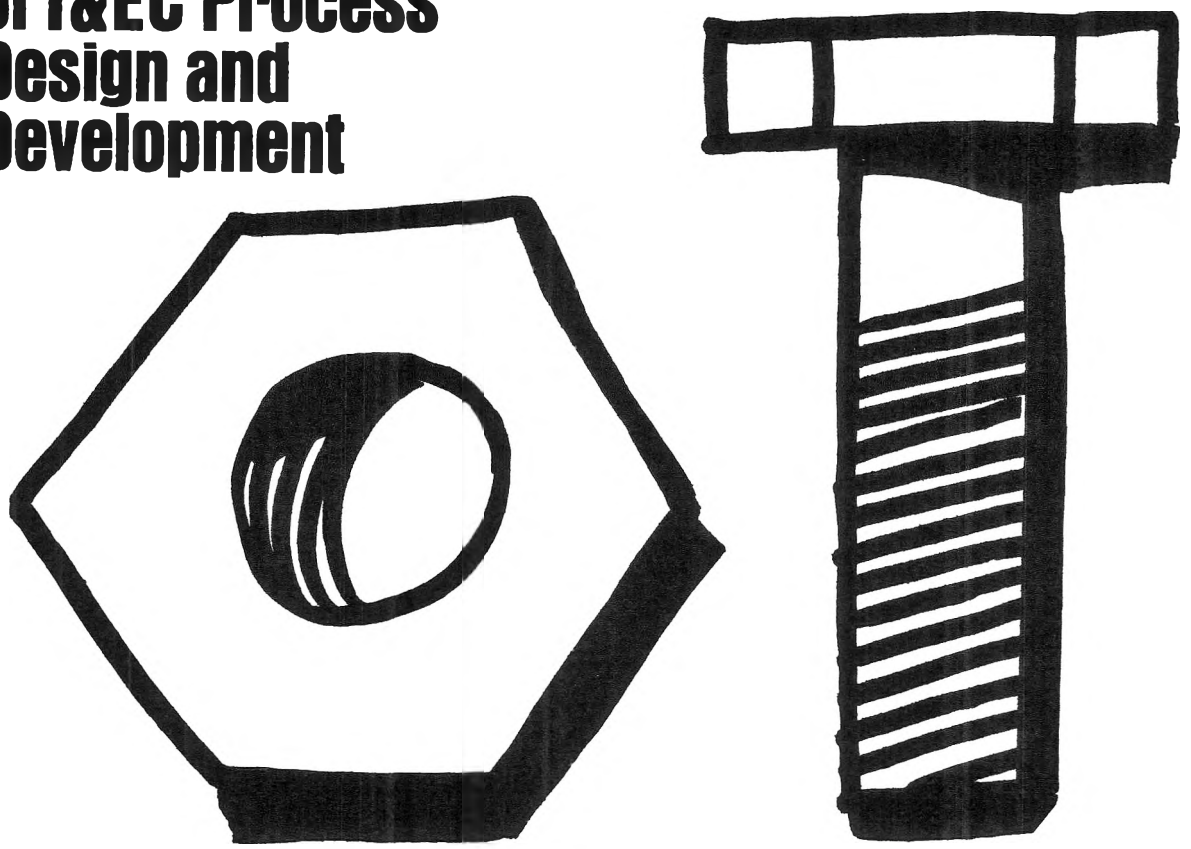

The original papers contained in this quarterly present theoretical and experimental results relating to the development of processes and process equipment—and the value of our publication is a known quantity to our constant readers. Subjects covered include:

- Empirical or Semi-theoretical correlations of data
- Experimental determinations of design parameters
- Methods of integrating systems analysis and process control into process design and development
- Scale-up procedures
- Many other experimental process development techniques.

Put us to the test. Complete and return the order form below today.

. . . *another ACS service*

I&EC Process Design and Development
American Chemical Society
1155 Sixteenth Street, N.W.
Washington, D.C. 20036

Yes, I would like to receive I&EC PROCESS DESIGN AND DEVELOPMENT at the one-year rate checked below:

	U.S.	*Canada*	*Latin America*	*Other Nations*
ACS Member Personal-Use One-Year Rate	☐ $ 7.00	☐ $10.00	☐ $10.00	☐ $10.50
Nonmember	☐ $21.00	☐ $24.00	☐ $24.00	☐ $24.50

Bill me ☐ Bill company ☐ Payment enclosed ☐

Name

Street Home ☐ Business ☐

City State *Zip*

O-73